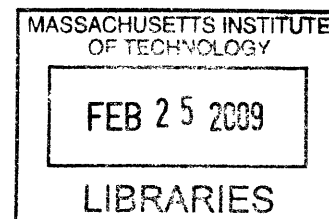# Chirality-Dependent, van der Waals - London Dispersion Interactions of Carbon Nanotube Systems

by

Richard F. Rajter

Bachelor of Science, Materials Science and Engineering
Massachusetts Institute of Technology, 2003

Submitted to the Department of Materials Science and Engineering in partial
fulfillment of the requirements for the degree of

Doctor of Philosophy in Materials Science and Engineering

at the

MASSACHUSETTS INSTITUTE OF TECHNOLOGY

February 2009

Signature of Author ....
Department of Materials Science and Engineering
February 2009

Certified by...
W. Craig Carter
MacVicar Fellow Professor of Materials Science and Engineering
Thesis Supervisor

Certified by...   ....
                                    Yet-Ming Chiang
                        Kyocera Professor of Ceramics
                                    Thesis Supervisor

Accepted by ....
                                    Christine Ortiz
Associate Professor of Materials Science and Engineering
Chairman, Department Committee on Graduate Theses

Chirality-Dependent, van der Waals - London Dispersion Interactions of Carbon Nanotube Systems

by

Richard F. Rajter

Abstract

The Lifshitz formulation is a quantum electrodynamic, first principals formulation used to determine van der Waals - London dispersion interactions in the continuum limit. It has many advantages over crude, pairwise potential models. Most notably, it can solve for complex interactions (e.g. repulsive and multi-body effects) and determine the vdW-Ld interaction magnitude and sign a priori from the optical properties rather than by parameterization. Single wall carbon nanotubes (SWCNTs) represent an ideal class of materials to study vdW-Ld interactions because very small changes in their geometrical construction, via the chirality vector [n,m], can result in vastly different electronic and optical properties. These chirality-dependent optical properties ultimately lead to experimentally exploitable vdW-Ld interactions, which already exist in the literature.

Proper use of the Lifshitz formulation requires 1) An analytical extension for the geometry being studied 2) The optical properties of all materials present and 3) A method to incorporate spatially varying properties. This infrastructure needed to be developed to study the vdW-Ld interactions of SWCNTs systems because they were unavailable at the onset. The biggest shortfall was the lack of the ϵ'' optical properties out to 30+ eV. This was solved by using an ab initio method to obtain this data for 63 SWCNTs and a few MWCNTs. The results showed a clear chirality AND direction dependence that is unique to each [n,m]. Lifshitz and spectral mixing formulations were then derived and introduced respectively for obtaining accurate Hamaker coefficients and vdW-Ld total energies for these optically anisotropic SWC-NTs at both the near and far-limits. With the infrastructure in place, it was now possible to study the trends and breakdowns over a large population as a function of SWCNT class and chirality. A thorough analysis of all these properties at all levels of abstraction yielded a new classification system specific to the vdW-Ld properties of SWCNTs. Additionally, the use of this data and an understanding of the qualitative trends makes it straightforward to design experiments that target, trap, and/or separate specific SWCNTs as a function of SWCNT class, radius, etc.

Acknowledgements

If there is one thing college made me realize, it is the truth of the axiom that "no man is an island." All my life I considered my achievements to be somehow personal rather than as a result of a complex system of support from both the permanent and transient people in my life. Realizing this has opened up the door for a continuous appreciation of all things in my life, good and bad.

I thank my mom for the many sacrifices that she made in her own life to make sure that my brothers and myself had the opportunities we've had. I like to thank my dad for teaching me some of life's most important lessons. Sometimes we learn the most from those who intentionally or unintentionally hurt us the most. I like to thank all those people from my home town who praised me and supported me to take a big leap out of the small town. Most especially, Mr. V., a math teacher who took me on an MIT visit that I wouldn't have made otherwise. Without him and many others, I probably wouldn't have had the audacity to leave my safe life and large support network to start all over at one of the toughest colleges out there.

As for my undergraduate years, a lot of praise and gratitude goes out to my track team and the good fella's at Phi Delta Theta. Without them, I probably wouldn't have made it through my freshman year without burning out. The lessons I learned in mental toughness and support for the team have helped me in incalculable ways these last few years. I'd like to thank my advisors, Professor Carter and Chiang for all the support and latitude given to me in my graduate work. In particular, sticking with me during the first two difficult years, where it seemed like nothing was working or progressing.

A huge thanks to Steve Lustig and his family for all the hospitality and letting me stay with them during my many months of being a visiting scientist at Dupont. To treat a random graduate student like family is something I'll never forget. The same praise is given to Roger French. A simple 5 minute conversation in his office was the spark that ultimately led to virtually everything contained in this thesis. The team of Roger, Wai-Yim Ching, Rudi Podgornik, and Adrian Parsegian was a most rewarding collaboration and has developed into a great friendship. Their advice, teaching, direction, and assistance can be found in every one of our publications.

I also must acknowledge a completely different branch of people that have inspired me greatly during the last 4 years of my life. I acknowledge the great men and women that seek the truth above all else and whatever the cost. They are the trouble makers of all things mainstream. The folks that refuse to leave well enough alone. Men and

women of my heart.

My journey down this path began during my "awakening moment" in 2004 while watching a constitution class video by Michael Badnarik (whom I can't thank enough). This iconoclast spoke with such a fiery passion that it gives me chills and goosebumps every time I watch it. Until this point in my life, I was slave to credentials, degrees, and other benchmarks of societal success. This led to misguided beliefs (e.g. the only people worth listening too were certified, were elected, had money, etc). Thankfully, Mr. Barnarik help me shatter such naive world views aptly and abruptly.

Since then my world views and belief systems have been constantly shifting as the illusions of the world continue to fade layer by layer. It is not an easy life by any means. It also bears a heavy costs on ones emotions, finances, and relationships... and occasionally gets one in legal trouble. But this happened to all of my greatest heroes across all of history: Socrates was executed for his refusal to capitulate on his morals, Copernicus was brought to trial against the church, and Tesla was bankrupted by JP Morgan. But these three and other troublemakers have started whole industries and fields of study that would never have existed if they just shut their mouths.

So why do we continue to do this to those pushing at the bleeding edge? Unfortunately, science continues to be suffering from these same afflictions. It has been infested with dogma rather than open minded inquiry (just watch how high emotions can get in debates on global warming, psi research, or the grand daddy of them all, evolution). If your research uncovers a painful truth, watch dog special-interest groups can and have censored it from well established, mainstream publications. Business interests can force good scientists into building better subscription based pills that can be patented rather than improving well-known and established cures that already exist in nature. To me, this is not the way science was meant to be.

It is for this and many reasons that I support, applaud, and acknowledge all the trouble-making truth seekers out there in the scientific community and beyond. Like me, they have a burning desire to learn the truth, heal the world, and make life better for all that follow after them. I can't thank them enough, even though I can't thank them publicly.

Table of Contents

List of Figures

List of Tables

List of Acronyms

AC Alternating current. Used to describe the dynamic, non-zero frequency terms

DC Direct current. Used to describe the static or zero frequency terms

DFT Density functional theory

DOS Density of states

EELS Electron energy loss spectroscopy. Used to obtain ϵ''.

EM Electromagnetic

EMA Effective mixing approximation

ES Electronic structure (i.e. the band structure)

KK Kramers-Kronig (a transformation for the ϵ'' to vdW-LDS conversion)

MWCNT Multi-wall carbon nanotube

OLCAO Orthaganolized linear combination of atomic orbitals

OP Optical properties

PDOS Partial density of states

S2SS Surface-to-surface separation (a.k.a. ℓ)

SWCNT single wall carbon nanotube

TE total energy

vdW-Ld van der Waals - London dispersion. A general adjective to describe energies, interactions, forces, and spectra related to van der Waals interactions. The explicit noting of "London dispersion" implies this entails using the Lifshitz formulation

vdW-LDS van der Waals - London dispersion spectrum (a.k.a. $\epsilon(\xi)$)

vHs van Hove singularities

zJ Zepto Joules: 10^{-21} Joules. It's equivalent to approximately 1/4 kT per molecule at room temperature

Glossary of Symbols

Notable Roman Symbols

a - radius from rod centers to atom centers of the SWCNTs

$\mathcal{A}(\ell, \theta)$ - Hamaker coefficient

$\mathcal{A}^{(0)}$ - Orientation independent contribution to the total Hamaker coefficient in anisotropic systems.

$\mathcal{A}^{(2)}$ - Orientation dependent contribution to the total Hamaker coefficient in anisotropic systems.

$\mathcal{G}(\ell, \theta)$ - vdW-Ld energy per unit area or length (depends on geometry)

$g(\ell, \theta)$ - vdW-Ld TE

ℓ, L - Surface-to-surface separation

$\mathcal{L}, \mathcal{R}$ - Left and right half spaces

n - Particular Matsubara frequency or power law scaling in $1/\ell^n$

$[n, m]$ - chirality vector

Notable Greek Symbols

Δ_{ij} - Spectral mismatch function between layers i and j.

$\epsilon'(\omega)$ - The real part of the dielectric spectrum at all real frequencies ω.

$\epsilon''(\omega)$ - The imaginary part of the dielectric spectrum at all real frequencies ω.

$\epsilon(\xi)$ - The dielectric spectrum at all imaginary frequencies ξ (aka vdW-LDS).

$\mu(\omega)$ - Magnetic polarizability as a function of frequency. Usually zero beyond 0 eV.

19

ω - Real frequencies.

ξ - Imaginary frequencies.

ξ_n - Matsubara frequencies: the evenly-spaced, temperature-dependent, imaginary frequencies of all vdW-LDS in the system that are in the Lifshitz summation and determine the vdW-Ld TE.

Chapter 1

Introduction

1.1 Motivation for Studying vdW-Ld Interactions of SWCNT

The superlative properties of SWCNTs have inspired a large community of scientists and engineers across many disciplines to try and include these amazing materials into a diverse range of applications[1, 2, 3, 4, 5, 6]. For example, their extremely high tensile strength[7] and other favorable mechanical properties[8] make them ideal for structural reinforcement in composites. These mechanical properties have such a large theoretical upside potential that they have even inspired ideas that are potentially more science-fiction versus a potential reality. The prime example of this is the continued talk of the creation of a space elevator with a shell thickness of approximately a couple nanometers[9]). Whether real or wishful thinking, such a thing would have never been a consideration if it wasn't for the discovery of these amazing materials.

The electron conduction properties of SWCNT systems are equally exciting and potentially have an even larger amount of attention within the community, particularly in the area of electronic structure characterization [10, 11, 12, 13]. The most unique feature of the SWCNT class of materials as a whole is that very small differences in the [n,m] chirality vector can result in very different ES properties. So far, it is possible to get ES metals, 1+ eV band gap semiconductors, and many different

variations in between. Contrast this to metallic materials like copper or insulators like diamond. In these case simple bond stretching or turning will often do very little to their overall ES. Additionally, the small feature sizes SWCNTs also make them highly sought after for the miniaturization of electronic circuitry, which will have huge implications for reducing power consumption because resistance scales with cross sectional area.

Unfortunately, the highly desirable ES properties for applications have largely been confined to simple experiments because of the difficulties that arise in assembling the devices. At the present moment, all publicly known SWCNT creation techniques produce many different chiralities simultaneously[14, 15, 16, 17]. However, most of the components used today in electronic circuitry (e.g. a MOSFET) require a very specific placement of both metallic and semiconducting wires in order to function properly. Therefore the first barrier that must be overcome is the inability to separate the "pasta" of as-created SWCNTs into their mono-disperse constituents.

And even if a technique existed that could either produce and/or sort SWCNT samples that were 99.9999999% pure of a specific chirality, the difficulty in SWCNT placement would still exist. Using the MOSFET example described earlier, it would be self-defeating to spend time and effort to obtain the correct SWCNTs needed for a 0.8 eV band gap if they could not ultimately be placed in the correct arrangement. Therefore, the creation of complex electronic devices (e.g. microprocessor) would require a) the right tubes being placed in b) the right positions for c) many million to billion repetitions with a d) very high degree of accuracy in order for the device to work.

Progress has been made on both of these issues. With respect to separation, experiments like DEP and Anion IEC have proven to be useful in shifting the balance between the semiconducting and metallic classes[18, 19, 20, 21]. They have also proven to be useful in isolating tubes of a single chirality (e.g. the [8,4,s] or the [6,5,s]). Most notably are the experiments by Zheng in which the [6,5,s] and [9,1,s] can be separated despite having an identical band gap and radius[19]. There were also techniques being pursued that used specific chiralities as seeds in producing or

growing a longer version of the same chirality, but its unclear if much progress was ever made on that front. Another variation was to create a nucleation site that was so specific that only one chirality type could be created there. So far, no significant progress has been made on this either to the best of my present knowledge.

For placement, one of the most unique solutions was a combination of AC/DC only attract SWCNTs while simultaneously repelling smaller charged molecules that might otherwise glom on as well[21]. Others have also used functional groups placed on the SWCNTs covalently in order to create a lock and key effect with their corresponding pairs on the substrate[22]. The difficulty here is ensuring perfect or acceptably working registry between the location of the functional groups on the SWCNT corresponding to the traps on the substrate.

But despite the progress of present day sorting/placement experiments, there is still a tremendous amount of work to be done in order to achieve wide-scale commercial and industrially usage. For instance: some of the working separation experiments have many different theoretical explanations as to why they work. Without knowing the exact mechanisms, making smart decisions on how to optimize them can be quiet difficult. One may in fact be optimizing a tertiary phenomenon and completely missing the sensitive parameters. For example, the first mechanism proposed for the Zheng experiments was based on image-charging effects[23]. The near infinite polarizability of a metallic SWCNT core versus a semiconductor SWCNT core material would drastically change around the effective charge on the phosphate backbone of the ssDNA, which was used as the surfactant to keep the SWCNTs from agglomerating.

This was a very logical avenue to explain the separation between the major electronic conduction classes (i.e. metallic versus semiconducting). And indeed the image charge model's results agreed with the observed phenomenon at the time. However the ability to routinely separate between semiconductors was later discovered. In this scenario, there is no longer the several order of magnitude difference in the 0eV or DC polarizability behavior. For semiconductors, this variation is at most a factor of 2 and usually much less than 1 for semiconducting SWCNTs of comparable diameter. Therefore the model needs to be revisited to see if there is still enough control via

this mechanism, or a new component needs to be added to the model altogether.

A study of the fundamental SWCNT interactions seems like a logical way to narrow down this list of explanations as well as provide a proper framework to make predictions and smart experimental design choices. I was particularly interested and motivated to study of the vdW-Ld interactions because they were largely unstudied or poorly approximated for SWCNT systems[25, 26, 27, 28]. Additionally, both image charging and vdW-Ld interactons depend on the chirality and orientation-dependent optical properties for each SWCNT. So a study of the vdW-Ld interactions would ultimately obtain that optical data required to answer both questions.

Actually completing a vdW-Ld analysis for SWCNTs proved to be quite a difficult task and multiple-year endeavor because several key needs were not available at the time. The two most notable were: 1) No publicly known optical property database for SWCNTs nor a published means of obtaining them. 2) The lack of a Lifshitz formulations specifically for optically anisotropic rods[27].

A non-linear formulation like the Lifshitz formulation is only as good as the input data that is fed into it. Otherwise the GIGO situation applies (i.e. garbage in, garbage out). This situation is particularly magnified by the numerous layers of abstraction within a SWCNT's optical properties versus [n,m] and numerous components contained within the Lifshitz summation. A simple error in band structure information will change around the DOS, ϵ'', the Hamaker coefficient, etc etc. This makes data analysis difficult because a tracked trend or novel feature may in fact just be a error propagating through each layer of abstraction.

So having quality data is essential. Unfortunately, obtaining this quality data over a frequency range large enough to satisfy the requirements of the Lifshitz formulation is quite difficult, if not impossible by experimental means for SWCNT systems. The small feature sizes of SWCNTs make it difficult to get measure its properties in the long wavelength range. And the optical properties of these very thin materials can be influenced/affected by whatever surfactant is coating them or whatever mounting device is used to hold them. The only exception to this has been the experimental EELS work by Stephan et al[29]. But while these experimental results greatly agree

and confirmation on some major optical features in the 10+ eV range, the data itself is insufficient for a quantitative analysis direction and chirality specific interactions.

Using the proper Lifshitz formulation is also very important, particularly when there is a substantial change in the weighting of the spectral mismatch functions[30]. Because this weighting can amplify or dampen some interactions more than others, the use of the wrong formulation can result in the incorrect relative magnitude of the interactions. It can even result in the wrong sign (attraction versus repulsion). While this type of attraction/repulsion reversal would not be typical for most simple vdW-Ld calculations (which are typically attractive or repulsive across all the energy ranges), more complex and designed systems can include these additional nuances. It is particularly important when there are many components present and many possible multi-body interactions.

These shortcomings (lack of robust optical properties and proper Lifshitz) are non-trivial. They are also required for any legitimate chirality-dependent analysis, whether it be focused on total or relative vdW-Ld energy. It is only then that one can confidently and quantitatively answer the fundamental questions relating to vdW-Ld interactions for SWCNT system.

Therefore the purpose of this thesis is two fold. The first is to develop the infrastructure needed to remove these two barriers in order calculate vdW-Ld interactions relevant to the experiments for end-users. An example of such a system is a surfactant coated SWCNT interacting with a coated substrate across water. The second major goal is to use this new infrastructure to a) find vdW-Ld dependent trends as a function of SWCNT radius and/or classification b) find breakdowns from these trends and describe their importance and why they occur c) using the knowledge in the previous steps, demonstrate how one can design systems to attract or repel SWCNTs of a specific chirality or set of chiralities. The developmental roadmap is as follows.

1.2 Development Road Map

Chapter 2 details the pertinent historical facts and overview of the modern day Lifshitz Theory for vdW-Ld interactions. It also pinpoint where the key shortcomings are in the formulation/framework that render it insufficient for chirality-dependent vdW-Ld interactions for SWCNTs. Figure 1-2 shows what was available and what was missing on the onset of this work. In contrast, the ultimate goal is to get to the completed framework shown in Figure 1-1, which is obtained in the following manner.

Chapter 3 introduces the ab initio method for determining the ϵ'' properties for the SWCNTs contained in this thesis. Included is a dicussion superior to all the other methods present for SWCNT systems, why it alone gives us the energy range necessary for true vdW-Ld interactions, and show the nature of the resulting chirality-dependent and direction-dependent vdW-LDS. At this stage, the required anisotropic rod-rod formulations are not present to use this information in the most accurate way possible. However, even crude pairwise radial-radial, radial-axial, and axial-axial calculations using the plane-plane Lifshitz formulation shows notable direction and chirality-dependance Hamaker coefficients[25].

Next, chapter 4 introduces the anisotropic rod-rod and rod-surface formulations at the near and far-limits[26]. Demonstrable differences in the chirality, orientation, and separation dependent Hamaker coefficients can not be obtained previously in chapter 3. The key features causing these effects (namely the changes in the spectral mismatch function behavior) are highlighted and discussed.

Chapter 5 introduces the spectral mixing formulations required for effective far-limit, vdW-Lds interactions[28]. Singly dispersed SWCNTs used by experimentalists are fundamentally multi-component and the ability to include the optical spectra of the SWCNT, the inner core, and the surfactant properties simultaneously is imperative for accurate results. The mixing formulation also allows for the creation of MWCNTs from SWCNT components.

Once completed, chapters 3, 4, and 5 represent the infrastructure portion of this thesis. Combined with other components of the Lifshitz foundation (Chapter 2),

Calculating a van der Waals - London
Dispersion Energy via Lifshitz Formulation
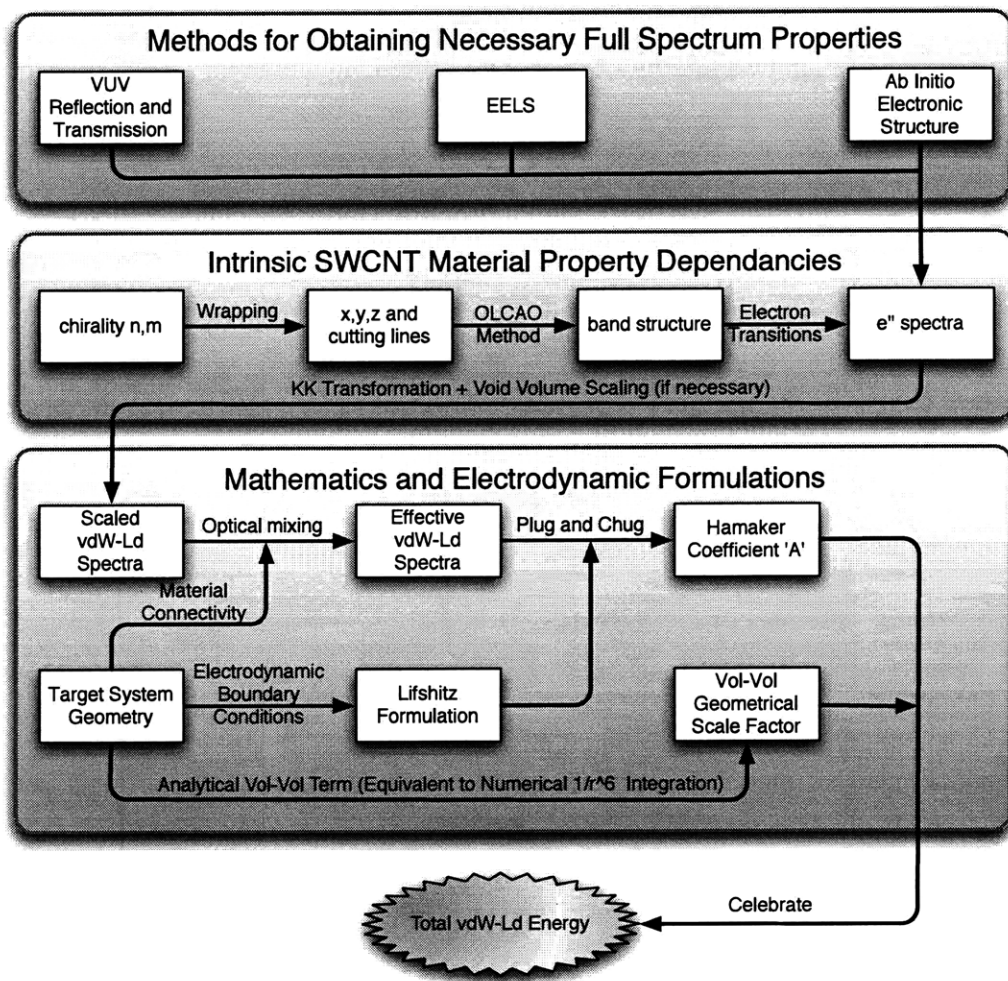
Figure 1-1: The complete flow chart of the Lifshitz formulation/framework that is necessary for calculating and understanding the physical origin of the chirality-dependent Hamaker coefficients and vdW-Ld total energies of SWCNT systems.

Status of a SWCNT vdW-Ld Calculation at the Onset of this Thesis.
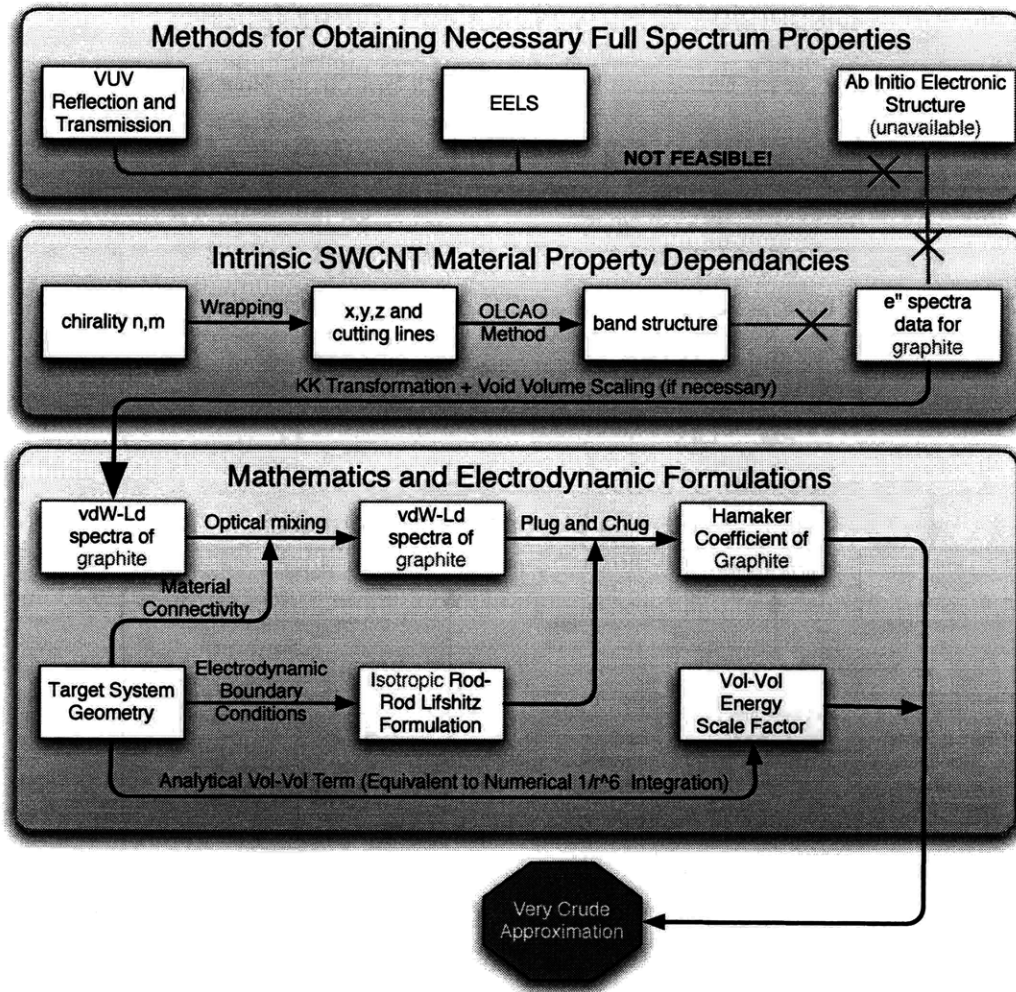
Figure 1-2: The state of the Lifshitz formulation/framework at the onset of this thesis as it relates to the determination of chirality-dependent Hamaker coefficients and vdW-Ld total energies for SWCNT systems. Significant barriers existed at the various stages, which required new formulations and methods to be developed and/or obtained.

it is now possible to perform a complete vdW-Ld TE calculation for an end-user quality SWCNT system. It is also possible to study these interactions as a collection and at all levels of abstraction shown in Figure 1-1. Chapter 6 is the culmination of this process and labeled "datamining" because of the large quantity of searching and sifting for trends, noteworthy effects, breakdowns, contradictions to previous classification systems, etc between all these various levels of abstraction.

What ultimately results from the datamining process is 3 things. The first is simply knowing how to trace and link all of these interactions back down to a single fundamental building block (i.e. the chirality vector [n,m]). Some of the results were non-intuitive based on the SWCNT classification systems typically used for ES properties[13, 37]. This leads the second important output, which is the need for a new way to classify the SWCNTs vdW-Ld interactions by a combination of their structure (zig-zag, armchair, or chiral) and well as their ES properties (metal, small-gap metal, and semiconductor). This need to include the structure descriptor arises due to the strong dependence of ϵ'', vdW-LDS, Hamaker, and vdW-Ld TE stages on the underlying geometry. Relying solely on ES classifications systems that are geared for ES properties prevents these effects from being properly grouped and studied.

The last and most important part arises out of a combination of the previous two. By knowing how the effects of [n,m] perpetuate through the various levels of abstraction and knowing how the different classes show patterns or trends in their effects, it is then possible design systems that can exploit these effects experimentally. This can empower the end-user immensely by giving them guidance as to the regimes the vdW-Ld interactions can contribute significantly for the desired objective (e.g. separation) and in what situations will these be effects be secondary, tertiary, etc.

Figure 1-3 pictorially shows these elements and how they relate to the given chapters in this thesis.

Thesis Roadmap

Things I had at the Onset

| e" spectra of graphite | Target System Geometry | Vol-Vol Integration Scale Factor | Plane-Plane Lifshitz Formulation |

Things I needed to Obtain/Derive/Use/Etc

| Ab Initio Electronic Structure Method | Anisotropic e" spectra of SWCNTs | Anisotropic Rod-Rod Lifshitz Formulation | Spectral Mixing Formulation for SWCNTs systems |
| Chapter 3 | Chapter 3 | Chapter 4 | Chapter 5 |

Results and Outcomes

| SWCNT Hamaker Coefficients | SWCNT Total vdW-Ld Energy |
| Chapter 6 | Chapter 6 |

Figure 1-3: The chapter roadmap of this thesis. The basic breakdown is 3 tiers: the foundations, the new infrastructure, and the resulting analysis.

Chapter 2

Lifshitz Formulation Primer for vdW-Ld Interactions

This chapter is intended to be a brief primer detailing the key historical milestones that lead up to the Lifshitz formulation, which is widely accepted the standard for determining quantitatively accurate, vdW-Ld interactions. I highly recommend the book *van der Waals Forces* by Parsegian[ ] and the review article *Origins and Applications of London Dispersion Forces and Hamaker Constants in Ceramics* by French[ ] for those needing/wanting a more thorough overview of Lifshitz theory from their respective theoretical and experimental vantage points.

2.1   The Beginnings: Pairwise Interactions

The study of van der Waals forces was essentially started by the discovery of a breakdown from the ideal gas law at very high pressures[ ]. It was in this high pressure regime that the assumptions of non-interacting and zero volume particles was no longer true. Two terms were added to account for these effects, and the original ideal gas law was modified as follows:

$$(p + \frac{a}{v^2})(v - b) = kT \tag{2.1}$$

31

Where 'p' is the pressure, 'v' is the volume, 'k' is the boltzmann constant, 'T' is the temperature. The variable 'b' is the excluded volume due to the finite size of the particle. The origin of the van der Waals interactions manifests itself as the variable 'a'. At the time, the value of 'a' included the combined intermolecular forces present in the system and not necessarily vdW only (i.e. it could include coulombic and acid base interactions as well). However for neutral gas molecules (having no fixed dipole moments), 'a' contained only vdW contributions.

As the interactions were studied more closely, it was further discovered that the contributions to the vdW interaction could be differentiated into 3 general categories: dipole-dipole (Keesom), dipole-induced dipole (Debye), and induced dipole-induced dipole (London or "dispersion")[34, 30, 33]. Of the three forces, only the London dispersion force is present in all systems because even neutral molecules experience temporary charge fluctuations away from neutral.

The Lifshitz formulation calculates all 3 terms simultaneously because the input vdW-LDS embeds both fixed dipole moments as well as the polarizability/optical properties across all frequencies[30]. The London dispersion term, however, is the only component that is always present and usually the most dominating in magnitude. From a purists perspective, anything calculated by the Lifshitz formulation can be rightly labeled as simply vdW because it embeds all 3 components. However, the term "van der Waals" or vdW term is so abused and misused throughout the literature as a catch all "fudge factor" for "pair-wise interaction" that I decided to call it vdW-Ld to clearly differentiate it from the rest. My reasoning was and still is that the only way to accurately determine the London dispersion component is through the Lifshitz formulation. Therefore any useage of vdW-Ld or vdW-LDS in this or any of my previous writings means that the discussion is related to the Lifshitz formulation and not 1) any of the various vdW approximation or 2) any of the other intermolecular forces that get lumped in with true vdW-Ld interactions.

Returning back to Equation 2.1, 'a' was initially parameterized from experiments because vdW interactions were assumed to be always attractive and pairwise. That is to say it was assumed that everything attracted regardless of the other materials

in the environment. It was also assumed that the interaction was purely dependent on the 2 interacting particles and the distance between them. This led to the widely Lennard-Jones Pair Potential form[30].

$$w(r) = -\frac{C}{r^6} + \frac{D}{r^{12}} \tag{2.2}$$

where

$$\mathcal{A} = \pi^2 * C * \rho_1 * \rho_2 \tag{2.3}$$

The $'w(r)'$ is the energy gained from each pairwise interaction with $'C'$ being the interaction coefficient and $'r'$ being the atom-to-atom separation distance. The $'D'$ and $'r^{1}2'$ terms are conveniently chosen fudge factors to provide the necessary repulsive force at contact. The interaction factor $'C'$ relates to the Hamaker coefficient by the $'\rho_1'$ and $'\rho_2'$ densities of the interacting objects[34, 30].

While this model can work surprisingly well for some simple systems, many problems can and do arise. The assumption of pairwise additivity excluded any and all multi-body effects. The only way to shoehorn them back in would be to tweak the $'C'$ parameters for include every possible environment scenario (i.e. the type and quantities of atoms present between and around the interacting pair). Clearly this would be far too difficult to achieve except for the simplest of combinations. Related to this was the assumption of no medium. This is equivalent to the claim that the Na+ and Cl- ions in NaCl would have the same vdW energy in air versus a high dielectric material like water. That is simply not the case. And finally, there really is no predictive behavior. If one brings in new elements or bond types into the simulation, there is no way to know what will happen a priori.

For a study of SWCNTs, the problem of a pairwise interaction runs a little deeper. Theoretically, how would one have chirality-dependent optical properties if the simulation pair potential of for all carbon atoms was the same for each chirality? One solution is that the parameter could be changed to account for differences in bond angles. Yet zig-zag tubes all have virtually the same bond angles and can exhibit

metallic or semi-conducting behavior[35]. Ultimately one would have to parameterize pair potential values between each set of chiralities. Using vdW-LDS and the Lifshitz formulation, this tedious hassle is not necessary and the interaction potentials can be determined from first principles a priori rather than fit after the fact. If necessary for atomistic simulations, the Lifshitz formulation values could be crudely bootstrapped into the pair-potential form without the need to parameterize from experimental values.

2.2 From Pairwise to First-Principles, Multi-Body Interactions

A major transition away from the vdW-Ld theory's pairwise paradigm occurred with the introduction of the Casimir effect in 1948[38, 39, 40, 41]. Rather than looking at the system as momentary fluctuations in matter, Casimir eliminated matter all together and only considered virtual EM fluctuations in the vacuum[30, 42]. Matter was replaced by perfectly conducting walls and the result EM pressure/attraction was caused by changes in the wave free energy between the plates as a function of separation. This formulation was successful, but limited to systems in vacuum that contained only perfectly conducting metals (i.e. no dielectric materials with finite polarizabilities). Despite this and additional (albeit it minor) limitations, the Casimir formulation was instrumental in being foundational groundwork for the more generalized Lifshitz formulation extension introduced just 6 years later in 1954[43, 44, 30].

The Lifshitz formulation provided many advantages over the shortcomings in pairwise vdW-Ld models. First, it is a completely a priori, first principals QED calculation. So rather than having to fit vdW-Ld interaction parameters for every possible combination of materials in a system, the formulation could take the material optical spectra (i.e. the input data for the Lifshitz formulation) and determine these interactions beforehand.

The inclusion of material properties also allows the Lifshitz formulation to account for all virtual EM fluctuations interactions from the 0 eV static term to infinitely fast frequencies. Practically this is upper limit isn't possible. But fortunately it is not typically needed because many materials will not have any appreciable ϵ'' optical transitions above 50+ eV. This gives a tremendous power in system design and interaction predictability. The addition of material properties in the Lifshitz also opened the door to study system well beyond perfect metals separated by vacuum. Now one could address intergranular films, colloids, etc.

The Lifshitz formulation was also inherently a multi-body interaction. In a pairwise material model, one primarily considers only the interaction parameter of object A and B scaled by some distance scale factor of the form $1/r^n$. But a virtual photon exchange will be altered by differences in optical properties between and around these interacting objects. This is most clearly demonstrated by the add-a layer formulation extension, in which an arbitrary number of coatings can be added to the system, with all of them altering the final or total vdW-Ld interaction. The pairwise formulations cannot handle such a complexity.

The exact form of the 3 component, isotropic plane-plane system Lifshitz formulations is as follows[36]:

$$G = \frac{kT}{8\pi L^2} \sum_{n=0,1,2..}^{\infty} \int_0^\infty x \, ln((1 - \Delta_{32}\Delta_{12} \, e^{-x})(1 - \bar{\Delta}_{32}\bar{\Delta}_{21} \, e^{-x}))dx \qquad (2.4)$$

$$\Delta_{ij} = \frac{x_j\epsilon_i - x_i\epsilon_j}{x_j\epsilon_i + x_i\epsilon_j} \quad \bar{\Delta}_{ij} = \frac{x_j\mu_i - x_i\mu_j}{x_j\mu_i + x_i\mu_j} \qquad (2.5)$$

$$x_i^2 = x_m^2 + (\frac{2l\xi_n}{c})^2(\epsilon_i\mu_i - \epsilon_m\mu_m) \qquad (2.6)$$

$$\xi_n = \frac{2\pi \, kT \, n}{\hbar} \qquad (2.7)$$

$$r_n = (2l\epsilon_m^{1/2}\mu_m^{1/2}/c)\xi_n \qquad (2.8)$$

Many systems do not need to use all parts of this complete form and/or certain approximations are made. First most materials exhibit no or very weak magnetic polarizability and therefore all the $\bar{\Delta}_{ij}$ terms (containing the μ) drop away. Often people neglect retardation effects and assume instant communication between the interacting materials. This is equivalent to setting the speed of light variable 'c' to infinity and therefore r_n goes to zero. At contact/adsorption distances, there is no retardation anyway and thus this assumption is ideal to use in simplifying the calculations. A Taylor series expansion on the integration term is typically done to give an equivalent form that eliminates the logarithmic portions. Since the higher order terms are typically much smaller than the first expansion, the integral can sometimes be eliminated all together. The only exception is for situations of extreme optical contrast (i.e. infinity versus 1). The result of all these approximations and assumptions is as follows[30].

$$\mathcal{G} = \mathcal{A} * \frac{1}{12\pi\ell^2} \tag{2.9}$$

$$\mathcal{A} = \frac{3kT}{2} \sum_{n=0,1,2..}^{\infty} \prime = \Delta_{ij} * \Delta_{kj} \tag{2.10}$$

$$\Delta_{ij} = \frac{\epsilon_i - \epsilon_j}{\epsilon_i + \epsilon_j} \tag{2.11}$$

Where $\mathcal{G}$ is the vdW-Ld TE, ℓ is the surface-to-surface separation, k is the boltzmann constant, T is the ambient temperature, $\mathcal{A}$ is the non-retarded Hamaker coefficient (actually a "constant" in the non-retarded domain, but I typically choose to use "coefficient" to describe the general sense in which retardation effects can change the Hamaker coefficient with distance), and the Δ_{ij}'s are the spectral mismatch terms that weight the optical contrast at their respective interfaces. The prime symbol on the summation indicates that the first term is multiplied by 1/2. The summation is over the discrete Matsubara frequencies denoted by n, which are spaced in 0.16 eV increments at room temperature as per Equation 2.7.

One should always use the full Lifshitz form whenever possible in order to calculate

the most accurate vdW-Ld TE and Hamaker coefficients. However for illustrative purposes, this form contains lots of extraneous details that get in the way of a quick explanation and understanding of where the areas of high impact reside. It is for this reason that I prefer to focus on the simplified, non-retarded form in order to clarify the effects optical properties, geometry, and spatial arrangement on the vdW-Ld interactions.

The Hamaker coefficient essentially represents the total vdW-Ld interaction strength density of components L and R across a medium 'm'. This total interaction is made up of an infinite summation of individual contributions at each Matsubara frequencies 'n'. These individual contributions can be zero, positive (attractive), or negative (repulsive) based the optical contrast at each phase interphase in a material.

The way that these optical properties are input into this summation is via each material's vdW-LDS (van der Waals - London dispersion spectra) or $\epsilon(\xi)$. The vdW-LDS is not a property that is typically calculated for any other reason besides vdW-Ld interactions. It is also a constant source of confusion for many people not already experienced with it primarily because of subtleties in the terminology. The vdW-LDS is the real part ϵ of the dielectric spectrum over all imaginary frequencies ξ. As a matter of fact, there is no imaginary part over imaginary frequencies, one can simply call $\epsilon(\xi)$ is the "real part of the dielectric spectrum over imaginary f. However because this is still wordy and because it is still easy to confuse $\epsilon(\xi)$ with $\epsilon'(\omega)$ and $\imath\epsilon''(\omega)$, I typically refer to $\epsilon(\xi)$ as simply vdW-LDS to avoid confusion and being overly verbose in description.

By contrast, there is a lot more study and literature on the real and imaginary parts of the dielectric spectrum over real frequencies ($\epsilon'(\omega)$ and $\imath\epsilon''(\omega)$ respectively). Since ϵ'' denotes the imaginary part over real frequencies, many tend to drop the $\imath$ label and assume it to be there. The same thing is true of the explicit (ω) because all optical properties are frequency dependent. Therefore, in another attempt to eliminate as much confusion and verbiage as possible, I use ϵ'' and vdW-LDS as short hand to differentiate between these two means of representing the material properties.

But regardless of this confusion, the relationship between vdW-LDS to the measur-

able material property ϵ'' is straightforward via the Kramers-Kronig (KK) transformation[45, 34, 33].

$$\epsilon(i\xi) = 1 + \frac{2}{\pi} \int_0^\infty \frac{\epsilon''(\omega) * \omega d\omega}{\omega^2 + \xi^2}, \tag{2.12}$$

Once the vdW-LDS are known for each material present in the system, calculating the magnitude and sign of each contribution for each summation term in Equation 2.10 is fairly straightforward. The magnitude of each contribution is primarily determined by the degree of optical contrast. For example, when L and R are both much more polarizable than the medium m, the Δ_{Lm} and Δ_{Rm} terms will be close to unity and contribute the maximum possible quantity of attraction possible at this frequency. If material L has a vdW-LDS identical in strength to the medium at the given frequency, then the contribution to the Lifshitz formulation is zero because material R would have no net preference of being around L or m. To put this in more vivid terms, two metals separated by vacuum would have a much stronger attraction than two polymers separated by a organic liquid of similar chemical composition. In the latter example, there is only a subtle difference in the polarizability and thus no overwhelming preference in which material to attract.

The sign of each contribution also depends on the stacking order of these relative vdW-LDS differences. For example, if the L and R materials have vdW-LDS strengths that straddle the medium, then L and R would experience a repulsive contribution. Conceptually this happens because the total energy of the system would be minimized by keeping these materials immersed in the medium rather than near each other. Conversely, if the two particles have vdW-LDS that are both stronger or both weaker than the medium over all frequencies, the total energy can be minimized by driving them together as an attractive force. Illustratively, this is similar in effect to a Galileo thermometer. For these devices, the relative buoyancy of the floating pieces compared to the density of the temperature-dependent medium determines which pieces float to the top and which pieces collectively sink to the bottom together.

It is important to note that the stacking order and magnitudes of each Lifshitz

summation contribution can potentially vary wildly for even 3-component systems. Some frequency contributions will be stronger and some weaker (particularly at very high energies when all vdW-LDS crash to a value of 1). Some summations will contain only attractive contributions and some only repulsive contributions. Sometimes the summation will contain strong and weak contributions of both attractive and repulsive terms. So the Hamaker coefficient ultimately embeds this balance of contributions from all polarization across all frequencies ranges for all material present in the system.

And there are other effects that can change this balance. One example is the inclusion of retardation effects as a function of S2SS when using the full Lifshitz equation. Basically what occurs as the S2SS is increased is that the higher frequency polarization quickly get out of phase and no longer contribute. Therefore the larger the S2SS, the smaller the effective frequency range contained in the Lifshitz formulation's summation[30, 33].

As an example, consider a situation in which a Hamaker coefficient has a net zero magnitude with positive contributions from the 0-20 eV energy range and negative contributions from the 20+ eV energy range. At contact, the two materials have essentially no net attraction or repulsion vdW-Ld force and can thereby drift away with brownian motion. However as they drift away, the interactions at high energies (which are negative or repulsive) drop out of phase and cease to contribute to the overall summation. The net neutral vdW-Ld force then becomes attractive and could, if stronger than the brownian motion, move the objects back together. And as they went back into contact, the higher frequencies would begin to contribute again and neutralize the net vdW-Ld interaction again. This is a more complicated version of retardation because most simple cases of retardation only "decay" in magnitude as the S2SS increases. But retardation in the general sense only means that the higher energy contributions are eliminated systematically until the materials are so far apart that only the 0eV DC interactions remain.

2.3 Subsequent Extensions to the Lifshitz Formulation

Although powerful, the demands upon original Lifshitz formulation required certain enhancements and additions to address the ever growing needs of end-users. Parsegian and Weiss extended the system from simple 3-component systems (2 semi-infinite substrates and a medium) to a 5-layer solution, which also allowed users to vary the thicknesses and material compositions of all three of the middle layers[31]. This extension to 5-layers was later generalized to any arbitrary number of isotropic layers of arbitrary thicknesses and became known as the "add-a-layer" formulation[30, 46]. This opened up the door to study vdW-Ld interactions of systems containing surfactants/coatings[33], graded interfaces[47], repeated stacking[48, 46], and so forth.

Another extension was the ability to calculate vdW-Ld interactions for geometries more complex than flat plates. Here the Derjaguin approximation was used to finely slice spherical and cylindrical objects into pseudo plane-plane add-a-layer solutions[49]. In this manner, it was still possible to calculate Hamaker coefficients using the exact same approach used for the add-a-layer solution. The only major change was how the geometrical portion of the vdW-Ld TE changed as a function of S2SS.

Later, the spectral mismatch functions were adjusted so that effects of optical anisotropy could now be addressed[50, 51, 52, 30]. This meant that the Hamaker coefficient was no longer just S2SS dependent. It now had the possibility of an angular component that could arise due to the crystallographic directions of the interfaces. These effects have been clearly demonstrated in the case of Al2O3[50, 51].

2.4 Benefits of a Thorough Understanding of vdW-Ld Interactions

Ultimately the vdW-Ld interactions are a very important, ever-present intermolecular force that manifests itself in several different ways. They contribute to (in partial or in full) the following areas of study: wetting angles, surface tension, adhesion, sintering, solution self-assembly, colloids, biological systems, and so forth[ ].

Despite their wide utility, the vdW-Ld are often poorly understood or again used as a catch all term for all intermolecular interactions or deviations things we cannot understand[ ]. While this is unfortunate, it opens the door for a lot of opportunities. As explained earlier, simple changes in the balance of the vdW-LDS strengths, the components present, and the geometries used can help taylor these forces and give more control over the interactions. Given the amount of flexibility in all of these parameters, there are a tremendous amount of possibilities if one has a clearly defined target and the means of searching over many different designs.

2.5 What is Available vs What is Missing

Getting back to the very basics, the vdW-Ld interactions can conceptually be thought of as material specific vdW-Ld interaction energy density $\mathcal{A}$ multiplied by the volume - volume integration component.

$$\mathcal{G}(\ell) = \mathcal{A} * \frac{g}{\ell^n} \tag{2.13}$$

Where ℓ is the S2SS, 'g' is a collection of geometrical factors, and 'n' is an exponent that varies based on the specific geometry presented. The Hamaker coefficient $\mathcal{A}$ depends both on the materials present as well as their spatial arrangement, so one cannot completely decouple the two. It should be noted that Equation 2.13 is the last juncture where the pairwise and Lifshitz model agree form wise. The major difference is in the determination of $\mathcal{A}$. The Lifshitz form calculates explicitly as a function

of all materials present and their spatial arrangement versus the parameterization that occurs for the pairwise form[30]. Thus the Lifshitz form is preferable because its predictive and can handle multi-components in multiple spatial arrangements (if formulation for that particular geometry exists).

Fortunately for most simple systems, the basic Lifshitz formulation and the extensions described in this chapter are usually sufficient for a determination of $\mathcal{A}$, which is the most difficult part of the vdW-Ld TE to obtain. However the SWCNT systems described in this thesis are complicated enough that the available extensions were insufficient in many different aspects. While a add-a-layer form exists for plane-plane geometries[30], no such form exists for cylinders. Without an add-a-layer solution, one has to resort to optical mixing and other means to account for surfactants, multi-wall CNTs, etc. Next, optical anisotropy extensions existed for semi-infinite slabs and rod-rod interactions at the far-limit, but not for rod-rod interactions at the near-limit. Rod-substrate formulations could not handle optical anisotropy for either limit. Coupling these formulation issues with the lack of input vdW-LDS, it is clear that a quantitative calculation of vdW-Ld interactions meaningful to end-users was not possible[27].

At the conclusion thesis, many of these issues have been resolved (see Figure 1-1). The few that are unresolved were not necessary for the analysis to proceed, but remain on the wish list of things that would be nice to have (e.g. cylinder add-a-layer solutions). They could potentially make this analysis more streamlined and accessible to an even broader audience as well as open the door for effects and trends yet undiscovered. But each work provides a stepping stone to the next, and the foundations presented here should adequately provide for those who may follow after.

Chapter 3

Ab Initio, Full Electronic Structure Calculations for Obtaining vdW-Ld Spectra

The lack of a large and publicly available vdW-LDS database is one of the key barriers to widespread adoption/usage of the Lifshitz formulations[ ]. At present, the biggest known data repositories are contained in a 3 volume set by Palik [ ] and the Gecko Hamaker database maintained by Roger French[ ]. Combined with other published materials, there is a grand total of approximately 100+ spectra usable for vdW-Ld calculations. Admittedly some of these materials are highly important and widely used in many applications. Water, for example, is needed in every aqueous colloid calculation. However, the quantity of materials that end-users have available and use in their systems can exceed this by 2-3 orders of magnitude or more. It is then frustrating from both a theoretician and end-user standpoint because it is difficult to even give qualitative answers to the relatively simple questions of colleagues. But without the data, such an answer is only speculation or educated guess versus a definitive answer.

Therefore from a pragmatic standpoint, it makes sense why many end-users don't bother to use the Lifshitz formulation for their calculations. Why go forth with all the effort to do the full calculation when the collection of vdW-LDS data used is

being approximated by a limited range of data in the optical regime, by a single value (e.g. index of refraction)[34], or just guessed arbitrarily[56]? This battle between Lifshitz adoption and available vdW-LDS tends to be a chicken or the egg scenario. The lack of end-users interested in Lifshitz formulations decreases the demand to characterize and catalogue the optical properties necessary to use them. That or they are just unable and/or unwilling to obtain the vdW-LDS despite their interest. Either way, the result is the same: a limited quantity of available vdW-LDS of the quality necessary for studying vdW-Ld interactions[53, 54, 55].

However, the vdW-LDS specific to each chirality must be obtained to answer the question of whether or not SWCNTs have exploitable chirality-dependent properties. It is not possible nor is it scientifically ethical to simply use ϵ'' spectra of graphite and graphene and arbitrarily vary it to make a [9,3,m] or a [6,1,s]. The output of the Lifshitz formulation, after all, is only as good as the data we provide it. Putting arbitrarily manipulated spectra will only result in arbitrary and unrealistic variations in output. GIGO: Garbage in, garbage out. Thus it essential to find a means to obtain this information in order to appropriately answer these initial questions.

3.1   Important $\epsilon''(\omega)$ Considerations

The imaginary part of the dielectric response function over real frequencies, $\epsilon''(\omega)$, is the key material component that embeds all of the necessary information to study vdW-Ld interactions (see Fig. 1-1). Ideally the $\epsilon''(\omega)$ is accurate and over as large an energy range as possible. But this begs 2 key questions: how accurate is accurate? And how much of the energy range is truly needed? The first question is primarily a question of the $\epsilon''(\omega)$ strengths and positions along the energy range. The second is mainly a question of the cutoff energy necessary for effective convergence for SWCNT systems. The convergence question is easier to address, so it'll be addressed first.

All experiments and ab initio calculations can only obtain optical transition data over a finite energy range (i.e. it is impossible to obtain all optical transitions out to infinite energy). Certainly newer and better experiments and more computational
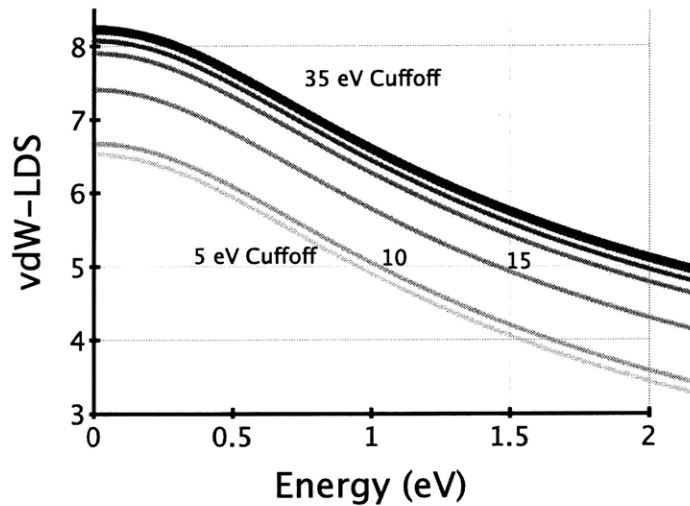
Figure 3-1: The [6,5,s] axial-direction vdW-LDS as a function of its ϵ'' cutoff energy. Visual convergence in the 0-10 eV energy range is achieved by a cutoff energy of 35 eV.

power can continue to push the limits of what is obtainable. But is it necessary? The KK transform (Equation 2.12) tends to dampen the overall effect of the higher energy $\epsilon''(\omega)$ transitions due to the ξ^2 behavior in the denominator. This means that the higher energy transitions have to be stronger/larger to meaningfully contribute. Eventually the dampening is so great that the vdW-LDS has converged. The way to test or locate this convergence energy is straightforward. Using a full SWCNT $\epsilon''(\omega)$ spectra from 0 to 45 eV, create vdW-LDS via the KK transformation using cutoff energies 5 through 45 in increments of 5 eV and test the convergence of the vdW-LDS and Hamaker coefficient across vacuum.

Figure 3-1 shows the [6,5,s] axial-direction vdW-LDS as a function of ϵ'' cutoff energies spaced 5 eV intervals apart. Figure 3-2 shows a chart of the non-retarded, $\mathcal{A}_{\infty \in \infty}$ Hamaker coefficients using these vdW-LDS at various cutoff energies across vacuum. The original raw ϵ'' spectra is shown in Figure 3-3. The whole picture can be understood by observing all 3 simultaneously. Both the vdW-LDS and the Hamaker coefficient are clearly converged by the 35 eV mark because the ϵ'' transitions strengths beyond 35 eV are very small or non-existent.

One might ask then why we would employ any cut off energy versus just using the
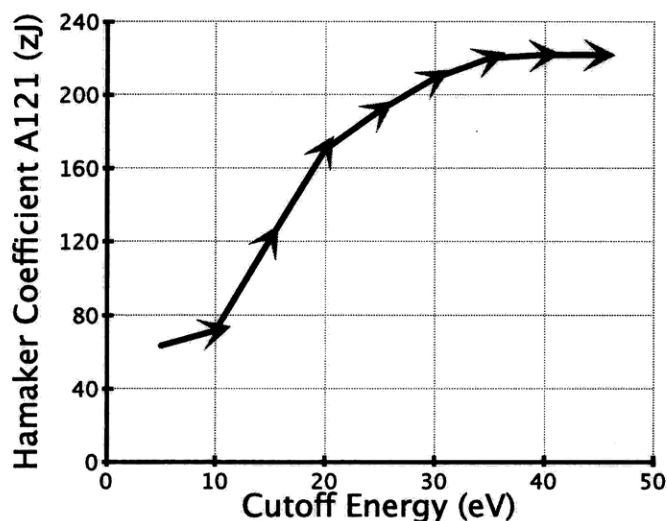
Figure 3-2: The Hamaker coefficient convergence of the [6,5,s] axial-direction spectra as a function of ϵ'' cutoff energy. The calculation is a simple demonstration that uses vacuum medium and the isotropic plane-plane Lifshitz formulation. Visual convergence is again achieved by 35 eV.

entire spectra to begin with. For optical data measured experimental, the answer is simply that there are limitations to how high in energy one can excite a material to measure such a response. Typically this is resolved by adding a high energy wing of the form $e^{-\beta * eV}$ to the end of the available energy range[33]. For ab initio calculations, we could in theory go out to very high energies (50-100+) by adding processing power and RAM. However, there is eventually some noise that appears at higher transitions due to a finite basis set (up to the 4s)[57, 58, 59, 60, 61]. Therefore some artifacts can appear at very large energies. For optical properties of SWCNTs obtained via ab initio calculations, these artifacts or discrepancies occasionally appear at energies above 30 eV. This is believed to be noise at the present moment and will only be verifiable when the codes and computational power can handle even much larger basis sets.

To strike a balance between convergence and potential noise appearing at very high transitions, I have selected a cutoff energy of 30 eV, which what was used in previous publications. Since our primary aim is relative energy variations between chiralities, the 30 eV cutoff should be sufficient, particularly for a light element like
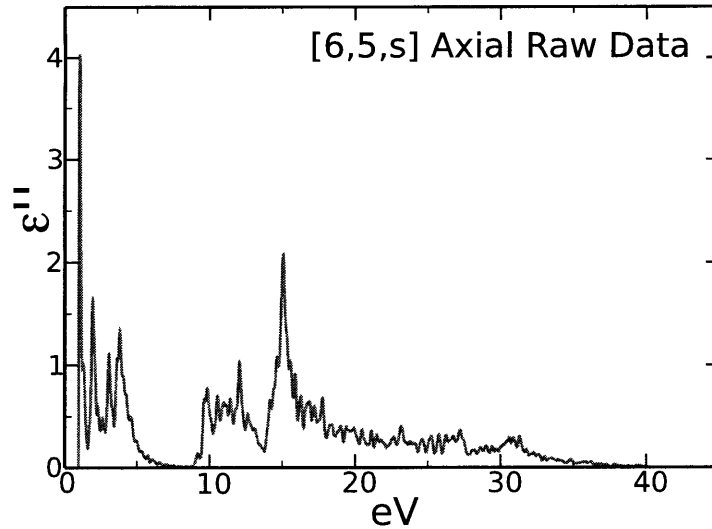
Figure 3-3: The raw ϵ'' of the [6,5,s] axial-direction from 0 to 45 eV without any magnitude scaling to eliminate the void space contained in the ab initio calculation. The transitions beyond 35 eV are small and do not contribute to or significantly alter the vdW-LDS or $\mathcal{A}_{121}$ in Figures 3-1 and 3-2

carbon. But to alleviate any concerns, the cutoff energy could be easily shifted to 35 eV and the analysis and phenomenology (particularly relative energies among individual SWCNTs and among SWCNT classifications) would change very little. The [6,5,s] is one of the tubes having questionable transitions above 30 eV anyway, so this "worst case" scenario convergence at 35 eV was likely do to noise rather than real ϵ'' transitions, but it's inclusive to say at this point. I personally feel more comfortable using a 30 eV cutoff to level the playing field by noise removal and accurate relative energies rather than trying to eke out a little more accuracy in the total energies at the cost of potentially adding noise.

Having addressed cutoff energies, it is useful to observe the effects of ϵ'' changes. Such a study helps us understand the dependancies that arise among ϵ'' and vdW-LDS as well as underscoring the need for accurate data. There are essentially 3 distinct ways to change a ϵ'' peak, which are to a) change the magnitude, b) change the energy at which the transition occurs and c) change the shape of the excitation while keeping total magnitude and average transition energy fixed. In short, we can change the area, position, and shape of ϵ''.
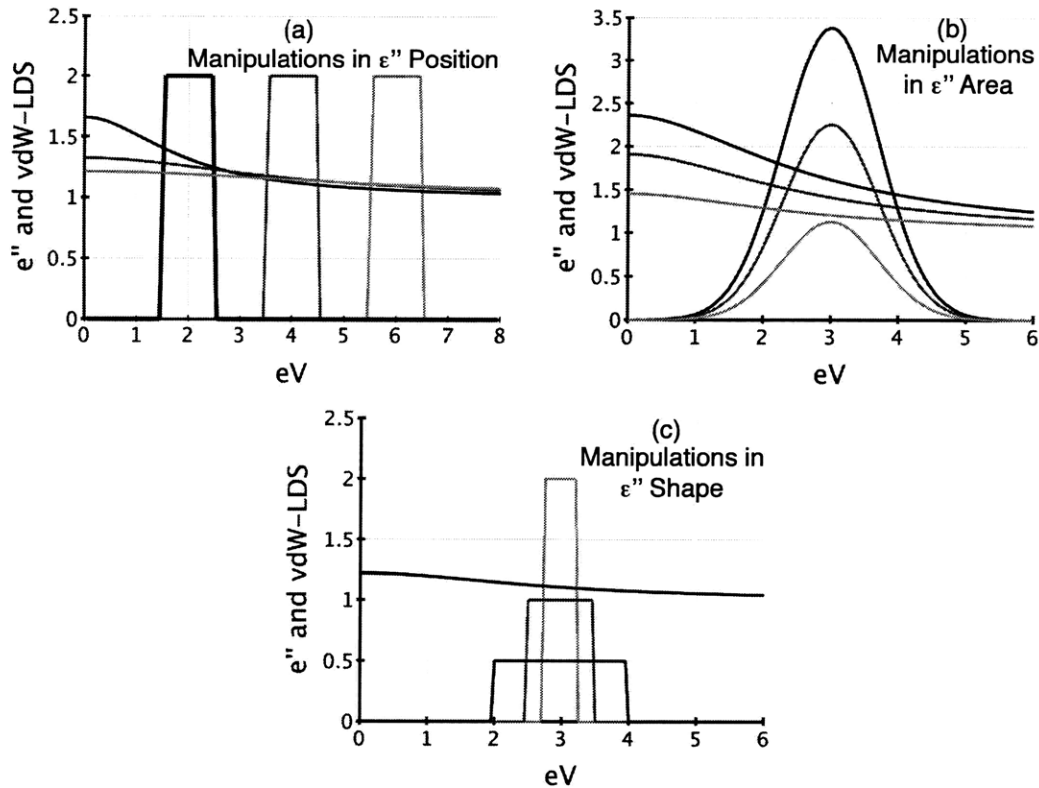
Figure 3-4: The ϵ'' 3 variations (position, area, and shape) and how they effect an overall vdW-LDS. Area and position lead to systematic and important changes. Symmetrical changes in shape generally cancel out as competing changes in position, resulting in a very small effect on the overall vdW-LDS.

Figure 3-4 shows fictitious ϵ'' curves being varied in these 3 distinct ways. Of the 3 variations, area and position have the greatest effect. An analysis of the KK transform (Equation 2.12) brings clarity as to why. Linearly increasing or decreasing the entire spectra is equivalent to simply multiplying the integral term by this scale factor. Therefore bigger transitions (by area and not just height) pull the entire vdW-LDS upward.

Changes in position are more interesting. The total area under the vdW-LDS curve is relatively insensitive to changes in position of a fictitious ϵ'' curve. However the shape of the vdW-LDS (more specifically the slope at the low and high energy limits) can change significantly. This effect can be understood by analyzing the KK transformation (Equation 2.12) at limiting values of ξ. At low values of ξ, the effective

weighting fraction upon $\epsilon''(\omega)$ varies at $1/\omega$. Therefore moving the $\epsilon''(\omega)$ peaks to larger energies decreases the vdW-LDS magnitude at that low energy ξ.

However at very large values of ξ, the effective weighting fraction changes because $\xi >> \omega$ and thus the magnitude of ξ now dominates the denominator. Now at low values of ω, the $\epsilon''(\omega)$ excitations get dampened by ω/ξ^2. The larger ξ, the more the lower excitations are dampened. Thus a very large spike at 0 eV effects the vdW-LDS at $\xi = 100$ eV very little. But if $\epsilon''(\omega)$ were to shift to larger energies, the contribution to the vdW-LDS at that given ξ would increase linearly due to the ω numerator in ω/ξ^2.

In short, the magnitude of vdW-LDS is more sensitive at a given ξ to changes in $\epsilon''(\omega)$ at $\omega \approx \xi$. Therefore changes in position to lower energies have an effect of raising a vdW-LDS low energy wing spike while simultaneously dampening the vdW-LDS at larger ξ. Conversely if we change the position of the excitation to higher energies, we can see the spectra flattening in the lower energy regime but remaining stronger in magnitude over the deep energy range. It is in this way that position changes of ϵ'' changes the shape (slope) of vdW-LDS.

Changes in ϵ'' shape appears to do very little to the overall vdW-LDS. One can imagine a single ϵ'' shape as a collection of smaller ϵ'' shapes comprising the same total area. If one were to change a tall but very narrow $\epsilon''(\omega)$ peak into a very small and wide dome area centered at the same eV, one could think of its effect upon the vdW-LDS like opposing changes in position. The portions shifting to the left tries to make the vdW-LDS look more like a sharply decaying exponential while the portions shifting to the right tends to flatten out the spectra over all energies. These competing forces cancel each other out. The important take home message here is that a huge but very narrow impulse can be equivalent to a somewhat flat but wide area of ϵ'' transitions. Therefore it is important to not place too much emphasis on the height of a spike unless it caries some girth. It is also important not to ignore large areas of low laying ϵ'' which may have a small difference in height over a large span of transition energies.

So how accurate is accurate? As long as the ϵ'' transitions are of the proper area

and centered at the proper eV, small changes in shape are not important. However to alleviate any and all concerns about possible distortions, the number of k-points used in the ab initio determination of ϵ'' was increased until all shape distortions were no longer present in both the radial and axial directions. This was particularly important for the 0-5 eV range, which tended to have larger ϵ'' shape distortions when a very coarse k-point mesh grid was used. But later comparisons to the converged ϵ'' showed that the resulting vdW-LDS between the two were nearly identical in all but a few cases.

It should now be clear that it is important to obtain accurate ϵ'' spectra over as large an energy range as possible. It is particularly important when searching for chirality-dependent variations for SWCNTs, because subtle changes in chirality have known shifts in optical excitation energies, particularly around the band gap. These systematic and sometimes subtle changes can propagate and become significant variations in the Hamaker coefficients and vdW-Ld interactions, which could potentially be exploited experimentally. Too small of a cutoff energy and all the crucial details are eliminated. Too much distortion in the ϵ'' signal and the vdW-LDS become meaningless.

Before the onset of this thesis, the question of chirality-dependent vdW-Ld properties could only be guessed and speculated, but not asserted and quantified. At the time, the only full spectrum properties available were graphite's in-plane and out-of-plane directions[54, 62] as well as and many papers having limited spectra via TBA models out to 5 or 10 eV[10, 63]. There were two notable exceptions. A paper by Mintmire contained the [7,5,s] optical properties in the axial and radial direction out to 30 eV[64]. Unfortunately his data wasn't publicly available nor was the method adaptable to MWCNTs and other considerations. He also mentioned that the [7,5,s] ϵ'' transitions in the 20-30 eV range were potentially overestimations of what should otherwise be weak in transitions. A comparison to graphite's spectra beyond 20 eV justifies this concern[54, 25].

The second exception is the experimental EELS spectra provided by Stephan et al[29]. Here we get great confirmation of the major peaks above 10 eV with the

ab initio results in Figure 3-3. There is also agreement with the qualitative trends of graphite and the claim by Mintmire for weaker transitions in the 20+ eV range. But what this EELS data lacks is important. First these spectra labeled are labeled strictly by diameter proportions and not chirality. This is unfortunate and hopefully only a result of not tracking this parameter. Second, the spectra information is not broken down to the radial and axial components. SWCNTs, graphite, and clear orientation-dependent optical property behavior [25, 63]. It's unclear from the published literature whether it's possible to extract this necessary behavior for orientation-dependent vdW-Ld considerations using the same EELS method.

Both the Mintmire and Stephan information gave valuable insights and direction, but neither contained all the pieces required for a detailed optical property and vdW-Ld analysis. As a result, there is still a need for a systematic way for obtaining this information as accurately as possible over as large of an energy range as possible for as large of a quantity of SWCNTs as possible.

3.2 Method Selection

It is probably obvious by now that the ϵ'' spectra in this thesis were obtained by an ab initio calculation (more specifically a DFT method with an OLCAO basis). However, it is still worth going over what was available experimentally and why those options were not used. Although there are many nuances within each method, we can categorize the experimental methods found back in Figure 1-1 in 3 ways: 1) Reflection/transmission 2) EELS, and 3) Ellipsometry.

Reflection/Transmission experiments have a number of shortcomings for vdW-Ld considerations. First the frequency range is typically capped to as far as the shallow UV regime (¡ 5 eV), which is considerably less than the highly sought after 30+ eV. Next, the experiments require a somewhat large bulk sample for the laser to penetrate through or reflect from. A single tube's 0.4nm diameter would be dwarfed by a laser beam having a $0.01mm^2$ area. To get around this, one would have a packed array of single chirality type, a feat that is hard enough to accomplish on its own and one

of the very reasons/inspiration for studying vdW-Ld interactions for SWCNTs in the first place. Having these SWCNTs packed together or in a composite matrix would also introducee neighbor-neighbor coupling due to non-linear secondary bounding / interactions. Another possible issue is end-cap effects when trying to obtain the axial direction[33].

Ellpsiometry gains the benefit of having a larger energy range to scan, but it suffers from the same issues as reflection/transmission with respect to not being able to measure isolated tubes[33].

EELS is potentially an experimental method worth pursuing because of its ability to measure very high energies as well as very tight resolutions (down to $1nm^2$) in certain high resolution microscopes[33]. The key advantage for this is being able to measure the properties of a single tube, versus a packed array of tubes, that is focused on with an SEM/TEM/AFM. This method's primary benefit would be in the radial direction. The axial direction's measured ϵ'' might be overpowered by the properties of the end-cap versus the longer tube part. There has been progress made by Stephan et. al. by using a glancing angle approach to measure just the axial direction[29]. However the information is not given into the axial and radial components. It's is unclear if that is by choice or an inherent measurement difficulty.

By comparison, ab initio calculations have a tremendous advantage over the experimental methods in the areas where it matters the most. First, it is possible to get isolated SWCNTs without having to worry about coupling effects from the substrate, a surfactant that cannot be removed after mounting, a polymer matrix holding them in place, etc. The axial vs radial directions are easily separated and achievable for energy levels up to 30+ eV. It's also quite straightforward to calculate data for every possible SWCNT, even the ones that are not readily made by the available techniques.

The downside of the method is that it cannot easily obtain fixed dipole information (e.g. low energy wing for water) or vibrational modes. However these shortcomings do not impair a vdW-Ld analysis for the following reasons. SWCNTs are charge neutral and have no fixed dipole moment anyway, so that is a non-issue. Vibrational components of the ϵ'' tend to contribute very little in comparison to a dipole moment

and the many UV contributions[30]. The vibrational models also tend be limited to a very few of the Matsubara frequencies. Finally, the ab initio codes not only capture the 0 eV metallic conductivity, but also electronic excitations within the energy range typical of the vibrational modes.

So in short, I claim that the ab initio calculations is the best method available and is well suited for SWCNTs.

Additional questions typically arise when discussing the usage ab initio optical properties over experimental methods. Most of these concerns can be summarized into the following two themes: 1) How can I be sure that this information is accurate and 2) What additional things can you do that warrant changing to ab initio method over experiments?

Question 1 tends to be a more critical one to address because it is a concern versus an opportunity. First the method has been well vetted and established in the literature at least as early as 1990[57]. It uses full electron shells and does not employ any approximations. Contrast this to other computational methods, such as the tight binding approximation, which tend to impose symmetry upon the conduction and valence bands. Such an approximation can potentially causing all sorts of distortions of new ϵ'' forming or shifting due to these symmetry changes. The full band structure calculation eliminates much to all of these shortcomings.

Additionally, comparisons between full ab initio calculations and experimental data have been quite supportive. The most important comparison was that of Al_2O_3, in which the differences between ϵ'' obtained from ab initio calculations and an experimental lab were similar and comparable to the differences typically observed between two experimental labs[65, 66]. Put bluntly, it would be difficult to pick out the ab initio ϵ'' Al_2O_3 spectra if it was unlabeled and graphed with experimental data of a similar energy range. Sure some features (particularly the high resolution) may give it away, but the overall trends, peaks, and so forth are essentially the same. A comparison of the excellent agreement of key features within Figure 3-3 to the experimental results by Stephen et al[29] further supports this claim.

This analysis was later repeated with water, which is a material that has had

a tremendous amount of attention placed on it due to its importance for vdW-Ld interactions of nearly all biological systems. The ab initio water calculation ϵ'' contained 340 molecules of water in a box that is 2.16641 nm^3. As mentioned in this section, the calculation cannot capture the dipole dependent term, which is a critical feature of water. However, If we simply add that low energy oscillator to the ab initio determined vdW-LDS for water, we again get a very close match comparable and impossible to distinguish from the other available models that exist.

Figure 3-5 shows the water vdW-LDS obtained via the OLCAO spectra with and without dipole oscillator and compares it to the Parsegian[30], Parsegian w/index matching[30], Roth[68], and Ackler[67] version of the water vdW-LDS. As we can see, the behavior in the UV regime is nearly identical to the Parsegian index-matched vdW-LDS. The Ackler spectra is 0.1 unit weaker and the Roth and Parsegian unadjusted vdW-LD are approximately 0.2 stronger in this eV interval range.

As an aside, a frequent question that comes up in questioning the validity of using ab initio ϵ'' spectra is that it cannot currently account for vibrational, multipole, and fixed dipole moments. While this is completely true, it appears to be a non-issue for SWCNTs. First, SWCNTs have no fixed dipole moment and the electronic 0 eV behavior of metals is well captured (see many of the figures in Chapter 6). As for the importance of the vibrational modes, we can clearly see that ab initio water vdW-LDS matched to many of the vetted water models in Figure 3-5. This was also true for the comparison of the experimental versus ab initio Al_2O_3 specta [65]. So while these effects certainly do exist and influence ϵ'', it doesn't appear that they are so large as to noticeably distort the resulting vdW-LDS. But if ultimately they do add nuances, techniques which can measure and add them in are certainly possible.

In terms of benefits, ab initio calculations opens the door for many exciting opportunities. First it can easily handle "soft" or "liquid" systems that are essentially impossible to do via ellipsometry. This is particularly important in biological systems, in which the structure of DNA changes depend on whether it is hydrated or not (hence the alpha and beta designation). Ab initio codes offers up the ability to calculate and quantify differences in each scenario as well as any other conceivable
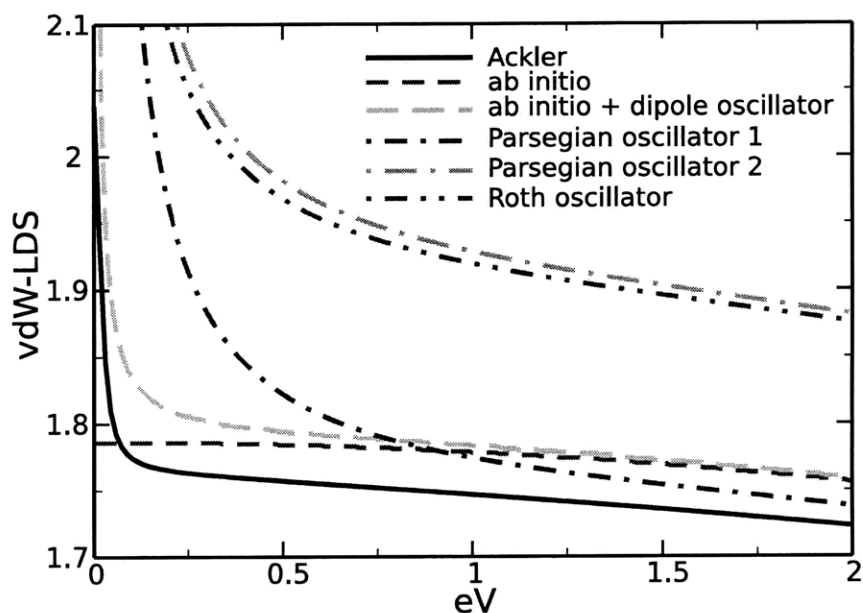
Figure 3-5: A comparison of various water vdW-LDS. The ab initio spectra is shown in 2 forms: raw and raw with a zero frequency dipole term added as per the Parsegian oscillator models. The other 4 water vdW-LDS were created from experimental data[30, 68, 67].

twisting.

It also makes it possible to spatially and directionally resolve the optical properties. For entities like DNA, spatial variation can potentially be huge because there is a substantial difference in the phosphate backbone versus the "greasy" nucleotide core.

There is also an ease, speed, and cost benefit of ab initio codes. The entire catalogue of 65 SWCNTs calculated for this paper took months instead of years and many dollars of effort. It opened the door for the rest of this analysis, which I claim would have been impossible any other way.

This is not to say that ab initio codes are a *replacement* for experimental methods. As shown in the water example, the very important dipole term still had to be added to the raw output data in order to bring us in congruency with established water spectra available in the literature. Further, the previously mentioned comparisons with Al_2O_3 [65] and the SWCNT ab initio data with that of Stephan et al[29] show the many benefits and confirmations that can be achieved by using both. Therefore it should be seen as a supplement and even a driving force for further experiments.

By using ab initio codes, it is possible catalogue a greater diversity of materials more quickly, and help expand the usage/adoption of the Lifshitz formulation. This can only benefit experimentalists as there will always be demand to do it the traditional way as a confirmation. The two methods will also point out each other's weaknesses and hopefully develop more as a result of this back and forth comparison.

3.3   Ab Initio Details

The primary equation for obtaining $\epsilon''(\omega)$ from the band structure is as follows[57, 58, 59, 60, 61]:

$$\epsilon''_{ij}(\omega) = \frac{4\pi^2 e^2}{\Omega m^2 \omega^2} \sum_{knn'\sigma} \langle kn\sigma | p_i | kn'\sigma \rangle \langle kn'\sigma | p_j | kn\sigma \rangle f_{kn}(1 - f_{kn'}) \delta(e_{kn'} - e_{kn} - \hbar\omega). \quad (3.1)$$

Here again $\epsilon''(\omega)$ is the imaginary part of the dielectric spectrum at a given frequency ω, with mass m, and Brillouin zone volume Ω. The momentum operators, p_i and p_j, operate on both the valence and conduction band wave functions, where the i and j subscripts represent the directions of the tensor in three dimensional space. The Fermi function (f_{kn}) terms ensure that only transitions between an occupied valence to an unoccupied conduction band transition are allowed, and the delta function ensures that only transitions corresponding to the particular energy $\hbar\omega$ are considered. Once $\epsilon''(\omega)$ is obtained, it is then trivial to use the Kramers-Kronig transform Eq. 2.12 to convert these data into a form useful for dispersion interaction computation.

The codes used for the data contained in this thesis have 3 levels of basis sets (MB, FB, and EB), which stands for minimal, full, and extended basis set. The MB includes up to the 2p x, y, and z. The FB goes up to 3p x, y, and z. EB, the basis set used for the SWCNT calculations, includes the 4s, 4p (3 orbitals), and the 3d level (5 orbitals)[57, 58, 59, 60, 61].

The box dimensions for the x and y direction were made at least 1nm larger than a SWCNTs outer diameter to eliminate any potential coupling with a neighboring

cell in the periodic array. The raw ϵ'' data from the codes begins at 0.01 eV and goes up to 45.01 in 0.01 eV increments. The quantity of the k-point mesh grid is typically several times larger than the grid used to converge the band structure because of the finer resolution required for the spectral properties. Because k-space is a reciprocal space of the lattice dimensions, the quantity of k-points * the cell height 'z' should be maximized according to the quantity of dispersion present. For the radial direction, in which the bands in the electronic structure are flat, only 2 to 4 points are typically needed. For the axial direction, there is a substantial amount of dispersion. A value of k*z ¿ 100 is typically a good baseline value to start with for most material, including the SWCNTs. However, some SWCNTs (notably zigzag metals) required an even larger values (k*z = 1000+) to obtain the metallic wing and/or check to make sure the ϵ'' values were well converged.

3.4 Scaling

It is important to note that Equation 3.1 is scaled by the box size volume[26, 27, 28]. If this were not the case, doubling the supercell size in all directions would lead to 8 times the volume and atoms used as well as a ϵ'' that is 8 times larger. The scaling by volume ensures that all variations will have the same bulk value for ϵ''.

SWCNTs, on the other hand, are notably different from bulk crystals in that they do not actually fill up the complete cell. A substantial amount of padding is used in the radial direction to ensure there is no coupling with SWCNT the next cell. Practically this means there is void space thats needs to be eliminated or scaled out of the original ϵ'' determination. In doing so, the scaling properly confines the ϵ'' properties to the space the carbon atoms occupy rather than the vacuum void space. To illustrate this to its logical extreme, imagine placing a SWCNT in a supercell that is meters in diameter. Leaving aside the issue of crashing a super computer to handle such a task, clearly the ϵ'' values for this cell size would be zero because the excitations of the whole box would be dominated by vacuum.

Therefore the ϵ'' data has to be scaled to eliminate this extra void space. The only

possible point of contention is the means on doing so. The strategy made most sense to me was to use the interlayer spacing of graphite sheet layers to provide an estimate of what can be considered the boundary or "shell." Within the shell represents the properties of just the SWCNs. The area or space beyond this could be vacuum, another SWCNT, water molecules, or anything else placed there in the calculation.

The interlayer spacing of graphite varies from .667 to .670 nm depending on which set of data is the most accurate[71]. This discrepancy is only 0.5% and effects the scaling results very little compared to other considerations. To get the "excluded volume" shell distance 't', this value is divided by 4 (graphite is an A - B - A spacing and therefore the shell thickness if 1/4 of this distance). The first paper publishing these results used a value of $t = 1.675$ Angstroms, so this value will be used for consistency [25].

The next question is whether or not we eliminate the void space within the SWCNT core as something that can be replaced. This filling could be vacuum, air, water, some other material, or any mixed percentage. The implications of this replacement is described later in this chapter and in Chapter 5 regarding spectral mixing. If we also assume that the curvature of the SWCNT does not influence the inner or outer distance of this "excluded volume" shell distance 't', then calculating the scaling for a solid cylinder would be done as follows.

$$S_s = \frac{x * y}{\pi(r + t)^2} \qquad (3.2)$$

Here S_s stands for the solid scale factor. The value 'r' is what the literature typically refers to as the SWCNT radius and is the shortest possible distance between the cylinder core and the atom nuclei. For a hollow cylinder we would would subtract off the inner core in order to confine the ϵ'' excitations strictly to the volume occupied by the SWCNT shell and that alone. This scaled factor was published as follows:

$$S_h = \frac{x * y}{\pi((r + t)^2 - (r - t)^2)} \qquad (3.3)$$

The magnitude of $S_h \geq S_S$ for all SWCNTs. Hollow scaling is the more versatile

data to keep because it properly confines the ϵ'' data where it belongs (just the sp2 shell). Solid cylinder scaling substantially misrepresents the vdW-LDS strength of large SWCNTs like the [24,24,m], which can reduce by as much as 60% percent! If however a vacuum core is later needed for a calculation, optical mixing (described in chapter 5) can be used to create any filling (e.g. 0, 50, 100, or arbitrary percentage of water). Thus a majority of this thesis uses hollow vdW-LDS unless specifically stated otherwise.

When using hollow cylinder scaling for ϵ'' and vdW-LDS, we get convergence among many important optical property features and benchmarks. Figure 3-6 is such an example showing the fsum calculation of the effective electron density for SWCNTs as a function of their respective radii. The fsum rule is a calculation used to find the effective number of electrons represented by the optical properties up to a particular excitation energy[ ]. When it converges at large tube radii, it is essentially saying that we have and equivalent electron density among all the tubes, which is something we should get and expect.

$$n_{eff}(\omega) = \frac{m}{2\pi^2 e^2} \int_0^\omega \omega' \epsilon(\omega') d\omega' \tag{3.4}$$

When we used solid cylinder scaling, this number clearly drops vs radius. This occurs because electron density is being thinned out as it is averaged over void volume. Therefore the fsum convergence helps validate the use of hollow cylinder scaling and warns of the dangers of using the solid cylinder scaling without thinking of the context it is used in (this will be addressed in more detail in 6).

Hollow cylinder spectra are also essential for more complicated mixing that we'll see with respect to creating MWCNTs from SWCNT constituents. This procedure really amplifies the utility of ab initio codes as we can essentially use mixing of single components to create any number of complex materials.
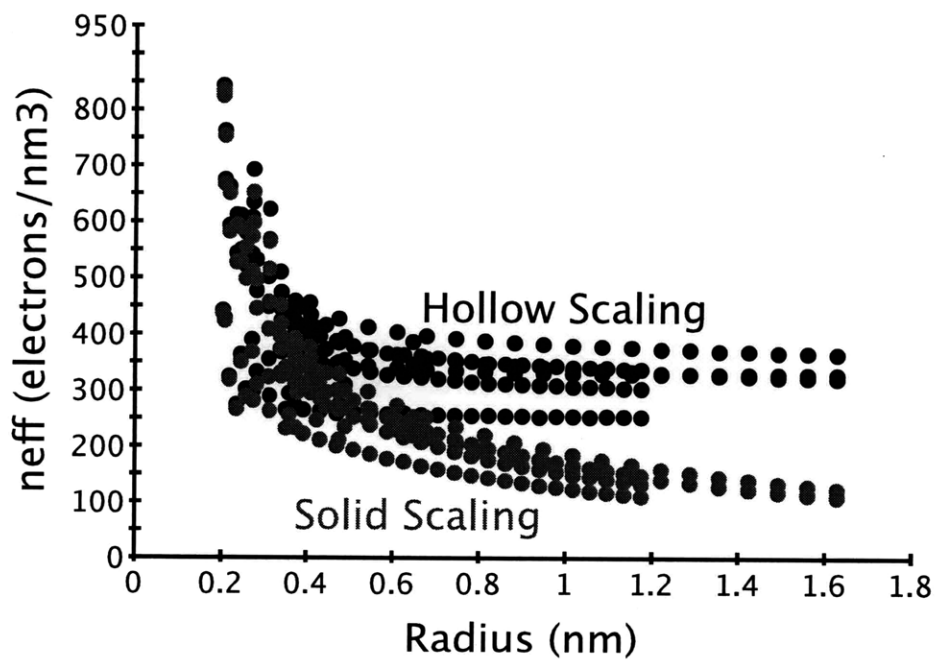
Figure 3-6: The effective electron density for all SWCNTs as a function of radius using both the hollow and solid cylinder scaling. All ϵ'' transitions up to 30 eV were included in the fsum rule.

3.5 Results and Further Implications

Prior to this thesis, the only full ϵ'' known to exist was the [7,5,s] SWCNT spectra by Mintmire and EELS results from Stephans[29].[1] Other works, particularly by Popov, showed that there was indeed evidence of the optical properties having an anisotropic or direction-dependent nature[63].

But the most important question that was not answered or quantified was the degree by which the variation manifested into a physical difference in orientation dependent vdW-Ld properties. After all, if the visible difference in ϵ'' did not result in a significant variation in vdW-LDS or $\mathcal{A}$, then all SWCNTs could be safely treated as optically isotropic and their vdW-Ld energies could be calculated using existing formulations. Additionally, it would also the answer the question of whether or not their was chirality-dependent vdW-Ld properties with an definitive "no".

Having obtained this data, it was discovered that there is in fact a quantifiable anisotropy existing for all SWCNTs. Anisotropy is particularly strong for "metal" SWCNTs because they actually behave like semiconductors in the radial direction, paving the way for a lot of optical contrast between the two directions. Semiconductors are semiconducting in both directions, but can still exhibit some noticeable variations, particularly at very small radii. In either case, there was clearly direction dependent vdW-Ld interactions.

Initially these orientation-dependent vdW-Ld interactions were studied qualitatively using the simple plane-plane formulation because the anisotropic rod-rod and rod-surface formulations were not complete at the moment. Although this was a crude first order approximation and the scaling procedure wasn't properly implemented at the time, there was undoubtedly a preference of the radial-radial and axial-axial interactions over the much weaker radial-axial interaction.

For the metallic [9,3,m] raw vdW-LDS immersed in water, the Hamaker coefficient in radial-radial interaction was twice as strong than the axial-radial interaction[25]. The axial-axial Hamaker coefficient was even twice as strong as that. One can then

---

[1]Both of these papers went largely unknown to me until near the very end because this information wasn't ultimately used for vdW-LDS, Hamaker coefficient calculation, or total vdW-Ld energy.

easily make the case that when one maximizes the axial-axial interaction, one simultaneously maximizes the radial-radial interactions. Therefore there should be a vdW-Ld driven alignment.

What was needed then was a more quantifiable way of doing this that could take into account the shape and optical anisotropy of the tubes. The difficulty was in determining the exact type of formulation to use. Should one use the Lifshitz formulations for anisotropic slabs? That would account for the optical anisotropy. But if we observe the far limit rod-rod Lifshitz formulation, their spectral mixing formulations were completely different. Thus the weighting of the spectral differences change in this geometry. Therefore using the anisotropic plane-plane formulation would incorporate optical anisotropy but change the weighting of these differences while the isotropic rod-rod formulations would properly weight the spectral contrast while leaving out or averaging the optical spectra! Clearly there was a need to bridge these two and the specifics on the formulations will be addressed in the formulations chapter (Chapter 4).

3.6 Recap Thus Far

As stated earlier, a lack of ϵ'' of the accuracy and energy range necessary for a proper vdW-LDS is one of the biggest blocks for people using the Lifshitz formulations. Unfortunately it is difficult to also obtain this information experimentally for SWCNTs because their nanoscale dimensions, optical anisotropy, and poly-disperse population of chiralities. Ab Initio codes, specifically a full band OLCAO method, conveniently provides us this information in a robust fashion.

Once the ϵ'' was obtained for just a couple of tubes (specifically the [6,5,s] and [9,3,m]), it was then possible to characterize the many differences that existed as a function of chirality and direction. That is to say there are differences between the direction-dependent ϵ'' properties in each tube (radial vs axial direction) as well as difference between different tubes. The first effect alludes to the possibility of orientation-dependent vdW-Ld interactions. The second implies chirality-dependency

as well. Both are of importance from a placement and separation standpoint and require a more accurate Lifshitz formulation to give quantitative results. It is also the first, but very important step in being able to solve for the total vdW-Ld interactions, which is one of the primary goals of this thesis.
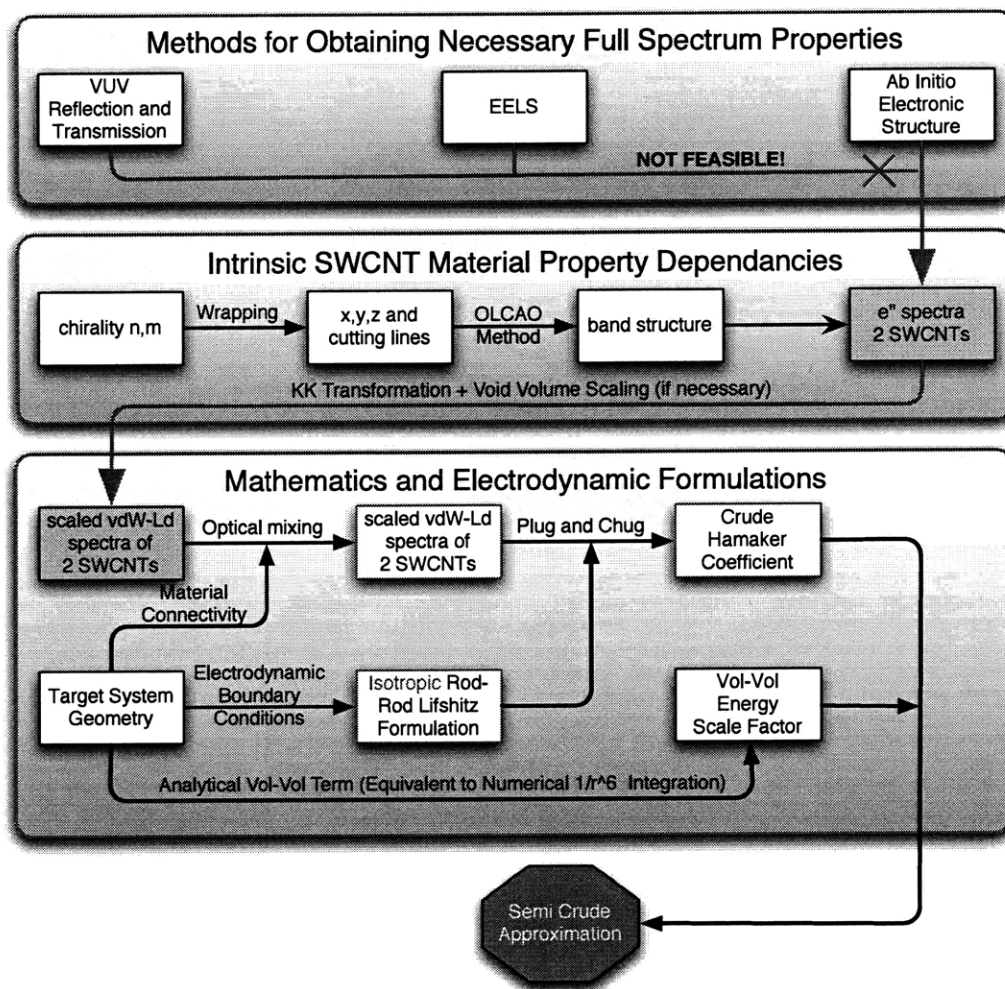
Figure 3-7: The introduction of ab initio properties provides a much needed component in the study of chirality-dependent vdW-Ld interactions.

Chapter 4

Anisotropic, Solid Cylinder Lifshitz Formulation Derivation and New Phenomenon

Obtaining the ϵ'' spectra was a critical and necessary step towards understanding the issues of chirality and orientation dependent vdW-Ld interactions. The next logical step is to obtain the Lifshitz formulations that can handle both the optical anisotropy and the geometry of the rod-rod and rod-surface systems. By the end of this chapter, I will have stressed the key differences between the new formulations and the crude pairwise method initially used as well as show why the new formulations are superior and necessary to obtain accurate total and orientation dependent interaction energies.

To begin, recall from Chapter 2 that the total vdW-Ld energy can be crudely thought of as a $1/r^6$ vol-vol integration multiplied by a Hamaker coefficient. The vol-vol integration is is important for every geometry and is simple to understand conceptually. It occasionally has to be given in "per unit length" or "per unit area" form to avoid divergence for interactions that persist in one or more directions[26]. The more conceptually difficult question to address is how the spectral contrast and overall Lifshitz summation terms are changed as a function of geometry.

Unfortunately, the Lifshitz formulations have a reputation for being unwieldy, difficult to understand, and/or hard to implement. However if we compare the non-

retarded versions for most geometries, the following general form drops out.

$$\mathcal{A}(\theta) = \frac{3}{2}kT * \sum_{n=0}^{\infty}{}' \frac{1}{2\pi} \int_0^{2\pi} \Delta_{\mathcal{L}m}(\phi)\Delta_{\mathcal{R}m}(\theta - \phi)d\phi \qquad (4.1)$$

When there is no angle dependance, the integration over 2π cancels out with the $\frac{1}{2\pi}$ coefficient and the result is the basic plane-plane non-retarded Lifshitz formulation in Equation 2.10. It is the spectral mismatch functions, $\Delta_{\mathcal{L}m}(\phi)$ and $\Delta_{\mathcal{R}m}(\theta - \phi)$, that are heart of the Lifshitz formulation / summation. These geometry-dependent terms determine the magnitude or effect of the optical contrast between neighboring interfaces. For example, the form of $\Delta_{\mathcal{R}m}$ for plane-plane isotropic system is $\frac{\epsilon_{\mathcal{L}} - \epsilon_m}{\epsilon_{\mathcal{L}} + \epsilon_m}$. The magnitude of this term can never exceed unity because the denominator will always be greater than the numerator (vdW-LDS are always positive and greater than zero). Thus there is a limit to just how strongly any given term can contribute to the summation.

By comparison, the anisotropic rod-rod geometry at the far limit contains spectral mismatch terms that are of the form $\frac{\epsilon_{\parallel} - \epsilon_m}{\epsilon_m}$. As demonstrated later on in this chapter, these terms can and do exceed values unity, even when there is no optical anisotropy present in any of the materials in the system.

But to give an illustrative example, suppose a system at n=0 (eV=0.00) contained an isotropic rod with a vdW-LDS value of 18 and a medium with a value 2. The $\Delta_{\mathcal{L}m}$ form for an isotropic plane-plane system would give a value of 0.8 while the anisotropic rod-rod version would be 2.4. Granted this example required a large initial spectra mismatch, but mismatches of this size and larger do exist when describing metallic SWCNTs in water. This problem is magnified further when we consider that this change impacts the spectral mismatches for all frequency terms in the summation.

4.1 Comparing the Various Models

The original plane-plane results are in Chapter 2 and won't be repeated here. The derivation of the anisotropic rod-rod and rod-surf equations are a bit involved and have been regulated to the Appendix A for the specific details. All other geometries

(primarily the anisotropic plane-plane and isotropic rod-rod) are found in Parsegian[ ].

1

4.1.1 Spectral Mismatch Terms

It's useful to compare both the spectral mismatch terms and the vol-vol integration terms for selected geometries to see how they influence total and orientation-dependent interactions. First the spectra mismatch terms, starting with the isotropic plane-plane system:

$$\Delta_{\mathcal{L}m} = \frac{\epsilon_{\mathcal{L}} - \epsilon_m}{\epsilon_{\mathcal{L}} + \epsilon_m} \qquad \Delta_{\mathcal{R}m} = \frac{\epsilon_{\mathcal{R}} - \epsilon_m}{\epsilon_{\mathcal{R}} + \epsilon_m} \tag{4.2}$$

This is the standard form that appears over and over again. The left and right terms can never exceed values of one and there is no angular dependance whatsoever. Incidentally the isotropic rod-rod formulations formulations at the near and far limits have the same mismatch functions because of the Derjaguin approximation (which essentially converts a near contact curve surface into a series of thin plane-plane slices.) So while the Hamaker coefficients would be identical for these two geometries of composed of the same spectral mismatching, the vol-vol energy scaling behavior would be noticeably different as a function of S2SS.

When optical anisotropy is added to the plane-plane system, the spectral mismatch terms gets more complex. The g_i term is introduced to capture this balance between the 3 orthogonal directions for each possible rotational direction within the plane.

$$\Delta_{\mathcal{L}m}(\phi) = \frac{\epsilon_z * g_{\mathcal{L}}(\phi) - \epsilon_m}{\epsilon_z * g_{\mathcal{L}}(\phi) + \epsilon_m} \tag{4.3}$$

$$\Delta_{\mathcal{R}m}(\phi - \theta) = \frac{\epsilon_z * g_{\mathcal{R}}(\phi - \theta) - \epsilon_m}{\epsilon_z * g_{\mathcal{R}}(\phi - \theta) + \epsilon_m} \tag{4.4}$$

---

[1]For full disclosure, it is worth noting that the anisotropic rod-rod (but not rod-surf) do appear in Parsegian's book. However they did not exist at the onset of the PRB paper and in fact were created through a collaboration[ ]. Thus the disclosure of the equations was done by Parsegian first and then PRB paper despite the work being done in the opposite order.

$$g_i^2 = \frac{\epsilon_x^i}{\epsilon_z^i} + \frac{(\epsilon_y^i - \epsilon_x^i)}{\epsilon_z^i} * \sin^2(\phi - \theta) \tag{4.5}$$

$$i = \mathcal{L}, \mathcal{R} \tag{4.6}$$

$$\tag{4.7}$$

The important thing to restate is that the boundary conditions used in later extensions upon the Lifshitz formulation can include up to 3 orthogonal, optically-independent directions[30]. The spectral mismatch terms always include at least two in-plane directions simultaneously and thus there is an intrinsic coupling that exists between these that cannot be removed. For example, when the $sin^2(\phi) = 0$, the effective spectral contrast term is a mixture of $\sqrt{\epsilon_z * \epsilon_x}$. A 90 degree rotation around the parallel plane ($sin^2(\phi) = 1$) and now the spectral contrast goes as $\sqrt{\epsilon_z * \epsilon_y}$. For all angles in between, the g_i will actually included all 3 components. This coupling is important to keep in mind when trying to approximate a Hamaker coefficient by using a pairwise analysis to average/add the interactions between independent directions (e.g. radial-radial, radial-axial, and axial-axial).

When changing from anisotropic planes to anisotropic rod-rod systems at the near limit, the spectral mismatch is now much simpler because two of the ϵ_i directions are now equivalent. The term g_i now morphs into γ, which is simple optical contrast function between the radial and axial directions.

$$\Delta_{\mathcal{L}m}(\phi) = \frac{\epsilon_\perp(\mathcal{L})\sqrt{1 + \gamma(\mathcal{L})\cos^2\phi} - \epsilon_m}{\epsilon_\perp(\mathcal{L})\sqrt{1 + \gamma(\mathcal{L})\cos^2\phi} + \epsilon_m} \tag{4.8}$$

$$\Delta_{\mathcal{R}m}(\phi - \theta) = \frac{\epsilon_\perp(\mathcal{R})\sqrt{1 + \gamma(\mathcal{R})\cos^2\phi - \theta} - \epsilon_m}{\epsilon_\perp(\mathcal{R})\sqrt{1 + \gamma(\mathcal{R})\cos^2\phi - \theta} + \epsilon_m} \tag{4.9}$$

$$\gamma = \frac{\epsilon_\| - \epsilon_\perp}{\epsilon_\perp} \tag{4.10}$$

Clearly the coupling is not as strong now because the move from 3 to 2 independent directions allows for some pure interactions to occur of a single direction (notably $\epsilon_\perp$). However the integration within the Lifshitz formulation over all 360 degree rotations

within the plane will still result in interpolations of these values, so the coupling will still remain. It would be possible to return to the additional complexity of Equations 4.7 if a rod system that had optically unique radial directions offset by 90 degrees. Whether such a material exists is yet to be determined.

A much more dramatic change in the spectral mismatch terms occurs when moving the rod-rod geometry from the near to the far limit. The derivation for this particular formulation is quite involved, but is essentially done by treating the total $\epsilon_{\parallel}$ and $\epsilon_{\perp}$ directions as a composite of the SWCNT and the liquid medium. To return back to a single pair of interacting SWCNTs (rod-rod), the Pitvaeski approximation is employed in the dilute limit (see Appendix for details)[30, 41]. The results are as follows:

$$\Delta_{\mathcal{L}m}(\phi) = -\left(\Delta_{\perp}(\mathcal{L}) + \tfrac{1}{4}(\Delta_{\parallel}(\mathcal{L}) - 2\Delta_{\perp}(\mathcal{L}))\cos^2\phi\right)v + \mathcal{O}(v^2)$$

$$\Delta_{\mathcal{R}m}(\phi - \theta) = -\left(\Delta_{\perp}(\mathcal{R}) + \tfrac{1}{4}(\Delta_{\parallel}(\mathcal{R}) - 2\Delta_{\perp}(\mathcal{R}))\cos^2(\theta - \phi)\right)v + \mathcal{O}(v^2) \quad (4.11)$$

$$\Delta_{\perp} = \frac{\epsilon_{\perp} - \epsilon_m}{\epsilon_{\perp} + \epsilon_m} \qquad \Delta_{\parallel} = \frac{\epsilon_{\parallel} - \epsilon_m}{\epsilon_m} \quad (4.12)$$

The $\Delta_{\parallel}$ term is by far the most important term introduced at this limit. Like γ, it can exceed values of one. However, γ's affects are much more limited than that of $\Delta_{\parallel}$. For starters, γ is a comparison between 2 directions of the same material. Thus it can only really get large when there is a substantial amount of anisotropy within that given material. γ is also highly dampened as it always exists under a square root sign in any spectral mismatch function that it appears. $\Delta_{\parallel}$, on the other hand, can be much much larger than 1 because it depends on the contrast between the SWCNT and the medium, which can be selected to have a much bigger discrepancy. $\Delta_{\parallel}$ also does not have the large dampening effect of a square root sign like the γ term.

4.1.2 Vol-Vol Interaction Terms

Less exciting, but still important, is a quick overview of the vol-vol integration terms. I am always biased towards using a numerical vol-vol integration versus analytical

solutions because there are situations (e.g. non-planar geometries) in which analytical scaling can only be used at the extreme endpoints. One of my primary collaborators does not like this decision because it tends to open the door back to pairwise thinking, which the the Lifshitz formulation so importantly left behind. Nevertheless, numerical integration is on only way to go for end-users requiring the highest accuracy possible for all S2SS. The analytical formulas are still useful as a foundational starting point in describing at the limits for each geometry, particularly in comparing how different geometries scale.

For the isotropic and anisotropic plane-plane, the vol-vol term per unit interaction area is as follows:

$$\mathcal{G}(\ell, \theta) = \frac{-1}{12\pi\ell^2} * (\mathcal{A}^{(0)} + \mathcal{A}^{(2)} \cos^2 \theta) \tag{4.13}$$

For isotropic plane systems, $\mathcal{A}^{(2)}$ is zero and the θ dependance is meaningless. This analytical scaling law works at all distance limits, from contact to a S2SS distance in which the assumption of semi-infinite half-spaces begins to fail. In contrast the anisotropic rod-rod geometries have a very different power law scaling behavior as a function of S2SS[ ]. An interpolation method for determining the limit the system is effectively in is in Appendix A. For the near limit, the total energy scales as follows

$$\mathcal{G}(\ell, \theta) = \frac{-(\pi a^2)^2}{2\pi\ell^4 \sin \theta} * (\mathcal{A}^{(0)} + \mathcal{A}^{(2)} \cos^2 \theta) \tag{4.14}$$

When the rods are fully parallel, the energy would be divergent for infinitely long rods. Therefore the form of the equation is now energy per unit length and the result is as follows.

$$g(\ell) = \frac{-3(\pi a^2)^2}{8\pi\ell^5} * (\mathcal{A}^{(0)} + \mathcal{A}^{(2)}) \tag{4.15}$$

When at the near limit, the power law behavior as a function of S2SS ℓ drops from 5 to 1.5. This is quite dramatic and, as shown in a later section, the distance by which this change over occurs relative to the SWCNT diameter is quite small. For brevity, only the near limit parallel rod-rod solution is listed (a longer derivation and

explanation is in Appendix A).

$$g(\ell, a) = \frac{-\sqrt{a}}{24\ell^{3/2}} * (\mathcal{A}^{(0)} + \mathcal{A}^{(2)}) \tag{4.16}$$

The important take home message here is that each geometry and separation regime has unique vdW-Ld TE scaling behavior as a function of S2SS, angle, and other dimensional effects (such as SWCNT radius). This is important to keep in mind for a few reasons. First, the Hamaker coefficient is the energy per unit vol-vol of interacting species. But if we are trying to design experiments to separate based on relative energy differences of total energies, two tubes of similar Hamaker coefficients can have vastly different total energies because of size. This is not to downplay the importance of the Hamaker coefficients. After all, a properly designed experiment could in fact could have one chirality exhibit an attractive Hamaker coefficient and the other a repulsive one with a given substrate. In this scenario, the quantity of cross sectional volume of the SWCNT would be irrelevant in determining whether a tube would attract or repel.

4.1.3 Across the Levels of Abstraction

Figure 4-1 summarize the various levels described so far and shows how the total energy scaling behavior and spectral mismatch functions change between the various geometries.

4.2 Additional Pragmatic Needs

A novice must be cautioned before simply using the formulations as is without addressing a few important questions. Namely: 1) When is it valid to use the hollow vs. solid spectra? 2) When does the regime change from near to far? The details of first question (i.e. hollow versus solid scaling) will be addressed in the next chapter. The questions of when it is valid to use the near vs. far Hamaker coefficient was solved as follows. The numerical volume-volome solution is assumed to be the true TE at

Figure 4-1: A comparison of the spectral mismatch terms and the total energy scaling behavior for 3 different system geometries at the far-limit: optically isotropic plane-plane, anisotropic plane-plane, and anisotropic rod-rod. Both the optically anisotropic systems assume only 2 independent, uniaxial optical properties with the primary axis in the plane.

(a)

Geometry

Energy

$$G(\ell) = -\frac{A}{12\pi\ell^2}$$

$$A = \frac{3}{2}k_BT\sum_{n=0}^{\infty}{}'\Delta_{\mathcal{L}m}\Delta_{\mathcal{R}m}$$

Hamaker Coefficients

Spectra Functions

$$\Delta_{\mathcal{L}m} = \left(\frac{\epsilon_{\mathcal{L}}-\epsilon_m}{\epsilon_{\mathcal{L}}+\epsilon_m}\right)$$

$$\Delta_{\mathcal{R}m} = \left(\frac{\epsilon_{\mathcal{R}}-\epsilon_m}{\epsilon_{\mathcal{R}}+\epsilon_m}\right)$$

Anisotropy Pieces

(b)

$$G(\ell,\theta) = -\frac{A^{(0)}+A^{(2)}\cos^2\theta}{12\pi\ell^2}$$

$$\mathcal{A}^{(0)} = \frac{3}{2}k_BT\sum_{n=0}^{\infty}{}'\frac{1}{2\pi}\int_0^{2\pi}\Delta_{\mathcal{L}m}(\phi)\Delta_{\mathcal{R}m}(\phi-90)d\phi$$

$$\mathcal{A}^{(0)}+\mathcal{A}^{(2)} = \frac{3}{2}k_BT\sum_{n=0}^{\infty}{}'\frac{1}{2\pi}\int_0^{2\pi}\Delta_{\mathcal{L}m}(\phi)\Delta_{\mathcal{R}m}(\phi)d\phi$$

$$\Delta_{\mathcal{L}m}(\phi) = \left(\frac{\epsilon_{\perp}(\mathcal{L})\sqrt{1+\gamma(\mathcal{L})\cos^2\phi}-\epsilon_m}{\epsilon_{\perp}(\mathcal{L})\sqrt{1+\gamma(\mathcal{L})\cos^2\phi}+\epsilon_m}\right)$$

$$\Delta_{\mathcal{R}m}(\phi) = \left(\frac{\epsilon_{\perp}(\mathcal{R})\sqrt{1+\gamma(\mathcal{R})\cos^2\phi}-\epsilon_m}{\epsilon_{\perp}(\mathcal{R})\sqrt{1+\gamma(\mathcal{R})\cos^2\phi}+\epsilon_m}\right)$$

$$\Delta_{\mathcal{R}m}(\phi-90) = \left(\frac{\epsilon_{\perp}(\mathcal{R})\sqrt{1+\gamma(\mathcal{R})\sin^2\phi}-\epsilon_m}{\epsilon_{\perp}(\mathcal{R})\sqrt{1+\gamma(\mathcal{R})\sin^2\phi}+\epsilon_m}\right)$$

$$\gamma = \frac{\epsilon_{\parallel}-\epsilon_{\perp}}{\epsilon_{\perp}}$$

(c)

$$G(\ell,\theta) = -\frac{(\pi a^2)^2(A^{(0)}+A^{(2)}\cos^2\theta)}{2\pi\ell^4\sin\theta}$$

$$G(\ell,\theta=0) = -\frac{3(\pi a^2)^2(A^{(0)}+A^{(2)})}{8\pi\ell^5}$$

$$\mathcal{A}^{(0)} = \frac{3}{2}k_BT\sum_{n=0}^{\infty}{}'\frac{1}{2\pi}\int_0^{2\pi}\Delta_{\mathcal{L}m}(\phi)\Delta_{\mathcal{R}m}(\phi-90)d\phi$$

$$\mathcal{A}^{(0)}+\mathcal{A}^{(2)} = \frac{3}{2}k_BT\sum_{n=0}^{\infty}{}'\frac{1}{2\pi}\int_0^{2\pi}\Delta_{\mathcal{L}m}(\phi)\Delta_{\mathcal{R}m}(\phi)d\phi$$

$$\Delta_{\mathcal{L}m}(\phi) = -\left(\Delta_{\perp}(\mathcal{L})+\frac{1}{4}(\Delta_{\parallel}(\mathcal{L})-2\Delta_{\perp}(\mathcal{L}))\cos^2\phi\right)$$

$$\Delta_{\mathcal{R}m}(\phi) = -\left(\Delta_{\perp}(\mathcal{R})+\frac{1}{4}(\Delta_{\parallel}(\mathcal{R})-2\Delta_{\perp}(\mathcal{R}))\cos^2\phi\right)$$

$$\Delta_{\mathcal{R}m}(\phi-90) = -\left(\Delta_{\perp}(\mathcal{R})+\frac{1}{4}(\Delta_{\parallel}(\mathcal{R})-2\Delta_{\perp}(\mathcal{R}))\sin^2\phi\right)$$

$$\Delta_{\parallel} = \frac{\epsilon_{\parallel}-\epsilon_m}{\epsilon_m} \qquad \Delta_{\perp} = \frac{\epsilon_{\perp}-\epsilon_m}{\epsilon_{\perp}+\epsilon_m}$$

all S2SS. The analytical endpoints are then interpolated in an effort to minimize the error across all S2SS. This is done using the following Fermi function form:

$$f(\ell, \ell_0, \beta) = \frac{1}{1 + e^{\beta(\ell - \ell_0)}} \tag{4.17}$$

While other interpolation functions could have been selected, the goal was simplicity in determining the cross over point. The Fermi function above essentially has two adjustable parameters: 1) ℓ_0, the midpoint of the transition and 2) β, the blurriness or width of the transition. Both parameters give us vital information. It is not just enough to know ℓ_0 and claim that this point is a discontinuity, with any point 0.00001 nm larger being the far limit and 0.00001 nm smaller being the near limit. The β term also helps determine the spread by which the two analytical endpoints contribute, also paving the way for making a better determination of when we are completely in the near vs. far limit.

There are several ways one could choose to obtain the optimal β and ℓ_0. In the end, I opted for the somewhat subjective test of what looked best visually and ensured the smallest maximum percentage discrepancy. That is, the fit would minimize the largest percentage difference between the numerical integration and the interpolated analytical endpoints[26]. Figure 4-2 shows the best fits for the rod-rod and rod-surface systems for SWCNTs with a 0.4nm radius.

However these scaling behaviors are not confined to a single radius, so there needs to be a way to scaling of these parameters such that a determination can be made for all possible SWCNT radii. For the rod-surface system, $\ell_0 = a$ and $\beta = 0.375 * a$ were the best fits as per my method selection. For the rod-rod system, the values were $\ell_0 = 0.7 * a$ and $\beta = 0.35 * a$. Therefore, for the purposes of total energies, the system can be considered at the far limit when $\ell_0 + 3 * \beta$ because at this point the fermi function uses 95% of the far-limit equation and only 5% of the near limit. This is I claim that the true far-limit regime occurs at a S2SS of approximately 2 * radius. To be more conservative this value is doubled and I use 2 full SWCNT diameters as the location denoting the pure far-limit.
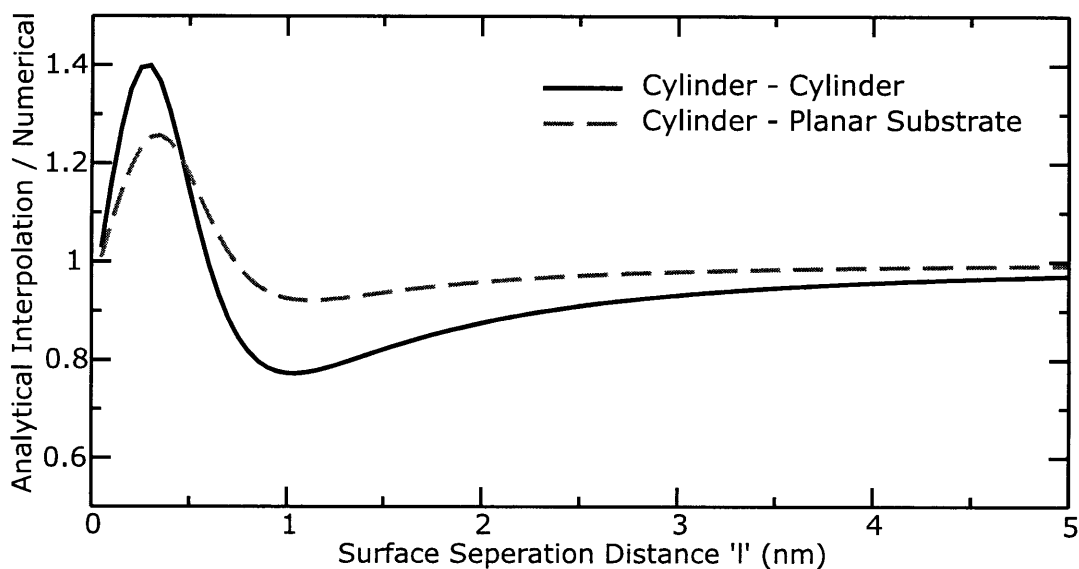
Figure 4-2: A comparison of volume-volume numerical integration versus a interpolation of the analytical near and far limit endpoints using a Fermi function.

A word of caution. This does not mean that the total energy will be off by at most 5% at a distance of $\ell_0 + 3 * \beta$ (where 95% of the far-limit endpoint is used). It only means that the balance of the equations used is 95% from the far limit analytical endpoint. Thus to retain any sort of total energy accuracy, one would still need to use the interpolation even far beyond this limiting case.

Why is this necessary? It is only by cancelation of errors that the interpolation occurs over such a narrow range of separation distances (narrow with respect to the ratio of S2SS vs. SWCNT radius or ℓ/a). The near limit analytical formulation greatly overestimates while the far limit greatly underestimates. After all, the power law scaling behavior is rapidly changing from 1.5 to 5.0 as the S2SS moves from contact to only a few diameters away. Figure 4-3 shows the exponent behavior as a function of the dimensionless ℓ/a factor, which is simply a ratio of SS2S over SWCNT radius. It is only at contact that the power law behavior truly approaches 1.5. In fact, by a S2SS of 0.25*a (SWCNT radius), the power law has already dropped to 1.8. By a distance $\ell = 2 * a$, the power law behavior is now almost perfectly averaged to a value of 3.0 (hence the change over in limiting behavior). It isn't until about 10 radii that the power law is 4 and it asymptotically gets closer to 5 beyond this.
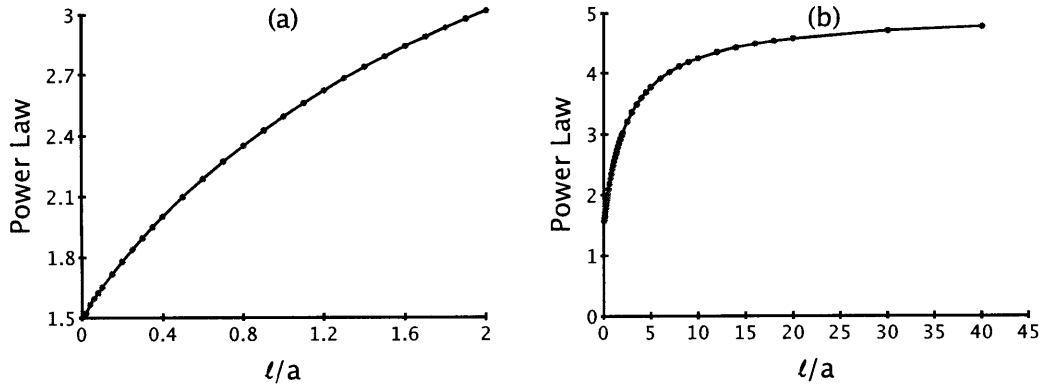
Figure 4-3: The changing power law behavior of $1/\ell^n$ as a function of the dimensionless scale factor ℓ/a. The analytical endpoints are only truly relevant at the extreme near (n=1.5) and far (n=5.0) limits for the rod-rod geometry.

So what is an end-user to do that just wants the proper total energy at all distances? Initially the formulations were published in PRB and recommended the interpolation as follows[ ].

$$
\begin{aligned}
g(\ell, a) \;=\; & -\frac{\sqrt{a}}{24\pi \; \ell^{3/2}} \left(\mathcal{A}_N^{(0)} + \mathcal{A}_N^{(2)}\right) f(\ell, \ell_0, \beta) \\
& -\frac{3 \; (\pi a^2)^2}{8\pi \; (\ell + 2 \; a)^5} \left(\mathcal{A}_F^{(0)} + \mathcal{A}_F^{(2)}\right) (1 - f(\ell, \ell_0, \beta)),
\end{aligned}
\tag{4.18}
$$

However on further reflection this interpolation is only necessary for the Hamaker coefficients and not necessary for the volume-volume interaction terms for these coefficients. After all, a numerical vol-vol integration is computationally cheap, straightforward, and gives a 100% TE scaling accuracy at all distances. Considering that the murky regime between the near and far limits is also the most important for many biological systems, it doesn't make sense forgo accuracy for the sake of being a purist with analytical formulations. Thus for end-users, it is recommended to use the following form instead.

$$
g(\ell, a) = -VV(\ell) \left(\mathcal{A}_N^{(0)} + \mathcal{A}_N^{(2)}\right) f(\ell, \ell_0, \beta) + \left(\mathcal{A}_F^{(0)} + \mathcal{A}_F^{(2)}\right) (1 - f(\ell, \ell_0, \beta)), \tag{4.19}
$$

where $VV(\ell)$ is a volume-volume integration term for the given geometry. For the parallel rod-rod system, it is simple to use a brute force cartesian method with 6 integrations over $\frac{1}{\ell^6}$. However a numerical short-cut is available that cuts the computation time down by approximately 2 orders of magnitude[ ].

$$VV(z, a_1, a_2) = \frac{2}{3z} \sum_{i}^{imax} \sum_{j}^{jmax} * \frac{\Gamma(i+j+1/2)^2}{i!j!(i-1)!(j-1)!} (\frac{a_1}{z})^{2i} (\frac{a_2}{z})^{2j} \quad (4.20)$$

$$\Gamma(n+1/2) = \frac{\pi^{1/2}}{2^n} \prod_{m=1}^{m=n} (2n-1) \quad (4.21)$$

$$z = \ell + a_1 + a_2 \quad (4.22)$$

The integration form is much simpler for the case of a cylinder with its axial direction parallel to the surface of a plane. In this case, it is only the shortest distance between a point on the cylinder to the substrate that matters. Therefore the first volume integration is skipped and one can start with the $1/\ell^3$ point - surface solution[,]. Since the axial direction is a linear integration in this spatial arrangement, the $VV(\ell, a_1)$ can be trimmed down further to the following, double integration.

$$VV(\ell, a_1) = \int_{r=0}^{r=a_1} \int_{\theta=0}^{\theta=2\pi} \frac{r}{6\pi(\ell + a_1 + r * \cos(\theta))^3} d\theta dr \quad (4.23)$$

In this way, one can achieve an accurate total energy at all separations while simultaneously using the Hamaker coefficients that dominate the particular regime. Ultimately this is the best and most pragmatic approach for the time being. Only when we have numerical methods to calculate Hamaker coefficients at all separations will we be able to adjust this Fermi interpolation of the Hamaker coefficient to a more accurate position and with an improved interpolation function. For now, I claim that this is sufficient.
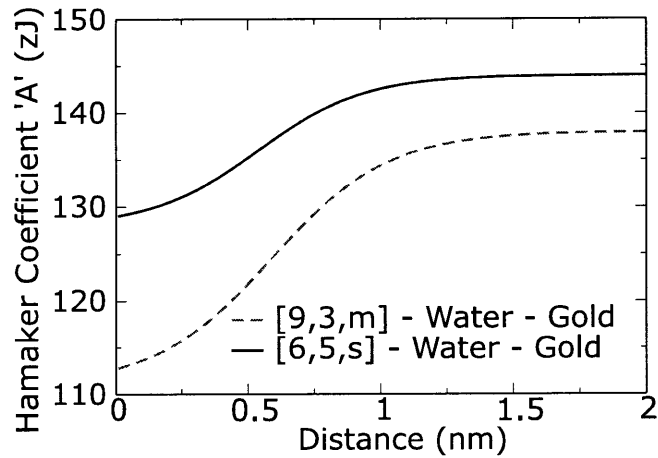
Figure 4-4: The Hamaker coefficients as a function of ℓ for the [6,5,s] and [9,3,m] SWCNTs with a gold substrate in a water medium. The anisotropic rod-surf formulation was used at the near and far-limits with the solid cylinder scaling of vdW-LDS.

4.3 Results

Having fully described the key aspects of the new anisotropic rod-rod and rod-surf formulations, it is now possible to look at their effects upon the ϵ'' for SWCNTs obtained in the previous chapter. It is also now possible to calculate accurate Hamaker coefficients for all chiralities over all S2SS. Figure 4-4 shows the Hamaker coefficients for the [6,5,s] and [9,3,m] SWCNTs over gold using the solid vdW-LDS for both limits. Technically it is more accurate to use the hollow cylinder spectra in the near limit regime (more on this in the mixing chapter). However, using the same vdW-LDS for each distance limit eliminates any additional changes that would result from ϵ'' scaling. In a sense, it isolates the effects of the near vs. far limit Lifshitz formulation, which are applicable to the general body of solid, single component materials.

Notice that for both SWCNTs, the far-limit Hamaker coefficients are larger. This increase can be traced back to the $\Delta_{\parallel}$ terms, which only exist at the far limit. The $\frac{a-b}{b}$ form of the $\Delta_{\parallel}$ terms result in very large contributions to the overall Lifshitz summation for frequencies that have very high optical contrast (such as the difference between the SWCNTs and water for a large energy range). The γ or $\Delta_{\perp}$ terms tend

	[6,5,s]	[9,3,m]
ϵ_m	2.02	2.02
$\epsilon_\parallel$	6.96	18.27
$\epsilon_\perp$	6.05	5.77
γ	0.15	2.17
$\Delta_\perp$	0.50	0.48
$\Delta_\parallel$	2.45	8.05
Δ_{Lm} Near	0.53, 0.50	0.67, 0.48
Δ_{Lm} Far	0.86, 0.50	2.25, 0.48
$\mathcal{A}^{(0)}, \mathcal{A}^{(2)}$ Near (zJ)	1.08, 0.82	1.47, 1.11
$\mathcal{A}^{(0)}, \mathcal{A}^{(2)}$ Far (zJ)	1.83, 1.52	6.05, 7.80

Table 4.1: A comparison of how the various spectral mismatch components contribute to the overall Hamaker coefficient for the [6,5,s] and [9,3,m] SWCNTs at the first Matsubara frequency (n=1 or approximately 0.16 eV at room temperature)

to have an intrinsic or effective limit to how much they can contribute for reasons described earlier.

A quick numerical comparison of these different parts can help drive the point home. Table 4.1 breaks down all the pieces and shows how they impact the n=1 (0.16 eV at room temperature) Matsubara frequency for the [6,5,s] and [9,3,m] in water.

A few things to note. The only spectra mismatch terms that exceed unity are γ, $\Delta_\parallel$, and the far-limit Δ_{Lm}. All other spectra mismatch function are capped at a maximum value of 1 and typically do not come close to this limit except for spectral mismatches that are an order of magnitude or greater in size. Although γ itself can be large and contribute to both the total and orientation-dependent energies, its location under a square root sign dampens its effect. Thus even for the highly anisotropic [9,3,m], the contribution of $\mathcal{A}^{(2)}$ at the near limit is 1.11 zJ.

This result is respectable and identifiable, but not huge because the n=0 and n=1 terms are the majority contributors to the Hamaker anisotropy for SWCNTs. Later terms in the Lifshitz summation, because of the steeply decaying nature of the $\epsilon_\parallel$ vdW-LDS for metallic wing SWCNTs, add much less to $\mathcal{A}^{(2)}$ despite still contributing largely to $\mathcal{A}^{(0)}$.

In contrast, the effects $\Delta_\parallel$ propagates through and add significantly to both total energy and orientation-dependent energy. For reasons that will make sense shortly, an optical contrast function that increases orientation-dependent interactions will also increase the total energy. First we see that that $\Delta_\parallel$ values are quite high due to the optical contrast between the SWCNTs and water. The value $\Delta_\parallel = 2.45$ for the [6,5,s] is larger than 1, but gets diminished to a value below unity by the 1/4 pre-factor in Δ_{Lm}. Still, the far-limit contribution to the total Hamaker coefficient is almost double that of the near limit and weighs in at just over 3 zJ for one Matsubara frequency.

When changing to the [9,3,m], $\Delta_\parallel$ now is now large enough for a drastic change. Despite the 1/4 coefficient on the $\Delta_\parallel$ term, the resulting Δ_{Lm} is 2.25. The result is a hefty value of 7.8zJ for $\mathcal{A}^{(2)}$ alone once Δ_{Lm} is multiplied by an equal Δ_{Rm}, integrated over all 360 degree rotations, and multiplied by the conversion to zJ. Therefore a single Matsubara frequency is responsible for nearly all the Hamaker coefficient anisotropy and raises the total energy significantly when alignment is achieved. The later frequencies also contribute to this effect, although in a much lesser capacity as the optical contrast by n=2 is much less.

So what is the overall effect of the new form of the far-limit formulations compared to the near limit? It is two-fold. The introduction of $\Delta_\parallel$ over $\Delta_\perp$ allows for a much larger contrast in the optical properties as a function of the rotation angle. This manifests itself, for the n=1 term, as a gain in $\mathcal{A}^{(2)}$ by a factor of 2 for the [6,5,s] and a factor of 7 for the [9,3,m]. What also occurs is an increase in the baseline $\mathcal{A}^{(0)}$ energy, moving up 80% for the [6,5,s] and 400% for the [9,3,m] for the n=1 term.

In summary, the $\Delta_\parallel$ form in the far limit Δ_{Lm} term increases the effects of existing optical contrast. This doesn't necessarily lead to a stronger total energy or anisotropy (because there are other nuances that can shift this for a carefully or creatively designed system). However, this will tend to be the case, particularly for symmetric SWCNT systems. Figure 4-5 shows the result of $\mathcal{A}^{(0)} + \mathcal{A}^{(2)} \cos^2 \theta$ for solid cylinder SWCNT spectra using the near and far limit rod-rod formulations. Notice how both the discussion points hold true. The Hamaker coefficient curves in the far-limit are both larger in energy and larger direction-dependent behavior.

(a)

(b)

Hamaker Coefficient 'A' (zJ)

— [6,5,s] Near
-- [9,3,m] Near

— [6,5,s] Far
-- [9,3,m] Far

Angle (Degrees)

Angle (Degrees)
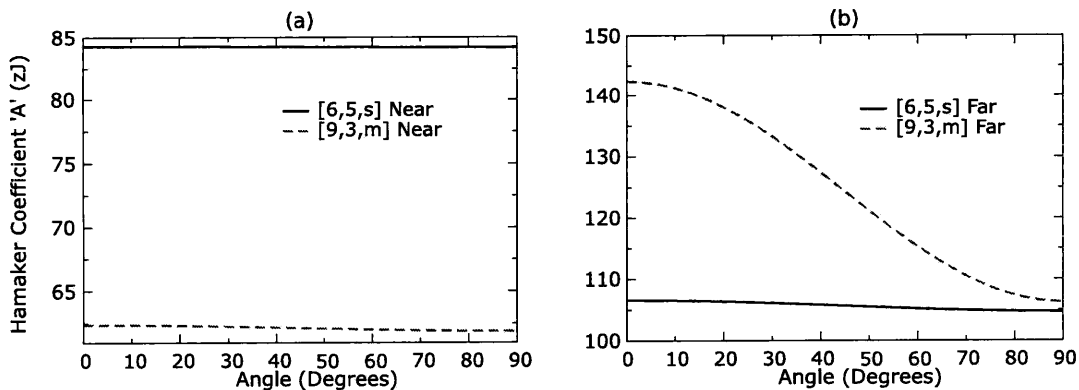
Figure 4-5: The orientation-dependent Hamaker coefficients for the [6,5,s] and [9,3,m] anisotropic rod-rod systems at the near and far limits

SWCNT	$\mathcal{A}^{(0)}$	$\mathcal{A}^{(2)}$	$\mathcal{A}_{zz}$	$\mathcal{A}_{rr}$	$\mathcal{A}_{rz}$	$\frac{\mathcal{A}_{zz}+\mathcal{A}_{rr}}{2} - \mathcal{A}_{rz}$	$\Delta\mathcal{A}^{(0)}$	$\Delta\mathcal{A}^{(2)}$
6,5 Near	84.4	0.1	70.7	91.6	80	1.2 (all data zJ)	-5%	1050%
6,5 Far	104.9	1.9	70.7	91.6	80	1.2	-24	-39
9,3 Near PRB	61.9	0.5	54	68.4	55	6.2	-11	1140
9,3 Far PRB	106.3	36	54	68.4	55	6.2	-48	-83
9,3 Near k3x	60.3	0.4	45.6	68.2	52.7	4.2	-13	950
9,3 Far k3x	78.5	6.2	45.6	68.2	52.7	4.2	-33	-32

Table 4.2: A comparison of Hamaker coefficients between the newly derived anisotropic rod-rod Lifshitz formulations with the crude pairwise values. Also included is the original and higher resolution [9,3,m] spectra to highlight the sensitivity of the far-limit spectral mismatch functions with respect to small variation in the low energy vdW-LDS behavior at 0 eV. The near-limit values are changed very little by comparison.

Next, it is important to compare these effects to the original, albeit crude axial-axial, radial-radial, and axial-radial pairwise interactions to see if one could in fact get away with such an approximation. Table 4.2 shows the results as compared to the full $\mathcal{A}^{(0)}$ and $\mathcal{A}^{(2)}$ calcs for the [6,5,s] and two versions of the [9,3,m].

First an aside as to why I used two different versions of the [9,3,m]. When the initial formulations paper was published[20], my collaborators and I believed we had well converged data and another ϵ'' calculated with a higher k-point grid mesh confirmed this. That is, the newer k3x calc had all the same features of the k1x data but was a little smoother (barely, but still noticeable visually). The calculations already contained the k1x and there appeared to be no reason to redo them as the input data

appeared identical for the 0-30 eV range.

However, when the data mining analysis was starting (see Chapter 6), the k3x and higher k-point mesh data was used because their were some convergence issues with a few SWCNTs (namely the zigzag metals). So the ϵ'' were recalculated for nearly all the SWCNT chiralities at k3x or higher k-points. What was interesting about this is that for the metallic SWCNTs, all the information above 0.2 eV was essentially numerically identical in terms of area and peak positions. However there were slight changes in the magnitude of the low wing spike around 0 eV. It was not clear how substantial these variations were until they were analyzed across numerous tubes. The analysis of the n=1 Matsubara frequency revealed an enormous difference due to a dramatic change in the vdW-LDS low energy wing. Figure 4-6 shows this result.

However, *REGARDLESS* of which one of the [9,3,m] vdW-LDS is the best bet, their exists SWCNTs from the entire population that have low energy ϵ'' spikes of all sizes. Thus it is still illustrative to see the effects of these low energy wings propagating through the new rod-rod formulations. This data can also be used to show whether one can use the axial-axial, radial-radial, and axial-radial analysis for determination of $\mathcal{A}^{(0)}$ and $\mathcal{A}^{(2)}$. But this issue of ϵ'' spike behavior will not be ignored and addressed more thoroughly in Chapter 6 (datamining).

Returning to the table data, one would speculate that a perfectly aligned set of tubes would essentially be an averaged interaction of $\frac{\mathcal{A}_{zz}+\mathcal{A}_{rr}}{2}$ and a 90 degree offset would be pure $\mathcal{A}_{rz}$. Thus $\mathcal{A}_{rz}$ would essentially mirror $\mathcal{A}^{(0)}$ (base line energy without maximum offset) and $\mathcal{A}^{(2)}$ would be the total energy when aligned minus this offset (i.e. $\frac{\mathcal{A}_{zz}+\mathcal{A}_{rr}}{2} - \mathcal{A}_{rz}$).

This is what results from these calculations and comparisons. The $\mathcal{A}_{rz}$ values are typically 5-10% less than $\mathcal{A}^{(0)}$ in the near limit. This is not too bad and at least the trends are all in the same direction. A close inspection of the new formulations shows that this discrepancy is likely a results of the $\cos^2$ term interpolating the effective spectra from the SWCNT from $\epsilon_\perp$ to $\sqrt{\epsilon_\perp * \epsilon_\parallel}$. By comparison, the axial-radial interaction is one between a pure $\epsilon_\perp$ and pure $\epsilon_\parallel$. Since the interpolation tends
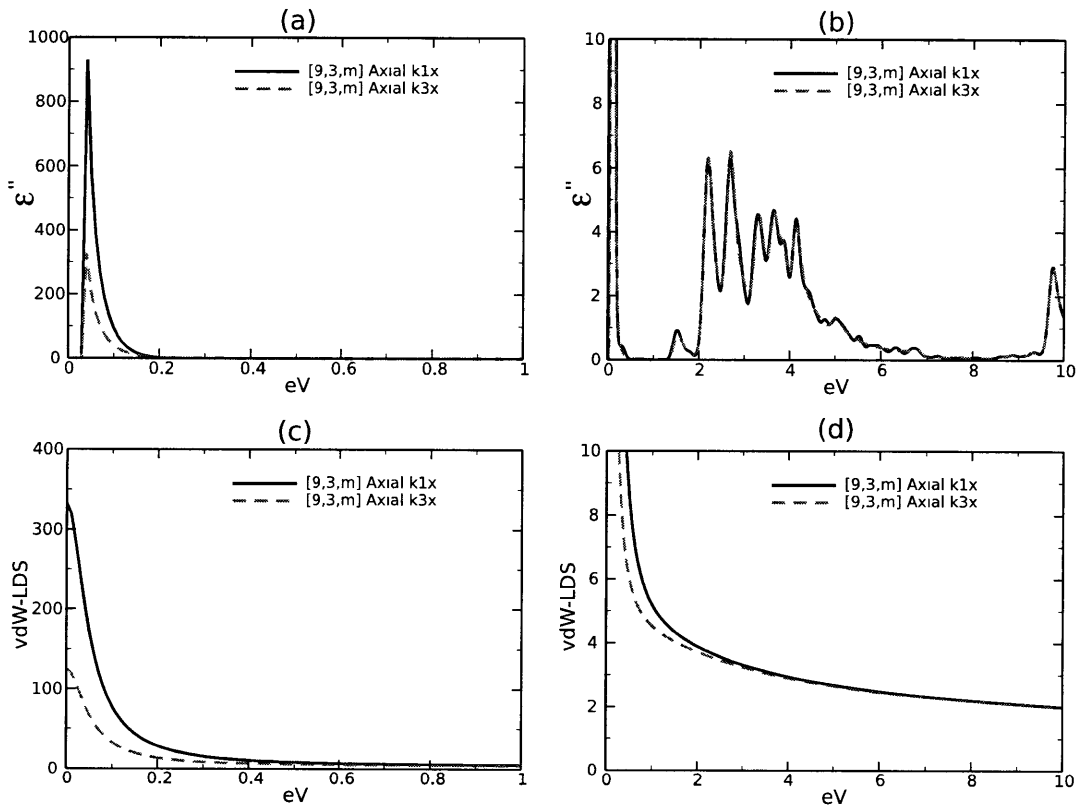
Figure 4-6: An analysis of the critical optical features of the original published [9,3,m] ϵ'' and vdW-LDS with a later [9,3,m] data set containing a larger quantity of k-points in the ab initio calculations. Most of the ϵ'' features are identical in both, with some additional smoothing that arises when we move to more points. However, the dramatic change in magnitude of ϵ'' is in the 0.04-0.1 eV range, which has a very large impact on the resulting vdW-LDS and resulting Hamaker coefficients.

to increase the impact when the spectral mismatch terms interact (for example, the endpoints 4*2 will always be less than a multiplication of the averaged 3*3), the $\mathcal{A}_{rz}$ should always be less than $\mathcal{A}^{(0)}$. One could try to adjust $\mathcal{A}_{rz}$ to account for this loss, but it would require the addition of more fudge factors.

The far limit is a different story. Because the $\Delta_\parallel$ can become very large for big differences in optical contrast, the true values of $\mathcal{A}^{(0)}$ are 20-50% larger than the pairwise $\mathcal{A}_{rz}$. In fact, no amount of averaging would counter this because all the combinations of radial and axial directions have Hamaker coefficients that are smaller than $\mathcal{A}^{(0)}$. One could again use a fudge factor and simply multiply a constant to adjust for this, but this factor would change slightly for all chiralities and is frankly unnecessary with the full formulations.

With respect to the direction-dependent component, values of $\mathcal{A}^{(2)}$ are horribly predicted by the pairwise interactions between radial and axial terms. One might speculate that there might be a better way of combining the axial and radial direction pairings to improve on these major discrepancies. However, using the form that seems to make sense from a geometry point of view, the near limit approximations appear to over-predict $\mathcal{A}^{(2)}$ by an order of magnitude in all cases. For the far limit, the approximation under-predicts $\mathcal{A}^{(2)}$ by 30-90 percent. It is unclear how any decided upon combination would fix both of these error simultaneously.

Therefore I claim that the radial-radial, axial-axial, and axial-radial can match only match the near limit behavior for $\mathcal{A}^{(0)}$. The other values ($\mathcal{A}^{(0)}$ far limit and near/far limit $\mathcal{A}^{(2)}$) only agree with (most) relative energy trends. Therefore the radial and axial comparisons was still good and relevant for what was available at the time of the first publication[ ]. But using such an crude calculations anymore should be avoided for any serious analysis now the full Lifshitz formulations are available.

4.4   Further Extensions Possible

While the formulations themselves are powerful in their current form, they do have a few places where further advancements can be made. The two most noteworthy

areas are 1) retardation and 2) add-a-layer formulations.

Retardation is particularly important at the far-limit in which the higher energy Matsubara frequencies will dampen out and reduce the overall total vdW-Ld energy[ ]. A potential reversal in sign is unlikely because the SWCNT vdW-LDS are much larger in magnitude than water across all chiralities and across nearly all energy ranges. However this could change in more complicated systems that contain more than 3 components and are carefully selected to achieve a particular effect. It could also change when the medium has a vdW-LDS much larger than water. Such scenarios are discussed later in Chapter 6.

Multi-layer effects are by far the most important for SWCNTs because surfactants are a necessity to disperse and suspend them in aqueous solutions. Of course they are not universally important at all S2SS. The $1/\ell^6$ behavior of the vol-vol integration diverges at near contact S2SS, meaning that the outer most material typically dominates the entire interaction between the two objects. Therefore any data given at the near-limit is only valid when using the properties of the outermost material.

Multi-layer effects and, more importantly, multi-component effects are mostly relevant at the far limit. Suppose a SWCNT is coated with a relatively thick surfactant (e.g. SDS). And suppose for a moment that the substrate was selected such that the SWCNT portion was attracted to the substrate while the SDS surfactant was repulsed. What would be the net effect? In the far limit, there would be competing forces: one attractive and one repulsive. And don't forget the SWCNT core, which can bed filled with water or other materials, such as other CNTS, water, ions, or nothing. So each colloidal SWCNT really has a minimum of 3 possible interactions with the other substrate: surfactant, shell, and core. One should rightly ask how to properly take these different points into consideration using the current Lifshitz formulations, which can only address a single "solid" or homogenous spectra input.

The ideal solution would be to have either a 1) analytical add-a-layer formulation for the rod-surf and rod-rod geometry or 2) a numerical formulation to solve arbitrary shapes and spatially varying optical properties. Dealing with them in reverse order, the numerical solution has already been partially solved. Rudi Podgornik solved the

system for arbitrarily shaped isotropic shapes at the contact or non-retarded limit[ ]. The next levels necessary would be to include arbitrarily varying optical properties at all points in space. This is likely a non-trivial task, and other colleagues have given up on this endeavor due to systems that simply would not converge. The add-a-layer analytical formulation thus far cannot be done from first principals, and any attempt to simply guess or propose a format involves an inherent risk.

Another possibility is what I've called the "prism mesh" method and it is a method that one can currently solve the vdW-Ld TE for any arbitrary shaped, spatially varying object as long as their is no orientation-dependence of the optical properties. If an anisotropic plane-plane solution existed with retardation (probably doable but no one has gone forth with such a task at the moment), then the prism mesh method would be theoretically able to solve, with retardation, every possible arbitrarily shaped object with anisotropic, spatially varying properties over a flat plate. This is no trivial feat, and will likely take lots of vetting to prove this. My notes for this method are included in Appendix B for now because a) it is not a mission critical part of this thesis, b) it will need later peer-review and vetting, and c) life's obligations may not afford me the time of getting around to it.

Therefore, the two best possible scenarios (rod-rod add-a-layer and prism mesh) are not presently available in our effort overcome the limitations in using purely solid cylinder formulations to describe multi-component systems. But multi-component effects need to be addressed for the systems relevant to end-users. This begs the question of of whether there is another possibility.

And yes, there is a plausible and thoroughly vetted alternative. That is to take the many components and use an accepted optical mixing formulation to create effective vdW-LDS at the different S2SS regimes. This is an important topic and will have the entire next chapter devoted to it. It is the last necessary step to (finally) give realistic total vdW-Ld energies for systems being studied by end-users.

As far as other extensions/advancements, there are a few minor assumptions in the solid rod-rod and rod-surf formulations that might also need closer scrutiny. For example, the $\sum_j^\infty \frac{1}{j^3}(\Delta_{Lm} * \Delta_{Lm})^j$ of the original Lifshitz from can be reintroduced

to account the higher order terms from the Taylor series expansion. However, there is a big problem in trying to bring them back into the formulations now that some spectral mismatch terms can go over unity. This would cause $\mathcal{A}^2$ terms to diverge to infinity, which clearly a non-physical effect. Because of this, it is better to remove those higher order terms for now until these over-unity terms can be more carefully studied.

4.5 Moving Forward

This section introduced the new optically anisotropic rod-rod and rod-surf formulations. It also introduced and described the many key differences and effects that result from the forms of the spectral mismatch functions. The important take home message is that these formulations are needed, particularly in the far limit, to achieve both an accurate total and orientation-dependent Hamaker coefficient. This crucial step, combined with the anisotropic optical properties, brings us another step closer to fully understanding and being able to solve total vdW-Ld energies for SWCNT systems. Figure 4-7 updates the roadmap to reflect this. What is the necessary next step is to introduce the concepts and effects of optical mixing formulations. Once we have this information, we will be then be able to study a whole diverse set of SWC-NTs and find trends necessary for trap/release/enrichment experiments and system design.

Status of a SWCNT vdW-Ld Calculation
After Aniso Rod-Rod Lifshitz Formulations
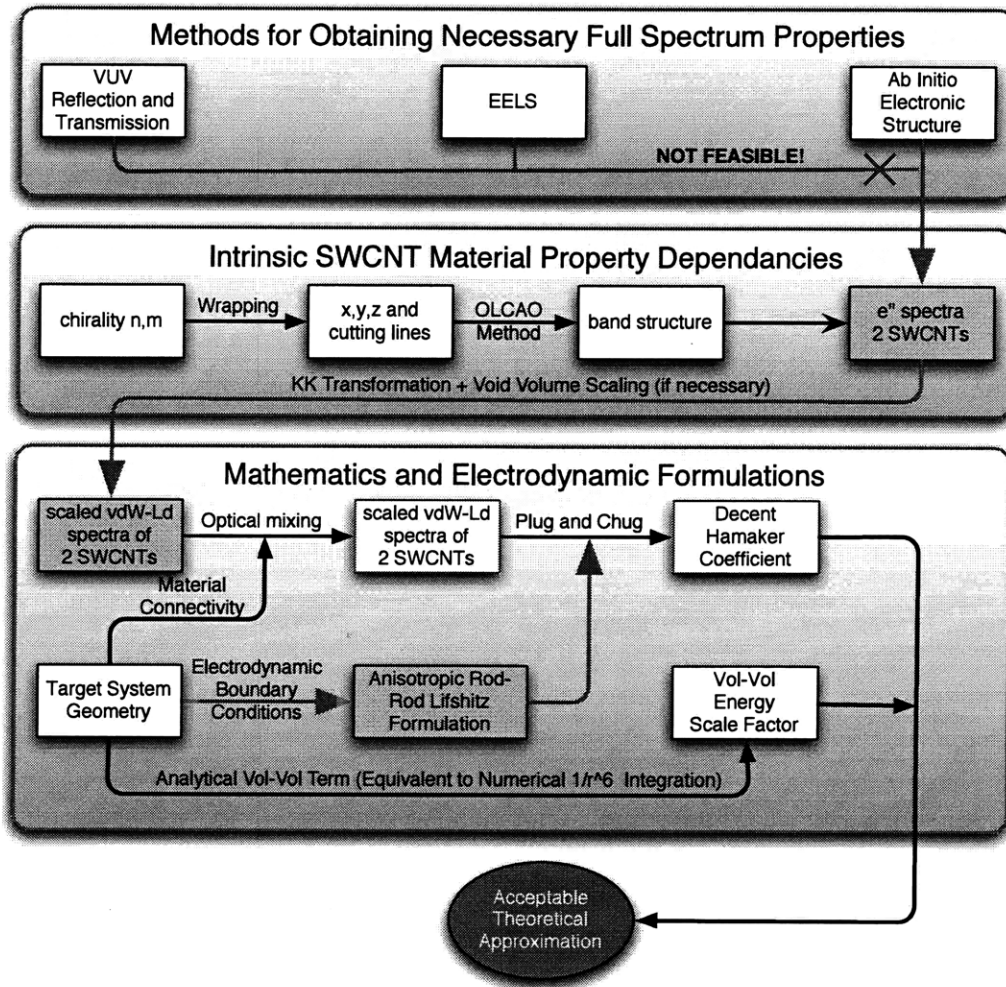
Figure 4-7: With the optically anisotropic rod-rod and rod-surface Lifshitz formulations now available, it is now possible to use the ϵ'' data obtained previously and begin to study the vdW-Ld interactions of SWCNT systems. The only major barrier remaining is to bridge these calculations to interactions for realistic SWCNT systems having surfactants, multi-components, and so forth.
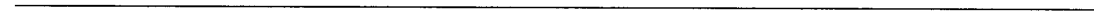
Chapter 5

Effective vdW-Ld Spectra for Multi-Component Cylinders via Optical Mixing Formulations

5.1 Motivation: Making the Case for Spectral Mixing

Most of the vdW-LDS that are publicly available and published (e.g. the compilation contained in Palik[ ]) are isotropic and bulk-averaged. This is not surprising because many of the initial materials studied were of a single, homogenous composition and the instrumentation used to measure them could not resolve feature sizes less than a nanometer in dimension. This may not seem like a very noteworthy statement at first. However, the implications of this are important as we begin to study the vdW-Ld interactions of multi-component systems and systems with significant variation in optical properties as a function of their feature sizes (e.g. DNA, proteins, nanoparticles, etc). Many of these materials having feature sizes smaller than a nanometer.

For example, a person claims that water's vdW-LDS has a strength of 1.91 at 2 eV, what exact position in space is responsible for this value at this frequency? Is it located at the oxygen? The hydrogen? The bond? And what about the thin

excluded volume sections that are created between the molecules in bulk. Certainly this area does not exhibit vacuum like optical behavior because the wave functions of the water molecules do in fact continue to spill out well beyond (albeit not nearly as large) the hard sphere distances. The truth is that we do not presently have a high resolution, 3D contour map of the vdW-LDS properties at all Matsubara frequencies. In actuality, almost all vdW-LDS are a "mixed" or averaged, which are then used with reasonably accurate results to describe the Hamaker coefficient and vdW-Ld TE of many systems. The point is that optical mixing is already being used out of necessity because of the inability to spatially resolve optical properties down to the Angstrom or smaller regime.

A logical followup question is thus, "Can we spatially resolve the vdW-LDS at all?" The answer is clearly yes, and that is done in obtaining every $\mathcal{A}_{121}$ colloid interaction across a medium. The large objects clearly can and do have different optical properties than the medium. At the present moment, it is possible to experimentally resolve feature sizes of approximately 1nm using VEELS and we can use ab initio calculations (specifically a PDOS decomposition) to get down to approximately 1 angstrom resolution. So while we it is not currently possible to resolve a full ϵ'' into a 3D grid with a 0.01 nm mesh size, it is possible to achieve information down to the atom level.

This type of atom-resolved ϵ'' could prove to be extremely beneficial if one is ever able to include a first principles Lifshitz method into an atomistic simulation as it would finally provide the necessary input information. Presently atomistic simulations either use parameterized coefficients in a Lennard-Jones pair potential[78, 34] or with DFT exchange functional[79, 80]. Another major advantage to having this sort of resolution would be in studying inter and intra-molecular vdW-Ld bonding of biomolecules (like proteins) which can have side chains and functionalizations that are clearly location dependent. One could imagine swapping our the R-groups ϵ'' to achieve the appropriate vdW-Ld interactions to fold into the desired 3D shape.

Despite the possible advantages of spatially resolved optical properties, the only way this information could practically be used for vdW-Ld considerations is if there

is a formulation that can handle it as an input. A great example of a system that can use them is the add-a-layer formulation available in the plane-plane system. In this particular formulation, one can slice the optical properties down to arbitrary numbers of layers with arbitrary thicknesses[30, 47]. In short, this allows for a continually varying vdW-LDS as a function of depth in each layer! Of course the model cannot handle variation within the plane perpendicular to the stacking direction. But for the studying of layered systems, that shortcoming is usually not relevant and the add-a-layer formulation retains its power.

However there are many other geometries (most notably the optically anisotropic rod-rod and rod-surface systems) that do not presently have an analytically tractable add-a-layer solution. These systems are therefore confined to using bulk averaged properties and cannot, for example, explicitly input the SWCNT + surfactant + core materials vdW-LDS individually into a single Lifshitz calculation. But the contributions of these components cannot be ignored either because they exist as necessary parts within the systems of interest by experimentalists (see Figure 5-1). SWCNTs and MWCNTs, by the very fact that they contain a core, will always have radially dependent vdW-LDS properties. Therefore to truly understand the vdW-Ld interactions in these systems, a strategy is needed that can address these considerations.

Fortunately there is a viable alternative to an add-a-layer formulation. Spectral mixing at the proper S2SS limits can be used to get an effective vdW-LDS and thus an equivalent total vdW-Ld energy. In principle, this is no different than if we took a highly spatially resolved vdW-LDS of water (clearly oxygen and hydrogen locations have different quantities of electrons and wave functions) and averaged it back to the isotropic value that has been thoroughly studied for decades[30, 67, 68, 69, 70]. But a key point that needs to be addressed is when bulk averaging is an acceptable practice as a function of the feature sizes versus S2SS. The next section will demonstrate that this is typically acceptable when the S2SS distance is larger than 2 times the largest feature size.
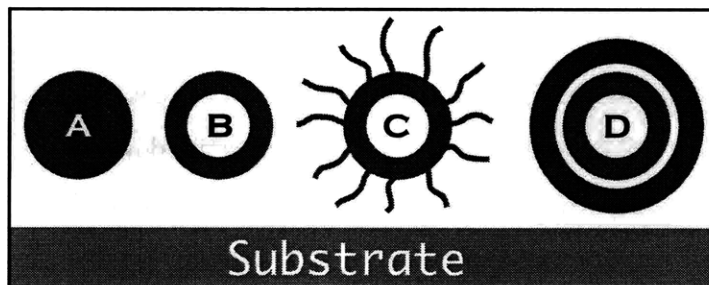
Figure 5-1: Increasing levels of complexity involving a SWCNT interacting with a substrate. a) A solid cylinder b) a hollow cylinder c) a hollow cylinder coated with a surfactant and d) a hollow cylinder within a cylinder.

5.2 Demonstrating vdW-Ld Total Energy Equivalence at the Far-Limit

Figure 5-2 shows the overall concept of what the effective vdW-LDS is at the limiting S2SS. Note that if the feature size is smaller than the surface-to-surface separation, then visually or effectively the materials can appear as bulk averaged. On the other hand, if the closest features of the neighboring materials are significantly larger than the S2SS, the Hamaker coefficient and total vdW-Ld energy can be determined solely by the optical properties of these neighboring materials.

This qualitative behavior of Figure 5-2 is a very useful guide, but a more rigorous, quantitative analysis will is more helpful in determining the cutoff range in which we can confidently use or not use spectral mixing. Figure 5-3 contains such an analysis by comparing the total vdW-Ld energy of ratios as a function of ℓ/a for 3 different add-a-layer configurations. For simplicity, the calculated the Hamaker coefficient uses fictitious vdW-Ld input spectra by using simple damped oscillators of the following form:

$$\epsilon(\imath\xi) = 1 + \frac{s}{1+\xi^2} \tag{5.1}$$

where s represents the magnitude or strength of the oscillator. For the values contained in Figure 5-3, the unmixed solid material in case C3 has a very large value of s=100. The vacuum material has no decaying oscillator behavior and therefore

has s=0. For the mixture material, the Bruggeman effective mixing approximation (EMA) was used at each Matsubara frequency (the details of the EMA mixing formulation will be described more rigorously in the next section)[,]. The total energy and Hamaker coefficients were calculated using the following simple, non-retarded isotropic plane-plane equations.

$$\mathcal{G}(\ell) = \frac{\mathcal{A}}{12\pi\ell^2} \tag{5.2}$$

$$\mathcal{A}_{\mathcal{L}m_1/\mathcal{R}m_2} = \frac{3}{2}\sum_{n=0}^{\infty}{}' \left(\frac{\epsilon_{\mathcal{L}} - \epsilon_{m_1}}{\epsilon_{\mathcal{L}} + \epsilon_{m_1}}\right)\left(\frac{\epsilon_{\mathcal{R}} - \epsilon_{m_2}}{\epsilon_{\mathcal{R}} + \epsilon_{m_2}}\right) \tag{5.3}$$

Case C2 and C3 required a slightly more complicated add-a-layer form of the overall energy. The following subscript notation (see ref [ ]), i.e. $\mathcal{A}_{\mathcal{L}m/\mathcal{R}m}$, is used so as to eliminate confusion. Here the slash in the subscript denotes the sides to the left and right of the medium. The first term in each subscript couple denotes the material furthest away from the middle/intervening separation layers. The EMA mixture material is labeled as 'm', the low value vacuum as 'v', and the high value of the solid material as 'h', which results in cases C1, C2, and C3 to be as follows.

$$C1 : \mathcal{G}(\ell) = \frac{-\mathcal{A}_{mv/mv}}{12\pi(\ell)^2} \tag{5.4}$$

$$C2 : \mathcal{G}(\ell) = \frac{-\mathcal{A}_{mv/mv}}{12\pi(\ell)^2} + \frac{-\mathcal{A}_{mv/vm}}{12\pi(\ell + a)^2} \tag{5.5}$$

$$C3 : \mathcal{G}(\ell) = \frac{-\mathcal{A}_{mv/hv}}{12\pi(\ell)^2} + \frac{-\mathcal{A}_{mv/vh}}{12\pi(\ell + a/3)^2} + \frac{-\mathcal{A}_{mv/hv}}{12\pi(\ell + 2a/3)^2} + \frac{-\mathcal{A}_{mv/vh}}{12\pi(\ell + 3a/3)^2} \tag{5.6}$$

Equations 5.6 may look bulky, but there is a clear and easy to understand pattern that arises when moving from C1 to C3. In short, the total energy equation for each case is merely a summation resulting in a single term for each interface pair across the intervening medium layer. The distance part in the denominator is equivalent to the separation distance between that given pair of interfaces. The Hamaker coefficient subscripts denote the optical properties of the two neighboring materials at each

of these interfaces using the ordering scheme described above (outer most material gets listed first). Thus each term can easily be constructed from the picture. As an example, the last interfaces in case C3 have a Hamaker coefficient $\mathcal{A}_{mv/vh}$ at a interface-interface separation distance of $\ell + a$. It is worth noting that in cases like C2, the Hamaker coefficients are equal in magnitude but opposite in sign simply because they include the same spectra and just have their subscript order reversed. If these interfaces were brought completely together, the two total energy terms would cancel out as expected because the interfaces would annihilate and disappear.

At the near-limit, it is clearly the materials closest to the intervening medium that dominate the total vdW-Ld energy interaction, which is demonstrated by the C1/C2 ratio converging to 1 and thus being effectively equal despite the fact that C2 is of a finite thickness and has an additional interface term. This effective equivalence is due to the divergent, $1/\ell^2$ behavior of the nearest interface-interface pair dominating the total energy as ℓ goes to zero. In effect, one can place any arbitrary number of interfaces at distances well beyond the leading term and they would have little to no impact on the total vdW-Ld energy. Therefore at contact, it is only the optical properties of the outermost layer that should be used and no optical mixing is required.

The opposite effect occurs at the far limit. The individual Hamaker coefficients found in all 4 terms of case C3 are much larger than the Hamaker coefficients for case C2 because the spectral contrast at each interface in C3 is much greater. One might be too quick to conclude that these larger Hamaker coefficients should lead to a larger total energy for case C3 as compared to C2. However the interfaces in C3 begin to pack more closely and thus the overall magnitudes of the $1/\ell^2$ terms (i.e. the geometrical components) of the neighboring interfaces get closer. These two effects (increasing Hamaker coefficients and decreased spacing) cancel each other out making cases C2 and C3 nearly identical in the far limit, with case C2 certainly giving us an advantage of reduced complexity.

Figure 5-3 (b) illustrates these effects visually for all values of ℓ/a. Additionally it is important to note that ratio of C3/C2 converges to a fixed value when $\ell > 2d$,

where d is the thickness of the finite layers in cases C3 and C2. This particular distance of convergence is an encouraging result because it is the exact same distance we determined to be far limit regime in our analysis of the anisotropic solid-cylinder Lifshitz formulations. For the purposes of stress-testing the EMA mixing rules, I purposely chose extreme values of 's' to mimic the vacuum (v: s=0) and metal (h: s=100) endpoints. Therefore this 23% discrepancy can be thought of as the maximum error that can exist between the total vdW-Ld energies of cases C2 and C3 in the far limit. If these values of 's' we close in magnitude (e.g. v: s=50 and h: s=100), then the difference in total energy drops to less than 4%. And of course, if materials 'v' and 'h' have identical spectra, cases the ratio of C2/C3 merges to unity at the far limit. Therefore one can confidently mix spectra that are on the same order of magnitude and be sure they are getting realistic results. When spectra are vastly different, there will be some discrepancies that need to be taken into account.

There is one final issue to note in Figure 5-3. Although the limiting separation regimes are easy to characterize, there is a transition range between the near and far limits which is harder to define. For those cases, one might best use the interpolation method described previously in order to get a reasonable Hamaker coefficient and total vdW-Ld energy at any separation distance. This process is beyond the scope of this thesis, which is primarily focused on the effects of mixing on the limiting behaviors. However those wishing to know this information within this regime can do so in a reasonably straightforward manner[ ].

5.3   Choosing a Proper Mixing Formulations

So far in this chapter I have explained and demonstrated the validity of optical mixing formulations for vdW-Ld interaction energy considerations. The next step is to pick the formulation that provides a high degree of accuracy and properly accounts for the cylindrical geometry of the SWCNT systems. Typically (or at least historically) the spectral mixing of optical properties is done via an effective medium approximation (EMA), such as Bruggeman EMA[ ]. The basic form is as follows:
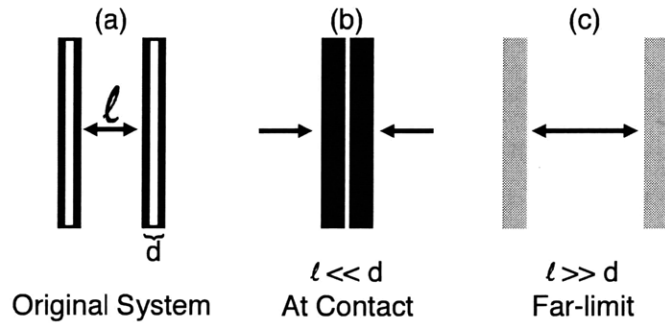
Figure 5-2: The effective vdW-LDS as a function of dimensionless scale factor ℓ/a at the near and far limits. A) Original layered system with a total thickness of '2a=d'. B) At near contact ($\ell/a \ll 1$), the optical properties near the respective surfaces dominate the interaction. C) At large separations ($\ell/a \gg 1$), the optical properties are a weighted average of the various components and typically dominated by the materials with the larger volume fraction.
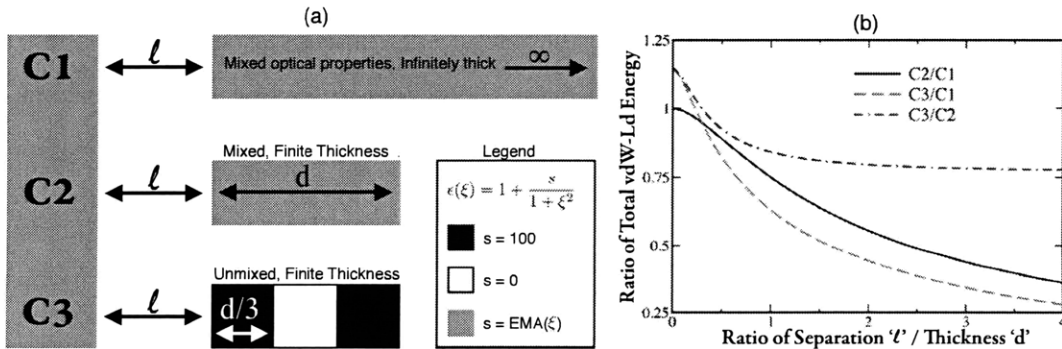
Figure 5-3: Comparing total vdW-Ld interaction energy ratios of three different systems to demonstrate mixing equivalence at far-limit. A) Case C1 uses the optically mixed material in an infinitely thick configuration. Case C2 is a finite block of the optically mixed material. Case C3 contains the unmixed material sandwiching a vacuum layer. B) The ratio of total vdW-Ld energies varies as a function of the dimensionless scale factor ℓ/a.

$$\sum_i \phi_i \frac{\epsilon_i - \epsilon}{\epsilon_i + 2\epsilon} = 0 \tag{5.7}$$

Where ϕ_i is the volume fraction of each component. From a physical standpoint, the unmodified Bruggeman EMA lacks any predominant geometrical arrangement of material connectivity in a particular direction. One can make a case that the radial direction of a SWCNT also lacks a predominant geometrical arrangement. If the cross section is sliced and discretized into small units, some parts would behave like a series capacitor and others (e.g. the circumferential portions within the cylindrical shell) would behave more like capacitors in parallel. Therefore using either of the endpoints (e.g. series or capacitor mixing) would not be a valid approach and the Bruggeman EMA appears to be the best balance.

In the axial direction, the polarization can easily be split into well defined regions of continuous connectivity. Therefore a cross sectional area weighting (i.e. a parallel capacitor averaging) is valid. This is particularly important for the metallic SWCNTs, which tend to have a very large (100+) vdW-LDS peak at 0 eV. If we used the EMA mixing rule, the axial direction spectra at 0 eV would be artificially lowered and the $\Delta_\parallel$ terms would not contribute as strongly to the overall total energy.

Figure 5-4 shows a comparison of the parallel capacitor, Bruggeman EMA, and series capacitor mixing formulations for two materials with varying volume fractions. When the spectral mismatch is small, the variation among the three models is also quite small. However, when the spectral mismatch is very large, the choice among the various models becomes very important. The parallel capacitor model will simply weight the spectra by their respective volume fractions, while the serial capacitor model will strongly dampen the averaged spectra towards the weakest of the contained spectra. The large difference in the capacitor endpoints is due to connectivity considerations. The Bruggeman EMA can be thought of as a intermediate arrangements of the material connectivity in 3D space and therefore its mixed value resides between these two limits. The important take home message is that for large spectral mismatch terms, choosing the proper model based on connectivity considerations

becomes very important.

It should be noted that there are many other mixing formulations available, such as Lorentz-Lorenz[76], Maxwell-Garnett[76], and Rayleigh[77]. However the Lorentz-Lorenz assumes a vacuum host instead of any arbitrary medium or additional materials. This would be insufficient to create a MWCNT out of 2 or more SWCNT components. The Maxwell Garnett assumes a dilute volume fraction within the host material. While the SWCNTs can certainly be dilute in the water medium, the mixing formulation itself is done within the confines of the other shell layer of the SWCNT. Therefore it really cannot be considered dilute from that perspective. The Rayleigh mixing tends to give far too much weight to the weaker of the two spectra, closely representing the effects of the series capacitor. Therefore it is also not an ideal candidate for SWCNTs.

The Bruggeman EMA mixing formulation tends to be the most appropriate for our SWCNT systems because it doesn't assume which material is the host (i.e. dominant or majority material) or assume a predominant connectivity. If such a situation did arise where one needed additional connectivity in the radial direction, but not quite reaching the parallel limit, straightforward interpolations are available to achieve every gradation in between[76]. In short, the Bruggeman EMA can be interpolated to all of the other models with a simple q factor varying from 0 (zero screening parallel capacitor) to 1 (series capacitor). I use the traditional Bruggeman EMA for the purposes of this paper, but leave the door open for further refinements on this q factor if it is needed in certain situations.

To quantify the impact of the mixing formulations, Table 5.1 compares the effects of 6 different mixing rules on a 50-50 mixture of the [25,0,s] radial direction with vacuum. This particular SWCNT was chosen because it does not have a metallic 0 eV behavior and its core void space is exactly 50% of the total volume of the entire SWCNT + core. The parallel and series capacitor methods are still the endpoints, resulting in the largest and smallest possible magnitudes respectively. The Maxwell-Garnett model resides between the EMA and parallel capacitor and the Lorentz-Lorenz and Raleigh models are much closer to the series capacitor model.
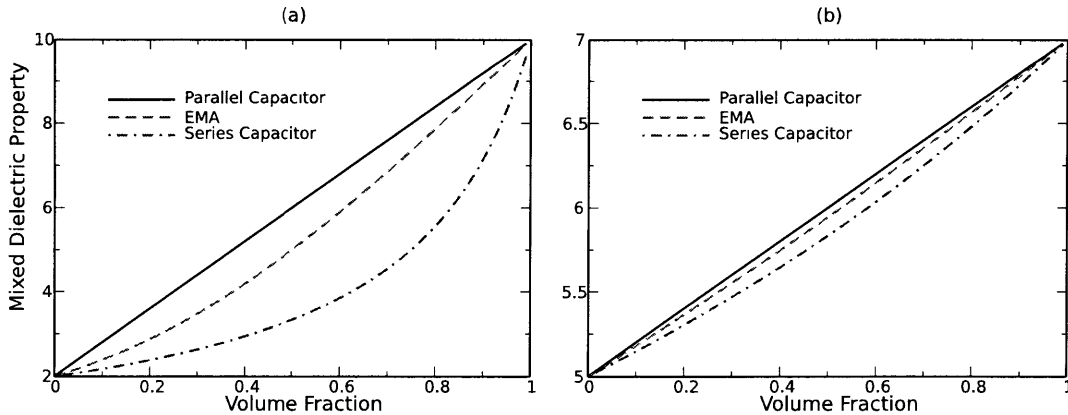
Figure 5-4: Comparing the effects of the parallel capacitor, Bruggeman EMA, and series capacitor spectral mixing approximations for small and larger optical mismatches. a) When the optical mismatch is very strong (which is typical at the 0eV limit of metallic SWCNTs), the effects of different models is significant, particularly at 50-50 mixtures. b) When the optical mismatch is very small, all three models converge regardless of the volume fraction of each material.

Table 5.1: A comparison of the effects of the different mixing formulations on a 50-50 mixture of the [25,0,s] radial direction and vacuum.

Mixing Formulation	vdW-Ld (0 eV)	vdW-Ld (1 eV)	$\mathcal{A}_{121}$
Parallel Capacitor	5.87	3.84	82.10
Perpendicular Capacitor	1.83	1.74	29.84
Bruggeman EMA	4.21	3.02	63.90
Maxwell Garnett	5.00	3.37	53.28
Lorentz-Lorenz	2.86	2.46	70.23
Rayleigh	2.42	2.17	44.92

The variation between these different models is quite large. Both the Hamaker coefficients and the effective vdW-LDS can vary by a factor of 3. Therefore, it is important to choose the model carefully for a given geometrical system, particularly for complex and multi-component systems.

5.4   Mixing Results for CNT Systems

With a specific mixing formulation selected, its effects on the effective vdW-LDS, Hamaker coefficients, and total vdW-Ld energies can now be tested. Of particular

interest in the effects of the core on simple SWCNT. But this this analysis also includes the topic of creating MWCNTs vdW-LDS from the SWCNT constituents as well as the effects of non-linear coupling on adjacent layers. Other effects (e.g. surfactants) are be described in subsequent sections.

5.4.1   SWCNTs

Figure 5-5 shows the [9,3,m] and [29,0,s] SWCNT hollow-cylinder spectra and the resulting mixed w/H_2O spectra in the axial direction using isotropic water uniformly distributed and filling 100% of each SWCNTs respective core. Of course the core can be filled with any percentage of water from 0 to 100%. In this study, the core is assumed to 100% filled and isotropic (i.e. no structural ordering) to have a standard benchmark across all tubes. Realistically, for some of the smallest nanotubes (e.g. the [5,0,s]), any water filling would not be possible as there is not enough void space to fit them within. A slightly larger diameter would allow for some water molecules, but they would not have all rotational degrees of freedom and the assumption of the isotropic spectra would not hold. The tubes presented in this study are large enough that these issues should not arise.

Although there are many alternative water spectra by which to choose from[67, 69, 68, 70], I use the index of refraction oscillator model by Parsegian because it accurately captures the zero frequency, matches index of refraction along the visible frequencies[30], and is easily recreated using simple damped oscillators. The other available models do make certain improvements (such as fulfilling the requirements of the f-sum rule[70], etc) and are equally valid for use. In general, the water spectrum is smaller in magnitude than the all SWCNT spectra for all frequencies. This has the effect of decreasing the overall magnitude of the effective, mixed w/H_2O spectra in comparison to the hollow-cylinder spectra. The effect is clearly strong for the [29,0,s], which is 55% hollow and therefore experiences a considerably shifting (The [9,3,m], by comparison, is only 18% hollow). The implications of this dampening shows up clearly in the Hamaker coefficient calculations between the various chiralities (Table 5.3). However, effects such as alignment and torque forces may increase or decrease
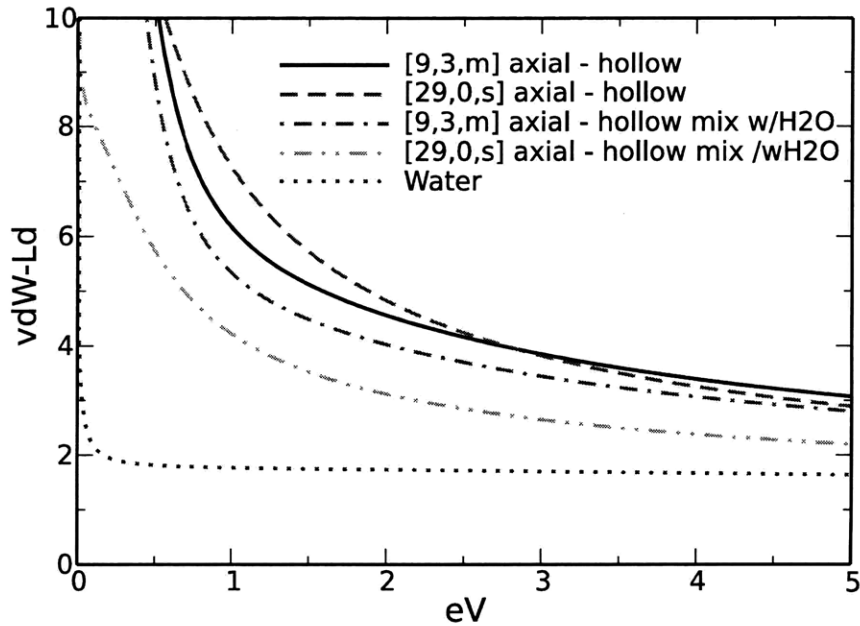
Figure 5-5: The effects of mixing on the [9,3,m] and [29,0,s] SWCNTs in the axial direction. The comparison is between their respective hollow-cylinder and hollow-cylinder spectra mixed w/H_2O vdW-LDS.

depending on the relative positioning on the initial and final vdW-LDS with that of the medium. In the particular examples found in this diminish, they all diminish. But they could actually increase if a high dielectric material was inserted into the core.

Figure 5-6 compares the [6,5,s] and [9,1,s] vdW-LDS in both the axial and radial directions. Although the [9,1,s] has a larger low energy wing, the [6,5,s] has spectra that are larger in magnitude for the remainder of energy range. It is important not to neglect this small but important difference because the spectral mismatch terms contained in the Lifshitz formulation can still contribute out to a very large energy range (e.g. 50+ eV). And even if an individual contribution at a given Matsubara frequency is not large all by itself, a lot of these terms put together can and do have noticeable effects. Table 5.2 lists the resulting energies for these two SWCNTs interacting with a polystyrene substrate across water. The polystyrene spectrum was obtained experimentally[82] and is publicly available[55]. In each limit, the [6,5,s] has the stronger Hamaker coefficient and thus has a stronger attraction. This result
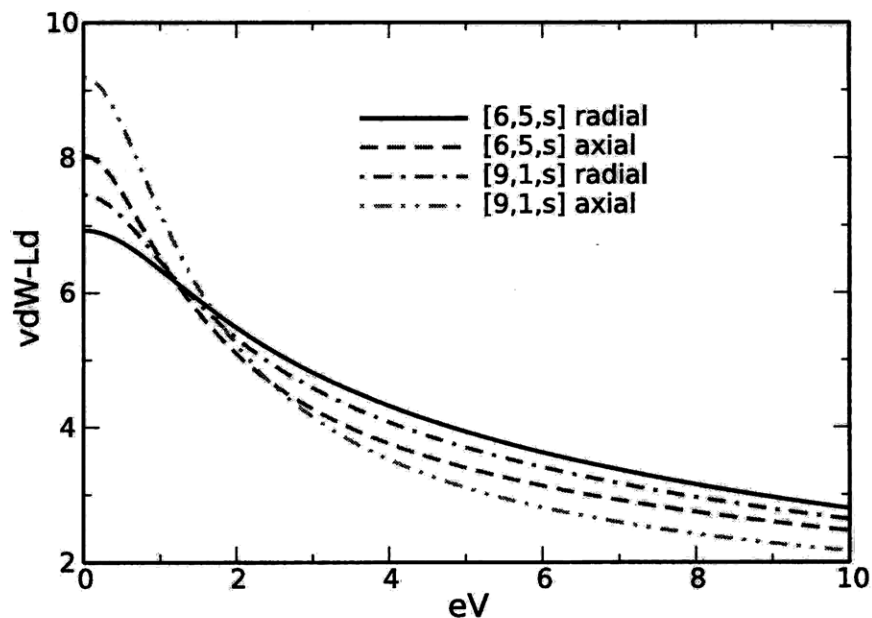
Figure 5-6: A comparison of the [6,5,s] and [9,1,s] vdW-LDS in the axial and radial directions. The chirality-dependent differences present are strong enough to cause a 5% change in the relative Hamaker coefficient strengths.

agrees with the experimental results of Zheng. This agreement is encouraging because it suggests that the vdW-Ld terms agree with the overall effect[19]. It remains to be see how well additional results will compare to the elution experiments as well as the separation experiments by dielectrophoresis[20].

5.4.2   MWCNTs Mixing, Neighbor Coupling, and Other Consideration

In Figure 5-3 and the surrounding text, I illustrated an example using simple damped oscillators to show how the mixed and unmixed cases converge to nearly the same total energy in the far limit. This demonstration using a fictitious system is convincing in and of itself. It would be even more convincing to use actual system that contains both the component and total target vdW-LDS. In particular, two important assumptions should be checked: A) That the neighboring materials exhibit little or no coupling and/or alteration of each other's optical properties and B) that the mixing formulations we chose for the radial and axial direction can in fact take constituent

vdW-LDS and accurately recreate a total vdW-LDS.

Fortunately, a comparison of MWCNT and SWCNT spectra affords just such an opportunity to check both assumptions. Figure 5-7 shows the raw, unscaled ϵ'' data for the [16,0,s + 7,0,s] MWCNT in comparison to the raw, unscaled spectra of the constituent [16,0,s] and [7,0,s] SWCNTs. Clearly the major trends are exactly additive. In the radial direction, the predominant discrepancies arise within the 10-20 eV range and are most likely the result of the out-of plane stacking effects between the two graphene like layers. In the axial direction, there are small but relevant shifts in the first van Hove singularities occurring between 0 and 5 eV. The distance between the radii of the [16,0,s] and [7,0,s] SWCNTs shells for a symmetrically arranged MWCNT is theoretically 3.523 angstroms and is thus only 0.2 angstroms larger than the equilibrium layer spacing in graphite. So I am reasonably confident that there is some coupling of the neighboring layers, but that this effect will not get much stronger than what is presently observed. It remains to be see whether or not the electronic conduction properties in the axial direction can be switched from semi-conducting to metallic or vice versa because of this interaction. I do not expect this to be the case, although some report theoretical examples in which large transverse electric fields can shift the electronic bands and turn metallic CNTs into semiconducting[88, 89, 90, 91].

The next assumption to test is the accuracy of the mixing rules, keeping in mind the effects of the non-linear coupling. Figure 5-8 shows the vdW-LDS for a [16,0,s+7,0,s] MWCNT, a MWCNT created by mixing the [16,0,s] and [7,0,s] SWCNTs, and the two SWCNT spectra. In both the axial and radial directions, the optical properties of the SWCNTs constituents are quite different from that of the MWCNT. But we obtain a very good approximation when we mix them via the combined parallel capacitor and Bruggeman mixing formulation described earlier. Note the excellent agreement in the axial direction with only a slight discrepancy of 8% at the 0 frequency term (which quickly drops to 2% difference for frequencies beyond 1eV). The discrepancy in the radial direction is approximately 5-6% over most of the frequency range.

Determining the physical origin of any resulting discrepancies is important so they
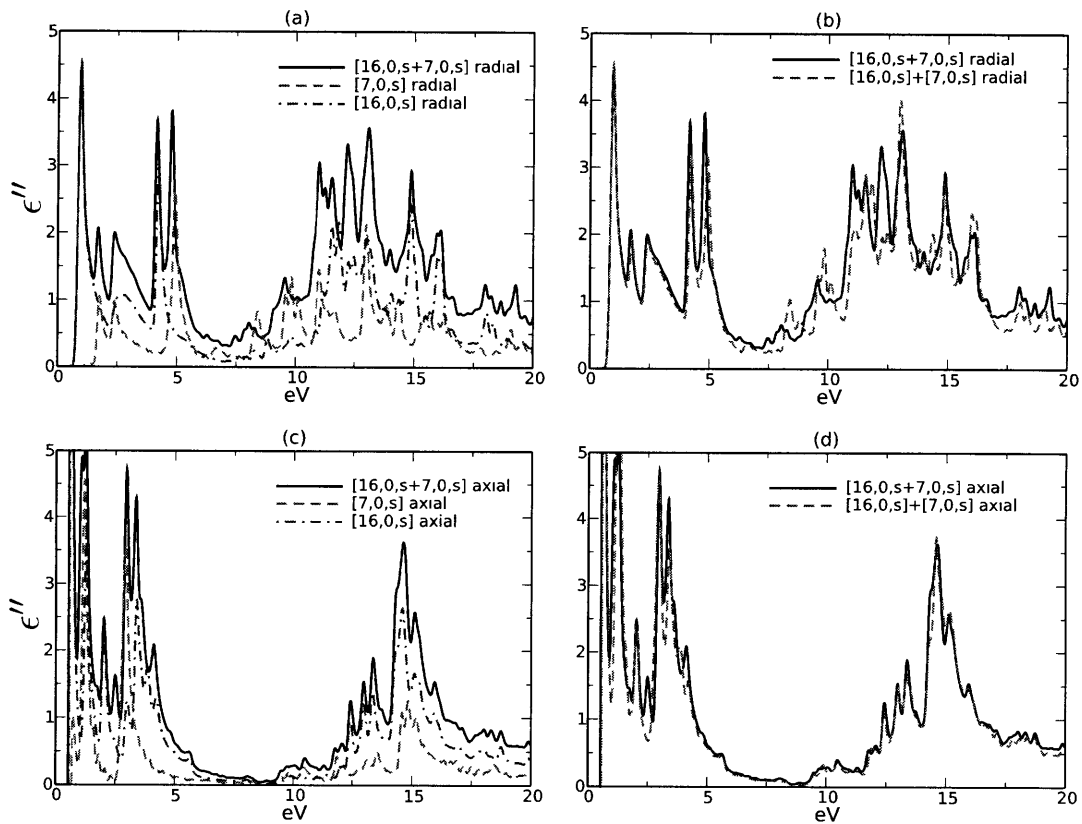
Figure 5-7: A Comparison of the unscaled [16,0,s + 7,0,s] MWCNT ϵ'' data with its constituents (unscaled [16,0,s] and [7,0,s] SWCNTs) in both the radial and axial directions.

are not compensated in such a way that may be improper or more problematic in the future for other systems. There are essentially 3 possibilities to address: 1) The wrong mixing formulation was chosen 2) Improper scaling of the raw spectra into the hollow-cylinder spectra for either the SWCNT or the MWCNT and/or 3) Nonlinear coupling effects existing between the neighboring layers. If the choice in the mixing formulation was the problem, then simply going from a Bruggeman EMA mixing in the radial direction to a parallel capacitor method would give us the needed boost to match the stronger vdW-Ld of the calculated MWCNT. However if a close look at the 0 to 1 eV range in the radial direction spectra in figure 5-8, the magnitudes of both constituent SWCNT spectra are below that of the MWCNT. Resolving this difference by changing the mixing rule is therefore impossible because the output values of all 3 mixing formulations are bound within the magnitude range of their pure constituents.
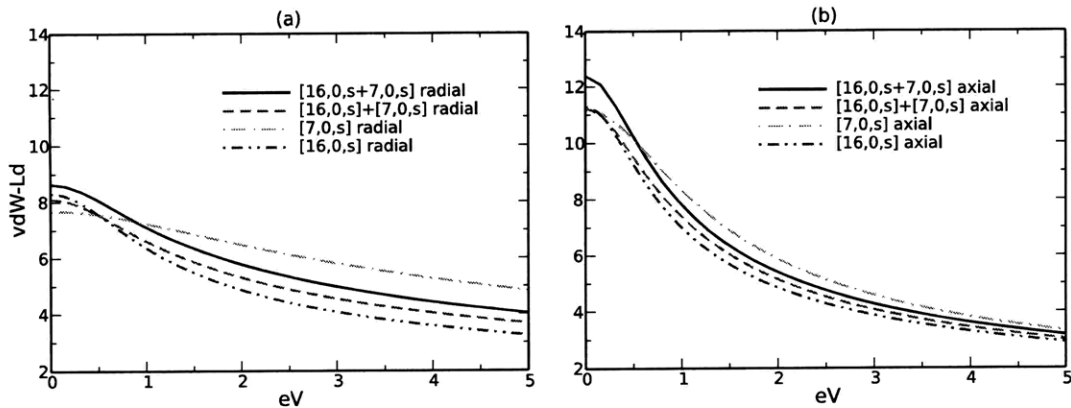
Figure 5-8: A Comparison of the hollow-core MWCNT [16,0,s+7,0,s] vdW-LDS versus effective MWCNT spectra created by mixing the [16,0,s] and [7,0,s] hollow-cylinder SWCNT constituents.

Perhaps the choice of scale factors is incorrect. If the thickness of the SWCNT cylinder boundaries layers was adjusted such that the inner and outer shells of our MWCNT overlapped, this could easily make the case for reducing the MWCNTs overall scale factor by approximately 3%. As it is, we specifically chose the [16,0,s+7,0,s] MWCNT because its equilibrium spacing between the shells is 0.2 angstroms greater than the equilibrium spacing for graphite. So while this certainly give the correct adjustment, it really depends on whether picking or assuming this larger thickness is in reality a physically appropriate change.

The third and most likely reason for this difference is some of the coupling that occurs between the neighboring layers that affects the underlying optical properties of each layer present. Observing Figure 5-7, it appears that the majority of the spectra the MWCNT behaves very much like a simple addition of the two SWCNT spectra. There are, however, small areas where the calculated MWCNT has stronger transitions. These significantly add to the overall vdW-LDS and give it its increased magnitude over spectra created from SWCNT.

In light of these minor discrepancies, a valid question to ask is why one would ever use SWCNT spectra to create MWCNT spectra instead of just obtaining the MWCNT properties directly. Their are a couple key answers. First, it eliminates much of the sheer computational difficulty that it would take to obtain the properties

of certain MWCNTs and other multi-component systems. For example: suppose one wanted to create a MWCNT that has almost an exact graphite interlayer spacing separation between the two SWCNT rings. An ideal choice with this separation distance would be the [10,10,m] and [6,4,s]. However, the ratio of their cell heights for the ab initio calculation is not commensurate and would require 11 repeat units of the [6,4,s] and 83 of the [10,10,m] in order to come close to synchronizing up. This would require 4,992 atoms – not an impossible number but certainly 1-3 orders of magnitude larger than most SWCNTs. And this is the low end, as it is possible to mix two SWCNTs together that might require even more atoms than this or require some form of stretching/distortion along the backbone in order to minimize this effect. Going to 3-ring or 4-ring MWCNTs would exacerbate this problem even further.

There is a second and equally important reason to use SWCNT components even if obtaining a particular MWCNT spectra was feasible. As explained in the analysis of Equations 5.6 for the cases C1/C2/C3 in Figure 5-3, it is the optical properties of the two closest interfaces across the separation medium that dominates the total vdW-Ld interaction energy at distances near contact. The total MWCNT spectrum is in fact an averaged set of optical properties in the radial and axial directions and wouldn't be valid at the near limit. By using the SWCNT pieces, we now can spatially resolve the optical properties in the way necessary to get the proper near-limit interaction. This effect would be the most important and influential when the different layers in a MWCNT contained both metallic and semiconducting species. Driving the point further, two MWCNTs might have very similar total vdW-LDS but differ greatly in their outer shell properties. Therefore, the Hamaker coefficients would be nearly identical in the far limit and potentially very different at contact.

5.4.3 Hamaker Coefficients as a Function of Scaling and Mixing

So far I've discussed the importance of using the properly scaled and mixed spectra at the proper surface-to-surface separation limit. But now it is time to demonstrate

quantitatively the effects of each combination of scaling and mixing (solid, hollow, and hollow mixed w/H$_2$O) at each limit to show that the differences are very noticeable. Table 5.3 lists the calculated values of $\mathcal{A}^{(0)}, \mathcal{A}^{(2)}$ in zJ for the [9,3,m], [6,5,s], [9,1,s], and [29,0,s] using all 3 spectra varieties in the near and far-limits of the optically anisotropic rod-rod systems.

The initial values for the [6,5,s] and [9,3,m] across water are identical to the values calculated and reported using the solid-cylinder optical properties[26]. When the optical properties are scaled to that of the hollow-cylinder spectra, the magnitudes become much larger. It should be noted though that this enlargement at the near limit is not unreasonable. In fact, it brings the Hamaker coefficient magnitudes into closer agreement to those previously published for the anisotropic graphite vdW-LDS in water[62, 25]. This is a direct result of the hollow-cylinder scaling, which properly confines the optical properties into the SWCNT shell where it matters most at contact S2SS.

Conversely, the Hamaker coefficients calculated from the hollow-cylinder spectra would be incorrect to use for a total energy calculation in the far-limit. A pure hollow cylinder spectra ignores the interactions of the SWCNT cores and possible surfactants, which would likely be different and possibly repulsive depending on the selection process. However, an accurate total Hamaker coefficient and total interaction energy can be obtained if the hollow-cylinder spectra is mixed with the materials present in the particular experimental system. In this analysis, the core is 100% fill of isotropic water. The resulting mixed Hamaker coefficients in the far limit are smaller than the hollow-cylinder spectra and slightly larger than that of the original solid-cylinder properties. These relative rankings are completely logical and expected as the hollow-cylinder scaling assumes a core material optically equivalent to the outer shell, the solid-cylinder scaling assumes a zero or vacuum core, and the mixed with water spectra uses a core material that has an optical spectra that is close but still larger than the vacuum vdW-LDS.

With respect to all the coefficients listed in Table 5.3, I cannot stress enough that only certain combinations are actually realistic despite the ease of which we

Table 5.2: The Hamaker coefficients for the optically anisotropic cylinder - water - polystyrene substrate system for the [9,1,s] and [6,5,s] SWCNTs in the near (hollow-cylinder spectra) and far (mixed w/H_2O spectra) limits. Values of $\mathcal{A}^{(2)}$ are all 0 because bulk amorphous polystyrene is isotropic and therefore there is no angular dependancy.

SWCNT	Limit	Spectra Type	$\mathcal{A}^{(0)}(zJ)$
[6,5,s]	Near	Hollow	29.4
[6,5,s]	Far	Mixed w/H_2O	29.0
[9,1,s]	Near	Hollow	27.4
[9,1,s]	Far	Mixed w/H_2O	27.2

Table 5.3: Calculated rod-rod Hamaker coefficients ($\mathcal{A}^{(0)}$, $\mathcal{A}^{(2)}$) for the [6,5,s] and [9,3,m] SWCNTs using the raw optical properties scaled to a solid cylinder, scaled to a hollow cylinder, and a hollow cylinder mixed with a water core. The solid and mixed w/H_2O spectra are equally valid at the far-limit depending on whether the core is filled with vacuum or water.

n	m	Near-limit $\mathcal{A}^{(0)}, \mathcal{A}^{(2)}$ (zJ)			Far-limit $\mathcal{A}^{(0)}, \mathcal{A}^{(2)}$ (zJ)		
		Solid	Hollow	Mixed w/H_2O	Solid	Hollow	Mixed w/H_2O
9	3	62.3, 0.5	91.7, 0.6	66.7, 0.5	107.0, 36.2	163.3, 56.6	113.3, 36.8
6	5	85.0, 0.1	111.8, 0.1	88.0, 0.1	105.6, 1.9	144.2, 3.3	110.5, 2.2
9	1	72.3, 0.4	95.6, 0.4	75.3, 0.3	92.8, 3.0	126.9, 4.9	97.4, 3.3
29	0	14.3, 0.0	71.8, 0.1	20.1, 0.1	18.5, 0.8	108.6, 8.6	26.2, 1.3
Valid	N	Y	N	Y	N	Y	

can calculate these values for any combination of system, distance limit, and spectra scaling/mixing. To avoid any confusion, I specifically note in the final row which are valid combinations to use.

5.5   Discussion and Further Considerations

Although scaling and mixing seem fairly simple, they are clearly important to keep in mind at different distance limits and for different SWCNT sizes. At the near-limit, changing from the solid to hollow-cylinder spectra can result in a substantial boost in the magnitude of the Hamaker coefficient by 20-50%, for even the small diameter SWCNTs. This effect is even stronger as the tube diameter increases and

the difference between the hollow and solid-cylinder spectra widens. For example, the [29,0,s] Hamaker coefficients vary by a factor of 5-10 when changing between the hollow and solid-cylinder scaling behavior. Therefore, it is critical to use hollow-cylinder spectra at near contact separations where the closest materials dominate.

The opposite is true in the far-limit. Here the optical properties must be averaged over the entire cylindrical container because the overall vdW-Ld interaction is a result of the potentially competing interactions of all the constituents. Large diameter SWCNTs (e.g. [29,0,s]) will then have an optical response that is highly damped by either the vacuum or water core. One might expect that the overall vdW-Ld total energy would be weaker because of a smaller Hamaker coefficient. However, the total energy for the SWCNT + water core system can still strengthen because of the a^4 power dependence on the vdW-Ld interaction energy in the far-limit (See Equation A.61).

As the size of the interacting objects increases, the total vdW-Ld energy at a given S2SS should also grow because there is more volume interacting. The Hamaker coefficient is primarily determined by the optical properties and essentially gives the per unit volume component of the total vdW-Ld energy interaction. Mixing of a SWCNT spectrum with water clearly dampens the magnitude of the overall Hamaker coefficients due to reduction in optical contrast. However, the volume of interacting substance can more than make up for this effect. For example: if we take far limit hollow mixed w/H_2O values from table 5.3, the Hamaker coefficient or vdW-Ld interaction energy density of the [6,5,s] is 4 times greater than the [29,0,s]. However when later multiplied by the a^4 scaling behavior, the total interaction energy of two [29,0,s] interacting at a fixed S2SS is 20 times stronger. Therefore these competing effects are important to keep in mind when making final determinations of what should happen in a given experimental procedure.

What then are the effects of surfactants? Although not specifically includeed in the previous result section, there is no additional conceptual difficulty from a computation or from a calculation standpoint to include them. For example: a MWCNT with a water core and a uniform layer of sodium dodecyl sulfate (SDS, a typical SWCNT

surfactant[81]) would simply behave as a cross sectional area weighted mixing of the constituent spectra in the far-limit and of pure SDS at the near-limit. One could then use the interpolation style suggested previously to obtain a vdW-Ld energy at all distances[26].

The biggest limiting step preventing us from including surfactant effects is, as described earlier, the lack of optical spectra for all potential surfactant candidates over an energy range sufficient for the Lifshitz formulations. There is some work being done in parallel to this thesis to begin filling up the spectra database, but more time and resources are needed for this endeavor. And until robust spectral data are available, I am unable to carry this analysis any further other than describing qualitative trends that can occur. At the near-limit, the ability to spatially resolve the SDS layer from the SWCNT or MWCNT is important for the same reason as described above when spatially resolving the SWCNT constituents from the bulk MWCNT optical property.

Experimental methods that determine bulk spectral properties of ssDNA/SWCNT hybrids and similar nano-structures would be pertinent for the far-limit only. The near-limit requires a spatial resolution and possibly directionally dependent properties, both of which are either impossible or extremely difficult to obtain experimentally for these types of systems. Specific examples are the situations in which the structure in water is different than the dry material structure (e.g. DNA). If one measured a dry structure, but later calculated an energy for a wet system, there might be some significant shifts or alternations based on the different electronic strucure. This further underscores the utility of ab initio methods as a viable and powerful alternative to obtain this information. Additionally, it underscores the need to catalogue even the most basic of materials. Currently the only organic materials we have publicly available (outside of the carbon based SWCNTs) are polystyrene, tetradecane, ethanol, and possibly a few others[82, 54, 83]. With a larger data base of SWCNTs and surfactant spectra, one can start data mining to find combinations favorable for one type of interaction over another.

Although the focus of this thesis is primarily on SWCNTs and MWCNTs, the

solid-cylinder formulations can be used for any liquid crystal, protein, collagen, or any material in which the overall shape can be described as cylindrical. As long as one has the optical properties, one can obtain the per unit length or total energy of interaction for any of these systems. One can also use the mixing rule analysis of the results section for other geometries. For example, the vdW-Ld interactions of surfactant coated spheres could also be optically mixed with the Bruggeman EMA for the far-limit. The overall themes described here have utility well SWCNTs.

5.6 Moving Forward

With a proper mixing formulation chosen and its effects demonstrated, it is now possible to accurately calculate vdW-Ld interactions for SWCNT systems realistic enough for end-users. This was no means a trivial accomplishment because it required the development of 3 key components that either did not exist (ab initio vdW-LDS and new Lifshitz formulations) or required lots of analysis and care in bridging to SWCNT systems (spectral mixing formulations). This again is summarized in the updated roadmap shown in Figure 5-9.

Having laid the foundational groundwork, it is now finally possible to begin to datamine and understand the chirality-dependent vdW-Ld interactions for SWCNTs. To do this rigorously, the intrinsic SWCNT material property dependencies at the various levels of abstraction (i.e. how n,m effects x,y,z effects brillouin zone effects band diagram, etc) need to be closely studied for 2 main reasons: 1) guidance in what trends to look for and 2) being able to link the results as a function of class and radius back to the fundamental chirality vector [n,m]. After this, more attention can be spent figuring out to how these variations manifest through the vdW-LDS properties and ultimately cause variations in the Hamaker coefficients and total vdW-Ld energies. With this initial study complete, many of the questions that started this entire investigation can now be answered as well as lead to new questions, further optimizations, impacts into other areas of study, and so forth.

Status of a SWCNT vdW-Ld Calculation
After We Introduced Spectra Mixing

Methods for Obtaining Necessary Full Spectrum Properties

VUV Reflection and Transmission — EELS — Ab Initio Electronic Structure

NOT FEASIBLE! ✕

Intrinsic SWCNT Material Property Dependancies

chirality n,m → Wrapping → x,y,z and cutting lines → OLCAO Method → band structure → e" spectra 2 SWCNTs

KK Transformation + Void Volume Scaling (if necessary)

Mathematics and Electrodynamic Formulations

scaled vdW-Ld spectra of 2 SWCNTs → Optical mixing → Mixed vdW-Ld spectra of 2 SWCNTs → Plug and Chug → Accurate Hamaker Coefficient

Material Connectivity

Target System Geometry → Electrodynamic Boundary Conditions → Anisotropic Rod-Rod Lifshitz Formulation

Vol-Vol Energy Scale Factor

Analytical Vol-Vol Term (Equivalent to Numerical 1/r^6 Integration)

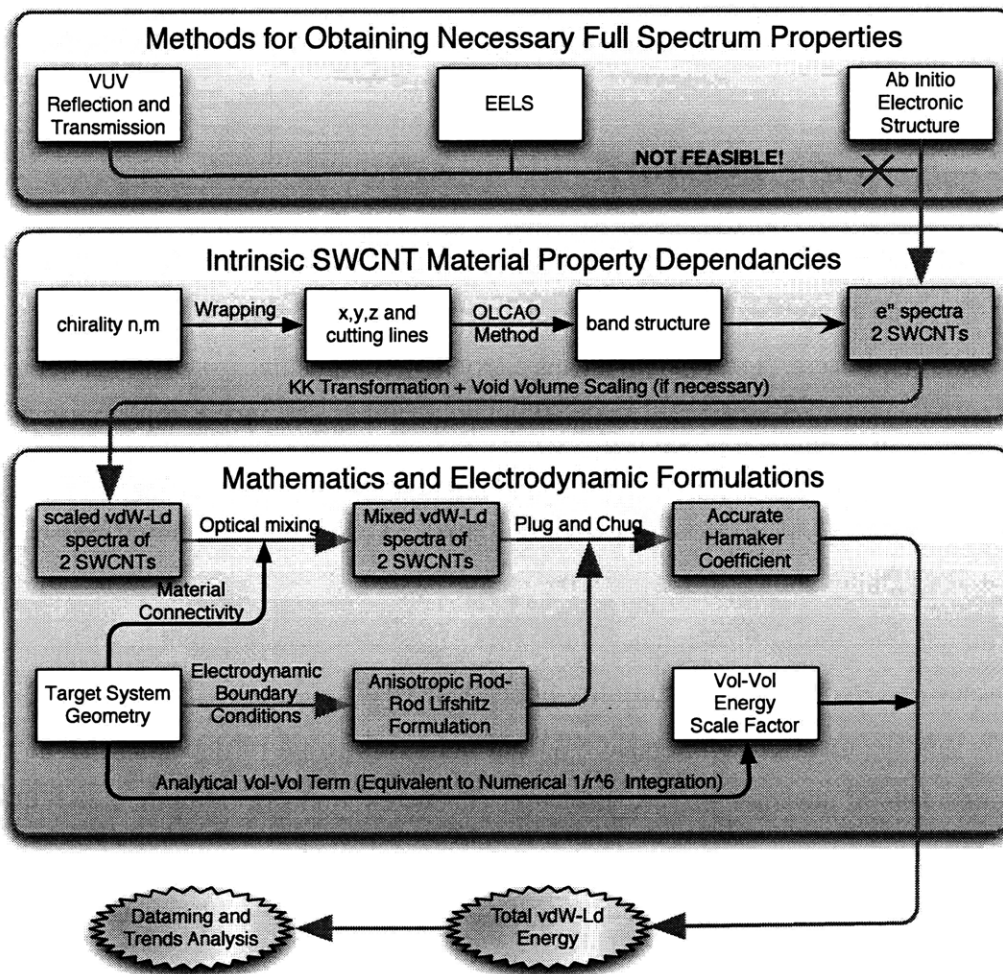Datamining and Trends Analysis ← Total vdW-Ld Energy ←

Figure 5-9: With spectral mixing formulations now in place, all the necessary components for end-user quality vdW-Ld calculations of SWCNTs systems are now possible.

Chapter 6

Datamining: How Chirality Impacts vdW-Ld Interactions at All Levels of Abstraction

6.1 Motivation: Occurrence, Effects, and Source of ϵ''/vdW-LDS Variation

Ultimately this study was started to discover and quantify the chirality-dependent vdW-Ld interactions for SWCNTs. The term "chirality-dependent" in the previous sentence implies carries with it an inherent assumption that there is in fact variation among the different tubes. But this assumption also needs to be tested. For any non-stochastic function (e.g. the Lifshitz formulation), a variation in the output can only be achieved if there is variation in the inputs parameters. So if all the SWCNTs had the exact same ϵ'' and vdW-LDS, then all the Hamaker coefficients would be identical and there would be no need to carry the analysis any further. But even if a variation in the input parameters exists, it doesn't necessarily follow that they are experimentally significant. And without this significant variation, a study of the vdW-Ld interactions for more than a couple of SWCNTs would be redundant and fairly boring. Therefore, this work proceeded very systematically along the following

strategy:

- Occurrence: Prove the existence in ϵ''/vdW-LDS variation.

- Effect: Prove that ϵ''/vdW-LDS variation led to meaningful Hamaker coefficient and vdW-Ld TE variations.

- Source: Study and datamine the layers of abstraction to understand the root cause for further understanding/exploitation.

The proceeding chapters specifically addressed the first two points very closely. Chapter 1 introduced and discussed the many results of the Zheng experiments. Initially separation was possible between the major classes (metals vs semiconductors) but further refinements ultimately led to the ability to separate SWCNTs of identical band gaps and radius. All of the experimental results and theoretical explanations for this phenomenon seem to be heavily linked to the underlying chirality. Therefore, vdW-Ld interactions are one of the prime candidates of interests because the Lifshitz formulations use optical properties as their input, which have known dependencies as a function of SWCNT chirality.

Next, chapter 3 proved that chirality-dependent vdW-Ld interactions exist. This was a direct result of the distinct variations in the ϵ'' and vdW-LDS between the to major classes (e.g. the semiconducting [6,5,s] vs the metallic [9,3,m]) as well as within the semiconductor class (e.g. the [6,5,s] vs [9,1,s] of nearly identical band gap and identical radius). Despite noticeable differences present, the Lifshitz formulations necessary to properly calculate the Hamaker coefficients for this geometry did not exist. Therefore a semi-crude approximation had to be used. Nevertheless, this crude approximation showed that different radial and axial direction interactions combinations could vary by more than 20%.

Chapters 4 and 5 then laid the ground work for an accurate Hamaker coefficients and total vdW-Ld of real, experimentally relevant SWCNT systems. What was again found is that indeed there are very real and quantifiable chirality-dependent differences. The variations in Hamaker coefficient magnitude could be as small as 6-7%

when comparing tubes of similar size and class. They could also vary as much as 80+% when comparing tubes of largely different diameter due to the effects of scaling and spectral mixing. The anisotropic rod-rod and rod-substrate can also have a large orientation-dependent effect on the Hamaker coefficient. Two interacting [9,3,m] rods at the far-limit will see the total Hamaker coefficient rise by more than 34% when they change from a 90 degree offset to having their axial directions perfectly aligned. And these variations were found only using a small quantity of SWCNTs. In total, 63 SWCNTs were calculated for this thesis, opening the door for the thorough study and analysis contained in this chapter.

But one important step remains before diving into that analysis. Having demonstrated the occurrence and also the significant effects of chirality-dependent ϵ'' and vdW-LDS, the final step is qualitatively and quantify show how the small variations in these root properties trace through the many levels of abstraction shown in Figure 5-9. I cannot stress enough how this is more than just an academic exercise. First, it is very useful in discovering the trending behavior with radius and classification, many of which are non-intuitive and/or would not have been found in any other way. The trending results will be useful for experimental design as well as the prediction of the vdW-Ld properties for SWCNTs beyond the 63 used in this analysis.

Next, the optical properties at 10+ eV or more is largely an unstudied area for SWCNTs because most of the community tends to be on focused on ES properties[10, 11, 12, 13, 36, 37], Raman spectroscopy[84], phonons[85], etc. This doesn't mean that the large energy regimes are unimportant. It is possible that the key features exists in this regime that ultimately that propagate through and influence later stages of the vdW-Ld analysis. This provides a new area for discovery, characterization, and classification. And most importantly, these ignored, high-energy features and figures of merit can ultimately require a new classification system specifically designed for vdW-Ld interactions in order to properly organize and categorize them for easy usage by end-users.

Therefore this chapter will contain two major datamining components. The first part will be a rigorous analysis showing how the chirality-dependent SWCNT prop-

erties manifest and propagate through the many layers of abstraction. In particular, there is a strong focus on the resulting ϵ'' and vdW-LDS that are ultimately the primary input data in the Lifshitz formulation. The second part then uses the 63 different vdW-LDS to calculate Hamaker coefficients and vdW-Ld TE. Combined with the content of the previous chapters, this will officially complete the goals delineated early in Chapter 1.

6.2 Trend Source and Effects

6.2.1 A Quick, Illustrative Case Study

The many flow diagrams (e.g. Figure 5-9, etc.) already show a conceptual overview of the intrinsic property dependancies from [n,m] to vdW-Ld TEs. However, it is far more instructional and motivational to create a similar overview using actual SWCNT data. Once the big picture is understood, it is easier to zoom in and address the more subtle and technical details while still being mindful why this details are important on the grand scale.

Figures 6-1 and 6-2 tracks this entire process for the [6,5,s] and [9,3,m] SWCNTs. Every qualitative and quantitative difference that exists as a function of direction and chirality propagates through each stage. And all of these differences ultimately link back to the fundamental chirality vector, [n,m]. Although some differences do not appear impressive or large, even the smallest of alterations can manifest into very large differences farther down the pipeline. One notable example is the huge difference in the Hamaker coefficient magnitudes among the different metallic classifications that depends on whether or not they have or lack the low energy wings (as shown later in Figure 6-27). Creating these global maps can be somewhat time consuming, but they are particularly helpful when studying smaller, chiral SWCNTs that break free from the cleaner trends that exist for larger SWCNTs. With the global map in hand, it becomes relatively straightforward to track these effects to the stage that created it.
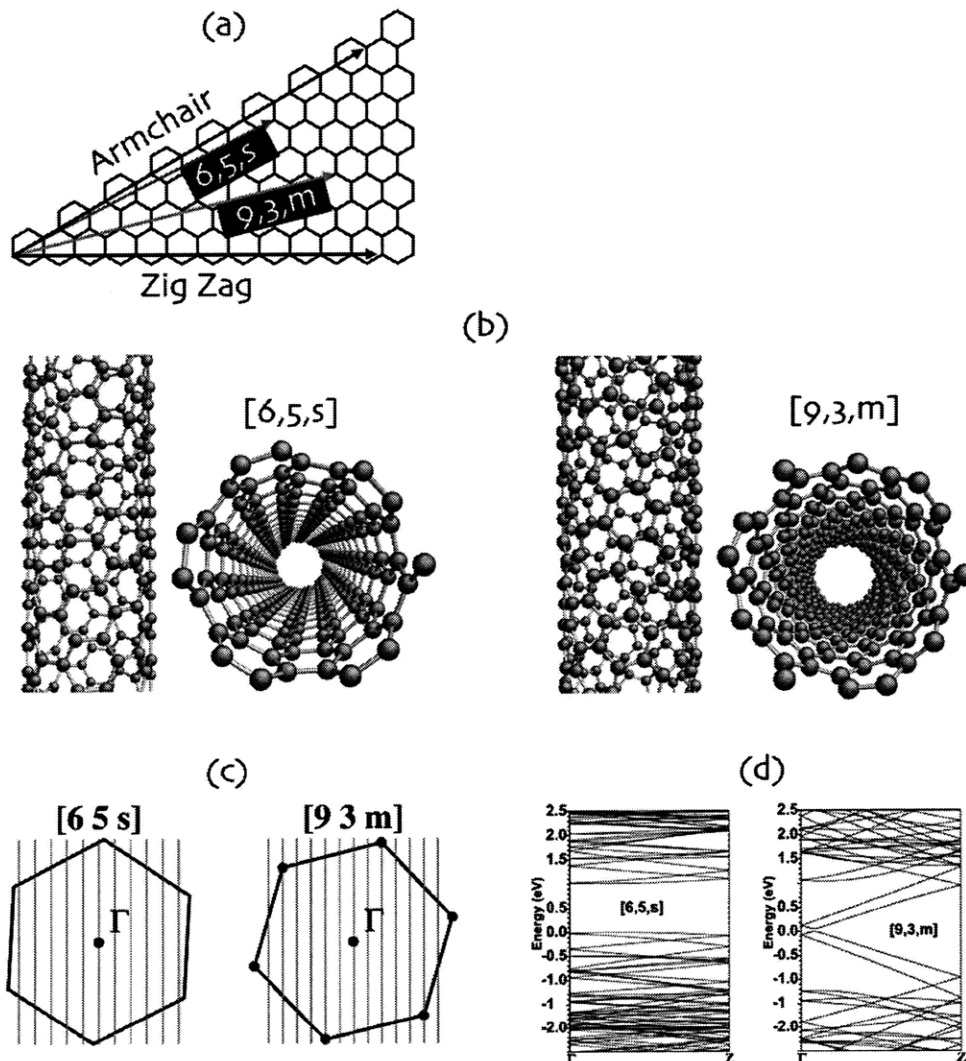
Figure 6-1: Part 1 of the chirality-dependent vdW-Ld interaction analysis for the [6,5,s] and [9,3,m]. A) The [n,m] vector placed upon the graphene sheet denotes the circumference of the SWCNT. B) The SWCNTs x,y,z positions in space. Note the structural difference in the twisting. C) The cutting lines within the Brillouin zone, varying in quantity and angle based on the specific [n,m] magnitudes and magnitude ratio between them. D) The band diagrams determined by the allowable states along the cutting lines. Stages E through G are continued in Figure 6-2
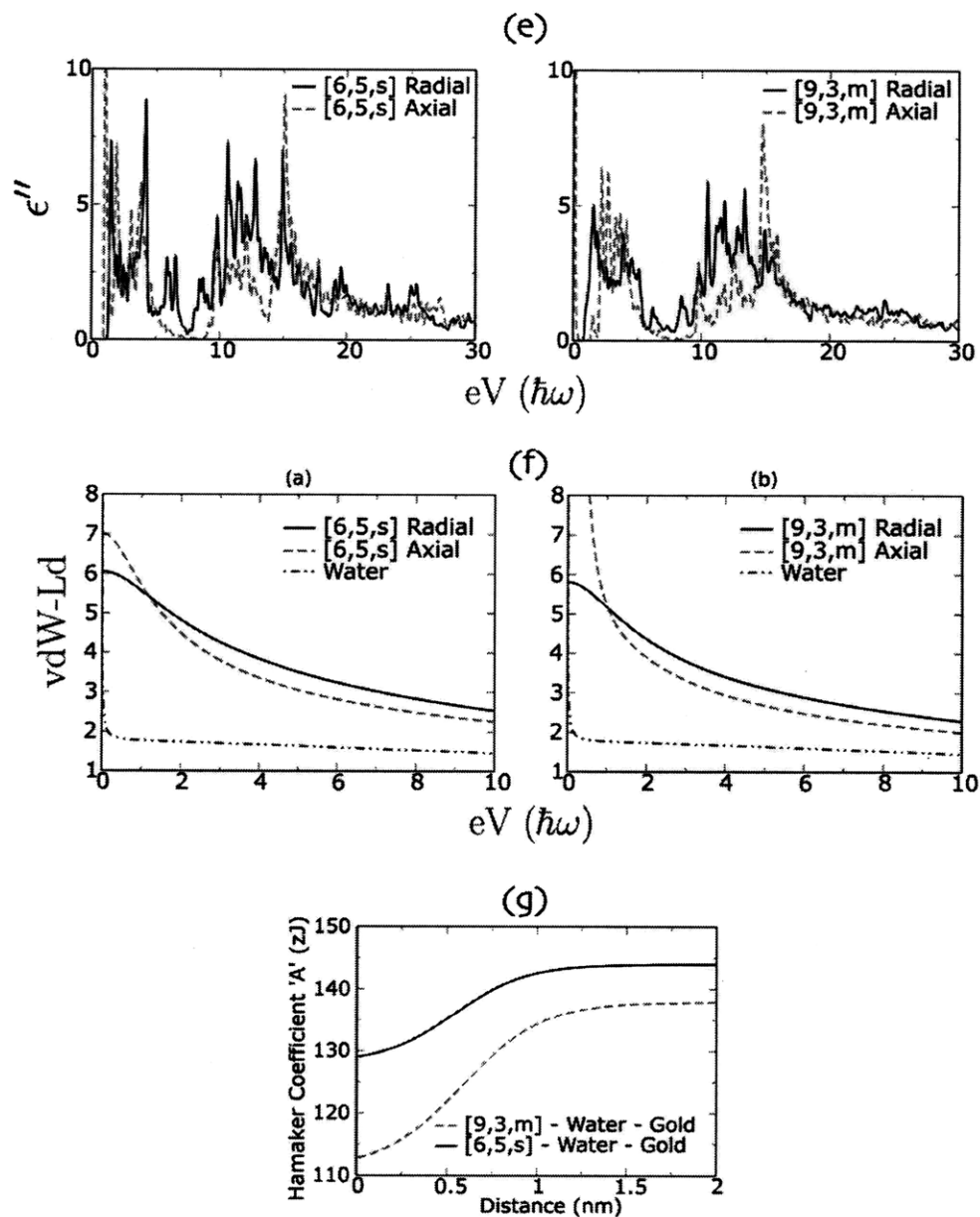
Figure 6-2: Part 2 of the chirality-dependent vdW-Ld interaction analysis for the [6,5,s] and [9,3,m]. E) The allowable single electron transitions determine the optical absorption part of the dielectric spectrum, $\epsilon''(\omega)$, over all real frequencies. F) The vdW-LDS obtained via the KK transform upon $\epsilon''(\omega)$. Note the differences between a SWCNTs radial and axial directions as well as the differences between the tubes. G) Hamaker coefficients in a solid cylinder SWCNT - water - gold substrate system as a function of ℓ. Additional and/or later stages include an analysis of DOS/JDOS as well as total vdW-Ld energies.

Now it is time to begin looking at these stages more closely.

6.2.2   n,m to x,y,z

The construction of a SWCNT's x,y,z coordinates from [n,m] is the simplest and most straightforward stage in the entire process[35]. Figure 6-3 shows how the circumference and wrapping angle of the sp2 bonds in the graphene sheet vary as a function of the chirality vector [n,m]. In the most common convention, m is restricted to the values $0 \leq m \leq n$ and of course only integer values are allowed in order to have discrete lattice translations. This results in 3 main structural configurations: zig-zag, armchair, or chiral. The zig-zag tubes are of type [n,m=0] and named this way because their sp2 bonds zig-zag equally back and forth in this direction along the circumferential direction. The other limit, the armchair class when [n=m], is the only class of SWCNTs that has sp2 bonds perfectly perpendicular to the axial direction. For all chiralities in between, there is a visual twist that occurs down the axial direction (recall part B of Figure 6-2). These SWCNTs are structurally described as "chiral" and represent all nanotubes that have wrapping angles between the zig-zag and armchair endpoints.

A paper by Dresselhaus et al does an excellent job of summarizing all the necessary equations to construct and calculate the cartesian coordinates positions, cutting lines, chiral angle, and other structural figures of merit[35]. For completeness, it should be noted that that these equations give the "unrelaxed" coordinates. What this means is that this construction assumes that one can literally roll the graphene sheet like a piece of paper and the nucleus positions of all carbon atoms will reside exactly where the roll dictates.

This ability to simply calculate x,y,z positions by equation, of course, does not hold true as we go to smaller and smaller SWCNTs. Later TBA structural relaxation calculations run by the Dresselhaus group and others show that SWCNTs typically "bulge" radially and shorten axial to compensate for the large bond angle distortion in the circumferential direction[37]. These distortions are important to keep in mind during the discussion of cutting lines and band diagrams in the following sections.
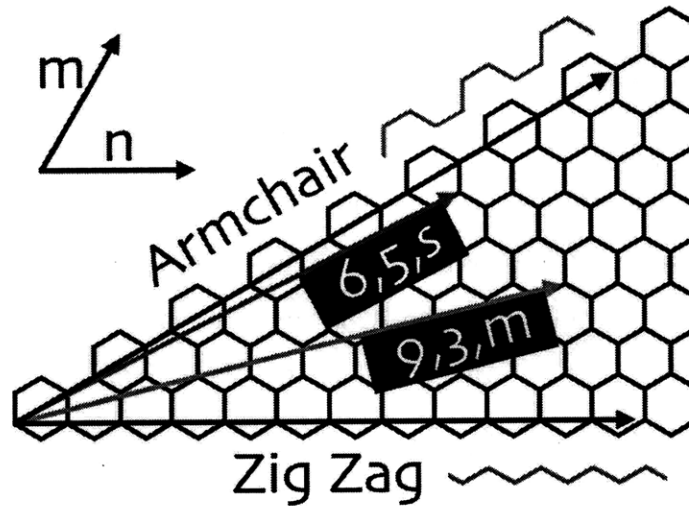
Figure 6-3: The construction of a SWCNT from graphene using the [n,m] vector as the circumference.

However, because of disagreements and difficulty in geometrical/structural relaxation using DFT models, I will ignore relaxation effects in order to keep this analysis manageable. If later enhancements are needed and a agreed upon relaxation methodology is created, it will be a simple and straightforward process to use the software architecture developed for this thesis to recalculate the data required for this analysis.

6.2.3   Brillouin Zone and Cutting Lines

There are numerous conceptual overviews on the origin of the cuttings lines are very useful guides in understanding the band diagram features for SWCNTs. My personal favorite is the one by Lambin because it is visual and succinct[13]. Essentially the electronic structure properties of graphene can be used as a baseline before adding the additional complexities (e.g. curvature, discrete cutting lines) present in SWCNTs. For ES considerations, the most important features of graphene's band structure is the location of the "K-points" at the corners of the hexagonal Brillouin zone. It is at these K-points that the valence and conduction bands meet exactly at the Fermi energy. The density of states shrinks to zero at the Fermi energy and therefore graphene is considered a zero-gap semiconductor or semi-metal.

These critical K-point features are also responsible for determining the ES properties of SWCNTs. The main difference between SWCNTs and graphene is the cyclical boundary conditions in the circumferential direction. This causes a discretization of the Bloch wave functions from the continuum of allowable states in graphene into evenly spaced lines of allowable states parallel to the SWCNT axial direction. These lines are typically called "cutting lines"[36, 37].

The quantity and angle of the cutting lines that exists Brillouin zone is a function of [n,m]. The quantity of lines rises with an increasing [n,m] while the angle depends on the relative magnitude. In the limit where the [n,m] and the SWCNT diameter goes to infinity, the number of cutting lines is also infinite. This would cause the cutting lines in the Brillouin zone to pack so closely that it would essentially return or converge to the continuum properties of graphene.

However there isn't as much interest in infinite radius SWCNTs from an ES standpoint because they are not readily produced and are all zero-gap semiconductors. Most of the interest in ES properties for devices is with the smallest tubes because of their small feature size and because the small semi-conductors have the largest band gaps. In the limit of a small SWCNT chirality vector [n,m], the Brillouin zone contains cutting lines that are spaced very far apart. The exact spacing and angle of these lines provides each smaller diameter SWCNT with its unique properties. This is the primary reason why small changes in [n,m] lead to unique optical excitations, ES properties, etc.

Figure 6-4 compares the cutting lines of for SWCNTs that represent the many different structural and ES classifications. The cutting lines are always directly in the axial direction (chosen as the vertical direction of the page) and the Brillouin rotates relative to it. The angle that forms between the cutting lines and the hexagon shape of the Brillouin zone is identical to the wrapping angle that varies between the zig-zag and armchair structural endpoints. The Γ-point is the center of the Brillouin zone and the K-points (the location where the conduction and valence bands in graphene meet) are at the corners. A blue dot is placed on the graph wherever a K-point is crossed or "grazed" (more on this detail later). The [6,6,m] represents the armchair

class and features a direct crossing of the K-point. This happens for all armchair tubes because the K-points are always directly above and below the Γ-point along the vertical cutting lines.

The [6,0,m] represents the metallic zigzag class. Although the cutting line through the Γ-point does not intersect a K-point, the symmetry of the system works out such that the cutting line spacing allows for later cutting lines to cross/graze them all. But this exact spacing can be interrupted. When we add an additional cutting line by moving from [6,0,m] to [7,0,s], this new cutting line changes the spacing among all the lines such that all the K-points are now missed. Therefore, the [7,0,s] is a ES semiconductor.

The [6,5,s] is another variation on that theme with a twist (of chirality that is). Not only does the quantity of cutting lines decrease by 1 relative to the [6,6,m], but the shift in the relative magnitudes of n and m introduces a change in angle of the Brillouin zone hexagon relative to the cutting lines. This is not to suggest that this angle alone determines the ES properties or prevents the K-points from being crossed. The inherent symmetry relationships between the cutting lines and Brillouin zone cause to the cutting lines to cross/graze the K-points and whenever $Mod(n - m, 3) = 0$. The [9,3,m] is just such an example.

The last SWCNT in Figure 6-4, the [24,24,m], represents what occurs for large diameter SWCNT. The electronic structure becomes more and more graphene-like because the cutting lines get closer together and approach a continuum. It is in this limit of many cutting lines that increasing from the [24,24,m] to a [30,30,m] or [40,40,m] will cause smaller changes in the electronic structure than a seemingly smaller move between the [5,5,m] and the [6,6,m]. But the move from [5,5,m] to [6,6,m] or vice versa results in a much bigger change in all the cutting line positions and what states are accessible from the Brillouin zone.

Because ES properties were (and currently still are) the predominant feature of interest in the SWCNT community, the crossing of K-points was the most significant factor in the original classification schemes. The original categorization was simply between those that behaved as an ES metal versus a semiconductor and therefore
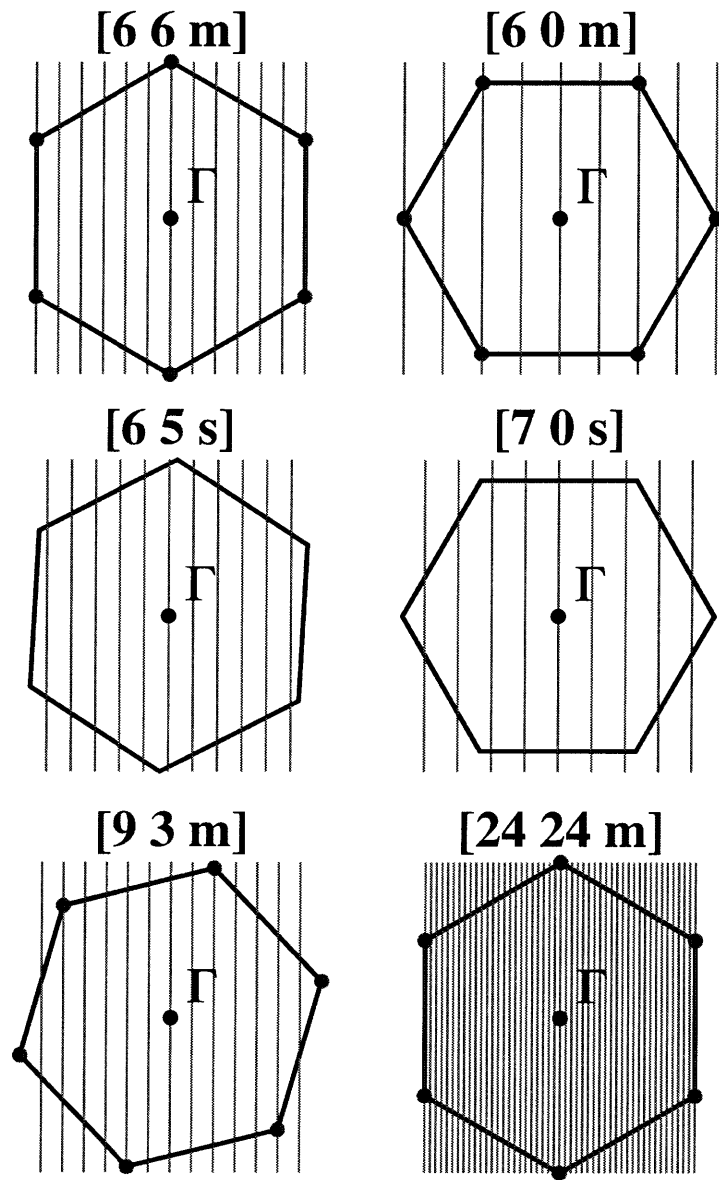
Figure 6-4: Cutting lines for 6 different SWCNTs representing various combinations of structural configurations and ES classifications.

the most important feature was whether the K-points were crossed/grazed via the $Mod(n - m, 3) = 0$ relationship[37].

As interest in SWCNTs grew, researchers discovered other nuances in the metallic classification that arose from departures from the graphene electronic structure baseline. This deviation was primarily caused by the introduction of curvature and structural relaxation effects. The result of these two effects is slight change in the angle and translation of cutting lines for metallic tubes as well as a distortion of the perfect hexagon shape of the Brillouin zone itself. What this does is cause the cutting lines of non-armchair metals to slightly miss or "graze" the K-points rather than hit them directly. Because the K-points are the only location where the conduction and valence bands meet (at least for graphene), this slight miss opens up a very small band gap, which is typically much less than 0.1 eV. Lambin et al differentiated these nearly ES metallic SWCNTS from the "true" ES metal armchairs by calling them "small-gap semiconductors". Therefore this classification system, which I'll call the "Lambin" classification, consists of 3 types: semiconducting, metallic, and small-gap semiconducting[13].

There are other proposed classification systems as well. The one by Dresselhaus et al is intriguing because it is based entirely on symmetry considerations for unrelaxed SWCNT structures and has 5 different types, (3 metallic and 2 semiconducting) which could potentially be used for increased granularity and differentiation[37]. But there are two related downsides in using this classification scheme for vdW-Ld interactions. The first is that it is incompatible with the Lambin system, which does an excellent job of differentiating the true ES metals versus those with a very tiny band-gap. This means that a single "metallic" class in the Dresselhaus system contains both true metals and small-gap semiconductors. Although this seems like a small and trite details, the importance of this distinction for vdW-Ld properties will be very important and very apparent later in this chapter.

The second issue is that the symmetry considerations of the cutting lines in this system are less fundamentally linked to the underlying sp2 structure (i.e. zig-zag, chiral, and armchair.) So an S1 or an S2 semiconductor can be chiral or zig-zag.

The metal 2P can be an armchair or chiral. Intuiting what constitutes these different classes is also a bit harder because the formulas used to differentiate them have many stages and considerations. In contrast, SWCNTs can easily be divided into the the zig-zag, chiral, and armchair scheme at a glance.

So despite symmetry being an intriguing classification scheme to match trends with, the Lambin classification system is far more useful in describing some (but not all) of features that become important for vdW-Ld considerations. Ultimately a new classification system will have to be developed because the OP and other parameters that influence vdW-Ld interactions are different than those which describe ES interactions. This will be done by the end of this chapter once all the SWCNT interdependencies are understood and can finally be grouped along their common features.

6.2.4 Cutting Lines to Bands

The cutting lines act as useful guides in determining the ES and OP, but there are times when they fail. For example, ab initio calculations find the [5,0,s] to be metallic experimentally despite no classification scheme predicting it as such[63]. There are also situations in which a cutting line can cross a K-point, but the resulting electronic structure can have some non-intuitive features. Such an example is when the band structure will have all the features of a ES metal, but the OP transitions can be prevented by symmetry (most notably for ϵ'') and result in a material that behaves optically like a semiconductor near the band gap region. Thus it is critical that the analysis does not end with the cutting lines. Instead, one should always ensure the real electronic structures and subsequent vdW-Ld properties are calculated to verify the predictions via the classification. The disagreement between ES and OP also demonstrates that we need to very careful in analyzing the remaining levels of abstraction and be very clear as to what parameters define what is a "metal" and under what context (i.e. ES band diagram versus the optical property ϵ'').

Figure 6-5 shows a comparison of the cutting lines and resulting axial direction band diagrams for 3 different SWCNTs, which represent all the SWCNT types in the

Lambin SWCNT classification system (metal, small-gap semiconductor, and semi-conductor). The resulting ab initio calculations show the [7,0,s] behaving as expected with a band gap typical of the semiconducting tubes. The [9,3,m] is not an arm-chair and therefore exhibits a very small band gap of 0.03 eV in accordance with what is expected by a "grazed" K-point. It is therefore classified as a ES small-gap semiconductor.

The [6,6,m] is a true ES "metal" by the definition of their being no band gap (i.e. the conduction and valence bands touch at the fermi energy). Therefore the Lambin classification system is (thus far) a reasonably good guide for determining the key band diagram features around the Fermi energy. And in particular, the concepts of crossing, not-cross, or grazing the of k-points is a useful visualization to keep in mind. However, there are later examples in this chapter that show how simply having no band gap and a continuous DOS through the fermi level does not necessarily result in ϵ'' excitations at near 0.0 eV. Thus it is possible (and it actually occurs) that a material can be an ES metal and OP semiconductor. This ultimately leads to a philosophical discussion of "what constitutes a metal" and in what context in order to mentally resolve these conflicting endpoints. However it is exciting to have a class of materials in which such a paradox does arise and which may lead to new device uses or phenomenon.

6.2.5 Cutting Lines and Bands to ϵ''/DOS

The $\epsilon''(\omega)$ property is calculated using the OLCAO formulation described in 3. Conceptually, $\epsilon''(\omega)$ can only exist at a given energy if valence to conduction transitions of that exact energy difference exist and (equally important) are allowed. Therefore, one shouldn't expect to see any $\epsilon''(\omega)$ peaks for semiconductors at energies below the band gap. More importantly (and sometimes surprisingly), one shouldn't expect to see all ϵ'' peaks for all possible valence to conduction band transitions just because they are available. Some of them are prevented/eliminated due to canceling dipole matrix elements in the OLCAO calculation upon the electronic structure. Remembering this can clear up a tremendous amount of confusion that can arise when
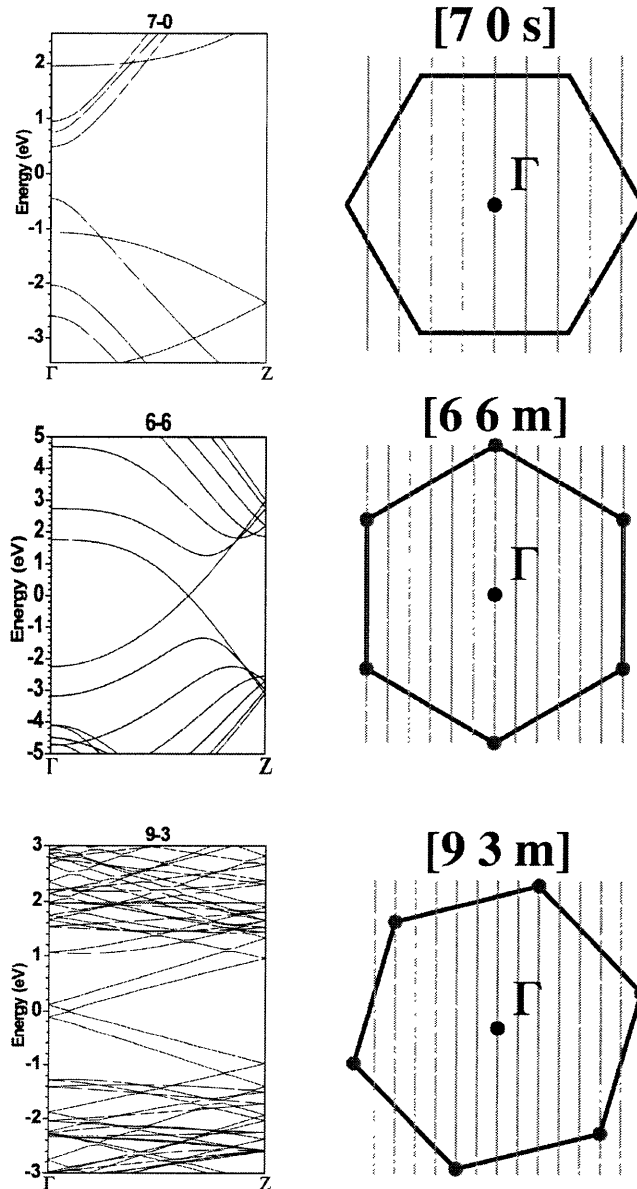
Figure 6-5: A comparison of the cutting lines for all 3 Lambin SWCNT types: the [6,6,m] armchair, the [7,0,s] zig-zag, and the [9,3,m] chiral respectively representing the metals, semiconductors, and small-gap semiconductors.

comparing the somewhat conflicting or paradoxical data from cutting lines, bands, DOS, ϵ'' of SWCNTs. In particular, it is important when comparing the optical properties in this thesis versus spectra obtained from TBA calculations, which artificially alter and/or parameterize the band structure to match experimental ES properties. This distortion may be beneficial for matching ES properties, but may distort the $\epsilon''(\omega)$ properties by mistakenly allowing or preventing particular transitions.

But before getting too caught up in the exceptions, it is useful guiding principal to study the major trends and characteristics that we should and do see using Figure 6-7. We should expect a clear distinction between the metals and the semiconductors for 2 major reasons. 1) The metals will cross/graze the k-points while the semiconductors will not. 2) The first major ϵ'' peaks arising from the cutting lines closet to (but not actually cross/grazing) the k-point will differ by a factor of 3 between ES metals and semiconductors of an equivalent radius.

The first point was explained earlier, but the second point may need some additional explanation. For practical purposes, the shortest distance between a cutting line and its nearest K-point determines the size of the gap between the valence and conduction bands for that particular cutting line[36, 37]. Therefore the closer the cutting line gets to the K-point, the smaller the gap and vice versa. All metallic/small-gap semiconductor SWCNTS have cutting line that crosses a K-point. Therefore the distance to the next cutting line is a full cutting line spacing away (see Figure 6-7 part B). A semiconductor, on the other hand, is positioned such that the next two neighboring cutting lines closet to the K-points are approximately 1/3 and 2/3 of it's maximum cutting line spacing away. Therefore, the metallic and small-gap semiconductor SWCNTs will have its first non-Drude metal peak at an energy three times larger than an equivalent diameter semiconducting SWCNT. These transitions are typically called "van Hove singularities" (vHs) and labeled E_{11}, E_{22}, and etc. to denote transitions between conduction and valence bands combing from the cutting lines 1, 2, and etc away from the K-point[87].

The next observable trend will be the systematic shift in these vHs (and therefore ϵ'' peaks) as a function of radius. In the discussion above, it was noted that the

distance from the cutting lines to the nearest K-point is what essentially determines the band gaps or vHs for each cutting line. The number of cutting lines increase with [n,m] as does the radius. Therefore an increase in [n,m] and SWCNT radius within a given class of materials will systematically decrease the spacing of all the cutting lines from the nearest K-point. This will systematically shift all low energy vHs to a lower energy for each added cutting line. If carried out to an infinite radius (n+m goes to infinity), the quantity of cutting lines would be so packed that the distance from the K-point to the nearest cutting line would be nil and the properties would return back to the zero-gap semiconductor behavior of graphene[13].

So in short, the cutting lines can help us determine/understand the origin of Drude metal peaks, the variation of the vHs as a function of [n,m] or radius, and the difference in magnitudes of these vHs peaks as a function of SWCNT class at a given radius. These relationships should and do hold up across many different SWCNTs down to the very smallest diameter SWCNTs, where the bond-bending distortions and other effects become to large for the trends to hold. Additionally, the higher energy transitions well above the band gap (10+ eV with non-TBA models) have largely been ignored and other trends between the cutting lines and ϵ'' will undoubtedly be discovered by observing the resulting DOS and ϵ'' spectra.

Figure 6-6 shows a comparison of the DOS of the [6,5,s], [6,6,m], and the [9,3,m]. The features around the band gap are just what one would expect for the DOS (semiconductors having zero states available band gap. Metals and small-gap semiconductors having available states through the Fermi energy). For the ϵ'' spectra, the biggest optical anisotropy occurs with the [9,3,m] because of the huge Drude metal spike around 0.0 eV. This spike rises dramatically to values in the hundreds before dropping sharply to 0 at 0.03 eV, which is same value of the the band gap we can see back in Figure 6-5.

The [6,6,m] exhibits DOS features similar to the [9,3,m] in and around the band gap region. However, the [6,6,m] lacks a Drude metal peak in the axial direction at 0 eV despite having no band gap in this direction. In fact, this SWCNT does not experience its first ϵ'' or vHs excitation in the axial until the peak at 2.4 eV. Therefore
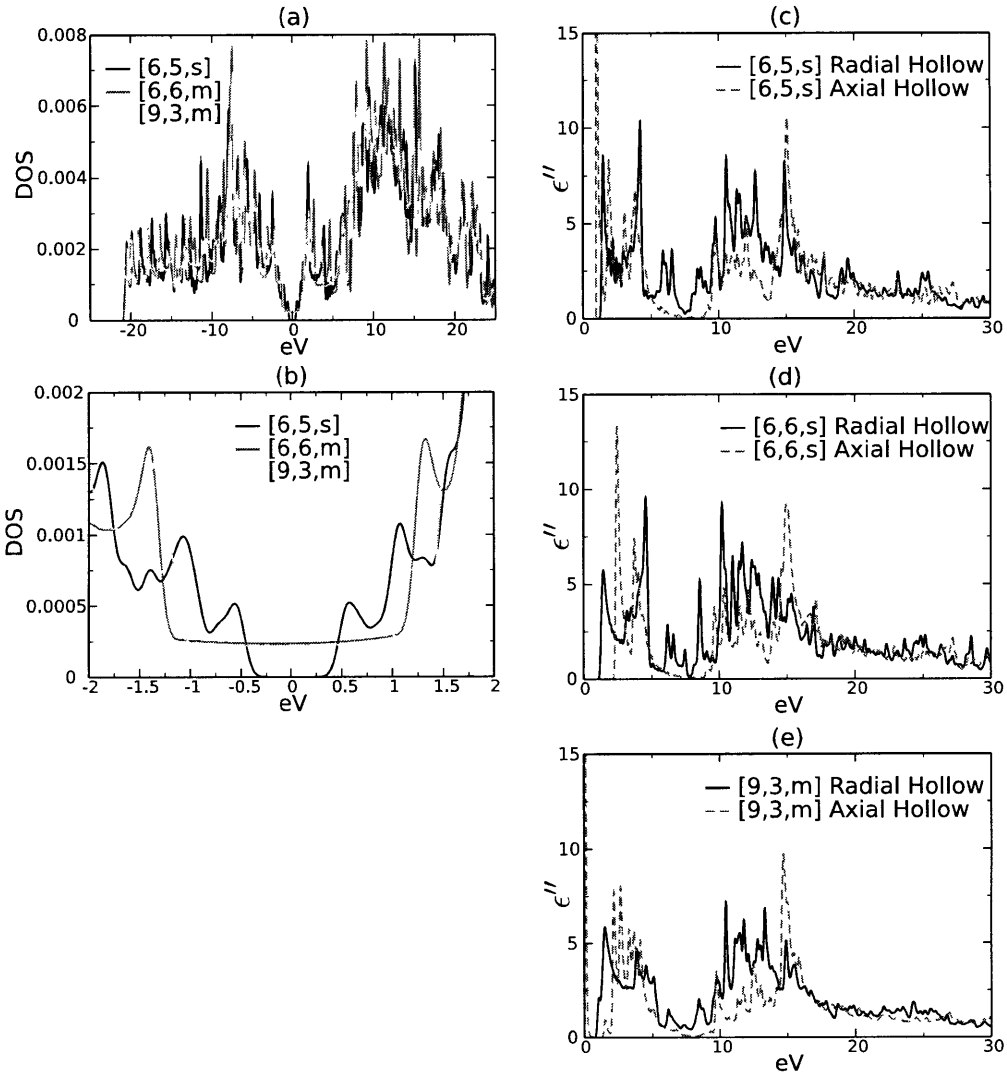
Figure 6-6: A comparison of the DOS and ϵ'' properties of the [6,5,s], [6,6,m], and [9,3,m]. (a) The global DOS trends for the valence electron transitions have generally the same features. (b) A close inspection around the Fermi level shows the small but constant DOS for the metallic tubes and smaller vHs for the [6,5,s] semiconductor. (c), (d), and (e) show the ϵ'' spectra of the [6,5,s], [6,6,m], and [9,3,m] respectively. Most notable is the simply having a continuous DOS through the Fermi level does not necessarily imply or result in ϵ'' activity in this area.
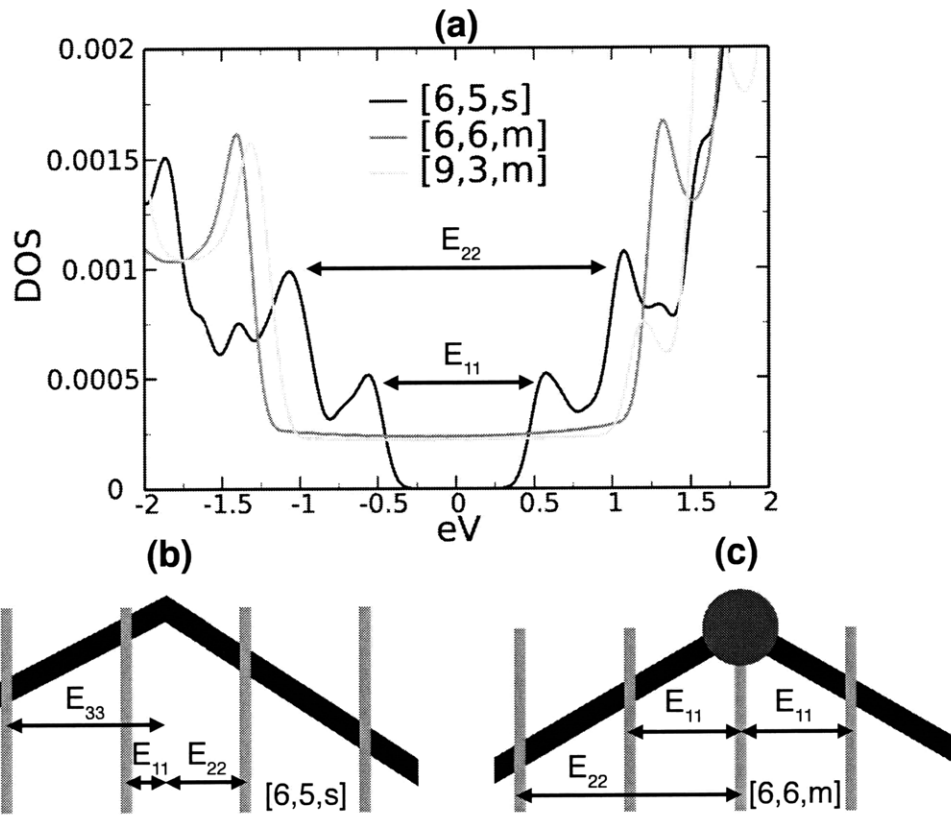
Figure 6-7: A comparison of the relationship between the cutting lines and the DOS for the [6,5,s] and the [6,6,m] SWCNTs. (a) The vHs E_{11} transitions are marked for the [6,5,s] semiconductor. The same pattern follows for the metallic tubes, although the first E_{11} occurs across a much wider range. (b) The cuttings lines for the [6,5,s]. Note how the E_{11} is approximately 1/3 of a full cutting line spacing away and the E_{22} is twice that. (c) The cutting lines for the [6,6,m]. Note how the first E_{11} is a full cutting line spacing away in both directions.

it is an ES metal but an OP semiconductor!

Also note how the metallic tubes [6,6,m] and [9,3,m] exhibit largely different vHs magnitudes between their axial and radial directions from 0 to 5 eV. As stated earlier, the E_{11} vHs for a metallic tube occurs at an energy 3 times larger for an equivalent diameter SWCNT. However, the radial direction behaves as a semiconductor for all SWCNTs regardless of class. So the ES metals exhibit a very large difference in the vHs in the axial and radial directions. Conversely, semiconducting SWCNTs (e.g. the [6,5,s]) are semiconducting in both directions and therefore have vHs that are much closer in magnitude.

There are several key points to understand in this simple comparison thus far. First the Lambin classification system does a great job in guiding and understand the relationships from [n,m] to cutting lines and finally to band diagrams and DOS. However, once in the realm of ϵ'' properties and above, neither the Dresselhaus or Lambin systems can explain or address the disagreement between ES and OP metal/semiconducter behaviors. Thus I reiterate that the cutting lines and classification systems are great guidelines up to band diagrams and other ES properties, but now new territory is being forged and new classifications and nomenclatures are needed to accurately describe the nuances of the OP properties.

The next focus is to observe the ϵ'' features across a larger set of SWCNTs to show whether or not the OP trend as expected due to the shifts in vHs as a function of radius described earlier. Additionally, it can be determined if the deep UV range transitions (5-30 eV) have the same trending features or if they have a different set of behaviors all together. Figure 6-8 shows the ϵ'' properties for large armchairs ([15,15,m], [18,18,m], and [24,24,m]) in the axial direction. The vHs below 4 eV shift and trend as expected from previous SWCNT classifications and analysis. However, the stronger and higher energy bonds remain largely fixed in location, magnitude, and features.

Compared to Figure 6-6, the ϵ'' peaks and features in Figure 6-8 above 5 eV are essentially identical or converged even as we increase the radius by 60% moving from the [15,15,m] to the [24,24,m]. However, all but one peak in the 0-5 eV range
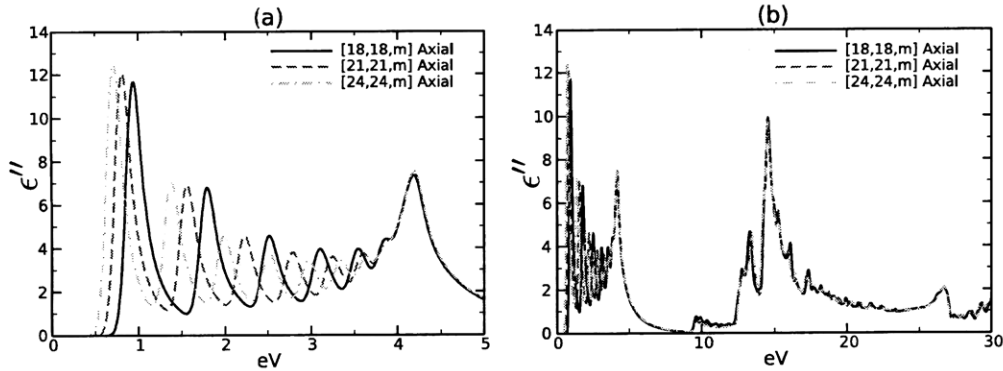
Figure 6-8: A comparison of the ϵ'' spectra for large armchair SWCNTs in the axial direction. (a) Most of the ϵ'' peaks in the 0-5 eV interval shift to a lower eV as a function of increasing SWCNT radius. (b) The peaks in the 5-30 eV range are nearly identical and relatively insensitive to changes in this range of SWCNT diameters.

vary smoothly and systematically in the same direction towards 0 eV with increasing radius. This difference between the two ranges can be understood by returning the cutting lines. The 0-5 eV ϵ'' peaks come from the first set of valence and conduction bands around the fermi energy and are highly influenced by the relationship between the cutting lines and the K-points. Systematically adding or subtracting more cutting lines then systematically moves all the cutting lines closer or farther away from the K-points.

In contrast, the upper level ϵ'' peaks (5-30 eV) arise from bands far away from the fermi-level and seem to exhibit no special trending behavior as a function of the cutting line density relative to the K-points. This seems to imply that either: 1) no dramatic feature changes exist in these bands as a function of distance from the the K-points or 2) if such features do exists, their impact upon ϵ'' peak magnitudes, shapes, and locations seem to cancel each other out (at least within the armchair classification). Because the trends seems to hold across a very wide range of SWCNTs, point number 1) seems more likely. Of course (just like the smooth trending of the 0-5 eV peaks with cutting-line density) this convergence of the ϵ'' peaks in this upper energy limit will break down as the cutting line density gets small enough such that discretization appears from the continuum. This breakdown amplifies when the chiral angle also changes, dramatically altering the allowable electronic states over all energy
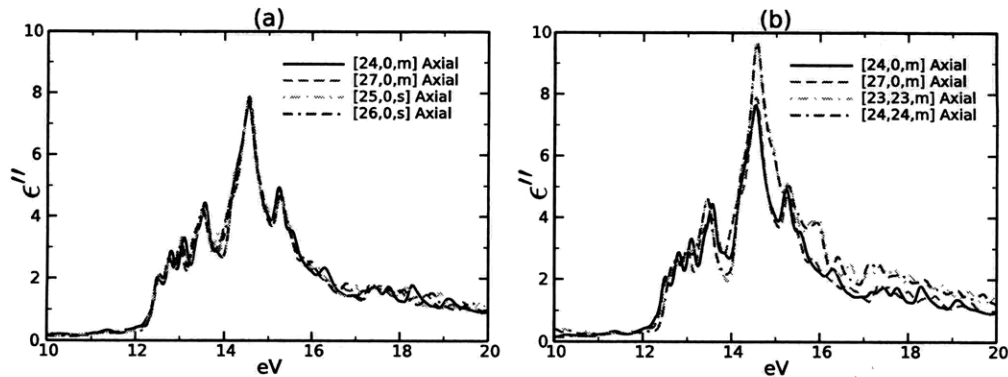
Figure 6-9: A comparison of the axial-direction ϵ'' spectra in the 10-20 eV range for (a) semiconducting vs ES metallic zig-zags and (b) armchairs vs semiconducting zig-zags.

levels.

Figure 6-8 only showed the convergence for armchair tubes only. But it is important to compare the armchairs with the other structural types (zig-zag or chiral) to see if the convergence in the 5-30 eV range is a universal function of diameter or if there is some cutting line angle component. Figure 6-9 (b) compares large diameter zig-zag semiconductors and armchair metals. Within each class, there is excellent convergence in shape, location, and magnitude. However there is a distinct difference between two different classes. Since cutting line density is large for both classes and there is no shifting of the peaks as a function of increasing cutting line line density, the only remaining explanation for this difference in the cutting line angle. To prove that it is based on cutting lines versus ES properties, Figure 6-9 (a) compares the ϵ'' spectra in the the 10-20eV energy range for metallic and semiconducting zig-zags (i.e. different ES properties but identical structure). The results are essentially the same. In fact, if the spectra were unlabeled, one would be hard pressed to split them into two groups. In short, the 10-20+ eV properties in the large radius limit seem to depend primarily on the cutting line density and angles and not at all about whether or not a K-point is crossed..

In a sense, these different energy regimes (0-5 vs 5-30 eV) seem to operate independently (thus far) for large large diameter SWCNTs. In Figure 6-9, the 10-20 eV peaks in part (b) are identical for all zig-zags regardless of ES properties. The armchairs,
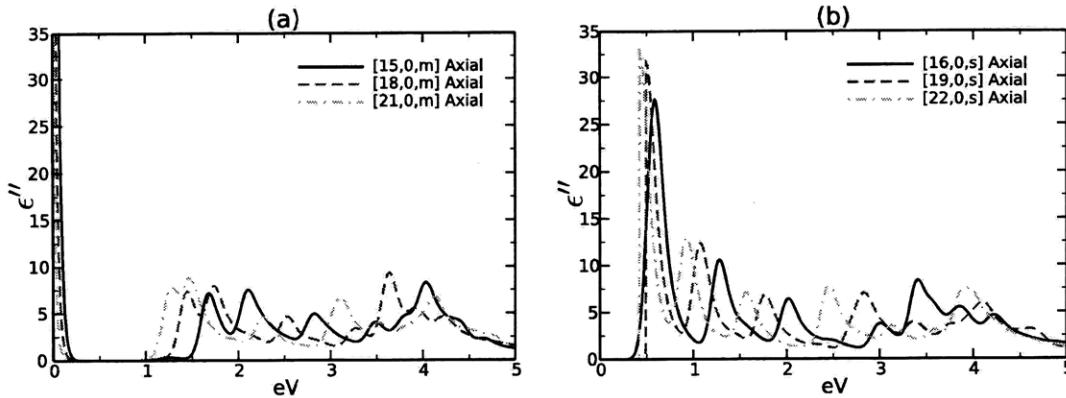
Figure 6-10: Comparison of the axial direction ϵ'' features in the the 0-5 eV range for large zigzag ES metals and semiconductors.

having a different geometrical structure, are also converged but to a slightly different ϵ'' shape in part (a). However in Figure 6-10 parts (a) and (b), the zigzag SWCNTs have vastly different ϵ'' spectra peaks in the 0-5 eV range between the semiconducting and metallic classes. But within each ES classification, there exists smooth and systematic trends as a function of radius. Therefore the higher energy peaks (10+ eV) seem to depend solely on the cutting line angles while the 0-5 eV peaks seems to depend on cutting line density and their relative location to the K-points.

To summarize this in a succinct way, there are essentially 3 factors that appear relevant for convergence of ϵ'' peaks as a function of an increasing radius: the cutting-line density, angle, and location relative to the K-points. The 0-5 eV peaks depend seem to depend on density (this moves cutting lines closer to or farther from K-points) and location (whether a cutting line crosses/grazes versus them all missing completely). Deriving all the way back to [n,m], the 0-5 eV energy range depends on the magnitude of n+m as well as the symmetry relationships between [n,m]. The 10-30 eV peaks depends more almost entirely on the cutting line angles, which is directly correlated to the amrchair, zig-zag, and chiral structures. In terms of [n,m], this would mean the 10-30 eV energy range depends entirely on the magnitude of the n/m ratio.

And finally, the trends for both energy regimes break down (or at least become very difficult to track) as the cutting line density gets very small, the sp2 bonds
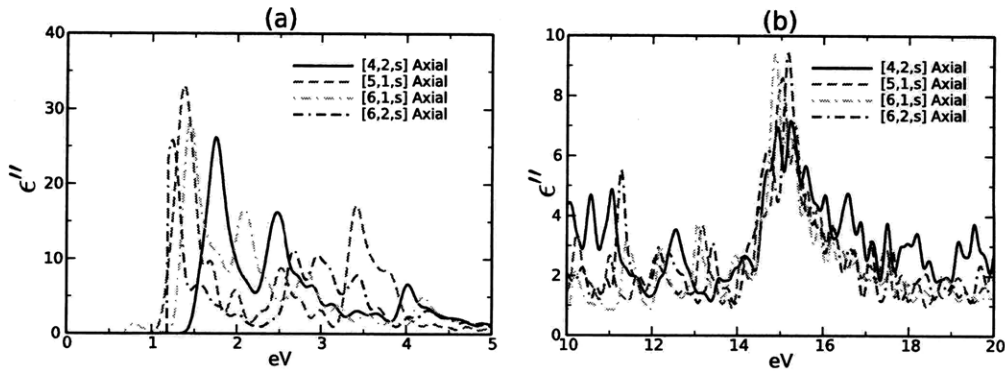
Figure 6-11: A comparison of the axial ϵ'' spectra for several small chiral SWCNTs. Note the lack of clear trending behavior in this regime.

become strained under increased curvature, and the chiral angle changes discontinuously between each neighboring chirality. Figure 6-11 shows a comparison of the ϵ'' properties in the axial direction for small-diameter, chiral semiconducting SWCNTs. Some of the major trends are still visible and applicable, but there is a tremendous amount of distortion, addition/subtraction of ϵ'' peaks, and so forth. The curvature effects on the overall band structure and the large difference in the cutting line behaviors within and between the SWCNT classes all play a role in these effects at this diameter limit.

6.2.6 Identifying Major optical peaks

Before analyzing the ϵ'' to vdW-LDS relationships, a short qualitative analysis of how the peaks move and appear/disappear as a function of radius is quite helpful. Specifically this helps to answer the question of what diameter range do the trends breakdown. The previous section already described the exact reason and nature of these shifting peaks. This section is more useful in showing where the shifts occur and by how much. This can be extremely useful for when studying the dependancies between ϵ'' and vdW-LDS through the KK transformation because the location and magnitude of these changes can be traced systematically and correlated to [n,m] (more on this in the next section).

The first part to address is locating this breakdown regime as a function of tube

diameter. When viewing ϵ'' graphs containing many full spectra, finding such a breakdown is very difficult. This is due to the tremendous amount of information contained in all the sharp peaks and wiggles in each ϵ'' spectra. Such an overload of information can make it difficult to pull out the salient details required to address just one facet of the entire wealth contained with the spectra data. However a peak analysis gives a very simple set of data points that can easily be viewed on a global scale across all SWCNTs and across the entire 0-30 eV energy range. Because this can still become bloated if left unrestricted, I decided to confine this analysis to the armchair class alone because it illustrates both the trending and the breakdown regime. But the effects detailed in the previous section still hold in comparing across the different ES classes and structural makeup.

Figure 6-12 shows the identification of the axial direction ϵ'' peaks and compares it to the largest armchair SWCNT spectra contained in this analysis, (i.e. the [24,24,m]). The particular details of the very simple algorithm to locate the peaks are not too exciting or important. What the script does is essentially capture all ϵ'' peaks that have a differential of 1.0 units on both the left and right sides within a +/-1 eV range. What is important is how these identified peaks shift within the 0-5 eV and 5-20 eV ranges as a function of radius (the 20-30 eV range is ignored because its peaks tend to be smaller and harder to trace from chirality to chirality). As expected from the discussion in the previous section, the peaks in the 10-20 eV range remain very stable for large diameter tubes and only begin to shift for tubes having a radius of approximately 0.8 nm or less. The 0-5 eV energy peaks all shift systematically with [n,m] (except for an invariant beak around 4.20 eV) because of the change in cutting line density moving the lines closer to or father from the K-point. Below the 0.8 nm radius threshold, shifts and peak additions begin to occur in the 10-20 eV regime while the 0-5 eV peaks still trend systematically. Below the 0.6 nm radius threshold, even the invariant 4.20 peak begins to shift downward towards the first vHs.

The peak trends in the radial direction (see Figure 6-13) are slightly different. The most notable difference is that there are really only 2 main peaks in the 0-5 eV range and they both tend to drift in the same direction across the entire energy range.
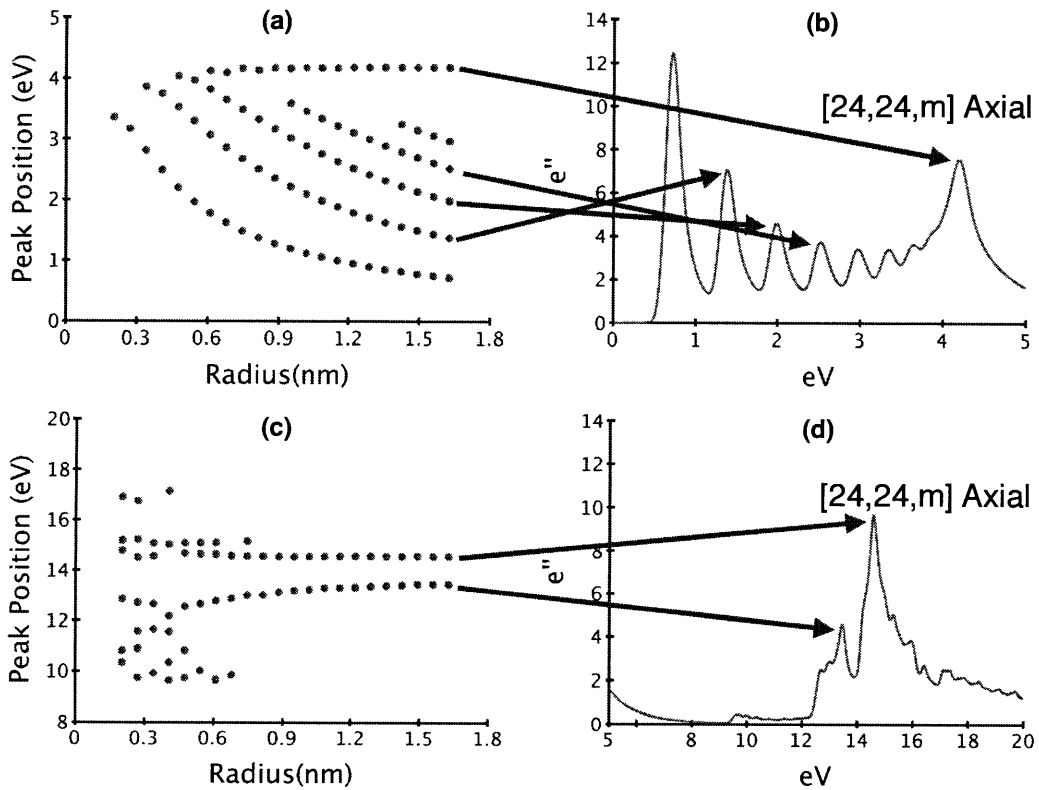
Figure 6-12: An axial-direction, ϵ'' peak identification plot for the armchair SWCNTs ranging from the [3,3,m] to the [24,24,m] in the (a) 0-5 and (c) 8-20 eV range. (b) and (d) A [24,24,m] axial direction ϵ'' spectra is included for comparison along these same eV range intervals.

There is also no invariant peak in this direction for this energy range. But like the axial direction, the peak trends have a systematic, inverse relationship with radius. The two peaks in the 0-5 eV range also tends to get closer together as the radius drops. But this convergence is much slower than what occurs in the axial direction and the endpoints remain largely separated, even in the regime of the smallest tube radii. The deeper 10-20 eV range begins to add many new peaks around and below a radius threshold of 0.7 nm. By 0.2 to 0.4 nm range, the peaks become very erratic in location

In summary, this peak analysis plot confirms some of the findings of the previous chapter and also gives insight into the change over diameter regime. Above a diameter of approximately 1.4 to 1.6 nm, the spectra are very well converged. Below this regime, the peaks become more numerous and erratic, opening the door for a lot of OP specificity as a function of individual chirality for tubes within and among different SWCNT classifications.

6.2.7   e2 to vdW-LDS

Now its time to see how these ϵ'' trending and other features manifest into variations in vdW-LDS. The armchairs are the easiest and best class to do this analysis for several reasons: 1) There is no change in the cutting line angle among them. Therefore it isolates the resulting vdW-LDS effects to the known ϵ'' vHs shifts in the 0-5 eV range. The 10-30 eV range (largely cutting angle dependent) remains fixed and unchanged down to the smallest diameter SWCNTs. 2) They are all ES metals and thus all the vHs will be large and systematic shifts relative to one another. 3) Pragmatically it is easy to calculate/obtain a very large number of this class of SWCNTs because of their relatively small z-height spacing in the OLCAO supercell. Of the 63 SWCNT ϵ'' spectra available, 22 are armchair tubes ranging form the [3,3,m] to the [24,24,m]. Chiral SWCNTs, by comparison, can require 1-2+ orders of magnitude more atoms and become very prohibitive computationally with what is readily available/obtainable on a reasonable budget.

Recall from Figure 3-4 that there are essentially 3 ways that ϵ'' effects vdW-LDS:
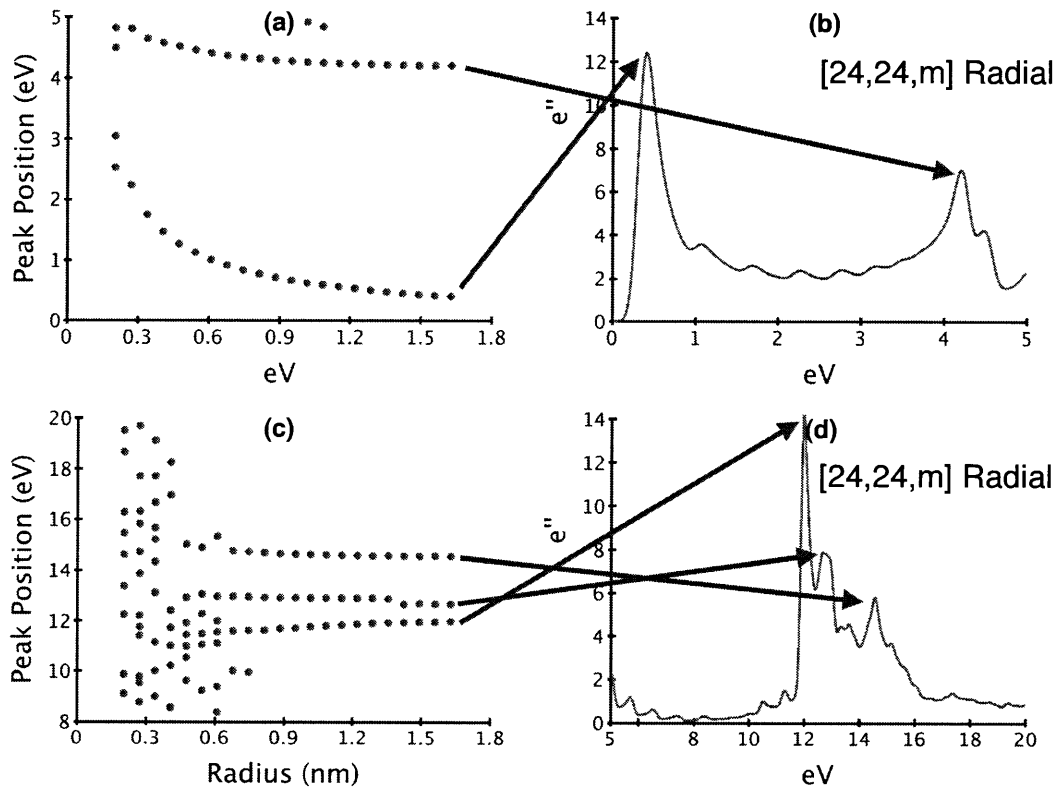
Figure 6-13: An radial-direction, ϵ'' peak identification plot for the armchair SWCNTs ranging from the [3,3,m] to the [24,24,m] in the (a) 0-5 and (c) 8-20 eV range. (b) and (d) A [24,24,m] radial direction ϵ'' spectra is included for comparison along these same eV range intervals.

shape, position, and area. The 2 components that had the most impact were area (pulls the entire spectra up linearly) and position (shifts in ϵ'' change the vdW-LDS slope at the high and low energy wings). With the ϵ'' trending and peak behavior now identified, we can analyze and understand the fundamental reasons as to why the vdW-LDS trend and behave as they do and ultimately link from [n,m] to vdW-Ld interactions.

Recall the distinct ϵ'' trending regimes in Figure 6-8. The peaks above the invariant 4.19 eV peak are all locked in position, shape, and magnitude. The peaks from 0-4 eV depend on the cutting line density and systematically shift lower with increasing radius while slightly increasing the total area under the curve. This slight increase in area makes sense in terms of balancing the fsum rule's effective electron density[72] (see equation 3.4), which scales as $\omega * (\epsilon'')^2$. So to maintain the same total of electrons, any total shift of a ϵ'' peak to a lower eV should raise its ϵ'' value in order to maintain a fixed quantity of valence electrons. It is yet another great confirmation between optical property theory, SWCNT trending, and the OLCAO calculations.

So understanding the KK both the relationship between ϵ'' and vdW-LDS in Figure 3-4 and the ϵ'' behavior for large armchairs in Figure 6-8, the following effects are expected: 1) The vdW-LDS for the largest tubes should have the sharpest slope near the low energy limit and remain lower and flatter in the higher energy limit as the vHs shift to a lower eV. 2) The slight increase in ϵ'' area for the larger tubes in the 0-4 eV regime should slightly increase the overall magnitude of the vdW-LDS across most some of the energy interval. 3) These first two effects will be additive in the low energy regime 4) These first two effects will be combat each other in the high energy interval.

Figure 6-14 shows a comparison of the ϵ'' and vdW-LDS of the larger diameter armchair SWCNTs in both the axial and radial directions. All of the expected trends between the two are present. First there is a clear rise of the vdW-LDS low energy wing as the radius increases and the ϵ'' peaks shift left and up. If the only change between the chiralities was the shifting of these 0-4 eV ϵ'' peaks, we should expect the larger tubes to also have a weaker vdW-LDS in the 5+ eV range similar to what

happens in 3-4. However, the small increase in ϵ'' area with increasing radius seems to pull the vdW-LDS up slightly such that they all have similar magnitudes beyond 1 eV in the radial direction and beyond 2 eV in the axial direction.

This leads to the next trend. The radial direction contains semiconducting vHs, which occur at much lower energies in comparison to the large first vHs in the axial direction. The resulting low energy vdW-LDS begins to rise dramatically the closer these vHs get to 0 eV. This means that the radial direction vdW-LDS for an armchair SWCNT will always have a larger low energy wing in comparison the axial direction. This topic will be addressed in more detail later, but highlights the sensitivity involved as ϵ'' peaks get closer to (and ultimately touch) 0 eV. However this large difference for the radial direction vdW-LDS is largely confined to 0-1 eV because the peaks beyond the first vHs in the radial direction do not shift much, if at all. The axial direction, having much more pronounced shifts at a larger energy, don't converge or cross over in their vdW-Ld until 2 eV. By 5 eV, the axial and radial direction vdW-Ld have magnitudes within 5% of each other. So in summary, these major differences in peak positions and trending between 0-5 eV in ϵ'' properties manifest as differences in vdW-LDS in the same energy regime. However they ultimately converge beyond 5 eV.

Next to study is the effects of scaling on the ϵ'' spectra and how it alters the trending behavior across the armchair SWCNTs. To simplify the analysis, only the axial direction is used. The effects will be similar for any SWCNT class and in the radial direction as well. Figure 6-15 compares the solid and hollow cylinder scaling procedures described in Equations 3.2 and 3.3. The void volume contained within the core pulls down the magnitude of ϵ'' and the vdW-LDS because the electron density is now averaged over this larger volume. Quite simply–the larger the tube diameter, the larger the dampening effect on both ϵ'' and vdW-LDS.

With hollow-cylinder scaling, the [24,24,m] has the largest magnitude at 0 eV with a value of approximately 8.5 because its first ϵ'' vHs is closest to 0 and gets the largest spike effect. However when using solid-cylinder scaling, the [24,24,m] is now the weakest spectra at 0 eV (with a magnitude of just over 3.5) because it has
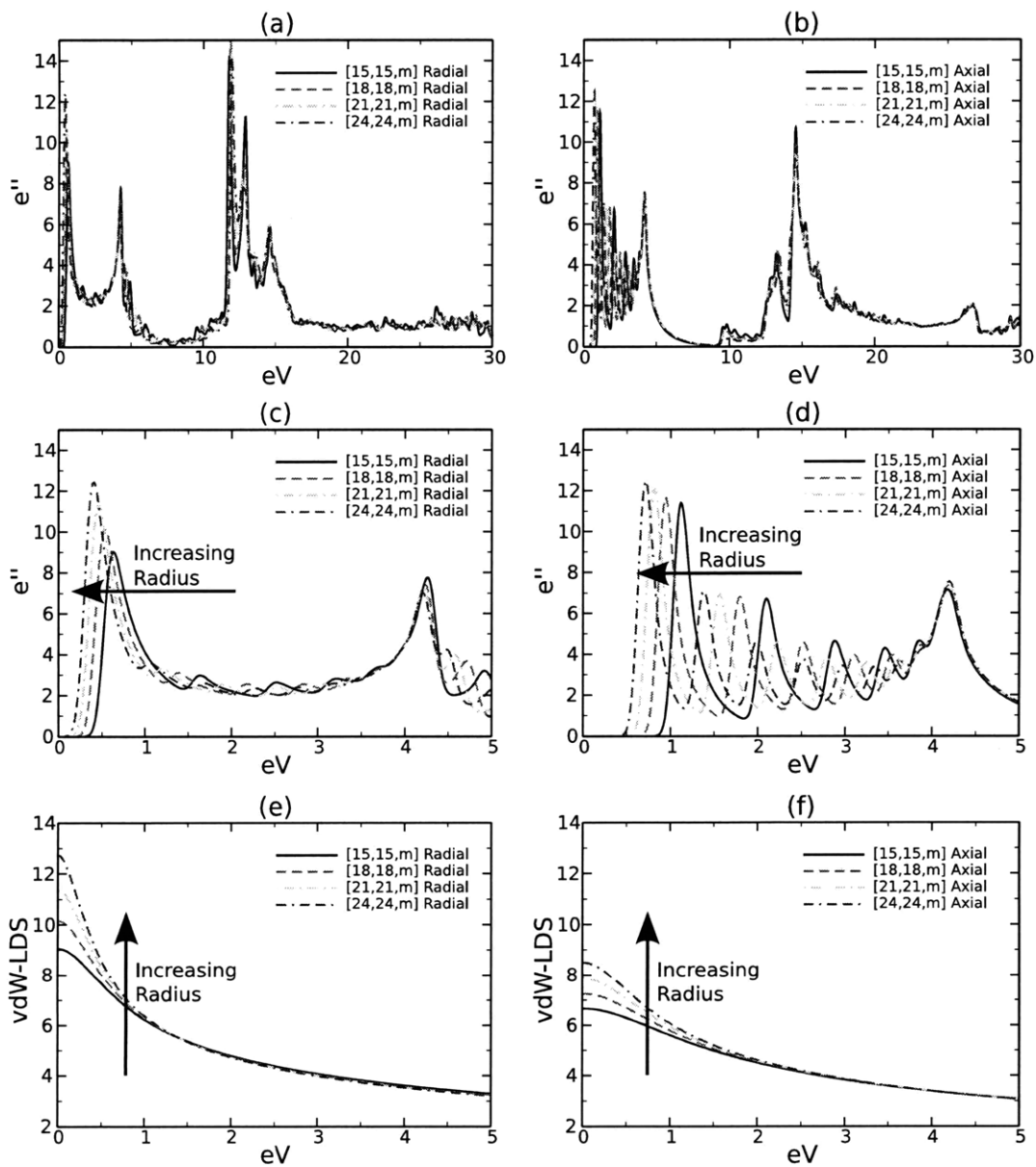
Figure 6-14: A comparison of the ϵ'' and vdW-LDS trends in the radial and axial directions for armchairs SWCNTs ranging from the [15,15,m] to the [24,24,m]
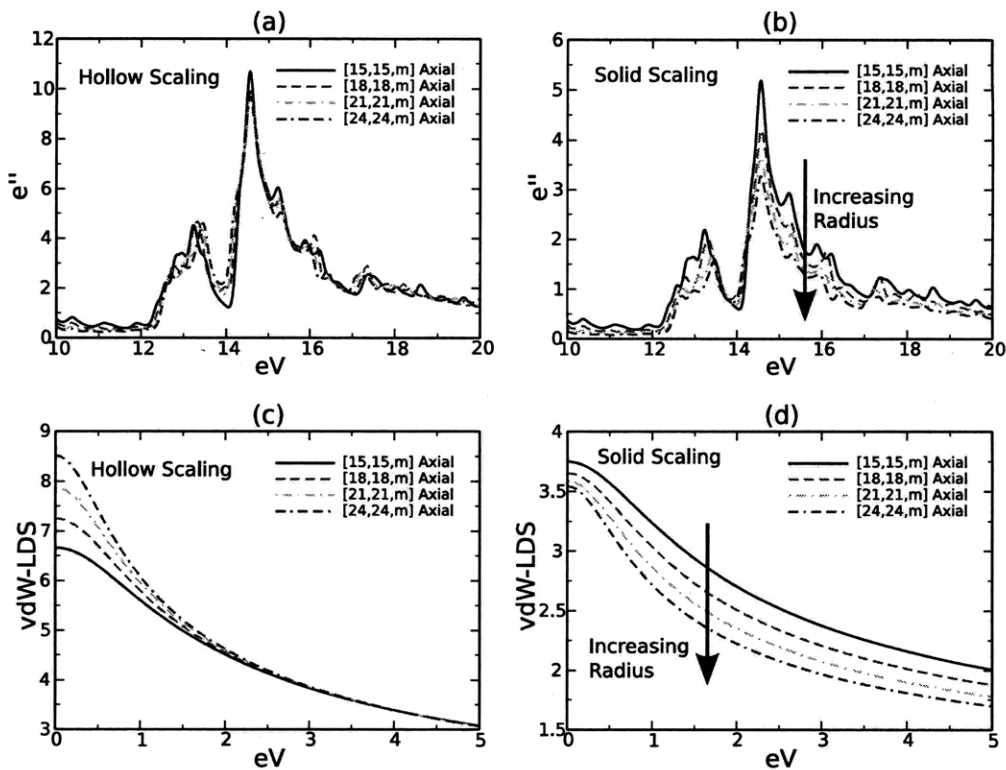
Figure 6-15: Comparing the effects of the hollow-cylinder and solid- cylinder scaling procedures on the ϵ'' and vdW-LDS for armchair SWCNTs in the axial direction.

the largest void volume of the SWCNTs studied. When looking across the entire vdW-LDS, all the armchair vdW-LDS pack very close together after 2 eV when using hollow-cylinder scaling, but have a tremendous amount of overall magnitude variation when using the solid-cylinder scaling. In short, the hollow-cylinder spectra are only altered by shifts in ϵ'' while the solid cylinder spectra are largely overpowered by the scaling of the ϵ'' area.

This strong impact on overall vdW-LDS magnitude when using the solid-cylinder scaling is important to keep in mind when studying Hamaker coefficients as a function of diameter. It also reiterates a point I hit on numerous times in Chapter 5 on the critical nature of picking the proper scaling behavior at the proper limit. Clearly the Hamaker coefficients will vary a function of radius and will depend strongly on the scaling selection method.

The remainder of the analysis comparing ϵ'' to vdW-LDS will use only hollow-
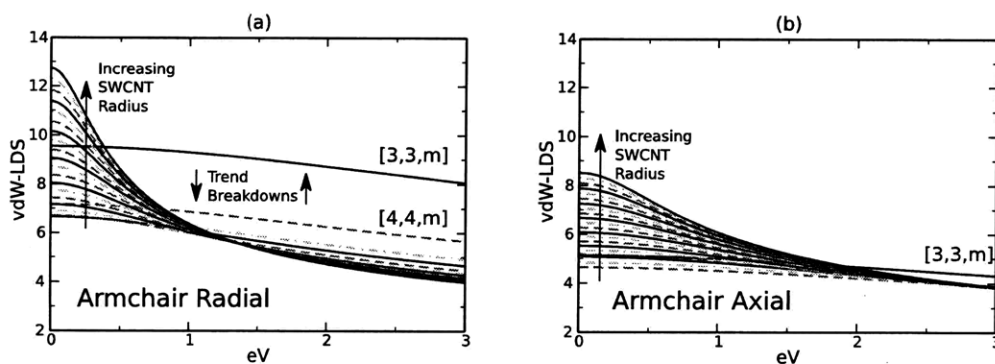
Figure 6-16: A comparison of all hollow-cylinder, armchair vdW-LDS in the (a) radial and (b) axial directions.

cylinder scaling in order to isolate and/or eliminate the huge effect of the scaling decision. This is primarily done so as to not overpower or overshadow the analysis of other effects. However one can easily implement or qualitatively understand the impact that a solid-cylinder scaling would have on everything that follows in this section. Solid and mixed cylinder spectra will also be used in the Hamaker and vdW-Ld TE calculations later in the chapter.

So far this analysis has largely been confined to the vdW-LDS trends for large diameter SWCNTs. Because there appears to be ϵ'' breakdowns and peak shifts around 0.8 nm as shown in Figure 6-12, a valid question to ask is whether or not those shifts/alterations would necessarily change vdW-LDS in a surprising way. After all, the case could be made that these differences could cancel out and still have a clean and systematic vdW-LDS trend down to the smallest SWCNT in a given class. Figure 6-16 demonstrates that is in fact possible, at least for the armchair classification. This is not to imply that the dramatic ϵ'' peak variations will not drastically change the vdW-LDS of the non-armchair classification (later demonstrations in this chapter will show how large these changs). But the armchairs represent a very resilient subset of the entire SWCNT family that trends beautifully in their vdW-LDS all the way to [5,5,m] in both directions. The [4,4,m] and [3,3,m] break away fairly strongly from the trends, which is likely a result of the tremendous amount of bond bending at this diameter limit.

To understand how this resiliency can come about, it is necessary to return to

the 3 possible KK transformation manipulations. Recall that shape did very little in the way of altering vdW-LDS. In reality, shape changes in ϵ'' can be seen as a set of competing shifts of many smaller peaks. For example: suppose 10 units of ϵ'' area existed at 10 eV as a very sharp and almost delta function-like peak. Now suppose this big peak is split it into two peaks and then each was shifted 1 eV in opposite directions. What is the effect of vdW-LDS? Answer: almost nothing. In fact, unless the change in shape occurs very close to 0eV and causes a sharp low energy wing, the effects will not have a substantial impact. It isn't until the [4,4,m] where the total ϵ'' area in the 10-30 eV range begins to rise dramatically and thus the trend breaks down.

One thing noticeably missing thus far was any sort of OP behavior that behaved like a metal. One would expect the armchair metals, being the only true ES metals according to Lambin et al, to be the most likely to exhibit OP metallic features by having a ϵ'' spike around 0eV. But all armchair ϵ'' properties for axial directions in Figures 6-14 to 6-16 lack such an effect. However, chiral metals, despite having very small band gaps between 0.01 to 0.05 eV, all have this effect and show it quite dramatically.

Figure 6-17 shows a comparison of the DOS, ϵ'', and vdW-LDS properties for armchair and chiral metals of generally the same diameter. Clearly both sets of tubes have a continuous DOS through the Fermi energy and are thus ES metals. But only the chiral metals have a dramatic peak of ϵ'' that rapidly ramps up to values in the several hundreds and beyond near 0 eV. However, these near 0.00 eV ϵ'' peaks for chiral metals tend to crash back down to zero just before reaching 0.00 eV due to their very small band gaps. The effect on vdW-LDS is equally dramatic, pulling the 0 eV vdW-LDS for the chiral metals up to values 3-4 magnitudes larger than the armchair counterparts for the axial direction.

This dramatic spike is a very important feature and results in a substantial degree of optical anisotropy because the radial direction is always semiconducting for all SWCNT chiralities. Figure 6-18 shows a comparison of the ϵ'' and vdW-LDS for the [6,5,s] and [9,3,m]. All SWCNTs, even semiconductors like the [6,5,s], exhibit some
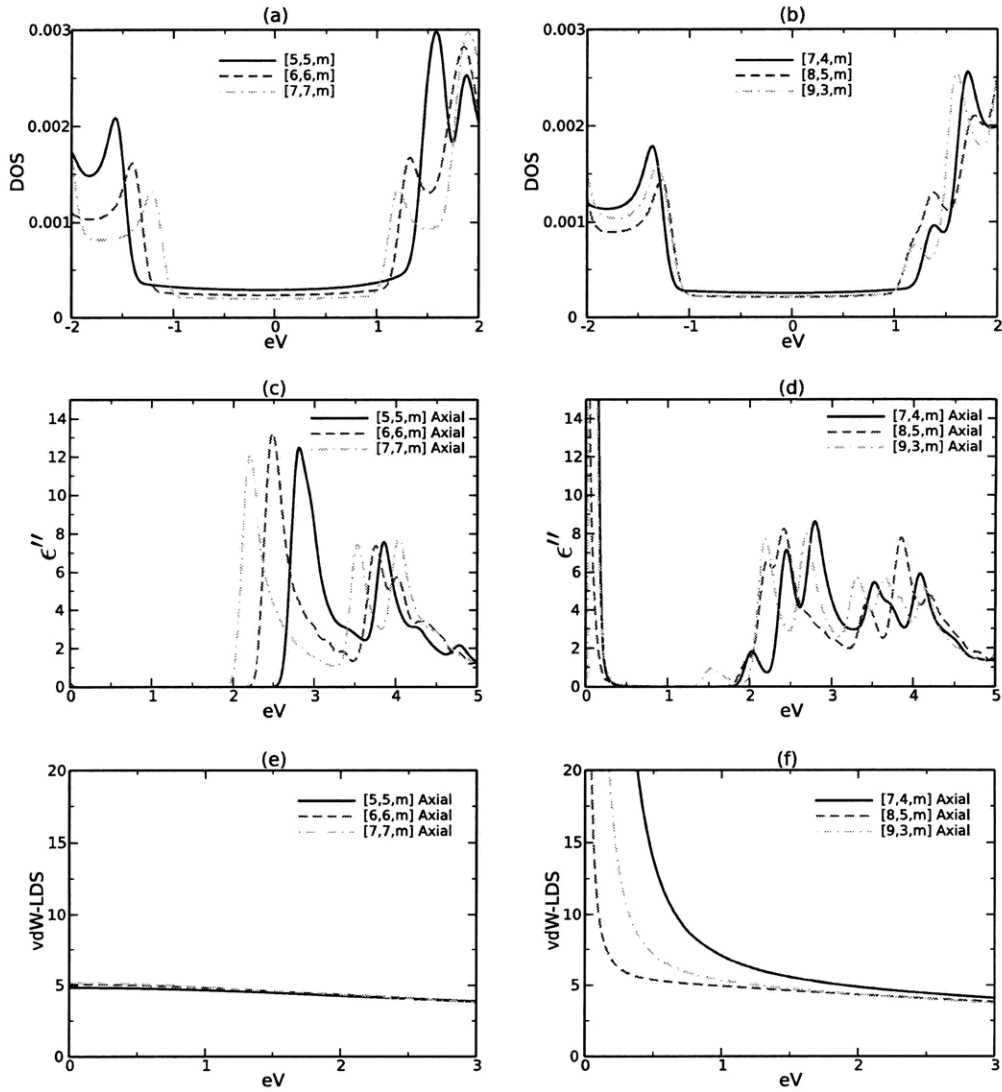
Figure 6-17: A comparison of the DOS, ϵ'', and vdW-Ld properties for between select armchair and chiral metals.
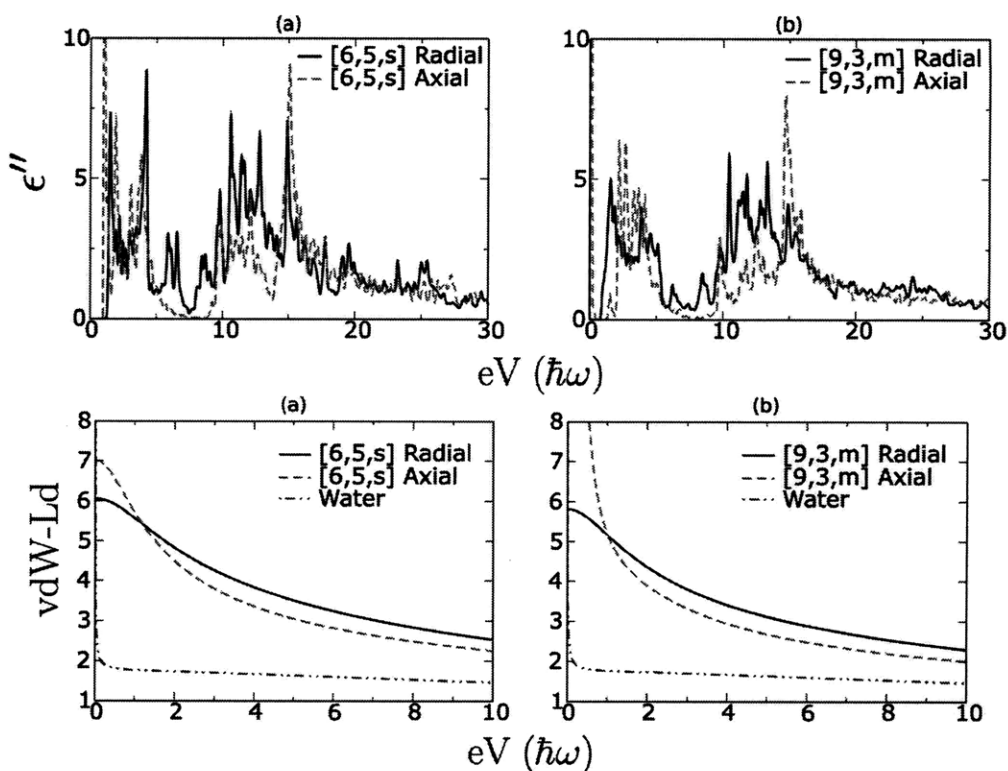
Figure 6-18: A comparison of the radial and axial optical properties for the [6,5,s] and [9,3,m] to demonstrate the large increase in the vdW-LDS due to the low energy ϵ'' spike near 0eV in the axial direction.

degree of anisotropy because the axial direction contains only in-plane sp2 bonds while the radial direction contains other orientations of the graphene honeycomb lattice. But it is the near 0.0 eV ϵ'' spike that gives the [9,3,m] the large, direction-dependent Hamaker coefficients (see next section).

If this ϵ'' and vdW-LDS spike at 0 eV is as important as I claim and will later demonstrate, its worthwhile to determine or denote which SWCNTs exhibit this feature. All of the armchair ES metals lack any significant ϵ'' behavior below the first vHs in the axial direction. All chiral metals exhibit a near Drude metal peak that doesn't quite reach 0.00 eV, but dramatically rises to its very small band gap (all less than 0.1 eV for the SWCNTs in this study). That only leaves the zig-zag metals. And the interesting feature of this class of ES metals is that there appears to be a cutoff radius in which the OP goes from having a perfect Drude metal peak to no

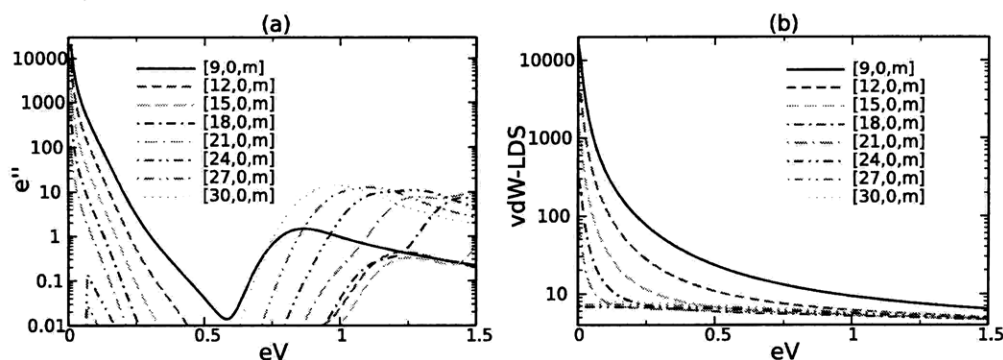Figure 6-19: The axial ϵ'' spectra for zig-zag metals in the energy range very close to 0 eV.

peak at all!

Figure 6-19 shows the axial ϵ'' and vdW-LDS of the [9,0,m] through [30,0,m] zig zag metals in the 0-2 eV range. The smallest diameter SWCNTs has the largest vHs gap (cutting line density effect) as well the most dramatic ϵ'' spikes rising all the way down to 0.01 eV (the smallest possible energy measurement in the OLCAO calculation). As the tubes get larger and the curvature gets smaller, the ϵ'' spike continues to pull down and eventually disappears altogether. The effect of this ϵ'' trend carries over to the vdW-LDS, where the [9,0,m] spikes up by the largest amount, eventually hitting the y-intercept with a value in the several thousands. The [21,0,m] is the last zigzag metal to contain this dramatic low energy wing. All zig-zag ES metals [24,0,m] and above mimic the armchair metals in their lack of a ϵ'' spike at 0.0 eV.

Having shown all the ES metal classes individually, it is useful to quickly compare the 3 different structural types (armchair, chiral, and zig-zag) on a single graph. Figure 6-20 shows the radial and axial vdW-LDS of similar diameter candidates from each structural class. The radial-direction spectra actually match up quite well and do in fact trend with the slight diameter differences that exist between the chiralities. By contrast, the axial direction can vary quite a bit depending on whether the low energy wing is present. The chiral and zig-zag metals that exhibit it are far greater in vdW-LDS magnitude for the first 0.5 to 1 eV range, but then quickly converge to a similar magnitude beyond this point.

The large diameter zigzag semiconductors are the last class of SWCNTs within
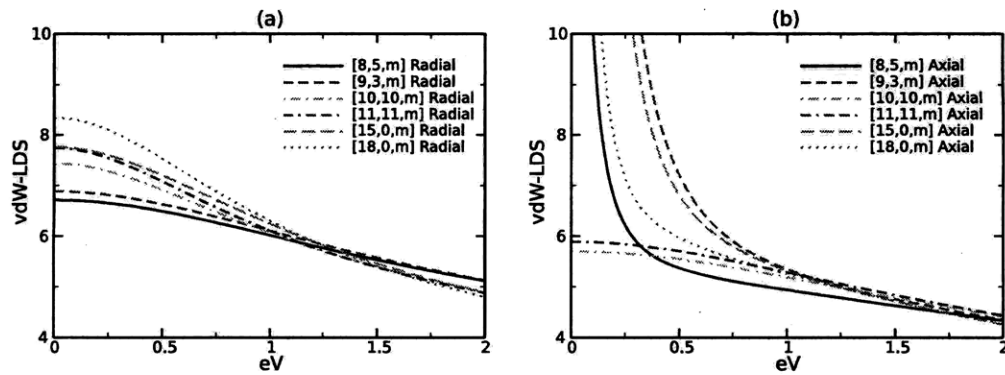
Figure 6-20: The axial and radial direction hollow-scaled vdW-LDS of SWCNTs representing all three structural types of ES metals: armchair, zig-zag, and chiral.

the 63 SWCNTs calculated that exhibit systematic vdW-LD behavior as a function of radius. Of course the current lack of trending for chiral semiconductors could simply be due to the computational limitations in being able to calculate large enough SWCNTs in this class to achieve convergence. But that question will have to be addressed in the future when such spectra are made available. Figure 6-21 shows a comparison of the large zigzag semiconductors compared to the armchair metals. Because of their much smaller vHs gap in the axial direction, the semiconductors actually exhibit a stronger 0 eV vdW-LDS wing that is much larger than the armchair metals. This non-intuitive result is again due to the lack of Drude metal peaks for this particular geometry. The radial directions for both SWCNT classifications seem to match quite well because large diameter SWCNTs have similar ϵ'' in the radial direction that are somewhat invariant to changes in tube diameter.

The next issue to address is what occurs when the radius gets very small and we open the analysis to the last structural type (chiral). Figure 6-22 shows a comparison of ϵ'' and vdW-LDS properties of armchair and chiral SWCNTs of varying ES properties. What is noticeable is that the ϵ'' spectra gets very noisy and the peak locations are unpredictable. In the armchair class, this erratic ϵ'' behavior seemed to cancel out and still leave smooth trends between neighboring tubes (e.g. the [15,15,m] versus the [14,14,m] and [16,16,m]). For the chiral tubes, these ϵ'' features change enough such that there are very real and significant variations in the resulting vdW-LDS.
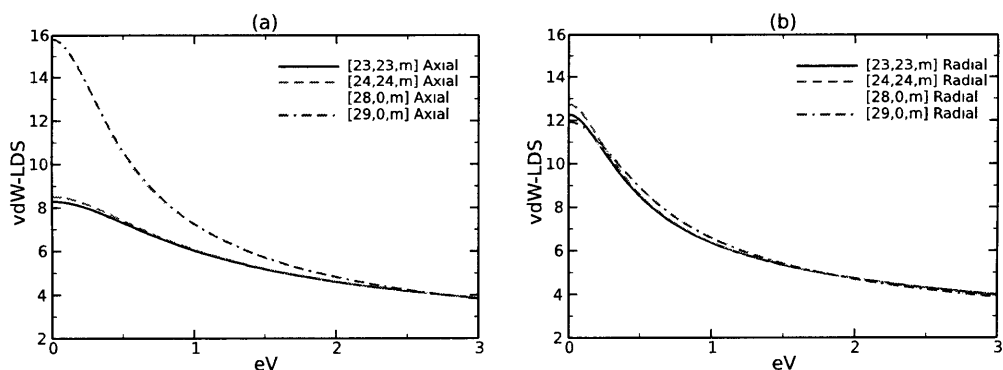
Figure 6-21: A comparison of the (a) axial and (b) radial vdW-LDS for the armchair and ES semiconducting zig-zag SWCNTs.

This is not to say that are not some small correlations. The [6,2,s] and [6,4,s] have nearly identical axial direction vdW-LDS, but differ greatly from the [6,1,s], which has a axial vdW-LDS similar to the [5,1,s]. The differences between even these pairs increases when we observe the radial direction. In short, there is no obvious dependence on radius, SWCNT classification, or any other presently known figure of merit to distinguish and group these small-diameter, chiral ES semiconductors on a global scale.

The next logical questions is whether or not this variation in vdW-LDS in meaningful at the Hamaker coefficient and vdW-Ld TE levels. Before delving into specific trends, a simple figure showing the quantity of variation answers this question with a resounding "YES". Figure 6-23 has the $\mathcal{A}_{121}$ Hamaker coefficients for all 63 SWCNTs using the axial-direction, hollow spectra across vacuum using the plane-plane Lifshitz formulation. What is clear is that there is a convergence beyond a critical radius of about 0.8 nm (around the [10,10,m] or [18,0,m] chiralities), which just happens to match the cutoff diameter for the peak convergence shown in Figure 6-12. Below this cutoff radius, there begins a formation of a widening envelope that encompasses all the variations and becomes larger as the tube diameters get smaller. For the smallest tubes, the difference in the Hamaker coefficients can be almost an order of magnitude.

The size of this variation envelope may diminish when we use the solid cylinder formulations or use the full anisotropic rod-rod formulations rather than isolated radial-radial and axial-axial interactions. But the take home message is that the
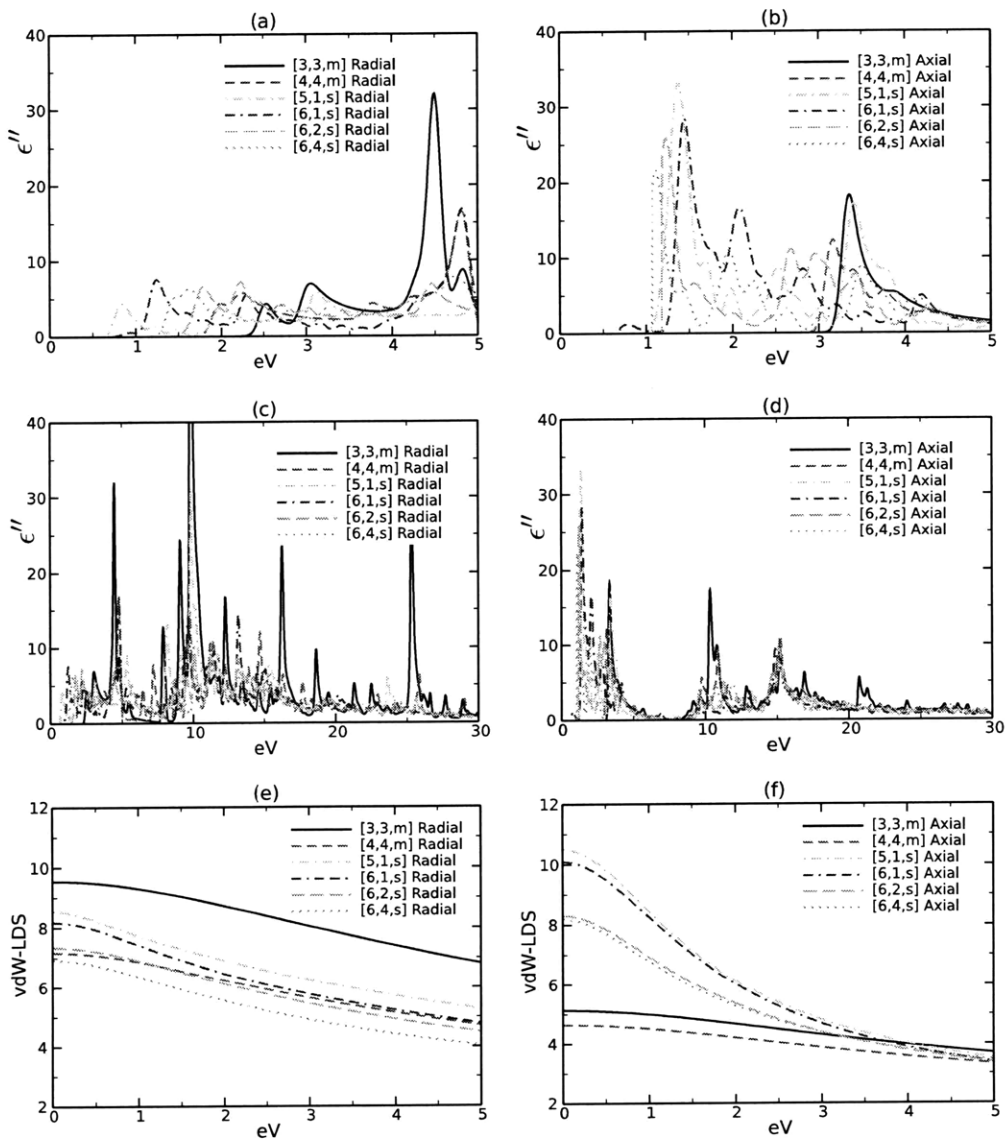
Figure 6-22: A comparison of the ϵ'' and vdW-LDS properties for very small diameter amrmchair and zigzag ES semiconducting SWCNTs in the axial and radial direction.
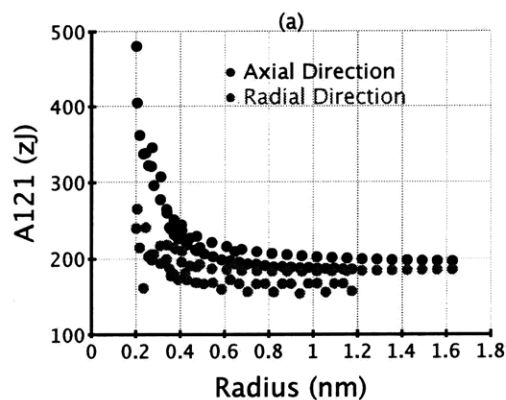
Figure 6-23: A quick comparison of simple A_{121} Hamaker coefficients versus radius to demonstrate the vdW-Ld trends as a function of class and/or SWCNT classification. The interactions are calculated as simple pairwise interactions (radial-radial and axial-axial) using the isotropic plane-plane Lifshitz formulation and hollow cylinder SWCNT spectra in vacuum.

large variation in vdW-LDS (due to variation in ϵ'', which depends on bands, which depends etc) causes a substantial variation in the Hamaker coefficients that could not have been predicted simply by TBA calculations, ES classification analysis, force-field modeling, or anything else of that nature. This plot of simple Hamaker coefficient also suggest that, above the cutoff radius regime around 0.8 nm, the vdW-Ld interactions variations have all converged. One can even extrapolate this convergence quite easily to predict the vdW-LDS properties for SWCNTs that are even larger in diameter than the ones listed in this analysis.

This analysis of the SWCNT ϵ'' to vdW-LDS dependencies could go on for many more pages considering the sheer quantity of data and the number of possible features to address, characterize, and so forth. However, most the details beyond what I've described are more relevant to very specific comparisons and applications that can be calculated and analyzed for that particular situation. Now it is time to move onto the final 2 stages and see how these vdW-LDS effect Hamaker coefficients and resulting vdW-Ld interactions. In particular, I will focus on the regimes below and above the convergence cutoff radius (approximately 0.8 nm).

6.2.8 Hamaker coefficients

One of the difficulties in describing the Hamaker coefficient results has to do with the quantity of detail required to explain each calculation and the number of possibilities at these different junctures. To describe them properly, one needs to state the

- Lifshitz formulation used (dozens of possibilities)

- Distance limit (usually 2 possibilities)

- Scaling (2 possibilities)

- Mixing (infinite number of possibilities)

- SWCNT classes involved (5+ possibilities of vdw classification for the 63 different SWCNTs in the analysis)

- Medium used (numerous possibilities)

- Miscellaneous (big vs small diameters tubes, the energy regime one's observing, etc.)

This poses two main difficulties: 1) being able to describe these 6+ details in a compact enough form that doesn't come off as tediously verbose while still not requiring the memorization of dozens of acronyms and 2) confining the analysis to just the most pertinent and illustrative examples without getting bogged down in a sea of esoteric details. After all, the goal is to give enough insights to empower end-users to be able to understand and predict these interactions instead of generating data for every possible scenario that is conceivable. So this study will be focused to only the most illustrative examples that help to flush out details, trends, and ideas described earlier in this and other chapters. There is also a system design example at the very end to merely motivate the future possibilities before turning attention towards total vdW-Ld interactions.

This first effect to expand upon is the level of diversity that arises between different chiralities and their different directions as introduced in Chapter 3. Recall the wide

range of available Hamaker coefficients in Figure 6-23 that resulted from the very diverse array of vdW-LDS in Figure 6-16. Now it is time to take it a step further beyond this global map and observe the trend breakdown between the axial vs. radial directions and the 5 different vdw classifications.

Figure 6-24 compares the Hamaker coefficients calculated with the isotropic Lifshitz plane-plane formulations for axial-axial and radial-radial interactions using hollow scaled vdW-LDs. What is clear from (a) and (b) is that the radial direction behaves very systematically as a function of radius when viewed globally for all classes simultaneously. The axial direction is the source of much more of the variation, particularly for the smaller radii tubes. This is not surprising simply because the radial direction is always a semiconductor and the variations in ϵ'' and vdW-LDS (even within a given class) are much less than the axial direction.

It should be noted that the small radius is not the only or primary cause of the increased variation for the small radius limit (but it certainly helps as per the cutting line to vdW-LDS analysis described). Rather certain SWCNT classes, most notably the chiral structure SWCNT, only show up in 63 SWCNT data set for these diameters. Thus it is likely that there might be some widening of the asymptotic behavior in the large radius limit when the database can include larger diameter chiral SWCNTs. However this variation will likely be quite small in comparison to the diversity at the very small diameter SWCNT limit.

For example: A close inspection of the large radius asymptotes in Figure 6-24 parts (b) and (c), shows that the 3 classes present (e.g. armchair, zigzag semi, and zigzag metal) exist in very defined layers of strength in both the radial and axial directions. Thus separation between classes for large diameter SWCNTs appears possible. Separation within a given class may be a little bit harder, but variations do exist because these asymptotes are not completely flat. Additionally the affect of total energy is dependent on radius, which opens the door for another possibility (more on this in the next section).

In my opinion, the take home messages from Figure 6-24 are as follows. All the SWCNT appear to fall on class-specific asymptotes for the large diameter limit. They

may in fact eventually meet as the radius goes towards infinity, or they may not as the cutting lines angles in the Brillouin zone still ultimately impact the shape of the 10-30 eV peaks. In the limit of smaller and smaller SWCNTs, the Hamaker coefficients all rise in value along a damped oscillator-like curve. The variation around this average is largest for the chiral class, but it effects all classes more and more as the radius goes to 0.

It should be noted that, thus far, all this trending behavior is for simple isotropic radial-radial and axial-axial interactions across vacuum. Thus these particular effects will not and should not hold in more complex setups. Rather their power and utility comes in helping to understand the dependancies from [n,m] to total vdW-Ld energies in the cleanest and most easily understood situations. It should be noted here that there are a couple experiments, most notable the DEP experiments by Peng[ ], in which separation strictly via SWCNT diameters was shown to occur within the ES semiconductor class. In the system design example given later in this chapter, I'll show how the proper selection of the liquid medium can alter the trending behavior across all radii and theoretically achieve the same results via vdW-Ld interactions only.

Figure 6-24 was simply a benchmark to show the direct effects of vdW-LDS to Hamaker coefficients, which allowed us to remove the geometrical effects of the rod-rod and rod-surface Lifshitz formulations out of the analysis. It also separated the effects arising from the independent radial and axial directions. But those nuances are now dealt with. The full anisotropic rod-rod and rod-surface Lifshitz formulations summarized in Chapter 4 and A will be used from here on out. Figure 6-25 shows a variety of different results at the near limit using the anisotropic rod-rod formulation.

In Figure 6-25 part (a) we see the near-limit aniso rod-rod $\mathcal{A}^{(0)} + \mathcal{A}^{(2)}$ in both a water and vacuum medium. For all but the smallest of SWCNTs, the Hamaker coefficient differences between these two mediums is essentially a factor of 2 across all chiralities. Additionally the variation envelope along the major trend lines is dampened in comparison the pure axial-axial interaction in Figure 6-24. This is due to the coupled nature of the anisotropic Lifshitz equations, which use both the
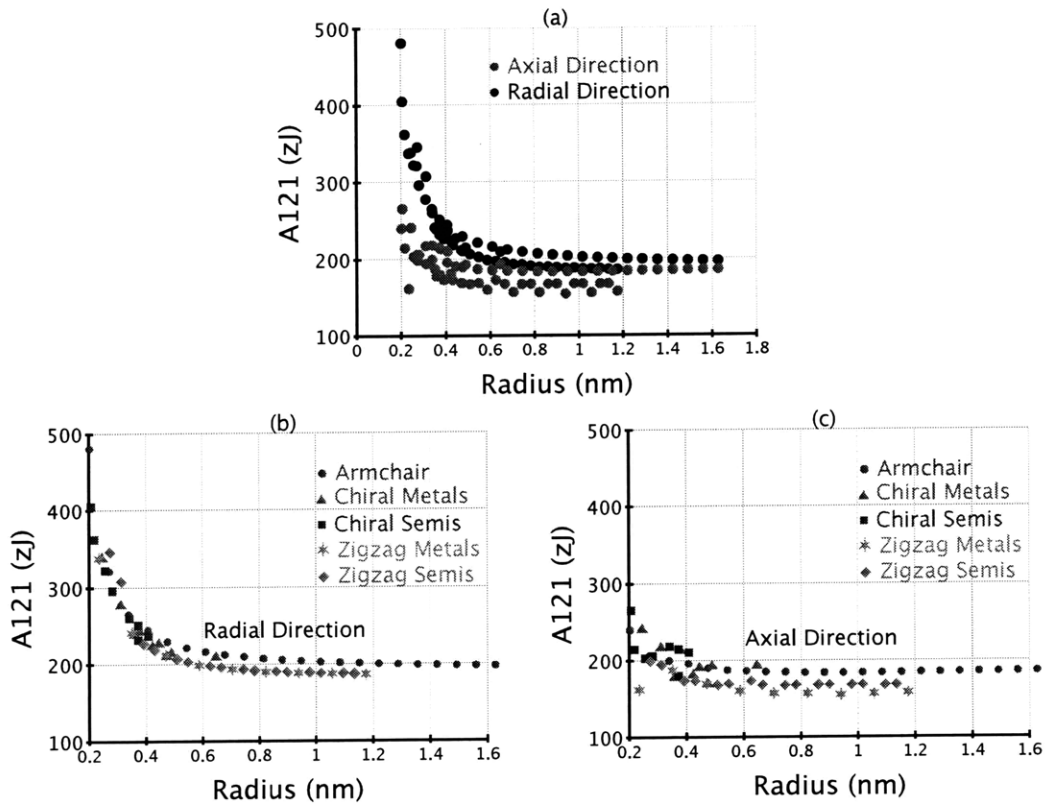
Figure 6-24: A comparison of all the pairwise interaction Hamaker coefficients using the isotropic plane-plane Lifshitz formulation and hollow cylinder vdW-LDS. Results are broken down into a) axial/radial directions as well as the 5 vdW-LDS classes in the b) axial and c) radial directions.

radial and axial vdW-LDS simultaneously within spectral mismatch functions (see Appendix A).

In Figure 6-25 part (b) the Hamaker coefficients for different vdW-Ld classifications are shown for the vacuum medium. Parts (c) and (d) zoom in to the different radius regimes. The larger diameter tubes in part (d) have a clear ranking in Hamaker coefficient strength as a function of vdW class. However, these trend lines begin to cross in the small radii regime in part (c) and there is also some additional noise/variation from the introduction of the chiral classes. Overall the Hamaker coefficient strengths for the SWCNTs in part (c) drops by a factor of 2 when going from the 0.2 nm to 0.5 nm radius SWCNTs. For tubes larger than 0.5 nm, the decay in strength is still continuing all the way through the largest tubes contained in this study. However, the difference in the Hamaker coefficients between the [23,23,m] and [24,24,m] is less 0.1% for this simple setup.

Thus far I've only shown the near-limit because the resulting magnitudes are more closely related to the isotropic plane-plane system. The far-limit formulations introduces unique new terms that are highly sensitive to large spectral mismatches between the vdW-LDS of the SWCNTs and surrounding medium. Figure 6-26 shows a comparison of the near are far-limit Hamaker coefficients for both the armchair metals and the chiral semiconductors in the 0.2 to 0.5nm radius range. Due to the $\Delta_\parallel$ term allowing for contributions well above unity, there is a substantial increase in the magnitudes across all chiralities by roughly 50% when changing from the near to far limit. For comparison sake, the Hamaker coefficients of a gold-water-gold and gold-vacuum-gold materials in the plane-plane geometry are approximately 220 and 360zJ respectively using the optical spectra from the Palik tables[54]. Experimental values of the Hamaker coefficient for gold in water typically range around 220-250zJ[67, 86]. SWCNTs Hamaker coefficients typically exceed the values of gold due to $\Delta_\parallel$ term caused by the rod geometry.

The next item to note is the slight difference shift in the magnitudes as a function of vdW class in the two limits. The chiral semi-conductors tend to be slightly weaker at the near limit and yet stronger at the far limit. This has to do with the first vHs for
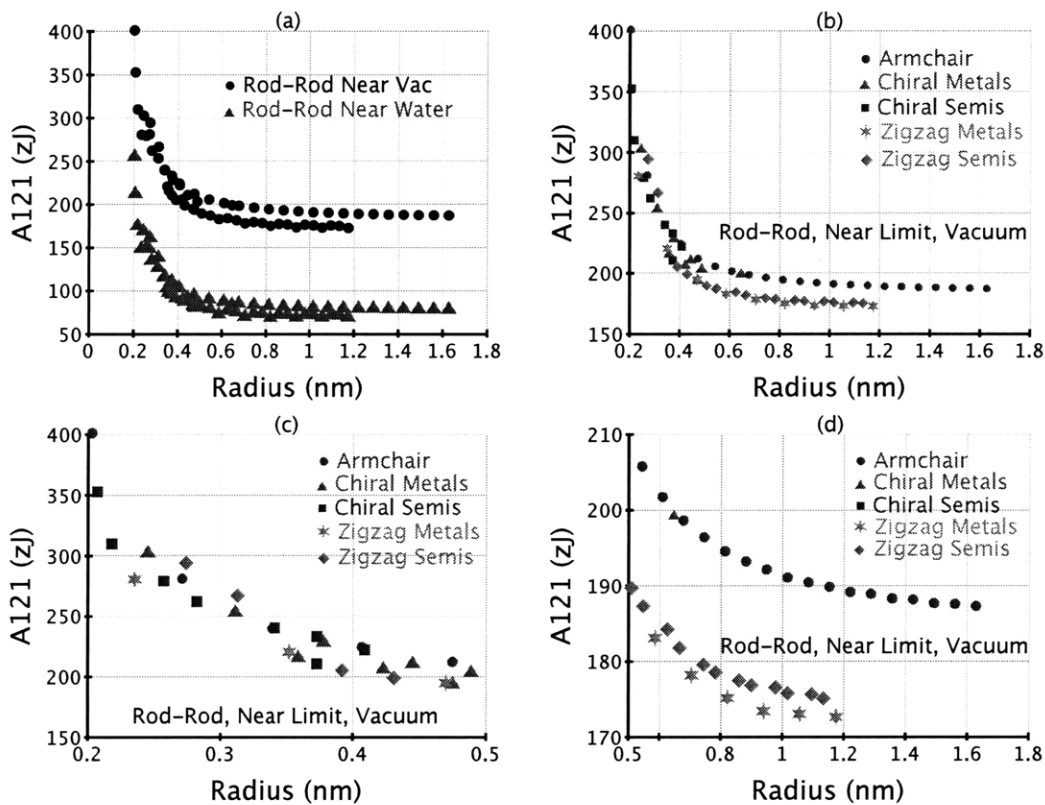
Figure 6-25: A comparison of Hamaker coefficients using the near-limit anisotropic rod-rod formulations and hollow cylinder vdW-LDS. A) Comparing all tubes in the vacuum versus water media. B) Comparing the 5 vdW-Ld classifications using a vacuum medium. C) Zooming in to the 0.2 to 0.5 nm range d) Zooming in to the 1.0 to 1.8 nm range

700

Rod–Rod, Near vs Far, Vacuum

▲ Armchair Near
■ Armchair Far
✳ Chiral Semis Near
◆ Chiral Semis Far

600

A121 (zJ)

500

400

300

200
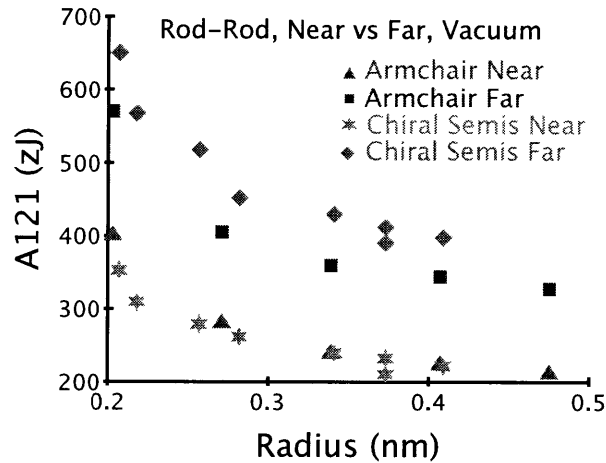
0.2   0.3   0.4   0.5

Radius (nm)

Figure 6-26: A comparison of the Hamaker coefficients at the near and far limits using the anisotropic rod-rod formulations for armchair and chiral-semiconducting SWCNTs. Hollow vdW-LDS were used across a vacuum medium.

the semiconductors being closer to 0 eV in comparison to the ES armchairs[,]. This results in a larger y-intercept in their vdW-LDS (see Figure 6-21), which feeds into $\Delta_\parallel$ more strongly.

I was very careful thus far in selecting vdW classes that did not have the dramatic 0 eV vdW-LDS spike that all chiral metals and the smaller zig-zag metals have. The reason is made clear in Figure 6-27, which compares the armchairs (ES metals and OP semiconductors), the zigzag metals (ES small-gap semiconductors and OT metals and/or semiconductors), and the chiral metals (ES and OT small gap semiconductors). The impact of these wings are the extremely large Hamaker coefficients ranging up in the several 1000's zJs in both vacuum and water mediums. The combination of huge Drude-metal vdW-LDS wings and $\Delta_\parallel$ are the primary cause of this.

To recap, $\Delta_\parallel$ is one of two (presently known) spectral mismatch terms that can actually exceed value of 1 (γ is the other, but it gets dampened via other means). Because of this, it is possible for a single Matsubara frequency to contribute an unrestricted amount to the Hamaker coefficient. The key point is that these extremely large Hamaker coefficients ($¿¿$ 1000 zJ) can only exist when there is a divergent vdW-LDS spike at 0 eV and a formulation that doesn't restrict the impact of this divergent spike among the first 2-3 Matsubara frequencies. By comparison, using the exact same

spectra in the near-limit results in Hamaker coefficients that are weaker in magnitude to the non-divergent armchair vdW-LDS (See Figure 6-27 parts (a) and (c)).

The take home message from the previous two figures is that $\Delta_\parallel$ term within the far-limit formulations will systematically increase magnitudes of each contribution to the summation in the Lifshitz formulation. This effect can result in Hamaker coefficients that are orders of magnitude stronger than the near-limit values for chiralities where the first few Matsubara frequencies have values of $\Delta_\parallel$ well over unity, which happens for all vdW-LDS with a divergent 0 eV wing.

A logical followup question is whether or not such Hamaker coefficient magnitudes are reasonable. After all, if the vdW-LDS became infinite at 0 eV, one could expect an infinitely strong Hamaker coefficient. Of course real SWCNTs will always have a finite ES and OT conductivity because of defects, end-cap effects, finite length effects, and so on. Even the Drude metal oscillator peaks assume an absorption coefficient that limits or dampens the vdW-LDS at 0 eV to finite values. And reasonable compared to what? Most coefficients that have been calculated and published thus far are for dielectric materials with band gaps exceeding 1 eV. It shouldn't be surprising that materials behaving as OT metals exhibit different behaviors.

For the remainder of this analysis, I'll use either the near-limit formulations or eliminate the OT metals in order to be able to compare values on a similar order of magnitude and eliminate the large $\Delta_\parallel$ effects.

The next item to address is the effect of scaling and mixing on the overall Hamaker coefficient because. As noted in Chapter 5, different scaling and spectral mixing is required in creating valid, effective vdW-LDS for the two distance limits. Figure 6-28 plots the resulting Hamaker coefficients for the solid cylinder scaling, hollow cylinder scaling, and the hollow cylinder mixed water vdW-LDS. The key thing to note is that the use of the solid cylinder and hollow mixed w/H2O spectra versus the hollow cylinder spectra noticeably weaken all the Hamaker coefficients, particularly the larger diameter SWCNTs. The vacuum and water spectra are much weaker than that of the SWCNTs, so any mixing as such will weaken the vdW-LDS. Therefore the larger the core, the stronger the dampening. This is what causes of the downward
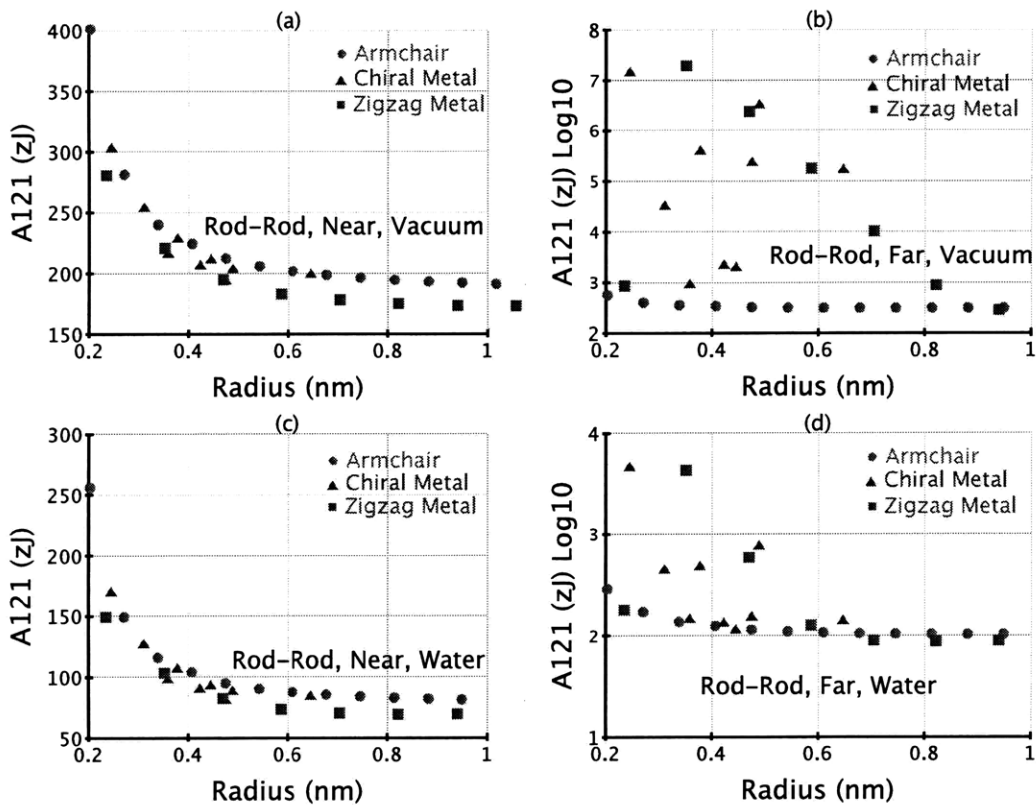
Figure 6-27: A comparison of Hamaker coefficients using the anisotropic rod-rod formulations at the a) near and b) far limits with the hollow cylinder vdW-LDS for all ES metal SWCNTs.
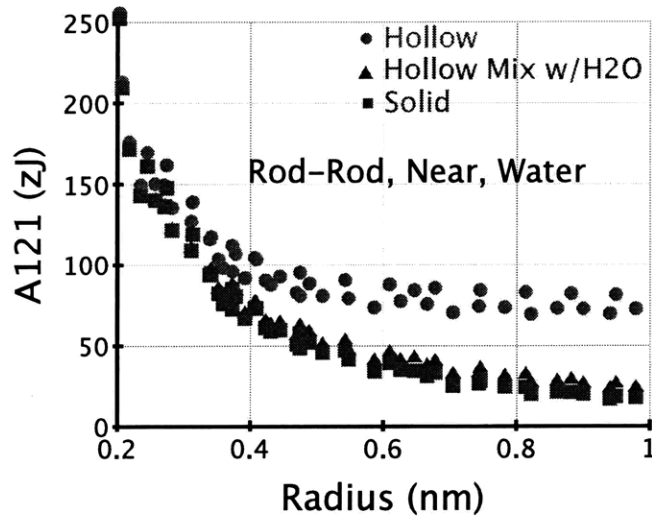
Figure 6-28: A comparison of the solid, hollow, and hollow mixed w/water vdW-LDS scaling effects on the near-limit, anisotropic rod-rod Hamaker coefficients.

trend of the Hamaker coefficients with tube radius.

All studied cases thus far were for fairly simple systems in order to isolate single effects that strictly related to how the different pieces impacted the Hamaker coefficients. Unfortunately these results really don't do any justice in showing the powerful possibilities of what can be done by exploiting the relative differences. This is where system design shines in trying to figure out clever and creative ways to manipulate the interactions for a desired outcome. Figure 6-29 compares the before and after Hamaker coefficients for a system designed for such an exploitation of chirality-dependent interactions. Part (a) contains the armchair metals using the Hollow mixed w/H2O vdW-LD across vacuum with polystyrene in the far limit. This shows the typical relative trending behaviors that we observed many times earlier.

However, in part (b) there is another calculation using a fictitious medium vdW-LDS that is much stronger than water across the board. In fact, this fictitious vdW-LDS is the [14,14,m] SWCNT radial direction mixed w/water. Technically we do not need to use a fictitious medium because there are real material's that are close to what we would need to use to achieve the same result, such as ethanol[ ]. However ethanol isn't good, but not a perfect selection because it only splits the SWCNT
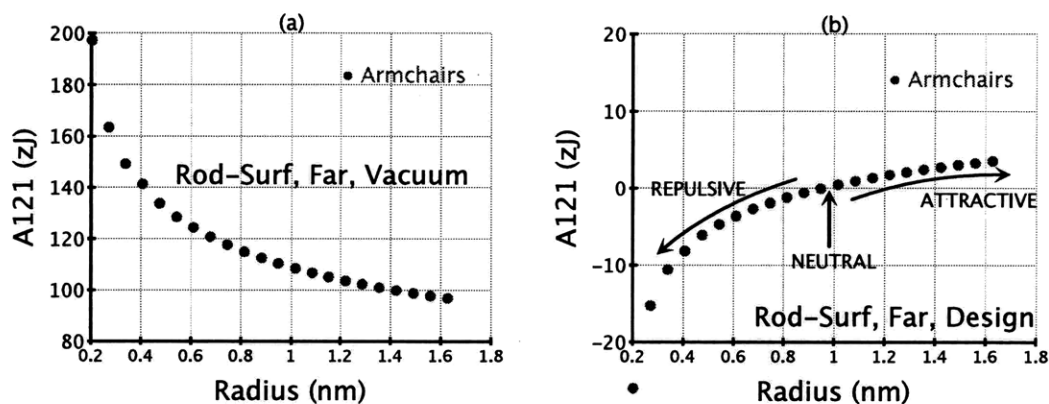
Figure 6-29: A system designed to create attractive/repulsive Hamaker coefficients for experimental separation via vdW-Ld interactions. The calculations used the anisotropic rod-rod formulation at the far-limit Lifshitz formulation with cylinder scaling and spectral mixing of isotropic water for the core material. The intervening mediums used were (a) vacuum and (b) a fictitious liquid medium identical to the [14,14,m] radial mixed w/water vdW-LDS. The substrate material is polystyrene.

spectra in the 0-2 eV range. It's possible there is a better organic solvent candidate that would provide an ideal optical spectra to achieve the same end. The lack of an optical spectra database for liquids makes this a difficult search, hence the need to use a fictitious spectra to demonstrate the point of system design.

Regardless of the issues surrounding the selection of the medium vdW-LDS used, the results of such a medium are far more important due to the introduction of near-zero and negative Hamaker coefficients in part (b) of Figure 6-29. So using this particular substrate (polystyrene) and medium (fictitious medium of [14,14,m] radial mixed w/water), we can selective attract the larger diameter tubes while pushing away the smaller tubes. The implications of this for separations, sorting, placing, enriching, and etc for SWCNTs can be quite enormous. Even more intriguing is the possibility of mimicking the electrostatic screening, salt-bridge effect by the Zheng experiments[18, 19]. But instead, one can use an optical property bridge by interpolating between two high index solvents to systematically shift the vdW-Ld interactions from attraction to repulsion for different SWCNTs. It would be a completely vdW-Ld controlled trap release.

I'd like to conclude this section with a quantitative Hamaker coefficient analysis of a small set of SWCNTs that were the primary motivation for this study. The Zheng experiments[18, 19] were a source of much of the inspiration for searching for chirality specific vdW-Ld interactions. Initially, the experimental results seemed to separate only between the ES metals and semiconductors. But later the technique and analysis was refined such that the experiments could sort between SWCNTs of identical classification and radius (e.g. the [6,5,s] and [9,1,s]). Tables 5.3 and 5.2 from the previous chapter give the raw data numbers for these and other candidate SWC-NTs to show how vdW-LDS can play a role in separation. All the effects described earlier (mixing, scaling, distance limit, classification) also manifest in the resulting coefficients.

With the Hamaker coefficients now calculated, analyzed, and explained, it is now time to address the last and final section-Total vdW-Ld interactions.

6.2.9 Total vdW-Ld vs Radius

Although the total vdW-Ld energy is very important for variety of physical properties, it is not uncommon to stop at the Hamaker coefficient level. There are several reasons for this. In many instances, the system design is for a particular geometry that is invariant with the material selection. This means that a choice of polystyrene versus silica beads does not inhibit one from using beads of any diameter ranging from 1 nm to 1 meter in diameter. Thus the geometry and the vdW-LDS are uncoupled except when down to the molecular level.

In contrast, the geometry and vdW-LDS for SWCNTS are highly coupled through [n,m] and change simultaneously (e.g. one cannot have a [9,3,m] vdW-LDS with a [6,5,s] radius). The only time when one can achieve some level of independence is for large diameter SWCNTs, which tend to have small changes in their Hamaker coefficient despite being able to largely vary the radius. For example, a 1% drop in the Hamaker coefficient between the [18,18,m] and [24,24,m] (near-limit, hollow cylinder spectra in vacuum medium) is small relative to the 33% increase in the radius. For this particular formulation, the vdW-Ld TE varies as $\sqrt{a}$. This means the two large

armchair SWCNTs will have a Hamaker coefficient variation of only 1%, but a TE variation of 13%.

So the Hamaker coefficients can be used as guides, but total energies must also be calculated in order to ensure that the overall trending features behave as expected and/or persist to and through this final level. Much like the Hamaker coefficient analysis, this analysis can be quite verbose if left unconstrained. Therefore I'm only going to focus on 4 cases (representing all possible combination of rod-rod and rod-surf geometries at near and far separation limits) in order to illustrate the overarching effects without getting lost in a sea of data. This analysis will also use armchair SWCNTs to keep the trends as smooth as possible, and not introduce other effects. In a sense, this will isolate the effect of the vdW-Ld TE scaling.

Figure 6-30 compares the Hamaker coefficients by themselves versus the Hamaker coefficient multiplied by the radius-dependent part of the TE equation in the rod-rod near-limit. What results is two competing effects. The Hamaker coefficients themselves drop as a function of radius and reach an asymptotic behavior around 0.8 nm radius and beyond. But recall that the Hamaker coefficient, in a loose sense, can be thought of a vdW-Ld TE density term. The geometrical portion of the vdW-Ld TE equation determines the rest and, for a given S2SS, should rise with increasing volume. Therefore it's not surprising to see the radial-dependent portion take over for the radius regime in which the Hamaker coefficient portion is relatively invariant and vice-versa. This results in the bowl shaped curve as a function of armchair radius, with the smallest and largest tubes having the largest vdW-Ld TE.

These effects are much different in the far-limit. Recall that mixing is a critical need in this limit to create an effective vdW-LDS with the core material properties. The far-limit also have a much different SS2S scaling behavior as well as a much larger a^4 dependance upon the radius sizes of the interacting SWCNTs. Figure 6-31 shows the results. Although the very small SWCNTs have large Hamaker coefficients, the larger tubes are clearly stronger from a TE perspective because they have a tremendous amount of cross sectional area comparatively speaking. So while the per volume interaction strength of the larger tubes can be a 50-75% weaker, the cross
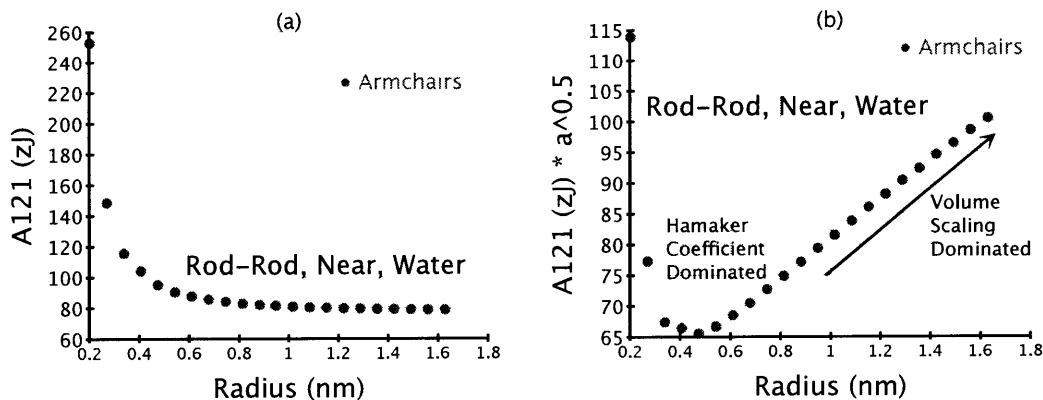
Figure 6-30: A comparison between the (a) Hamaker coefficients versus (b) the Hamaker coefficients multiplied by the radius dependent part of the TE equation at the near-limit. The Hamaker coefficients were calculated using the anisotropic rod-rod near-limit formulation with hollow armchair vdW-LDS

sectional area can be two orders of magnitude greater. That is why part (b) of Figure 6-31 is essentially radially-dependent only (at least for the armchairs only, lacking the 1000+ zJ Hamaker coefficients of the divergent OT metals).

The take home message thus far is that the trends depend heavily on the radius-depdent part of the vdW-Ld TE at the far-limit and for large diameter SWCNTs. The opposite is true for the near-limit and small diameter tubes, where variation in the Hamaker coefficient appears to dominant the relative differences in the vdW-Ld TE. For other possible combinations (small tubes at the far limit), the calculations should be done explicitly because the balance between the effects can be more subtle.

Next to address is the effects of the radius-dependance at a given SS2S on the rod-surf geometry. To make things interesting, I am going to use the design medium calculations from the previous section (see Figure 6-29). In this example, the fictitious medium (i.e. equal to the hollow-cylinder mixed w/water [14,14,m] radial direction vdW-LDS) was selected such that their were SWCNTs having positive, negative, and near-zero valued Hamaker coefficients. The reason for including this system design data is to demonstrate cases in which the Hamaker coefficient information (attractive, repulsive, or neutral) can still be the dominating factor for well designed systems.

Figure 6-32 shows the comparison of Hamaker coefficient of the rod-surf design
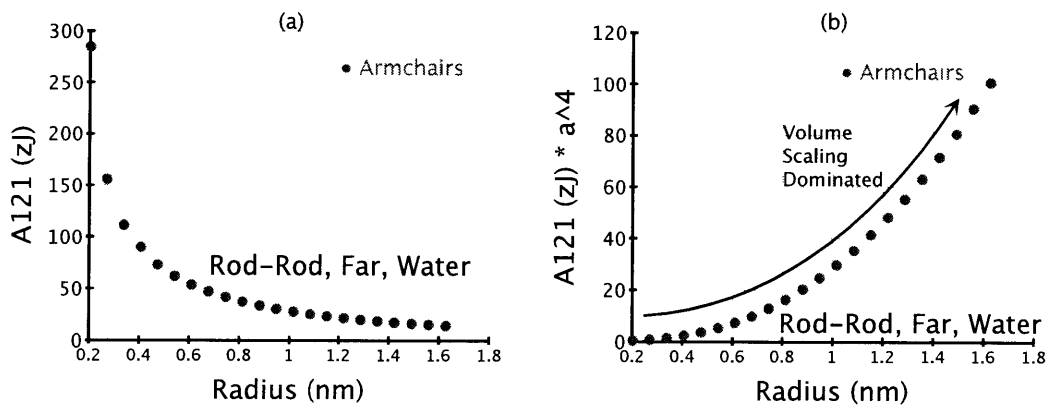
Figure 6-31: A comparison between the (a) Hamaker coefficients versus (b) the Hamaker coefficients multiplied by the radius dependent part of the TE equation at the far-limit. The Hamaker coefficients were calculated using the anisotropic rod-rod far-limit formulation with hollow mix w/water armchair vdW-LDS

system before and after being multiplied by the radial-dependent part of vdW-Ld TE equation. The obvious effect is that the magnitudes of the Hamaker coefficient for the smaller tubes are dampened relative to the larger diameter SWCNTs. However the more subtle point is as follows. Regardless of how little or how big the SWCNTs diameters are for a given chirality, chiralities with positive Hamaker coefficient will remain attractive and negative Hamaker coefficients will be repulsive. The volume scaling of the vdW-Ld TE is irrelevant in this attractive/repulsive nature. In the rod-rod comparison (Figure 6-30), one could only potentially enrich or separate tubes via a gradation as a function of relative strength. However, for the designed system of Figure 6-32, one could conceivable separate SWCNTs above and below a dividing radius. This type of separation will likely be easier because its a stick vs no-stick mechanism instead of a trap and graded release mechanism.

When moving to the rod-surf far-limit, the radial-dependent component charges from $\sqrt{a}$ to a^2. However, the SWCNTs still are either attractive or repulsive. Figure 6-33 shows this effect and the new trending shape that result. As an added bonus, the systematic difference in the Hamaker coefficients for the large diameter tubes could also allow for a grading separation as well.

And these effects were created using the simplest of systems. There are many

Figure 6-32: A comparison between the (a) Hamaker coefficients versus (b) the Hamaker coefficients multiplied by the radius dependent part of the vdW-Ld TE equation at the near-limit for the design systems. The Hamaker coefficients were calculated using the anisotropic rod-surf near-limit formulation with hollow armchair vdW-LDS, the fictitious hollow [14,14,m] radial mixed/water medium, and a polystyrene substrate.

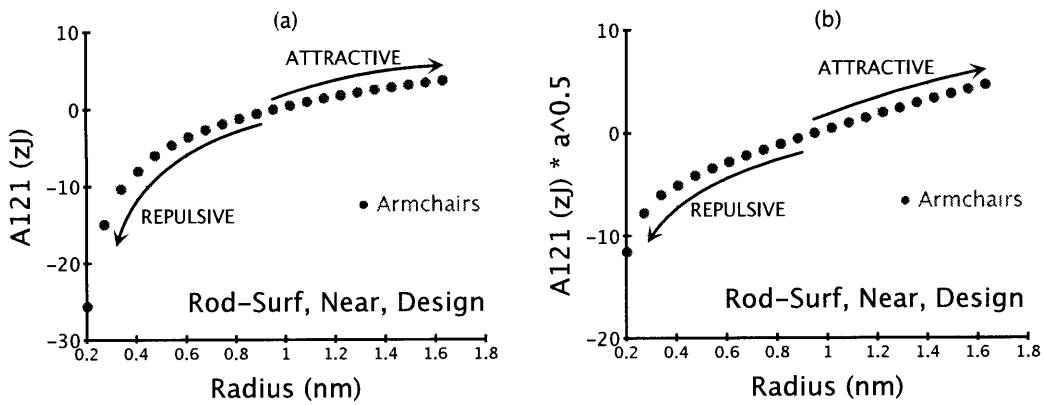Figure 6-33: A comparison between the (a) Hamaker coefficients versus (b) the Hamaker coefficients multiplied by the radius dependent part of the TE equation at the far-limit for the design systems. The Hamaker coefficients were calculated using the anisotropic rod-surf far-limit formulation with hollow armchair vdW-LDS, the fictitious hollow [14,14,m] radial mixed/water medium, and a polystyrene substrate.
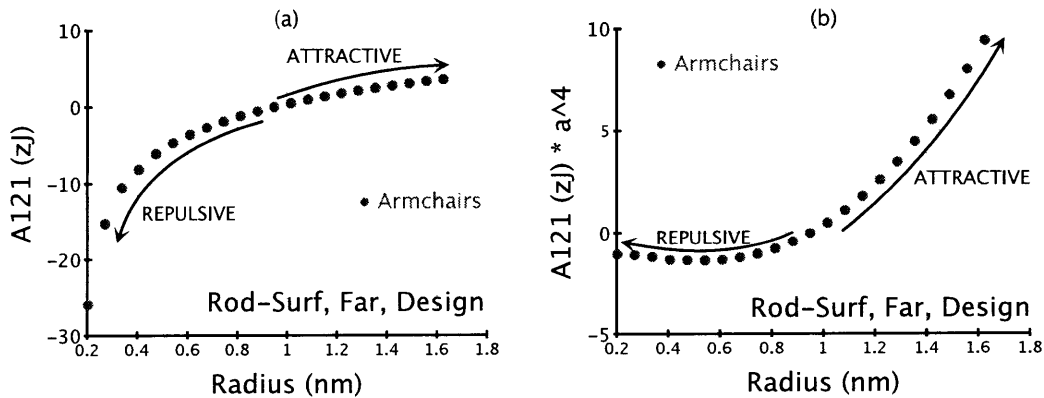
other variations one can play to create exploitable chirality-dependent differences in the vdW-Ld TE (e.g. surfactants on the SWCNT, on the substrate, MWCNTs, etc). The greater the variation in the vdW-LDS, the more likely the variation in Hamaker coefficients in a particular distance regime against a particular target substrate. However, going beyond this is left up to the reader at this point because one can play and design and endless array of experiments. The basic interdependencies from [n,m] to vdW-Ld TE should be well understood by this stage, at least from a qualitative level. There is just one more topic to address before concluding, and that is the development of a proper naming and classification system.

6.3   Discussion Classifications Breakdowns

Having completed the analysis portion from [n,m] to vdW-Ld TE, I'd like to quickly revisit my claim that the previous classification systems do a wonderful job in describing ES properties, but they are insufficient for OP relevant to the vdW-Ld stages of ϵ'' and beyond.

The standard classification clearly misses out by treating all ES metal and small-gap semiconductors the same. But armchair SWCNTs behave very different from chiral and zig-zag metals. None of the armchair metals have the OP Drude metal peak in the axial direction and appear optically like semiconductors. The importance of Drude metal peaks on the total and directionally dependent vdW-Ld energies is huge. Therefore it is a clear disservice to explain vdW-Ld interactions using this particular classification.

The Lambin classification system adds a critical improvement by differentiating metals into true ES metals (conduction and valence bands touch at the fermi energy) versus tubes that have a very small band gap of less than 0.1 eV. This is important because the difference between having or lacking this low energy wing split the armchairs SWCNTs from the other metals. However, the difference in the ES and OP correlations is exactly opposite along this divide. The small-gap semiconductors (zig-zag and chiral metals) behave like OP metals while the ES metals have virtually

no ϵ'' behavior at 0 eV and behave like OP semiconductors. So the particular division or categorization of armchairs versus the chiral and zigzag metals is an improvement, but the expected correlation is flipped.

The Dresselhaus classification system is quite intriguing because it differentiates strictly on the basis of symmetry considerations. There is even a suggestion that these difference may manifest as differences in physical properties, which I wholeheartedly agree! Unfortunately the differentiation is incompatible with the Lambin system and it also allows the armchair SWCNTs to be grouped in with certain chiral SWCNTs. From a vdW-LDS perspective, there are clear differences at all abstraction levels between the armchairs and chiral metals. Therefore this classification is worse than the Lambin system with respect to vdW-Ld interactions. It is also difficult to see if there is any inherent advantage and/or correlations between the new semiconductor groupings in this classification because the OP trends depend more on geometrical structure. And a close look at the Dresselhaus system shows that all but one of the 5 classes (Metal 2m) span 2 of the 3 available structure types (armchair, zigzag, and chiral).

Ultimately I prefer to the 5-classification, vdW system for 1 primary reasons— the root cause by which the differentiation is made in this systme. The standard and Lambin systems categorize using band gap results with very little need for the cutting lines otherwise, except maybe for the characterization of the low energy vHs. The Dresselhaus system improves on this by showing that the cutting lines angles and positions can be refined further, even between different semiconducting tubes. However the manner in which this differentiation was done was still based solely on symmetry considerations that hasn't (yet) manifested in observable or notable OP differences for vdW-Ld interactions.

Because the vdW-LDS and other properties depends on the total electronic struc- ture, a classification system to describe them should focus on more than just the band gap and the first few vHS. After all, the cutting lines affect every single transi- tion down from the Fermi level to energies 30 eV and above. So it is not just about whether or not the cutting lines cross, graze, or miss the K-points. The angle and

density of these lines in the Brillouin zone makes a huge difference over the entire energy range. This was demonstrated by the ϵ'' features in Figure 6-9, which converged as a function of cutting line angle and were irrelevant to ES properties. Therefore it seems logical to included the ES properties (ES metal, small-gap semiconductor, and semiconductor) and structure (armchair, zig-zag, and chiral) in every available combination to describe the overall vdW-Ld behaviors.

This is not to say the vdW system is not without its flaws. Some of the classes may ultimately be redundant to the Lambin system. At this juncture I can only speculate that it will not based how the features depend on the combination of cutting lines angles (structure) and ES properties. However, what I cannot speculate on is whether or not those differences around ϵ'' will justify the all 5 classes at the Hamaker coefficient and vdW-Ld TE levels. More vdW-LDS for larger chiral metals and semiconductors will be needed to confirm/deny those speculations. The vdw system is also unable to explain and/or predict the loss the Drude metal peak for large diameter zig-zags. It may turn out that large diameter chiral metals lose this feature as well (but computational limits currently prevent such a determination). But to be fair, none of the classification predict the correlation of the Drude metal peak as a function of radius for ES metal SWCNTs.

There are also other considerations that may require revisiting this system. The effects of structural relaxation[87], phonons[88], bending moments[8], functionalization[81], and interlaying coupling[28] may in fact cause armchair tubes to lose some of its symmetry and regain a low energy spike. Or a high transverse electric field may in fact cause the band gaps to open up[88, 89, 90, 91]. These effects are well beyond the scope of this thesis, but should be kept in mind when pushing forward even more to see if some differentiations are redundant or if new sub-classes need to be formed. But even if these changes around the 0-5eV arise, the difference from 10-20 eV should still maintain and justify the 5 classes in the vdW classification system.

6.4 Datamining Conclusions and Further Considerations

It's one thing to logically know of the trends one should expect when changing from [n,m] to vdW-Ld, but there is a lot of learning and insights to gained when having the spectra data to actually demonstrate and track these effects through each level. This analysis contained within this chapter is exactly that and represents the culmination of the infrastructure built and introduced in the previous chapters (ab initio optical properties, Lifshitz formulations, and mixing formulations). The following is demonstrated in this chapter.

- The diversity of the material and interaction properties at all levels can be quite dramatic even with very small changes in [n,m] (the root source).

- Band gaps can be non-existent (metal), very small (small-gap semiconductor), or large (semiconductor) as a result.

- The ϵ'' spectra can have Drude metal peaks that depend on the structure (armchair, zig-zag, and chiral) of the ES metal as well as whether or not its above or below the a critical cutoff radius.

- Systems can be designed to exploit Hamaker coefficients between tubes of identical diameter.

But despite this large diversity in results and effect, there are clear trends at every stage. Some are already well known and have been characterized for over a decade (such as the vHs trends with radius) and others were not so obvious (decay of Hamaker coefficients as a function of increasing radius). But whether it is how the Hamaker coefficients and vdW-Ld TE vary with radius or how the low energy wings for zig-zag metals changes as a function of radius, all of these trends gives us general insights that can aid in experimental design and prediction before having to do the nitty gritty calculations.

A new classification system was introduced and compared to those previously used for ES properties. Also introduced was a system design example, which demonstrated how picking the correct medium can selective attract and repel a SWCNT off of a polystyrene substrate. The implications of this and other possible designs is quite profound in that it could allow for targeted trapping of some chiralities and not others.

And this is clearly the beginning. When the surfactant properties, MWCNT properties, substrate surface layers, and many other effects and included, the power of these techniques will greatly increase for the SWCNT community. Many of the concepts and frameworks included within this study can also be applied to other biological molecules and systems in an attempt to create nanodevices, solution sort various molecules, and so forth. Now its only a matter of plugging and chugging for one's particular system of interest to make such a determination for the vdW-Ld component of the interaction.

Calculating a van der Waals - London
Dispersion Energy via Lifshitz Formulation

Methods for Obtaining Necessary Full Spectrum Properties

VUV Reflection and Transmission

EELS

Ab Initio Electronic Structure

Intrinsic SWCNT Material Property Dependancies

chirality n,m → Wrapping → x,y,z and cutting lines → OLCAO Method → band structure → Electron Transitions → e" spectra

KK Transformation + Void Volume Scaling (if necessary)

Mathematics and Electrodynamic Formulations

Scaled vdW-Ld Spectra → Optical mixing → Effective vdW-Ld Spectra → Plug and Chug → Hamaker Coefficient 'A'

Material Connectivity

Target System Geometry → Electrodynamic Boundary Conditions → Lifshitz Formulation

Vol-Vol Geometrical Scale Factor

Analytical Vol-Vol Term (Equivalent to Numerical 1/r^6 Integration)

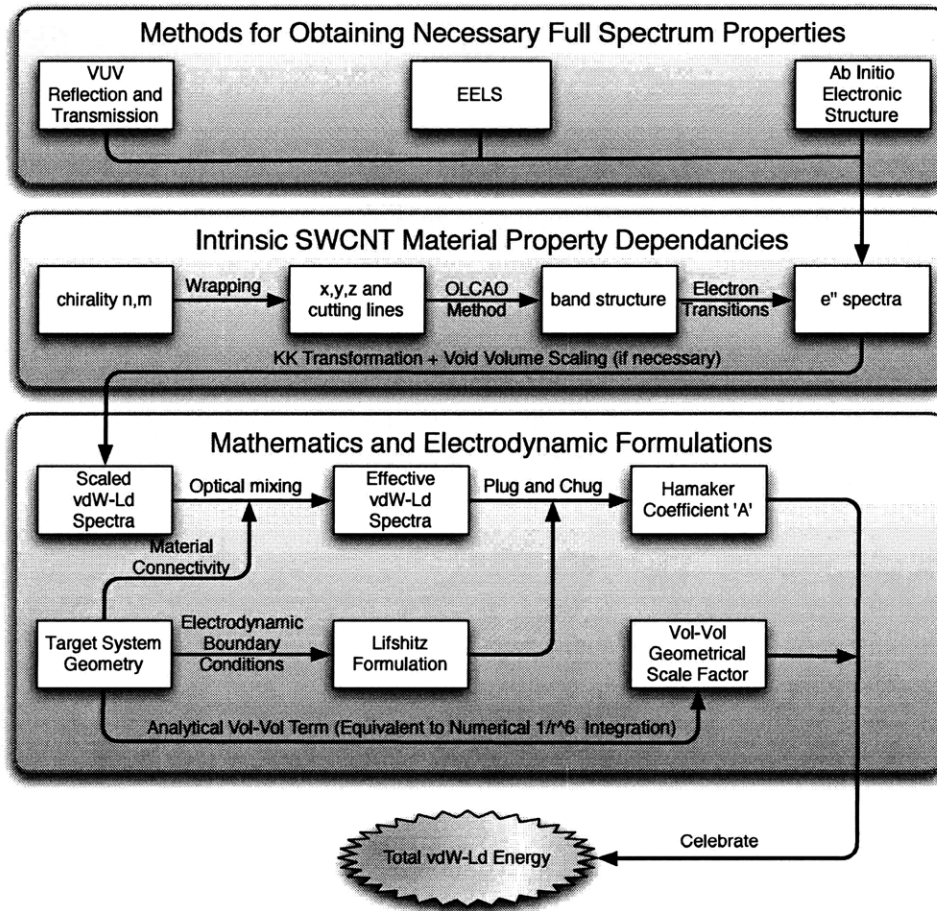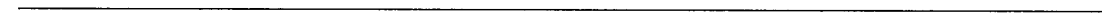Total vdW-Ld Energy ← Celebrate

Figure 6-34: The concluding flow chart of the Lifshitz formulation/framework with all the necessary stages implemented for continued chirality-dependent vdW-Ld analysis of SWCNT systems.

Chapter 7

Conclusions and Future Work

I would like to conclude this work in 4 parts:

- Enumerate what was accomplished in this thesis for the SWCNT community.

- Describe the broader impacts of these accomplishments for other fields of study.

- Propose future work and next actions for those who with to go further with vdW-Ld interactions for SWCNTs.

- Describe the greater needs and opportunities for studying vdW-Ld interactions in the next decade.

7.1 Completed Objectives

The overarching goal of this thesis was to be able to determine the chirality-dependent vdW-Ld interactions for SWCNT systems. This would ultimately require a rigorous understanding of the source of these interactions as a function of SWCNT chirality [n,m], how these effects trend with different SWCNT classifications, and how the interactions could be exploited for solution separation experiments. However, some of the key components necessary for a first-principles Lifshitz calculation were missing at the onset of this work. Therefore, these critical extensions to the Lifshitz framework and infrastructure needed to be developed first, which can be summarized as follows:

- Obtaining the direction-dependent optical properties for a large and diverse set of SWCNTs representing all the possible classifications over a wide diameter range.

- Deriving Lifshitz formulations specifically designed for optically anisotropic rod-rod and rod-surface geometries.

- A proper mixing formulation to create effective optical properties to take into account surfactants, multiple SWCNT shells, the inner core material, and etc.

The first barrier was eliminated by using an ab initio OLCAO method to obtain ϵ'' out to 45 eV using a basis set up to the 4s orbitals. The benefits of such a method were tremendous because the only limitation is computer memory and processing power. Therefore, it was straightforward to obtain the spectra properties for even very large diameter tubes. This step alone would have required an extraordinary effort if done experimentally. Additionally, the resulting experimental data would have likely been insufficient both in terms of the energy range and direction dependancies for each chirality, as well as the quantity of SWCNTs available. The ab initio method, in contrast, allowed for a quantitive understanding of the optical anisotropy between the radial and axial directions as well as between the different chiralities.

Spectra data alone, however, is insufficient in even a qualitative analysis of vdW-Ld interactions. The particular Lifshitz formulations selected can and will alter the degree by which the vdW-LDS inputs contribute to the overall Hamaker coefficient by changing the optical contrast weighting of the nonlinear spectral mismatch functions contained within the summation. The newly derived anisotropic rod-rod and rod-surface formulations changed that. Now the radial and axial vdW-LDS were properly included and coupled for both the near and far limits. Components of the new spectral mismatch term, most notably the $\Delta_\parallel$ term at the far-limit for rods, had a tremendous impact on both the total Hamaker coefficient as well as introducing very strong orientation-dependent components. These quantitive calculations also allowed for the first comparison and prediction of vdW-Ld interaction strength between

different chiralities. The [6,5,s] and [9,3,] coefficients alone could vary by as much as 30% in strength (see Table 5.3).

And the final infrastructure component was the implementation of a spectral mixing formulation to create effective vdW-LDS for multi-component SWCNTs. Unlike Hamaker coefficients of large substrate slabs or colloidal beads, SWCNTs have optical properties that vary spatially and sometimes abruptly at that. Mixing was therefore needed in the far-limit to account for the competing interactions among the SWCNT shell, core, and surfactant, which can have interaction strengths that vary significantly in sign and/or magnitude.

Many different mixing models were available from the literature to describe systems of varying connectivity. Ultimately, the usage of a parallel capacitor in the axial direction and the Bruggeman EMA formulations for the radial direction made the most logical sense based on the different material connectivity in the respective directions. Mixing is not required at contact distance because this domain is dominated by the outermost material and can even be solved as a pseudo plane-plane interaction via the Derjaguin approximation. But mixing is essential at the far-limit because it allows for an accurate Hamaker coefficient and vdW-Ld TE determination, which would otherwise be impossible due to a lack of an explicit, analytical add-a-layer solution for this geometry.

Once this infrastructure was in place, a rigorous analysis of all the dependancies from [n,m] was now feasible in order to search for and elucidate features, trends, breakdowns from trends, etc. Many things were discovered. The most useful discovery, in my honest opinion, was how many of the properties could be well grouped and sectioned off into the 5 different vdW SWCNT classifications at all the layers of abstraction (i.e. [n,m] to vdW-Ld TE).

Some of these results were also quite surprising. There were cases when a material would have ES properties that were clearly metallic, but they behaved optically like a semiconductor (armchairs and large diameter zigzag metals). The impact of this paradox on vdW-Ld TE and vdW-Ld torques can be quite staggering, particularly in the far-limit when the Hamaker coefficients can go to over 1000+ zJ because of a

divergent vdW-LDS wing at 0 eV. This and many other effects could also be used in creating experiments that would attract one chirality or set of chiralities and not the others, providing another mechanism for SWCNT enrichment/separation.

7.2 Broader Impacts

Although the focus of this thesis is vdW-Ld interactions for SWCNTs systems, the major infrastructure additions can and likely will be used to expand this study to other classifications of materials. For example, most experimental methods of calculating the required ϵ'' properties for materials are bulk averaged over large, dry samples. Biological molecules (e.g. DNA, proteins, collagen) typically are too small to measure with these devices and they also have significant structural changes in the dry versus wet states[ ]. These molecules also vary spatially depending on the base pairs or side groups present. The ability to resolve these features is critical at S2SS near contact, which is where a majority of the interest in chemistry and biology resides.

The solid cylinder Lifshitz formulations can also be locally applied in segments for other rod-like entities, such as collagens, liquid crystals, and etc. The spatially and direction dependent properties received from the ab initio codes could then be used to find which pairs of base pairs, side chains, and so forth are the most favorable for an attractive/repulsive vdW-Ld interaction.

Mixing would clearly be useful for these biological materials when moving from the far-limit (mixed) to the near limit where the individual base pairs and R-group interactions are more important. Mixing could also be employed in varying levels at different S2SS limits, moving from the continuum far-limit to the atomistic-like near-limit.

Predictions and experimental design via datamining could also be used, but in a different way than I have currently outlined for SWCNTs. SWCNTs can have drastic changes in vdW-Ld as a result of small differences in [n,m]. However this analysis was limited in other arenas, such as the effects of various mediums, various coatings, various shapes, etc. The inability to search different materials is a particularly

troublesome barrier, which is simply caused by a lack of vdW-LDS information. But being able to explore through these other parameters spaces will undoubtedly aid in predicting which particular target and medium will achieve the desired effect. Of course these parameters could also be applied on top of the SWCNT analysis if/when they become available.

7.3 Future Work for SWCNTs

Although I am quite pleased with the integration of this work in a coherent top to bottom study of vdW-LDS interactions for SWCNT systems, there is always a perpetual wishlist of what would've, could've, and should've been done given infinite time, resources, and intelligence. The first on that list is the desire to add retardation effects in the current anisotropic rod-rod and rod-surf formulations. Retardation effects are critical for particular systems that have separation-dependent Hamaker coefficient that switch sign. Perhaps the most famous and notable of which is the equilibrium thickness of water on ice[ ]. In fact, anytime vdW-LDS cross in a multi-component system there is the possibility of a shift in balance between attractive and repulsive terms in the Lifshitz summation as a function of S2SS. The primary reason this effect is neglected in the anisotropic rod-rod and rod-surf equations has to do with the difficulty of tracking the speed of light through anisotropic media and layers. Thus not even the plane-plane add-a-layer formulation contains retardation effects. However, if/when such a an implementation is possible it should easily transfer over to the SWCNT formulations to create a more generalized version.

Regardless of whether optical anisotropy is included, the ability to have an analytical add-a-layer formulation for cylindrical systems that is valid at all S2SS would be a tremendously powerful addition. The mixing formulations would no longer be required at the far-limit. Also, there would be no need to interpolate between the near and far limits as the Hamaker coefficient solution would be exact at all separations. I have actually had some reasonable success in doing this via a method I call the "prism mesh" method (see Appendix B). What this method does is essentially

discretizes any arbitrarily shaped object over a flat surface into an array of parallel plane add-a-layer solutions. Each piece is then summed up and an effective total Hamaker coefficient can be backed out. This method has proven to be quite powerful, but it not first principles and is beyond the scope of this thesis. It also requires that at least one of the objects is a semi-infinite half space. So what it gains in power, it loses in being universally applicable to all geometries. Still, the insights gained in these rod-surf determinations can likely be transfered over to other shapes, etc.

More vdW-LDS from the chiral SWCNTS classes would also be helpful to determine whether their trends also have asymptotic limits at large diameters, or if they continue to exhibit more personality than the other classifications. There are also many other smaller diameter SWCNTs that can be filled out to complete the entire set (i.e. the [7,2,s], the [7,3,s], the [7,6,s], etc). Additionally there are also the effects non-linear coupling that need to be addressed when surfactants and the liquid medium alters the quantity and shape of the ϵ'' spectra of the original, bare SWCNT.

Thus far, these are the vdW-Ld wishlist items specifically for the SWCNT community. There are also items that are desirable for the vdW-Ld community as a whole, which I'll delineate next.

7.4 Greater Needs

The greatest need (in my opinion) for the vdW-Ld field as a whole is the availability of a large spectra database. The original Lifshitz formulation has been in existence for over 54 years[13], and yet the calculations are limited to the liquid mediums of air, vacuum, water[30, 67, 68, 69, 70], and 2-3 organic solvents available[30, 33, 83]. And the water vdW-LDS is still being tweaked and updated every couple of years as more data becomes available and/or they are altered to fulfill the requirements of the f-sum rule. The situation for solid materials is equally bleak. Yes the Palik tables[54] do in fact have spectra for over 60 materials, but that pales in comparison to the quantity of materials available in any crystallographic database. And worse yet, the vdW-LDS for biological materials and building blocks are simply non-existent. This puts

a tremendous damper on system design and usually results in the parameterization of pairwise interactions or guessing of Hamaker coefficient for these systems.

On the other side, the need for a formulation that could handle two arbitrarily shaped objects with spatially varying optical properties would be the Holy grail of any and all Lifshitz analysis. Combined with the large database of spatially resolved vdW-LDS mentioned above, one could in theory solve the vdW-Ld interactions for any shapes, at any distance, for any material. That would be quite powerful, but it appears unlikely that this will be reality in the short term despite progress being made on that front. Podgornik[73] et al have created a version that can handle two arbitrary shapes numerically. But it is presently confined to systems that are isotropic and at the near-limit only. Other collaborators have also tried to obtain the vdW-Ld interactions for arbitrary spatial properties by solving for energy minimization of the Maxwell stress tensor. However, they had a very difficult time getting the answers to converge, and the research was ultimately put on pause.

There also exists tremendous opportunity in bridging the gap between the continuum Lifshitz models and the atomistic methods (both classical and quantum mechanical). The Lifshitz approach has a much stronger theoretical foundation, but cannot be bootstrapped as a multi-body interaction for atomistic calculations, which are either determined at ground state (i.e. no EM fluctuations) or using pairwise additive potentials[34, 30]. Therefore much is being done in the atomistic regime to try and design the best and most accurate parameters and functionals, but there is always a tremendous amount of tweaking involved. For example, how would a single carbon-carbon functional alone give us the diversity in vdW-Ld TEs found in this thesis unless they were embedded with different parameters for each chirality configuration? And if so, how would those functionals be determined a priori or on the fly during a simulation? If one could resolve whether those sp2 carbon bonds were a [9,0,m] metal versus a [8,0,s] or [10,0,s] semiconductor, how would the simulation handle momentary fluctuations that might make it appear briefly as a [9,1,s]?

So there is a gap between these two communities (continuum versus atomistic) where a tremendous amount of learning could take place and borrow from each other's

strengths to make up for each other's weaknesses.

The last need (again, in my honest opinion) is more sociological and marketing based rather than scientific. There are certain attitudes, beliefs, and fears with respect to vdW-Ld interactions. Sometimes vdW-Ld interactions are seen as the unimportant 10 pound monkey versus the 800 pound gorilla known as electrostatic forces. In these circumstances, it seems customary to just ignore the vdW-Ld interactions altogether despite the fact that they still influence the system. There is also a pervasive belief that vdW-Ld forces are very vanilla (i.e. all attractive and don't vary much between different systems) and that simple Lennard-Jones potentials will work. However the equilibrium water on ice problem would still be regulated to "pressure" explanations, which don't hold up when scrutinized to even back of the envelope calculations. Ignoring the optical property and vdW-LDS variations would also result in predictions that all SWCNTs behave equally, which is simply not true, even in systems that have no predominating electrostatic contribution[20].

This and many more issues were expanded upon further in an upcoming publication entitled *Long Range Interactions.*[3] To be fair, although vdW-Ld interactions are often mislabeled or misapplied, they are still well known. Acid-Base reactions, by comparison, are an entire class of interactions that have also proven very powerful in explaining many phenomenon, and yet they are by far the least known and used. Perhaps its due to lack of predictive qualities or the ability to easily include into DFT or atomistic calculations. However if the interaction is and has proven to be important, then it should be studied and addressed appropriately. I feel the same is true for all the needs I've outlined for the vdW-Ld community, and hope that I've at least inspired others to join in exploring these exciting scientific opportunities.

Bibliography

[1] X. Y. Kong and Z. L. Wang. Nano Lett. 3, 1625 (2003).

[2] C. A. Bessel, K. Laubernds, N. M. Rodriguez, and R. T. K. Baker. J. Phys. Chem. B. 105, 1115 (2001).

[3] J. P. Kim, B. Y. Lee, S. Hong, and S. J. Sim. Anal. Biochem. 381, 193 (2008)

[4] A. Srivastava, O. N. Srivastava, S. Talapatra, R. Vajtai, and P. M. Ajayan2. Nature Mat. 3, 610 (2004)

[5] Y. Hayamizu, T. Yamada, K. Mizuno, R. C. Davis, D. N. Futaba, M. Yumura, and K. Hata. Nature Nanotech. 3, 289 (2008)

[6] J. Kong and H. Dai. J. Phys. Chem. B 105, 2890 (2001).

[7] C. Wei, K. Cho, and D. Srivastava. Phys. Rev. B 67, 115407 (2003)

[8] J. Bernholc, D. Brenner, M. B. Nardelli, V. Meunier, and C. Roland. Annu. Rev. Mater. Res. 32, 347 (2002)

[9] N. M. Pugno. Acta Materialia 55, 5269 (2007).

[10] V. N. Popov, Mat. Sci. and Eng. R 43, 61 (2004).

[11] C. T. White, J. W. Mintmire, J. Phys. Chem. B 109, 52, (2005).

[12] I. Cabria, J. W. Mintmire, C. T. White, Phys. Rev. B 67, 121406, (2003).

[13] P. Lambin, C. R. Physique 4, 1009 (2003).

[14] D. E. Resasco, W. E. Alvarez, F. Pompeo, L. Balzano, J.E. Herrera, B. Kitiyanan, and A. Borgna. J. Nanoparticle Research 4, 131 (2002)

[15] P. Nikolaev, M. J. Bronikowski, R. K. Bradley, F. Rohmund, D. T. Colbert, K. A. Smith, and R. E. Smalley. Chem. Phys. Lett. 313, 91 (1999)

[16] A. G. Rinzler, J. Liu, H. Dai, P. Nikolaev, C. B. Huffman, F. J. Rodriguez-Macias, P. J. Boul, A. H. Lu, D. Heymann, D. T. Colbert, R. S. Lee, J. E. Fisher, A. M. Rao, P. C. Eklund, and R. E. Smalley. Appl. Phys. A 67, 29 (1998).

[17] C. Journet, W. K. Maser, P. Bernier, A. Loiseau, M. L. De La Chapelle, S. Lefrant, P. Deniart, R. Lee, and J. E. Fisher. Nature 388, 756 (1997)

[18] M. Zheng, A. Jagota, M. S. Strano, A. P. Santos, P. Barone, S. G. Chou, B. A. Diner, M. S. Dresselhaus, R. S. Mclean, G. B. Onoa, G. G. Samsonidze, E. D. Semke, M. Usrey, D. J. Walls, Science 302, 1545 (2003).

[19] M. Zheng and E. D. Semke, J. Am. Chem. Soc. 129, 6084 (2007).

[20] H. Peng, N Alvarez, C Kittrell, R. H. Hauge, and H. K. Schmidt, J. Am. Chem. Soc. 128, 8396 (2006).

[21] J. Chung, K. H. Lee, J. Lee, and R. S. Ruoff. Langmuir 20, 3011 (2004).

[22] W. Yang, M. J. Moghaddam, S. Taylor, B. Bojarski, L. Wieczorek, J. Herrmann, and M. J. McCall. Chem. Phys. Lett. 443, 169 (2007)

[23] S. R. Lustig, A. Jagota, C.Khripin, and M. Zheng, J. Phys. Chem. 109, 2559 (2005).

[24] S. Manohar, T. Tang, and A. Jagota, J. Phys. Chem. C 111, 17835 (2007).

[25] R. F. Rajter, R. H. French, W.Y. Ching, W.C. Carter and Y. M. Chiang, J. Appl. Phys. 101, 054303 2007.

[26] R. F. Rajter, R. Podgornik, V. A. Parsegian, R. H. French and W. Y. Ching, Phys. Rev. B 76, 045417 (2007).

[27] R. F. Rajter and R. H. French, J. of Phys.: Conf. Series, 94, 012001, (2008).

[28] R. F. Rajter, R. H. French, R. Podgornik, W. Y. Ching, and V. A. Parsegian, J. Appl. Phys. 104, 053513 (2008).

[29] O. Stephan, D. Taverna, M. Kociak, K. Suenaga, L. Henrard, and C. Colliex. Phys. Rev. B. 66, 155422 (2002).

[30] V. A. Parsegian, *Van der Waals Forces*, Cambridge University Press, Cambridge (2005).

[31] V. A. Parsegian and G. H. Weiss, J. Colloid Interface Science 40, 35 (1971).

[32] J. D. van der Waals, *On the continuity of the gas and liquid state*, PhD Thesis at Leiden University (1873).

[33] R. H. French, J. Am. Ceram 83, 2117 (2000).

[34] J. Israelichvili. *Intermolecular and SurfaceForces* 2nd edition, Academic Press (1991).

[35] M. S. Dresselhaus, G. Dresselhaus, A. Jorio , A. G. Souza Filho, and R. Saito, Carbon 40, 2043 (2002)

[36] R. Saito, K. Sato, Y. Oyama, J. Jiang, Ge. G. Samsonidze, G. Dresselhaus, and M. S. Dresselhaus, Phys. Rev. B 72, 153413 (2005).

[37] E. B. Barrosa, A. Joriob, Ge. G. Samsonidze, R. B. Capazc, A. G. Souza Filhoa, J. Filhoa, G. Dresselhause, M. S. Dresselhausf Phys. Rep. 431, 261 302 (2006)

[38] H. B. G. Casimir, Proc. K. Ned. Akad. Wet. 51, 793 (1948).

[39] H. B. G. Casimir, D. Polder, Phys. Rev. 73, 360 (1948).

[40] H. B. G. Casimir, J. Chim. Phys. 46, 407 (1949).

[41] T. Emig, R. L. Jaffe, M. Kardar, and A. Scaricchio, Phys. Rev. Lett. 96, 080403 (2006).

[42] H. B. G. Casimir, Comments Mod. Phys. 56, 175 (2000).

[43] E. M. Lifshitz, Sov. Phys. JETP 2, 73 (1956).

[44] L. D. Landau, E. M. Lifshitz, and L. P. Pitaevskii. *Electrodynamics of Continuous Media* 2nd Edition, Elsevier (2004).

[45] F. Wooten, *Optical Properties of Solids*; p. 49. Academic Press, New York, 1972.

[46] R. Podgornik, R. H. French, and V. A. Parsegian, J. Chem. Phys. 124, 044709, (2006).

[47] K. van Benthem , G. Tan, R. H. French, L. K. Denoyer, R. Podgornik, and V. A. Parsegian, Physical Review B 74, 205110 (2006).

[48] R. Podgornik and V. A. Parsegian, J. Chem. Phys. 120, 3401 (2004).

[49] B. V. Derjaguin, Kolloid-Z. 69, 155 (1934).

[50] K. M. Knowles, J. Ceram. Proc. Res. 6, 10 (2005).

[51] K. M. Knowles and S. Turan, Ultramicroscopy 83, 245 (2000).

[52] R. Podgornik and V. A. Parsegian, Phys. Rev. Lett. 80, 1560 (1998).

[53] NEXT ACTION - Find citation

[54] E. D. Palik (Ed.), *Handbook of Optical Constants of Solids* Vol. I, 1985; Vol II, 1991; Vol. III, 1998. Academic Press, New York.

[55] see http://sourceforge.net/projects/geckoproj

[56] A. Popescu and L. M. Woods, Phys. Rev. B., 77, 115443 (2008).

[57] W. Y. Ching, J. of Amer. Ceram. Soc. 71, 3135 (1990).

[58] R. H. French, S. J. Glass, F. S. Ohuchi, Y. N. Xu, and W. Y. Ching, Phys. Rev. B 49, 5133 (1994).

[59] W. Y. Ching, Y. N. Xu, and R. H. French, Phys. Rev. B 54, 13546 (1996).

[60] Y. N. Xu, W. Y. Ching, and R. H. French, Phys. Rev. B 48, 17695 (1993).

[61] Y. N. Xu and W. Y. Ching, Phys. Rev. B 51, 17379 (1995).

[62] R. R. Dagastine, D. C. Prieve, and L. R. White, J. Colloid Interface Sci. 249, 78 (2002).

[63] V. N. Popov and L. Henrard, Phys. Rev. B 70, 115407 (2004).

[64] J. W. Mintmire and C. T. White, Synth. Met. 77, 231 (1996).

[65] R. Ahuja, J. M. Osorio-Guillen, J. S. d. Almeida, B. Holm, W. Y. Ching, and B. Johansson. J. Phys. Condensed Matter, 16, 2891 (2004)

[66] R. H. French and W. Y. Ching, private correspondence.

[67] H. D. Ackler, R. H. French, and Y. M. Chiang, J. Colloid Interface Sci. 179, 460 (1996).

[68] C. M. Roth and A. M. Lenhoff, J. Colloid Interface Sci. 179, 637 (1996).

[69] R. R. Dagastine, D. C. Prieve, and L. R. White, J. Colloid Interface Sci. 231, 351 (2000).

[70] J. M. Fernandez-Varea and R. Garcia-Molina, J. Colloid Interface Sci. 231, 394 (2000).

[71] R. Ahuja, S. Auluck, J. M. Wills, M. Alouani, B. Johansson, and O. Eriksson. Phys. Rev. B 55, 4999 (1997).

[72] E. D. Palik (Ed.) and D. Y. Smith, *Handbook of Optical Constants of Solids* Vol. I, 1985, pg 35. Academic Press, New York.

[73] G. Veble and R. Podgornik. NEXT ACTION - NEED FULL CITE

[74] D. A. G. Bruggeman, Ann. Phys. 24, 636 (1935).

[75] Ph. J. Roussel, J. Vanhellemont, and H. E. Maes, Thin Solid Films 234, 423 (1993).

[76] H. Fujiwara, J. Koh, P. I. Rovira, and R. W. Collins, Phys. Rev. B. 61, 10832 (2000).

[77] Lord Rayleigh, Sec. R.S. pp. 481-502, Philosophical Magazine, (1892)

[78] K. Cahill and V. A. Parsegian, J. Chem. Phys. 121, 10839 (2004).

[79] M. Dion, H. Rydberg, E. Schrder, D. C. Langreth, and B. I. Lundqvist, Phys. Rev. Lett. 92, 246401 (2004)

[80] T. Thonhauser, V. R. Cooper, S. Li, A. Puzder, P. Hyldgaard, and D. C. Langreth, Phys. Rev. B 76, 125112 (2007).

[81] C. Richard, F. Balavoine, P. Schultz, T. W. Ebbesen, and C. Mioskowski, Science 300, 775 (2003).

[82] R. H. French, K. I. Winey, M. K. Yang, and W. Qiu, Aust. J. Chem. 60, 251 (2007).

[83] J. N. Munday, F. Capasso, V. A. Parsegian, and S. M. Bezrukov. Phys. Rev. A. 78, 032109 (2008)

[84] M. S. Dresselhaus, G. Dresselhaus, R. Saito, and A. Jorio, Physics Reports, 409, 47 (2005).

[85] M. S. Dresselhaus and P. C. Eklund, Advances in Physics 49, 705 (2000).

[86] G. Palasantzas, P. J. van Zwol, and J. Th. M. De Hosson, Appl. Phys. Lett. 93, 121912 (2008)

[87] Ge. G. Samsonidze, R. Saito, N. Kobayashi, A. Gruneis, J. Jiang, A. Jorio, S. G. Chou, G. Dresselhaus, and M. S. Dresselhaus, Appl. Phys. Lett. 85, 5703 (2004).

[88] Y. Li, S. V. Rotkin, and U. Ravaioli, Nano Lett. 3, 183-187 (2003).

[89] Y. Li, S. V. Rotkin, and U. Ravaioli, Appl. Phys. Lett. 85, 4178 (2004).

[90] Y. Li, U. Ravaioli, and SS V. Rotkin, Phys. Rev. B 73, 035415 (2006).

[91] Y. Li, S. V. Rotkin, and U. Ravaioli, Proc. IEEE Nanotechnol. 3, 1 (2003).

[92] L. A. Wilen, J. S. Wettlaufer, M. Elbaum, and M. Schick. Phys. Rev. B. 52, 12426 (1995).

[93] A. A. Kornyshev, D. J. Lee, S. Leikin, and A. Wynveen. Reviews of Modern Physics, 79, 943 (2007).

[94] J. Chun, J.L. Li, R. Car, I. A. Aksay and D. A. Saville, J. Phys. Chem. B 110 16624 (2006).

Appendix A

Solid Cylinder Derivation

In this section we derive the non-retarded van der Waals - London interaction between a semi-infinite anisotropic substrate and an anisotropic cylinder in two limits: the **far limit**, corresponding to a large R (note that R is the separation between the surface of the substrate to the surface of the cylinder), and the **near limit,** corresponding to the Derjaguin limit valid in the case of small separation from the substrate. The substrate is assumed to be optically uniaxial and have a dielectric response function $\epsilon_\|$ in the direction parallel to the surface and $\epsilon_\perp$ in the other two directions. The cylinder is also uniaxial with dielectric response functions $\epsilon^c{}_\|$ and $\epsilon^c{}_\perp$ parallel and perpendicular to the cylinder axis.

The philosophy of our approach is based on consecutive application of the *Parsegian method* and the *Pitaevskii method* for two semi-inifinite anisotropic media ([ ], p. 236):

- In the cylinder - substrate case we first formulate the Lifshitz interaction energy for two plane-parallel semi-infinite anisotropic media and then use the *Pitaevskii method* to extract an interaction free energy between a single anisotropic cylinder and a semi-infinite anisotropic substrate. The limiting procedure of going from the anisotropic composite to a single long anisotropic cylinder is based on the application of the *Parsegian method* of composite anisotropic media.

- In the cylinder - cylinder case we start again from the Lifshitz interaction en-

193

ergy for two plane-parallel semi-infinite anisotropic media but then use the *Parsegian method* of composite anisotropic media for both of them. Applying the *Pitaevskii method* to both media now allows for an extraction of the interaction free energy between two anisotropic cylinders.

For the first case listed above a related computation was performed in an nevertheless unrelated context by Chun *et al.* [94]. The main difference between this approach and the one described in detail here is that we have now circumvented all linearization assumptions and thus our formulas are exact to all orders in the orientational dependence, we have derived the interaction formulas for any value of the substrate anisotropy, and we have used the *Pitaevskii method* to go from the slab-slab interaction to the cylinder-substrate interaction.

We first calculate the Lifshitz interaction free energy for two anisotropic media $\mathcal{L}$ and $\mathcal{R}$ across m of thickness ℓ in the non-retarded limit.[1] We introduce two components of the uniaxial dielectric response of the substrate $\mathcal{L}$ as $\epsilon_\parallel$ and $\epsilon_\perp$ and $\overline{\epsilon_\parallel}$ and $\overline{\epsilon_\perp}$ as the two components of the uniaxial dielectric response of the substrate $\mathcal{R}$.
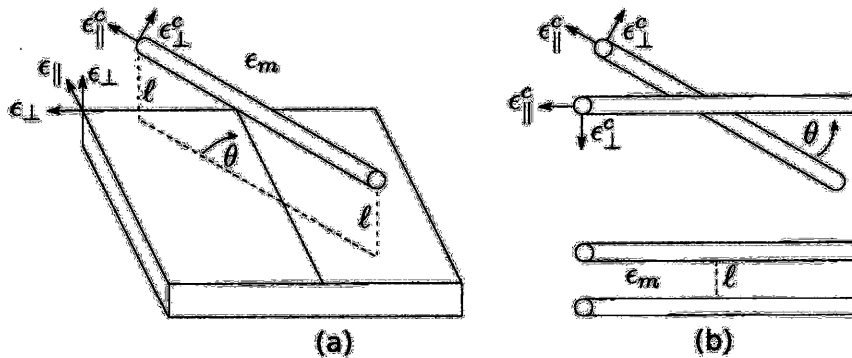

Figure A-1: Schematic showing the geometry of the (a) anisotropic cylinder-anisotropic planar substrate and (b) anisotropic cylinder-anisotropic cylinder systems.

The angle between the two principal axes of media $\mathcal{L}$ and $\mathcal{R}$ is defined as θ, see Fig.A-1. ϵ_m is the dielectric response of the isotropic medium between the two semi-infinite substrates. ϕ is an integration variable used to capture the interactions

---

[1]The non-retarded case applies at small induced-dipole separations when $\omega d/c$ is small and no phase lag develops between the oscillations of the induced dipoles due to a finite speed of light, c.

between all possible directions within the plane normal to the stacking direction. The interaction free energy for this system is given by the following expression ([ ], p.320)

$$
G(\ell, \theta) = \frac{k_B T}{4\pi^2} \sum_{n=0}^{\infty}{}' \int_0^{2\pi} d\phi \int_0^\infty QdQ \log\left(1 - \Delta_{\mathcal{L}m}(\phi)\Delta_{\mathcal{R}m}(\theta - \phi)e^{-2Q\ell}\right). \qquad \text{(A.1)}
$$

All the dielectric functions have to be taken as their Kramers - Kronig transforms at $i\xi_n$, i.e., $\epsilon(i\xi_n)$, where $\xi_n = 2\pi n\frac{k_B T}{\hbar}$. Q is the magnitude of the wave-vector in the plane of the two opposed interfaces. Also here

$$
\Delta_{\mathcal{L}m}(\phi) = \frac{\epsilon_\perp\sqrt{1 + \gamma\cos^2\phi} - \epsilon_m}{\epsilon_\perp\sqrt{1 + \gamma\cos^2\phi} + \epsilon_m}, \qquad \text{(A.2)}
$$

where medium $\mathcal{L}$ anisotropy is defined as

$$
\gamma = \frac{\epsilon_\| - \epsilon_\perp}{\epsilon_\perp}. \qquad \text{(A.3)}
$$

If the substrate $\mathcal{L}$ is isotropic then $\epsilon_\| = \epsilon_\perp$ and $\gamma = 0$. For the medium $\mathcal{R}$ we have analogously

$$
\Delta_{\mathcal{R}m}(\theta - \phi) = \frac{\overline{\epsilon_\perp}\sqrt{1 + \overline{\gamma}\cos^2(\theta - \phi)} - \epsilon_m}{\overline{\epsilon_\perp}\sqrt{1 + \overline{\gamma}\cos^2(\theta - \phi)} + \epsilon_m}. \qquad \text{(A.4)}
$$

with an anisotropy of

$$
\overline{\gamma} = \frac{\overline{\epsilon_\|} - \overline{\epsilon_\perp}}{\overline{\epsilon_\perp}}. \qquad \text{(A.5)}
$$

Again if the substrate $\mathcal{R}$ is isotropic then $\overline{\epsilon_\|} = \overline{\epsilon_\perp}$ and $\overline{\gamma} = 0$. The interaction free energy $G(\ell, \theta)$, Eq. A.1, can be evaluated at any separation between the interfaces of $\mathcal{L}$ and $\mathcal{R}$, ℓ, as well as at any angle between the two principal axes of media $\mathcal{L}$ and $\mathcal{R}$, θ.

A.1 Cylinder - planar substrate interaction

In order to get the interaction free energy between an anisotropic cylinder and an anisotropic substrate we use the *Parsegian method*, *i.e.*, we assume that one of the semi-infinite substrates, *e.g.*, $\mathcal{R}$, is a composite composed of oriented anisotropic cylinders at volume fraction v, with $\epsilon^c_\perp$ and $\epsilon^c_\parallel$ as the transverse and longitudinal dielectric response functions of the cylinder material. For the semi-infinite composite medium of oriented anisotropic cylinders $\mathcal{R}$ the anisotropic bulk dielectric response function can be derived in the form ([ ], p.318)

$$\overline{\epsilon_\parallel} = \epsilon_m \left(1 + v\Delta_\parallel\right), \qquad \overline{\epsilon_\perp} = \epsilon_m \left(1 + \frac{2v\Delta_\perp}{1 - v\Delta_\perp}\right), \qquad \text{(A.6)}$$

where

$$\Delta_\perp = \frac{\epsilon^c_\perp - \epsilon_m}{\epsilon^c_\perp + \epsilon_m} \qquad \Delta_\parallel = \frac{\epsilon^c_\parallel - \epsilon_m}{\epsilon_m} \qquad \text{(A.7)}$$

and ϵ_m is again the dielectric function of the isotropic medium between cylinders as well as between regions $\mathcal{L}$ and $\mathcal{R}$.

We now apply the *Pitaevskii method* to this composite system, which allows us to extract the interaction between a **single** anisotropic cylinder and a semi-infinite anisotropic substrate from an interaction energy between **two** semi-infinite substrates, of which one is a composite defined above. We start from the free energy of interaction $G(\ell, \theta)$, Eq. A.1, where the composite of uniaxial cylinders is at a volume fraction $v = N\pi a^2$, where N is the cross-sectional number density, and a is the radius of the cylinders. For this case one can derive that ([ ], p.236)

$$-\frac{\partial G(\ell, \theta)}{\partial \ell}|_\ell = Ng(\ell, \theta). \qquad \text{(A.8)}$$

Here $g(\ell, \theta)$ is the interaction free energy **per unit length** between a cylinder with $a/\ell \longrightarrow 0$, and a semi-infinite substrate $\mathcal{L}$, while $G(\ell, \theta)$ is the interaction free energy **per unit surface area** between a semi-infinite region, $\mathcal{L}$, with a semi-infinite composite region, $\mathcal{R}$, at separation ℓ and angle θ, composed of parallel anisotropic

cylinders embedded in medium m. $g(\ell, \theta)$ is thus obtained by expanding $G(\ell)$ to the first order in v. This is the essence of the *Pitaevskii method*.

A.1.1 Far limit

We formally define the far limit as the limit $a/\ell \longrightarrow 0$ and use the result of the previous section to explicitly derive $g(\ell, \theta)$. In order to use the *Pitaevskii method* we expand $\Delta_{\mathcal{R}m}(\theta - \phi)$ to lowest order in v,

$$\Delta_{\mathcal{R}m}(\theta - \phi) = -\left(\Delta_\perp + \tfrac{1}{4}(\Delta_\parallel - 2\Delta_\perp)\cos^2(\theta - \phi)\right)v + \mathcal{O}(v^2) \qquad (\text{A.9})$$

To this order in v the Q integral in Eq. A.1 can then be done explicitly

$$G(\ell, \theta) = -\frac{k_B T}{16\pi^2 \, \ell^2} \, v \sideset{}{'}\sum_{n=0}^{\infty} \int_0^{2\pi} d\phi \; \Delta_{\mathcal{L}m}(\phi)\left(\Delta_\perp + \tfrac{1}{4}(\Delta_\parallel - 2\Delta_\perp)\cos^2(\theta - \phi)\right). \qquad (\text{A.10})$$

Now apply Eq. A.8 and thus extract the interaction free energy **per unit length** of a cylinder

$$g(\ell, \theta) = -\frac{k_B T}{4\pi^2} \frac{\pi a^2}{2\ell^3} \sideset{}{'}\sum_{n=0}^{\infty} \int_0^{2\pi} d\phi \; \Delta_{\mathcal{L}m}(\phi)\left(\Delta_\perp + \tfrac{1}{4}(\Delta_\parallel - 2\Delta_\perp)\cos^2(\theta - \phi)\right). \qquad (\text{A.11})$$

Integration over ϕ leads to a term that is independent of θ plus a term that goes as $\cos^2\theta$. This can be proved simply by Taylor expanding the above equation in $\cos^2\phi$ and evaluating the ϕ integrals order by order. Tedious but straightforward. Therefore we can write $g(\ell, \theta)$ in the compact form

$$g(\ell, \theta) = -\frac{k_B T \, (\pi a^2)}{4\pi \, \ell^3}\left(\mathcal{H}^{(0)} + \mathcal{H}^{(2)}\cos^2\theta\right). \qquad (\text{A.12})$$

We define $\mathcal{H}^{(0)}$ and $\mathcal{H}^{(2)}$ by picking two convenient angles θ in Eq. A.11 as $\theta = 0$ and $\theta = \frac{\pi}{2}$. For $\theta = 0$

$$\mathcal{H}^{(0)} + \mathcal{H}^{(2)} \quad = \quad \frac{1}{2\pi} \sum_{n=0}^{\infty}{}' \int_0^{2\pi} d\phi \; \Delta_{\mathcal{L}m}(\phi) \left(\Delta_{\perp} + \tfrac{1}{4}(\Delta_{\parallel} - 2\Delta_{\perp}) \cos^2 \phi \right), \quad \text{(A.13)}$$

and for $\theta = \frac{\pi}{2}$,

$$\mathcal{H}^{(0)} \quad = \quad \frac{1}{2\pi} \sum_{n=0}^{\infty}{}' \int_0^{2\pi} d\phi \; \Delta_{\mathcal{L}m}(\phi) \left(\Delta_{\perp} + \tfrac{1}{4}(\Delta_{\parallel} - 2\Delta_{\perp}) \sin^2 \phi \right). \quad \text{(A.14)}$$

$\mathcal{H}^{(0)}$ and $\mathcal{H}^{(2)}$ can be evaluated explicitly since all the integrals are elementary, but the expressions obtained contain various elliptic functions and are not particularly illuminating. They can be obtained easily with *Mathematica*.

In order to cast the result in a form that can be easily evaluated and interpreted we first define two Hamaker coefficients as

$$\mathcal{A}^{(0)} = \tfrac{3}{2} k_B T \; \mathcal{H}^{(0)} \qquad \text{and} \qquad \mathcal{A}^{(2)} = \tfrac{3}{2} k_B T \; \mathcal{H}^{(2)} \qquad \text{(A.15)}$$

$\mathcal{A}^{(0)}$ describes the orientation-independent part of the interaction; and $\mathcal{A}^{(2)}$ the orientation-dependent part. The interaction free energy **per unit length** between a cylinder of radius a and a planar anisotropic substrate at surface-surface separation ℓ, Eq. A.12 becomes

$$g(\ell, \theta) = -\frac{(\pi a^2) \left(\mathcal{A}^{(0)} + \mathcal{A}^{(2)} \cos^2 \theta \right)}{6\pi \; \ell^3}. \qquad \text{(A.16)}$$

This is the main result that we will use in order to quantify the van der Waals - London dispersion interaction between a cylindrical CNT and an anisotropic semi-infinite substrate. Note that in Eq. A.16 all the ℓ and θ dependencies are explicitly given.

For completeness we also give the results for the force and torque on the cylinder. The force **per unit length** of the cylinder is thus

$$f(\ell, \theta) = -\frac{\partial g(\ell, \theta)}{\partial \ell}, \tag{A.17}$$

$$\xi_n = \frac{2\pi k_B T n}{\hbar} \tag{A.18}$$

or

$$f(\ell, \theta) = -\frac{(\pi a^2) \left(\mathcal{A}^{(0)} + \mathcal{A}^{(2)} \cos^2 \theta \right)}{2\pi \; \ell^4}. \tag{A.19}$$

The corresponding torque **per unit length** is the derivative

$$\tau(\ell, \theta) = -\frac{\partial g(\ell, \theta)}{\partial \theta}, \tag{A.20}$$

explicitly,

$$\tau(\ell, \theta) = -\frac{(\pi a^2) \; \mathcal{A}^{(2)} \sin 2\theta}{6\pi \; \ell^3}. \tag{A.21}$$

These last results in the far limit give the force **per unit length** $f(\ell, \theta)$ and the torque **per unit length** $\tau(\ell, \theta)$ as a function of the separation ℓ and the angle between the two dielectric axes θ.

A.1.2 Near limit

We now investigate the opposite limit, $\ell/a \longrightarrow 0$, which we term the near limit. Here one uses the *Derjaguin method* to get the interaction energy of two cylinders, one of which has an infinite radius of curvature, from the interaction energy between two half spaces. In this case the interaction energy **per unit length** between cylinders of radii a_1 and a_2 can be derived as([ ], p.204).

$$g(\ell, \theta; a_1, a_2) = \int_{-\infty}^{+\infty} G(\ell + \alpha(a_1 x)^2, \theta) \; a_1 dx, \tag{A.22}$$

where

$$\alpha = \frac{a_1 + a_2}{2a_1 a_2}. \tag{A.23}$$

The Derjaguin *method* Eq. A.22 is based on a summation of interactions between quasiparallel sections of the two cylinders. From Eq. A.1 and A.22 it follows that

$$\int_{-\infty}^{+\infty} G(\ell + \alpha x^2, \theta) d(a_1 x) =$$
$$= -\frac{k_B T}{4\pi^2} \sum_{n=0}^{\infty}{}' \int_0^{2\pi} d\phi \int_0^{\infty} Q dQ \; \Delta_{\mathcal{L}m}(\phi) \Delta_{\mathcal{R}m}(\theta - \phi) e^{-2Q\ell} \int_{-\infty}^{+\infty} e^{-2Q\alpha(a_1 x)^2} d(a_1 x), \tag{A.24}$$

and thus

$$g(\ell, \theta; a_1, a_2) = -\frac{k_B T}{16 \, \ell^{3/2}} \sqrt{\frac{2a_1 a_2}{a_1 + a_2}} \sum_{n=0}^{\infty}{}' \frac{1}{2\pi} \int_0^{2\pi} d\phi \; \Delta_{\mathcal{L}m}(\phi) \Delta_{\mathcal{R}m}(\theta - \phi). \tag{A.25}$$

For the interaction between a cylinder and a plane, let $a_1 \longrightarrow a$ and $a_2 \longrightarrow \infty$. Also let one of the semi-infinite slabs, again say this is $\mathcal{R}$, be composed of the anisotropic cylinder material so that

$$\Delta_{\mathcal{R}m}(\theta - \phi) = \frac{\epsilon^c{}_\perp \sqrt{1 + \gamma^c \cos^2(\theta - \phi)} - \epsilon_m}{\epsilon^c{}_\perp \sqrt{1 + \gamma^c \cos^2(\theta - \phi)} + \epsilon_m}. \tag{A.26}$$

Here again

$$\gamma^c = \frac{\epsilon^c{}_\parallel - \epsilon^c{}_\perp}{\epsilon^c{}_\perp}, \tag{A.27}$$

and $\epsilon^c{}_\perp$ and $\epsilon^c{}_\parallel$ are the transverse and longitudinal dielectric responses of the cylinder and ϵ_m that of the solution medium.

This formula is valid for any angle between the two cylinders, or equivalently between the two principal axes of the dielectric response: the axis of the cylinder and the principal axis of the anisotropic substrate. The angular integral is analytically

solvable for any anisotropy by the same methods as used to derive Eq. A.12 and leads to the interaction free energy **per unit length** between a cylinder and an anisotropic substrate,

$$g(\ell, \theta; a) = -\frac{k_B T \sqrt{2a}}{16 \ \ell^{3/2}} \left(\mathcal{H}^{(0)} + \mathcal{H}^{(2)} \cos^2 \theta \right). \tag{A.28}$$

Here $\mathcal{H}^{(0)}$ and $\mathcal{H}^{(2)}$ are obtained in complete analogy to Eq. A.12 from

$$\mathcal{H}^{(0)} + \mathcal{H}^{(2)} = \frac{1}{2\pi} \sum_{n=0}^{\infty}{}' \int_0^{2\pi} d\phi \left(\frac{\epsilon_\perp \sqrt{1 + \gamma \cos^2 \phi} - \epsilon_m}{\epsilon_\perp \sqrt{1 + \gamma \cos^2 \phi} + \epsilon_m} \right) \left(\frac{\epsilon^c{}_\perp \sqrt{1 + \gamma^c \cos^2 \phi} - \epsilon_m}{\epsilon^c{}_\perp \sqrt{1 + \gamma^c \cos^2 \phi} + \epsilon_m} \right) \tag{A.29}$$

and

$$\mathcal{H}^{(0)} = \frac{1}{2\pi} \sum_{n=0}^{\infty}{}' \int_0^{2\pi} d\phi \left(\frac{\epsilon_\perp \sqrt{1 + \gamma \cos^2 \phi} - \epsilon_m}{\epsilon_\perp \sqrt{1 + \gamma \cos^2 \phi} + \epsilon_m} \right) \left(\frac{\epsilon^c{}_\perp \sqrt{1 + \gamma^c \sin^2 \phi} - \epsilon_m}{\epsilon^c{}_\perp \sqrt{1 + \gamma^c \sin^2 \phi} + \epsilon_m} \right). \tag{A.30}$$

In order to cast the result in an easily evaluated and interpreted form, we define Hamaker coefficients as

$$\mathcal{A}^{(0)} = \tfrac{3}{2} k_B T \ \mathcal{H}^{(0)} \qquad \text{and} \qquad \mathcal{A}^{(2)} = \tfrac{3}{2} k_B T \ \mathcal{H}^{(2)}. \tag{A.31}$$

Coefficient $\mathcal{A}^{(0)}$ again describes the orientation-independent part of the interaction and $\mathcal{A}^{(2)}$ the orientation-dependent part of the interaction. The interaction free energy **per unit length** between a thick cylinder (near limit) and a planar anisotropic substrate at surface-surface separation ℓ, Eq. A.28 becomes

$$g(\ell, \theta, a) = -\frac{\sqrt{2a} \left(\mathcal{A}^{(0)} + \mathcal{A}^{(2)} \cos^2 \theta \right)}{24 \ \ell^{3/2}}. \tag{A.32}$$

This is the second main result that we will use in order to quantify the van der Waals - London dispersion interaction between a cylindrical CNT and an anisotropic semi-infinite substrate at close separations. Note that here, too, all the ℓ and θ

dependencies are explicitly given.

The corresponding force **per unit length** is then according to Eq. A.17

$$f(\ell, \theta, a) = -\frac{\partial g(\ell, \theta, a)}{\partial \ell}, \tag{A.33}$$

or

$$f(\ell, \theta, a) = -\frac{\sqrt{2a}\left(\mathcal{A}^{(0)} + \mathcal{A}^{(2)} \cos^2 \theta\right)}{16\ \ell^{5/2}}. \tag{A.34}$$

The torque **per unit length** is then again

$$\tau(\ell, \theta, a) = -\frac{\partial g(\ell, \theta, a)}{\partial \theta}, \tag{A.35}$$

or explicitly

$$\tau(\ell, \theta, a) = -\frac{\sqrt{2a}\ \mathcal{A}^{(2)} \sin 2\theta}{24\ \ell^{3/2}}. \tag{A.36}$$

This completes the near limit for the interaction free energy **per unit length** $g(\ell, \theta, a)$ in the cylinder-planar substrate system as an explicit function of the surface separation ℓ and the angle θ between the two principal dielectric axes.

A.2   Cylinder - cylinder interaction

In order to get the interaction free energy between two anisotropic cylinders we again use the *Parsegian method*, assuming now that both $\mathcal{L}$ as well as $\mathcal{R}$ are composites composed of oriented anisotropic cylinders at volume fraction v, with $\epsilon^c_\perp$ and $\epsilon^c_\parallel$ as the transverse and longitudinal dielectric response functions of the cylinder material. The rest of the derivation is very similar to the case of the cylinder and a semi-infinite substrate. We again decompose it into the far and the near limit.

A.2.1 Far limit

Start from the interaction between two semi-infinite media, both composed of uniaxial cylinders at a volume fraction $v = N\pi a^2$, where N is the crossectional number density and a is the radius of the cylinders.

Depending on θ, in this case Eq. A.8 comes in two variants. If the cylinders in each of the composite media are parallel, $\theta = 0$, then ([30], p.234)

$$\frac{d^2 \mathcal{G}(\ell, \theta = 0)}{d\ell^2} = N^2 \int_{-\infty}^{+\infty} g\left(\sqrt{\ell^2 + y^2}\right) dy. \tag{A.37}$$

Here $g(\ell)$ is the free energy of interaction between parallel cylinders **per unit length** at a separation ℓ. If on the other hand the angle θ is finite, *i.e.* $\theta \neq 0$, then the corresponding expression becomes ([30], p.234)

$$\frac{d^2 \mathcal{G}(\ell, \theta)}{d\ell^2} = N^2 \sin\theta \; G(\ell, \theta). \tag{A.38}$$

Here $G(\ell, \theta)$ is the interaction free energy between the two cylinders, skewed at an angle θ. For two semi-infinite composite media Eq.A.1 now becomes

$$\mathcal{G}(\ell, \theta) = \frac{k_B T}{4\pi^2} \sum_{n=0}^{\infty}{}' \int_0^{2\pi} d\phi \int_0^{\infty} Q dQ \log\left(1 - \Delta_{\mathcal{L}m}(\phi)\Delta_{\mathcal{R}m}(\theta - \phi)e^{-2Q\ell}\right), \tag{A.39}$$

where

$$\Delta_{\mathcal{L}m}(\phi) = \frac{\overline{\epsilon_\perp(\mathcal{L})}\sqrt{1 + \overline{\gamma(\mathcal{L})}\cos^2\phi} - \epsilon_m}{\overline{\epsilon_\perp(\mathcal{L})}\sqrt{1 + \overline{\gamma(\mathcal{L})}\cos^2\phi} + \epsilon_m}. \tag{A.40}$$

and

$$\Delta_{\mathcal{R}m}(\theta - \phi) = \frac{\overline{\epsilon_\perp(\mathcal{R})}\sqrt{1 + \overline{\gamma(\mathcal{R})}\cos^2(\theta - \phi)} - \epsilon_m}{\overline{\epsilon_\perp(\mathcal{R})}\sqrt{1 + \overline{\gamma(\mathcal{R})}\cos^2(\theta - \phi)} + \epsilon_m}. \tag{A.41}$$

We have kept the option that the two cylinders are composed of different materials, $(\mathcal{R})$ and $(\mathcal{L})$. The other definitions are trivially generalized, for $(\mathcal{R})$ and $(\mathcal{L})$, from

$$\overline{\gamma} = \frac{\overline{\epsilon_\parallel} - \overline{\epsilon_\perp}}{\overline{\epsilon_\perp}}, \tag{A.42}$$

with

$$\overline{\epsilon_\parallel} = \epsilon_m \left(1 + v\Delta_\parallel\right), \qquad \overline{\epsilon_\perp} = \epsilon_m \left(1 + \frac{2v\Delta_\perp}{1 - v\Delta_\perp}\right), \tag{A.43}$$

where

$$\Delta_\perp \equiv \frac{\epsilon^c{}_\perp - \epsilon_m}{\epsilon^c{}_\perp + \epsilon_m} \qquad \Delta_\parallel \equiv \frac{\epsilon^c{}_\parallel - \epsilon_m}{\epsilon_m}. \tag{A.44}$$

Starting first with the expansion of $\Delta_{\mathcal{R}m}$ and $\Delta_{\mathcal{L}m}$ in terms of v

$$\Delta_{\mathcal{L}m}(\phi) = -\left(\Delta_\perp(\mathcal{L}) + \tfrac{1}{4}(\Delta_\parallel(\mathcal{L}) - 2\Delta_\perp(\mathcal{L}))\cos^2\phi\right)v + \mathcal{O}(v^2)$$

$$\Delta_{\mathcal{R}m}(\phi) = -\left(\Delta_\perp(\mathcal{R}) + \tfrac{1}{4}(\Delta_\parallel(\mathcal{R}) - 2\Delta_\perp(\mathcal{R}))\cos^2(\theta - \phi)\right)v + \mathcal{O}(v^2). \tag{A.45}$$

To second order in v this gives

$$\mathcal{G}(\ell, \theta) = -\frac{k_B T}{2\pi} N^2 (\pi a^2)^2 \sum_{n=0}^{\infty}{}' \left(\mathcal{H}^{(0)} + \mathcal{H}^{(2)}\cos^2\theta\right) \times \int_0^\infty Q dQ \ e^{-2Q\ell}, \tag{A.46}$$

by using $v = N(\pi a^2)$. Here

$$\mathcal{H}^{(0)} + \mathcal{H}^{(2)} = \frac{1}{2\pi}\int_0^{2\pi} d\phi \left(\Delta_\perp(\mathcal{L}) + \tfrac{1}{4}(\Delta_\parallel(\mathcal{L}) - 2\Delta_\perp(\mathcal{L}))\cos^2\phi\right)\left(\Delta_\perp(\mathcal{R}) + \tfrac{1}{4}(\Delta_\parallel(\mathcal{R}) - 2\Delta_\perp(\mathcal{R}))\cos^2\phi\right),$$
$$\tag{A.47}$$

and

$$\mathcal{H}^{(0)} = \frac{1}{2\pi}\int_0^{2\pi} d\phi \left(\Delta_\perp(\mathcal{L}) + \tfrac{1}{4}(\Delta_\parallel(\mathcal{L}) - 2\Delta_\perp(\mathcal{L}))\cos^2\phi\right)\left(\Delta_\perp(\mathcal{R}) + \tfrac{1}{4}(\Delta_\parallel(\mathcal{R}) - 2\Delta_\perp(\mathcal{R}))\sin^2\phi\right).$$
$$\tag{A.48}$$

We can now extract interaction formulae for a pair of skewed or parallel cylinders. In the simpler skewed case, Eqs. A.38 and A.46 give

$$\sin\theta \; G(\ell,\theta) = -\frac{k_B T}{2\pi}(\pi a^2)^2 4 \sum_{n=0}^{\infty}{}' \left(\mathcal{H}^{(0)} + \mathcal{H}^{(2)} \cos^2\theta \right) \int_0^{\infty} Q^3 dQ \; e^{-2Q\ell}, \qquad (A.49)$$

or

$$G(\ell,\theta) = -\frac{3 \; k_B T \; (\pi a^2)^2}{4\pi \; \ell^4 \; \sin\theta} \sum_{n=0}^{\infty}{}' \left(\mathcal{H}^{(0)} + \mathcal{H}^{(2)} \cos^2\theta \right). \qquad (A.50)$$

Introducing two Hamaker coefficients

$$\mathcal{A}^{(0)} = \tfrac{3}{2} k_B T \; \mathcal{H}^{(0)} \qquad \text{and} \qquad \mathcal{A}^{(2)} = \tfrac{3}{2} k_B T \; \mathcal{H}^{(2)}, \qquad (A.51)$$

we can write the interaction free energy between two thin cylinders (far limit) of radius a skewed at an angle θ and at a (smallest) separation ℓ in the form

$$G(\ell,\theta) = -\frac{(\pi a^2)^2 \left(\mathcal{A}^{(0)} + \mathcal{A}^{(2)} \cos^2\theta \right)}{2\pi \; \ell^4 \; \sin\theta}. \qquad (A.52)$$

Note that this is now a total interaction free energy and **not** interaction free energy per unit length. This is the third main result that we will use in order to quantify the van der Waals - London dispersion interaction between two cylindrical CNTs at large separations. Note too that all the ℓ and θ dependencies are explicitly given.

For completeness, we also derive the expressions for the force and the torque. The corresponding force is again obtained from

$$f(\ell,\theta) = -\frac{\partial G(\ell,\theta)}{\partial \ell}, \qquad (A.53)$$

or

$$f(\ell,\theta) = -\frac{2(\pi a^2)^2 \left(\mathcal{A}^{(0)} + \mathcal{A}^{(2)} \cos^2\theta \right)}{\pi \; \ell^5 \; \sin\theta}. \qquad (A.54)$$

Similarly the torque is

$$\tau(\ell, \theta) = -\frac{\partial G(\ell, \theta)}{\partial \theta}, \tag{A.55}$$

or

$$\tau(\ell, \theta) = -\frac{(\pi a^2)^2}{2\pi \ \ell^4} \ \left(\frac{\mathcal{A}^{(0)}}{\sin^2 \theta} + \mathcal{A}^{(2)}(2 + \cot^2 \theta) \right) \cos \theta. \tag{A.56}$$

For parallel cylinders the derivation proceeds along a different line, since now the interaction energy scales proportional to the total length of the cylinders. Start with Eq. A.37 giving

$$\int_{-\infty}^{+\infty} g(\sqrt{\ell^2 + y^2}) \ dy = -\frac{k_B T}{2\pi}(\pi a^2)^2 \ 4 \sum_{n=0}^{\infty}{}' \left(\mathcal{H}^{(0)} + \mathcal{H}^{(2)} \right) \int_0^{\infty} Q^3 dQ \ e^{-2Q\ell}. \tag{A.57}$$

By the inverse Abel transform

$$h(\ell) = \int_{-\infty}^{+\infty} g(\ell^2 + y^2) dy \qquad \longrightarrow \qquad g(\ell) = -\frac{1}{\pi} \int_{\ell}^{\infty} \frac{h'(y) dy}{\sqrt{\ell^2 - y^2}}, \tag{A.58}$$

we obtain

$$g(\ell) = -\frac{1}{\pi}\frac{k_B T}{2\pi}(\pi a^2)^2 \ 8 \sum_{n=0}^{\infty}{}' \left(\mathcal{H}^{(0)} + \mathcal{H}^{(2)} \right) \int_0^{\infty} Q^3 dQ \ K_0(-2Q\ell) \tag{A.59}$$

by using the standard identity

$$\int_{\ell}^{\infty} \frac{e^{-2Qy} dy}{\sqrt{\ell^2 - y^2}} = K_0(-2Q\ell). \tag{A.60}$$

From here it is easy to write explicitly the interaction free energy **per unit length** between two parallel cylinders of radius a,

$$g(\ell) = -\frac{9 \ k_B T \ (\pi a^2)^2}{16\pi \ \ell^5} \sum_{n=0}^{\infty}{}' \left(\mathcal{H}^{(0)} + \mathcal{H}^{(2)} \right). \tag{A.61}$$

The Matsubara sum $\sum_{n=0}^{\infty}{}'$ is as before. With the two Hamaker coefficients

$$\mathcal{A}^{(0)} = \tfrac{3}{2} k_B T \, \mathcal{H}^{(0)} \qquad \text{and} \qquad \mathcal{A}^{(2)} = \tfrac{3}{2} k_B T \, \mathcal{H}^{(2)}, \tag{A.62}$$

we remain with

$$g(\ell) = -\frac{3 \, (\pi a^2)^2 \left(\mathcal{A}^{(0)} + \mathcal{A}^{(2)} \right)}{8\pi \, \ell^5}. \tag{A.63}$$

This is the free energy of interaction between two parallel thin cylinders at a separation ℓ in the far limit. This is the fourth main result that we will use in order to quantify the van der Waals - London dispersion interaction between two parallel cylindrical CNTs at large separations.

Again, for the sake of completeness, we quote the results for the corresponding force **per unit length** as

$$f(\ell, \theta) = -\frac{\partial g(\ell, \theta)}{\partial \ell}, \tag{A.64}$$

or

$$f(\ell, \theta) = -\frac{15 \, (\pi a^2)^2 \left(\mathcal{A}^{(0)} + \mathcal{A}^{(2)} \right)}{8\pi \, \ell^6}. \tag{A.65}$$

A.2.2 Near limit

In the limit of small separations between the two cylinders $\ell/a \longrightarrow 0$, we reformulate the approach based on the *Derjaguin method* and introduced for a single cylinder and a substrate. For closely opposed curved surfaces where c_1^1, c_2^1 are the principal curvatures of the surface 1 and c_1^2, c_2^2 are the principal curvatures of the surface 2, the *Derjaguin method* leads to the interaction energy of the form([ ], p.204)

$$G(\ell, \theta; a_1, a_2) = \int \int_{-\infty}^{+\infty} \mathcal{G}(\ell + \tfrac{1}{2} c_1 x^2 + \tfrac{1}{2} c_2 y^2) \, dx dy, \tag{A.66}$$

where c_1 and c_2 are defined as

$$c_1 c_2 = (c_1^1 c_2^1 + c_1^2 c_2^2) + (c_1^1 c_1^2 + c_2^1 c_2^2) \sin^2 \theta + (c_1^1 c_2^2 + c_1^1 c_2^2) \cos^2 \theta. \tag{A.67}$$

With polar variables the integral Eq. A.66 can be rewritten as

$$G(\ell, \theta; a_1, a_2) = \int_0^{2\pi} \int_0^{+\infty} \mathcal{G}(\ell + \tfrac{1}{2}\rho^2) \, \frac{\rho d\rho \, d\phi}{\sqrt{c_1 c_2}}. \qquad (A.68)$$

For two cylinders with radii a_1 and a_2 at an angle θ the above equations can be cast in the form

$$G(\ell, \theta; a_1, a_2) = \frac{2\pi\sqrt{a_1 a_2}}{\sin\theta} \int_\ell^\infty \mathcal{G}(h, \theta) dh. \qquad (A.69)$$

This gives to the lowest order in the Δ's

$$G(\ell, \theta; a_1, a_2) = -\frac{\sqrt{a_1 a_2}}{8\pi} \frac{k_B T}{\ell \, \sin\theta} \sum_{n=0}^{\infty}{}' \int_0^{2\pi} d\phi \, \Delta_{\mathcal{L}m}(\phi) \Delta_{\mathcal{R}m}(\theta - \phi). \qquad (A.70)$$

Taking into account Eqs. A.40 and A.41 the angular integral is again analytically solvable for any anisotropy and leads to the following result for the interaction free energy of two cylinders of equal radii $a_1 = a_2 = a$

$$G(\ell, \theta; a) = -\frac{a \, k_B T}{4 \, \ell \, \sin\theta} \left(\mathcal{H}^{(0)} + \mathcal{H}^{(2)} \cos^2\theta \right), \qquad (A.71)$$

where $\mathcal{H}^{(0)}$ and $\mathcal{H}^{(2)}$ are obtained from

$$\mathcal{H}^{(0)} + \mathcal{H}^{(2)} = \frac{1}{2\pi} \sum_{n=0}^{\infty}{}' \int_0^{2\pi} d\phi \left(\frac{\epsilon^c_\perp(\mathcal{R})\sqrt{1 + \gamma^c(\mathcal{R})\cos^2\phi} - \epsilon_m}{\epsilon^c_\perp(\mathcal{R})\sqrt{1 + \gamma^c(\mathcal{R})\cos^2\phi} + \epsilon_m} \right) \left(\frac{\epsilon^c_\perp(\mathcal{L})\sqrt{1 + \gamma^c(\mathcal{L})\cos^2\phi} - \epsilon_m}{\epsilon^c_\perp(\mathcal{L})\sqrt{1 + \gamma^c(\mathcal{L})\cos^2\phi} + \epsilon_m} \right) \qquad (A.72)$$

and

$$\mathcal{H}^{(0)} = \frac{1}{2\pi} \sum_{n=0}^{\infty}{}' \int_0^{2\pi} d\phi \left(\frac{\epsilon^c_\perp(\mathcal{R})\sqrt{1 + \gamma^c(\mathcal{R})\cos^2\phi} - \epsilon_m}{\epsilon^c_\perp(\mathcal{R})\sqrt{1 + \gamma^c(\mathcal{R})\cos^2\phi} + \epsilon_m} \right) \left(\frac{\epsilon^c_\perp(\mathcal{L})\sqrt{1 + \gamma^c(\mathcal{L})\sin^2\phi} - \epsilon_m}{\epsilon^c_\perp(\mathcal{L})\sqrt{1 + \gamma^c(\mathcal{L})\sin^2\phi} + \epsilon_m} \right). \qquad (A.73)$$

For two identical cylinders the $\mathcal{L}$ and $\mathcal{R}$ values are the same. Again we omit writing the explicit frequency dependence of all the dielectric functions. This dependence

should be entered when numerical calculations are performed.

As above we now introduce the Hamaker coefficients according to the definitions

$$\mathcal{A}^{(0)} = \tfrac{3}{2}k_B T \, \mathcal{H}^{(0)} \qquad \text{and} \qquad \mathcal{A}^{(2)} = \tfrac{3}{2}k_B T \, \mathcal{H}^{(2)}, \tag{A.74}$$

and thus obtain for the interaction free energy of the two cylinders of equal radii $a_1 = a_2 = a$

$$G(\ell, \theta; a) = -\frac{a}{6 \, \ell \, \sin\theta} \left(\mathcal{A}^{(0)} + \mathcal{A}^{(2)} \cos^2\theta \right). \tag{A.75}$$

This is the final expression for the interaction free energy between two CNTs at a general angle θ and separation ℓ in the near limit. Note again that all the ℓ and θ dependencies are given explicitly. Again for completeness the corresponding force is given by

$$f(\ell, \theta; a) = -\frac{\partial G(\ell, \theta; a)}{\partial \ell}, \tag{A.76}$$

or

$$f(\ell, \theta; a) = -\frac{a}{6 \, \ell^2 \, \sin\theta} \left(\mathcal{A}^{(0)} + \mathcal{A}^{(2)} \cos^2\theta \right). \tag{A.77}$$

The corresponding torque is obtained straightforwardly as

$$\tau(\ell, \theta; a) = -\frac{\partial G(\ell, \theta; a)}{\partial \theta}, \tag{A.78}$$

which can be rewritten as

$$\tau(\ell, \theta; a) = -\frac{a}{6 \, \ell^2} \left(\frac{\mathcal{A}^{(0)}}{\sin^2\theta} + \mathcal{A}^{(2)}(2 + \cot^2\theta) \right) \cos\theta. \tag{A.79}$$

These are the results for two near cylinders at a surface to surface separation ℓ, at a mutual angle θ and of a common radius a. This is the fifth main result that we will use in order to quantify the van der Waals - London dispersion interaction between two cylindrical CNT's at small separations.

Examine now the interaction free energy of two identical anisotropic cylinders of radius a at zero mutual angle. In this case the interaction free energy **per unit length** can be obtained in the form ([ ], p.172)

$$g(\ell, \theta; a) = -\frac{k_B T \sqrt{a}}{16 \; \ell^{3/2}} \left(\mathcal{H}^{(0)} + \mathcal{H}^{(2)} \right), \tag{A.80}$$

where $\mathcal{H}^{(0)}$ and $\mathcal{H}^{(2)}$ are obtained in complete analogy to Eq. A.12 from

$$\mathcal{H}^{(0)} + \mathcal{H}^{(2)} = \frac{1}{2\pi} \sum_{n=0}^{\infty} {}' \int_0^{2\pi} d\psi \left(\frac{\epsilon^c{}_\perp(\mathcal{R}) \sqrt{1 + \gamma^c(\mathcal{R}) \cos^2 \psi} - \epsilon_m}{\epsilon^c{}_\perp(\mathcal{R}) \sqrt{1 + \gamma^c(\mathcal{R}) \cos^2 \psi} + \epsilon_m} \right) \left(\frac{\epsilon^c{}_\perp(\mathcal{L}) \sqrt{1 + \gamma^c(\mathcal{L}) \cos^2 \psi} - \epsilon_m}{\epsilon^c{}_\perp(\mathcal{L}) \sqrt{1 + \gamma^c(\mathcal{L}) \cos^2 \psi} + \epsilon_m} \right). \tag{A.81}$$

Of course, for two identical cylinders, the ϵ values for $\mathcal{L}$ and $\mathcal{R}$ are the same. Introducing again the Hamaker coefficient as before, we get the interaction free energy per unit length of the parallel cylinders as

$$g(\ell, \theta; a) = -\frac{\sqrt{a}}{24 \; \ell^{3/2}} \left(\mathcal{A}^{(0)} + \mathcal{A}^{(2)} \right). \tag{A.82}$$

This is now the sixth and last result that we will use to quantify the van der Waals - London dispersion interaction between two parallel cylindrical CNTs at small separations.

Appendix B

Prism Mesh

Although in its infancy, I wanted to include the prism mesh method into this thesis in case I never got around to publishing it in full. Personally, I find it to be the most exciting discovery of this entire project because of the power and flexibility that it can ultimately bring for studying vdW-Ld interactions of arbitrary shaped objects over a flat plate at all distances with spatially varying properties. The best solution would allow both shapes to vary arbitrarily, but this will provide for an adequate launch pad.

Because a thorough and glossed up introduction would take some time to create, I am posting here in it's raw hand notes and mathematica confirmation format. I've done my best job to comment where approrpriate, so it should still be fairly easy to navigate and understand what is being demonstrated and claimed. But I do apologize for not putting my best foot forward here. However I feel its far better to get this out there rather than potentially letting this disappear forever.

✸ New Analytical and Numerical "Mesh Prism" Approximation ✸

Goals:

- Resolve mixing discussion issues in the near limit
- Solve for a multi-coated cylinder at all distances.
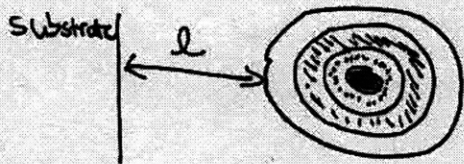
Substrate ← l →

And do so in a way that can make everyone happy! ☺

Old Way → Cyl - Substrate System Near contact via Derjaguin Approximation

← l → a as $a \gg l$

slice and use a pseudo plane-plane approach
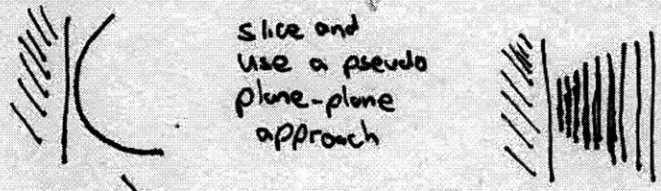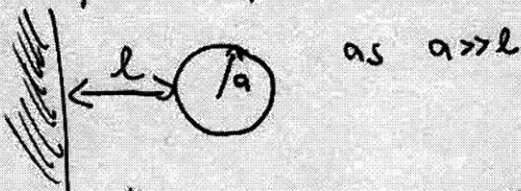
Advantages
- Analytical solutions for curved geometries!
- Can be add-a-layered to include spatially varying vdW-Ld

Disadvantages
- Near Limit only

Questions
- Can we design a new method that will work for all distances?

☆ New Proposal - slice and dice the other way! ✸

← l → ⇒ ← l → ⇨
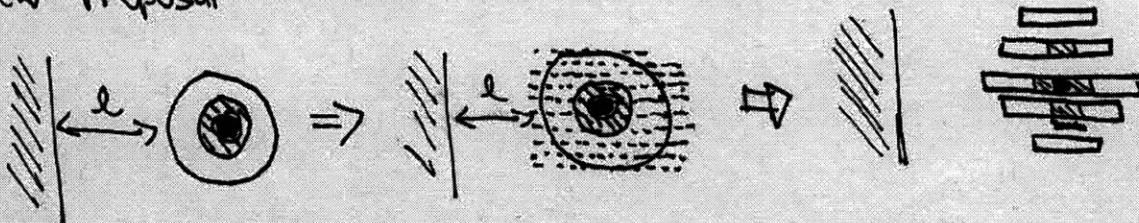
but much much finer mesh! each slice turns into an area weighted plane-plane add-a-layer solution

Advantages of this new "Prism Mesh" Approximation

- Arbitrary curvatures
    (after all, we can always cut up smaller until the
    end caps exhibit trivial separation variation from the substrate)
- Arbitrary distances
    plane-plane Add-a-layer does not have distance restrictions
- Numerically simple
- Arbitrary spatial variation of optical properties

5 Level Approach

Level I → prove "Prism Mesh" volume-volume integration
    is equivalent to the exact cyl-surf solution
    at all distances

Level II → Total Energy Algorithm

Level III → Effective Hamaker coefficients for arbitrary
    layers at all distances

Level IV → Far limit equivalence / self consistency with
    EMA Bruggeman mixing rules

Level V → Analytical add-a-layer formulation
    for the Surface-cylinder system.

- Each level builds upon the previous
- Sanity checks at each level
- Stress test for cases that can break this approximation
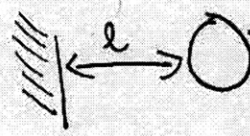
★ **Level I** Volume – Volume Integration
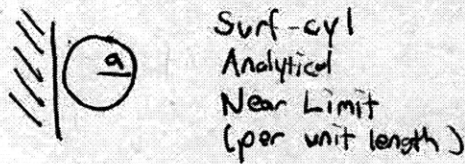
Surf-cyl
Analytical
Near Limit
(per unit length)

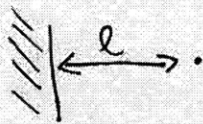$$G(\ell) = -A \frac{\sqrt{2a}}{24 \, \ell^{3/2}}$$
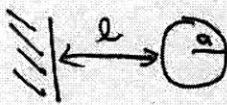
Surf-cyl
Analytical
Far Limit
(per unit length)

$$G(\ell) = -A \frac{\pi a^2}{6\pi (\ell+a)^3}$$

Surf-cyl
Integration
all distances
(per unit length)

$$G(\ell) = -A \int_{\theta=0}^{2\pi} \int_0^a \frac{r \, dr \, d\theta}{6\pi (\ell + a + r\cos\theta)^3}$$

Surf-point
pre-point volume integration
per unit volume of point

$$G(\ell) = \frac{-A}{6\pi \, \ell^3}$$

⇒ This last case can be integrated over any volume on the right hand side to obtain the total vdW-Ld energy for a given Hamaker coefficient A.

⇒ Need to have Mesh Prism Approximation match the Surf-cyl Integration case to be valid

★ **Prism Mesh Volume Integration** uses the plane-plane add-a-layer for

Left medium   Layer medium

$$G(\ell) = \frac{-A_{Lm/Rm}}{12\pi (\ell)^2} \cdot \frac{A_{Lm/mR}}{12\pi (\ell+a)^2}$$
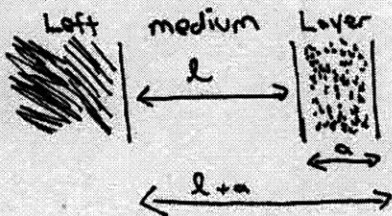
and since $A_{Lm/Am} > -A_{Lm/mR}$

$$\boxed{G(\ell) = -A_{Lm/Am} * \left[\frac{1}{12\pi \ell^2} - \frac{1}{12\pi (\ell+a)^2} \right]}$$

★ we need to apply this for every slice, which means we need an accurate ℓ and "a" for each slice.

☆ Level I continued
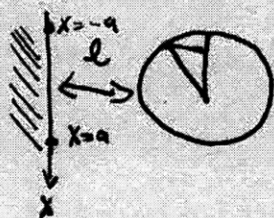
at a given surface location "x", the seperation to the near edge is

$l + a - \sqrt{a^2 - x^2}$ and the far side is

$l + a + \sqrt{a^2 - x^2}$

The overall energy is thus

$$G = \sum_{x=-a}^{x=a} -dx \; A \left[\frac{1}{(l+a-\sqrt{a^2-x^2})^2} - \frac{1}{(l+a+\sqrt{a^2-x^2})^2} \right]$$

→ where $dx \approx \frac{a}{20}$

☆ Equivalency Test

— comparing the ⊕ Surf-cyl integration with the Prism Mesh Summation at all distances of l from ~~0.05~~ 0.05 to 50 nm, we found a discrepancy maximum of 0.04%. Therefore the discretization does NOT introduce any artifacts at any distance!
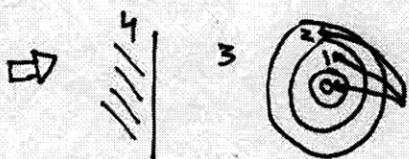
☆ Level II — The Algorithm

   — The solid cylinder case in Level I didn't really gain us anything because it was still ONE material. Now we move to the more difficult cases.

Notation: For reasons that will make sense later, the following terms/Notations are used.

⇒ $vdW\text{-}Ld(i\xi) = 1 + \frac{m}{1+\xi}$ is the form of the dummy oscillators used to represent material properties. m=0 represents vacuum

⇒ The inner material is 0 up until the number of coatings. In this case, it is 2. The medium is +1 on this number, the Left half space +2.
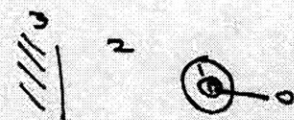
 An alternate setup would be here.

    imax = number of coatings on the original cylinder. In the first case, it is 2, on this last one, imax=1.

⇒ Rad(i) → Array of the cylinder radii. Rad(0) would be the inner cylinder. Rad(1) would be coating 1.

~~⇒ Chord(i,x) Array of the Rad laters~~

⇒ Chord(i,x) Array of the chord lengths as a function of position and ~~the original~~ the layers original radius Rad(i)

⇒ Aspec $[3,2,1,2] = A_{32/12} = \sum_{m=0}^{\infty}\left(\frac{\xi_3-\xi_2}{\xi_3+\xi_2}\right)\left(\frac{\xi_1-\xi_2}{\xi_1+\xi_2}\right) * \frac{3}{2}kT$

⇒ Aeff → effective Hamaker coefficient

⇒ Eslice → total vdW-Ld energy of a slice at position x

⇒ Etotal → Algorithm summing up all Eslices

⭐ Level 2 continued.

→ This may look ugly, but if you go through all of the steps, you'll find out it gives exactly the Hamalter coefficient ordering and correct chord lengths.
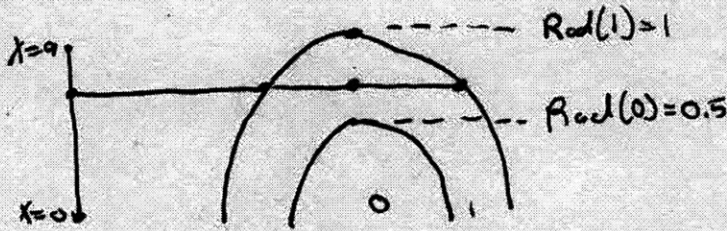
⟹
$$\text{Chord}(x)$$
$$\text{For } [\,i=0;\; i \leq i_{max};\; i{+}{+}$$
$$\quad \text{if } |x| < |\text{Rad}(i)|$$
$$\qquad \text{chord}(i) = \sqrt{\text{Rad}(i) - x^2}$$
$$\quad \text{else}$$
$$\qquad \text{chord}(i) = 0$$
$$]$$

A chord of "0" means that at this particular value of x, there is no gap for material "i" and thus the

$$\frac{1}{(\ell + dx)^2} - \frac{1}{(\ell + dx)^3} \text{ terms}$$

cancel out!

⟹ $$E_{slice}(x, \ell) = \sum_{i=0-i_{max}}^{i=i_{max}+1} - \frac{A_{spec}[i_{max}+2, i_{max}+1, |i|, |i-1|]}{12\pi \left(\ell + \text{Rad}(i_{max}) + \frac{i - 0.5}{|i-0.5|}\text{chord}(\text{Rand}(|i-0.5|)-1)\right)^2}$$

⟹ $$E_{total}(\ell) = \sum_{x=-a}^{x=a} dx \cdot E_{slice}(x, \ell)$$

⭐ Numerous Test cases were run for this level. The final check was creating a ⥮↔◎ system where Materials 0 and 1 (ie the core and first coating) where given an identical vdwld spectra. The results were compared to

$$A \pm \int_{\theta=0}^{\pi} \int_{r=0}^{\text{Rad}(1)} \frac{r\,dr\,d\theta}{6\pi \left(\ell + \text{Rad}(1) + r\cos\theta\right)^3}$$

and the difference was 1.1%

Level ❶III→ Effective Hamaker Coefficient

⇨ We all know that $G = -A *$ geom factors, so to back out a total A_{eff}, we simply divide the value of E_{total} from the Prism mesh approximation by the volume volume integration.

⇨ Ideally we test and compare against the forward direction solution to see how close they compare. Again, let's set the outer coating to have the same properties as the core.

$m=7 \begin{array}{c} i=2 \\ m=1 \end{array}$

$i=3$

$i=$ index number/ordering
$m=$ oscillator magnitude

$i=1$
$m=5, i=4$

$$A[3,2,1,2] = A_{32/12} = 48.73z)$$

$$E_{total}(l=50nm) / \iint \frac{1}{6\pi(l+\ldots)^3} = 48.17z)$$

$$E_{total}(l=0.05nm) / \iint \frac{1}{6\pi(l+\ldots)^3} = 48.73z)$$

⇨ After this test case we can see that forward or backward results in the same magnitude. Sanity checks where run with all types of oscillator magnitudes and the discrepancy never exceeds 1-2% and is usually almost nil.

☆ Non-uniform Test cases

Now we can begin to see the effects of different layers on the effective Hamaker ~~coefficient~~ with distance. Let us analze the extreme limit when we have a mix of attractive and repulsive interactions

$m=8 \mid m=4$

$\xleftarrow{l}$

$m=2$

$i=1$

$\bar{i}=3 \mid \bar{i}=2$
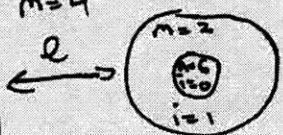
Rad(i) = 1 nm
Rad(o) = 0.5 nm

The 8→4→2 sequence is repulsive.
The 8→4→6 sequence is attractive.
The attractive core is only 25% of the total area.

☆ Level ~~●~~ III continued.

Now ● let's compare Magnitudes

$A[3,2,1,2] = -13.44 zJ$ (interaction of surface with coating)

$A[3,2,0,1] = 10.96 zJ$ (interaction of surface with core)

$A_{effective} = -7.88$ in far limit.   since repulsive coating is large this is exactly as expected

$A_{effective} = -13.83$ at ~~contact~~.   Therefore core is still ~~influ~~

$l = 0.1nm$ influencing a little bit at near contact.

And Graph

↑ fairly converged after ~ 3nm or so even for this extreme case.

(Axis labels: A_{eff} (zJ), vertical: -7, -8, -9, -10, -11, -12, -13; horizontal: 0.1, 1nm, 2nm, 3nm; x-axis labeled x)

☆ Note... If we drop l from 0.1 to 0.01, $A_{eff} = -13.45$, which is then identical to $A[3,2,1,2]$ of -13.44 in the forward direction. Thus at contact, the outer material completely dominates and no mixing is needed.

⇒ However... the beauty of the Prism Mesh approximation is that mixing is taken into account automatically!
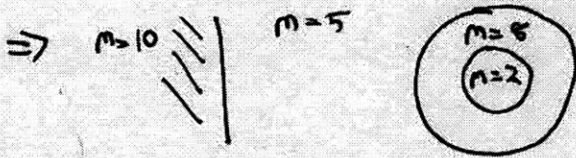
Level IV — Comparing Prism Approximation to EMA of Solid Cylinder

⇒ Here we put the approximation and the EMA to the test, because if they are both truly working, then they should agree right out of box in the far limit

⇒ m=10 ∥ m=5

Rad(i) = 1 nm
Rad(o) = 0.5 nm

⇒ Again, we pick the most difficult case when there is a mix of attraction and repulsion. The all attractive and all repulsive setups have much smaller discrepancies

⇒ EMA of m=8 and m=2 at 25-75% ratio
= m = 6.14

 VS
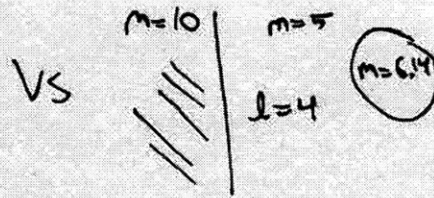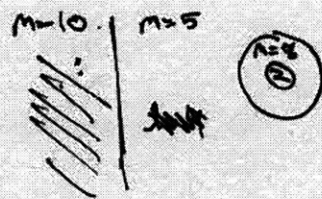
$l=4$ $A_{eff} = 7.71 z$]
$l=10$ $t_{off} = 7.36 z$] ⟷ $A_{eff} = 7.59 z$]

— This is pretty awesome!

⇒ The all attractive and all repulsive cases had values on the order of 0.5 - 0.05% discrepancy.
So this attractive/repulsive case is the worst case by far, and it is pretty solid.

⭐ Level V — Analytical cyl-surface add-a-layer

⇒ With the success of the previous EMA vs Mesh Prism Approximation, I decided to go the final step and see if I could get the convergence of EMA, Mesh Prism, and analytical add-a-layer. To get all 3 would... be a thesis!

⇒ Luckily the first test function I tested was the one that ultimately worked.

$$IntCylSurf(a, \ell) = \int_{0}^{2\pi}\int_{0}^{a} \frac{r\,dr\,d\theta}{c\pi(\ell + a + r\cos\theta)^3}$$

$$E_{total} = -A[3,2,1,2] * IntCylSurf(Rad(1), \ell)$$
$$-A[3.2, 0,1] * IntCylSurf(Rad(0), \ell + Rad(1))$$
$$-Rad...$$

Rad(1) = 1
Rad(0) = 0.5

Essentially the form is identical to the plane-plane case with the ~~addition coefficients~~ addition of the radius consideration.

Comparisons

I'll first start with an easy case and then move to an extremely complex 4 layer attraction/repulsion system.

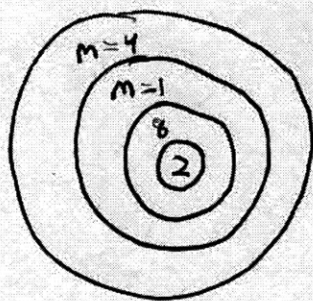CASE 1 — All attractive, 1 coating

n=10 | n=1

Prism Mesh Near Energy = −52.1522 ω
Analytical Near Energy = −52.22

Prism Mesh Far Energy = −0.01075
Analytical Far Energy = −0.01044

Level $\underline{V}$ continued.

Difficult Case

m=10 | m=5

$R(3) = 2$
$R(2) = 1.5$
$Radius(1) = 1$
$Rad(0) = 0.5$

Note alterating attraction and repulsion w/ Left half space!

Prism Mech Near Energy = 5.23
Analytical Near Energy = 5.18
Prism Mech Far Energy = 0.0151
Analytical Far Energy = 0.0155

So... EMA matched Prism which matches analytical. And Life is good.

Final Thoughts

- The mesh prism (gotta come up with a better name!) has several advantages ~~or~~ over the ~~particular~~
  - EMA version, mainly that it already interpolates between the endpoints without the need of defining "limits"
- For systems like ssDNA wrapping a SWCNT, this method is perfect because it can handle partially coated surfaces. No "mixing" is required to get an effective coating percentage.

- Works for shapes not easily defined by smooth curves or sharp edges.

- Can contain retardation just like plane-plane add-a-layer.

Few Pitfalls

- Currently requires other object to be a semi-infinite substrate for all the scaling to hold true.

- Still can't do Anisotropy + Retardation simultaneously because it doesn't exist in the add-a-layer formulation

- Lose control of ~~an~~ an easy to tinker with analytical solution... at least far beyond Cylinder-surface.